Silicon Based Direct Methanol Fuel Cells

Larsen, Jackie Vincent

Publication date:
2013

Document Version
Publisher's PDF, also known as Version of record

Silicon Based Direct Methanol Fuel Cells

Jackie Vincent Larsen

Supervisor: Erik V. Thomsen

Department of Micro- and Nanotechnology

Technical University of Denmark

September 15, 2013

Contents

Abstract

The purpose of this project has been to investigate and fabricate small scale Micro Direct Methanol Fuel Cells (μDMFC). They are investigated as a possible alternative for Zinc-air batteries in small size consumer devices such as hearing aids. In such devices the conventional rechargeable batteries such as lithium-ion batteries have insufficiently low energy density. Methanol is a promising fuel for such devices due to the high energy density and ease of refueling compared to charging batteries, making μDMFC a suitable replacement energy source.

In this Ph.D. dissertation, silicon micro fabrication techniques where utilized to build μDMFCs with the purpose of engineering the structures, both on the micro and nano scales in order to realize a high level of control over the membrane and catalyst components.

The work presents four different monolithic fuel cell designs. The primary design is based on a perforated silicon plate which acts as a mechanical support structure a proton conducting polymer membrane, which connects catalyst layers deposited through spray coating on either side of the silicon device.

An improvement of this design is also presented which integrates the catalyst layer into the current collector electrodes. This design is based on catalytic in situ growth of carbon nanotubes and atomic layer deposition of active catalyst particles.

The additional two fuel cell designs utilize a porous silicon structure as the mechanical support, using respectively a spray coated catalyst and atomic layer deposition for. This method of integration was investigated as a high internal volume support structure with potential for rapid batch fabrication.

In characterization of the devices the work presents the development of an electrochemical impedance spectroscopy measurement setup capable of determining the ionic conductance of the devices. Along side this a simple model for the ionic conductance is developed.

A theoretical framework for the device performance is developed, and amongst the chief theoretical results are the determination of the tradeoff between conductivity and cross-over which results from variation in the path length through the proton conductive phase. In addition the trade-off between mass transfer losses and activation losses deriving from the catalyst layer density is developed.

Resumé

Formålet med dette projekt har været at undersøge og fabrikere små Micro Direct Methanol Fuel Cells (μDMFC). De er blevet undersøgt som et muligt alternative til zink-luft batterier til brug i høreapparater. Da litium batterier har for lav energi tæthed er der ikke mange genopladelige muligheder for sådanne apparater. Methanol brændselsceller er en lovende mulighed grundet den højre energi tæthed af metanol og muligheden for hurtig og nem genoptankning. Dette gør μDMFC til en passende erstatnings energikilde.

I denne Ph.D. afhandling, bliver silicium fremstillingsteknologier anvendt til at fremstille μDMFC med henblik på at strukturere dem på mikro- og nano-skala for at opnå et forøget niveau af kontrol over den proton ledende membran og katalyse lagene.

Arbejdet præsentere fire forskellige monolitiske brændselscelle designs. Det primære design er baseret på en perforeret silicium plade, der fungerer som en mekanisk støtte struktur for den proton ledende membran, der agerer som forbindelse mellem spray-coatede katalyselag på hver sin side af cellen.

Et forbedret design bliver samtidigt præsenteret, hvor katalyselagene er integrerede i elektroderne. Dette design er baseret på in-situ katalytisk vækst af kulstof-nanorør hvor atomic layer deposition teknikken anvendes til at definere katalyse partikler.

En teoretisk ramme for enhedernes ydeevne bliver udviklet, og bland de primære resultater er konklusionen at der er en afvejning mellem protonledningsevnen og diffusionen af brændstof gennem membranen alt afhængig af længden gennem den protonledende fase. Samtidigt fremvises en lignende afvejning mellem mass-transfer tab og aktiveringstab afhængig af katalyse lagets densitet.

Preface

This thesis is submitted as a partial fulfillment of the requirements to obtain the Ph.D. degree at the Technical University of Denmark (DTU). The work has been carried out at the Department of Micro- & Nanotechnology (DTU Nanotech) at DTU in the period between the 15. September 2010 to 16. September 2013. The project has been supervised by professor Erik Villain Thomsen. The project is a part of the 3 year project MicroPower.DK, which was funded by The Danish National Advanced Technology Foundation, and constitutes a collaboration between DTU Nanotech, The Danish Technological Institute, Aalborg University and the hearing aid manufacturer Widex. The vision of the MicroPower.DK project is to allow the creation of fuel cell powered hearing aids, with the hopes of increasing the power density compared to zinc-air batteries, and allowing rechargeable cells. Towards this goal, the focus of this Ph.D. project has been to investigate the potential of using clean-room technology in the down scaling efforts of fuel cell technology with the hopes of allowing improved performance and more control over the design on the micro and nanoscale.

Acknowledgments

I would like to thank my main supervisor professor Erik Villain Thomsen for his enormous support and valuable guidance throughout the project. I would also like to thank assistant professor Bjarke Thomas Dalslet for his collaboration on the project and valuable discussions. I would also like to thank the extremely talented employees of The Danish Technological Institute, who it was a pleasure to collaborate with, in particular Christian Kallesøe, Torsten Lund-Olesen and Jan Harry Hales for their continual input on the direction of the project as well as Christian Madden and Kenneth Brian Haugshøj for their aid in fabrication.

I would also like to thank the many hard workings students I have supervised; Joachim Thomsen, Sara Engberg, Søren Gregersen, Louise Møller Borregaard, Kaspar Haume, Mikkel Maag Pedersen, Alexander Bagger, Kristoffer Skaftved Mathiesen, Kasper Ingerslev, Nicolai Frost-Jensen Johansen, Birgitte Bakke, Mathias J. G. Mølgaard, Kim Christiansen and Milan Laustsen, all of which contributed meaningfully to the project.

I would also like the thank the employees at DTU Danchip, who maintain the equipment that made this project possible, and have provided valuable instruction and education in its use and function through the project.

Finally I would like to specially thank my significant other, Maja Lind-Nielsen for her moral and editorial support through the final periods of the project.

Jackie Vincent Larsen

Kgs. Lyngby September 16. 2013

1 Introduction

Portable power sources are today used in a wide range of application areas, such as in consumer electronic devices, medical devices and backup power sources. The requirements varies widely based on application, and for many of these uses, fuel cells are a new potential energy source which comes with the potential of higher energy densities, higher efficiencies and more even the prospect of sustainable production of the fuels to fight global warming. Since the 1970's the prospects of a hydrogen society have been raised [1], with the dream being that the needs for portable power in our future society would be provided by hydrogen which burns cleanly to water and thus solves the problem of pollutants emitted through the burning of hydrocarbons. The hydrogen itself could be created from sustainable sources such as through electrolysis of water using wind turbines or even directly through photocatalytic splitting of water [2]. Hydrogen however has its problems as a energy storage media and has not fared well as a replacement for hydrocarbons, and in most larger application areas for portable power, hydrocarbons are still dominant.

Depending on the specific application the requirements and thus applicability of

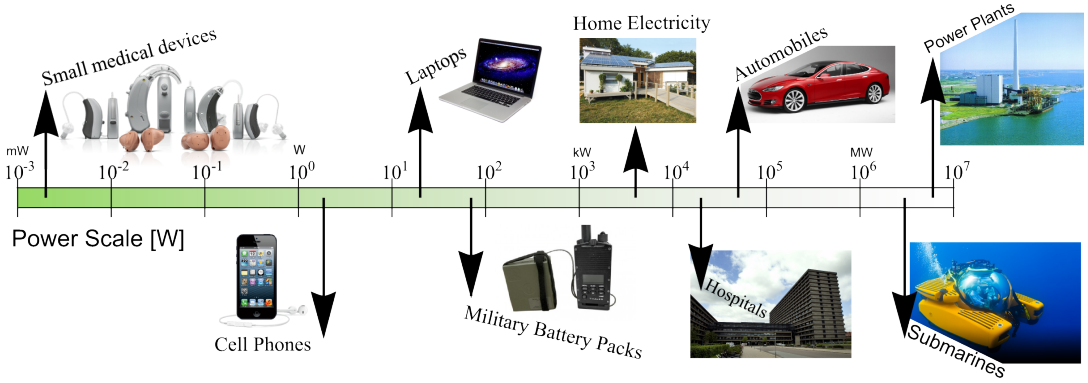

Figure 1.1: Power requirements of a range of application areas where fuel cells show promises for the future. The figure also shows the power usage of power plants for comparison.

different types of portable energy storage will vary. Figure 1.1 shows an overview of several application areas where fuel cells show promise as a future power source. As can be seen, both the power requirements and scale of operations vary by several orders of magnitude. Fuel cells could for instance be used as uninterruptible power sources to supply emergency power at hospitals which today uses diesel generators, or as power generators for houses that are expensive to connect to the power grid. For such an application the total weight and volume of the fuel cell systems are of less consideration compared to reliability and performance, therefore systems weighing tons and taking up multiple cubic meters can still prove competitive. Fuel cell systems can however also be envisioned as power sources in areas such as mobile phones and laptops in the future. Consumer products are already available, like the powertrekk myFC [3], which act as chargers for phones and other small electronic devices. The fuel cells systems used in these devices are however still to large in volume to be considered for internal usage in the electronics devices themselves. For consumer electronics in modern times, size is of the essence.

A multitude of small scale electronic devices have become part of peoples daily lives. Devices such as mobile phones, digital music players, laptops and digital cameras have become common to the point where they are no longer considered just luxuries but rather just everyday tools of communication and productivity. Small scale electronic medical devices have also begun to play a vital role in the lives of people such as diabetics who rely on blood sugar measuring devices to balance their daily sugar intake, and hearing aids provide a boost to the diminished hearing capability of the hard of hearing. The barrier to further down-scaling of such devices have historically been the complex electronic circuitry needed for their operation, however, the evolution of electronic have made them a much smaller concern size-wise in current generation devices.

The last two decades have seen an accelerated down-scaling trend in consumer electronics devices. The potential for smaller devices has in large parts been brought on by the continual down scaling of both semiconductor technology and electronics. A fixed element of electronic devices which has however not seen a large improvement towards down-scaling of size, is the battery technology. While battery technology has increased in merits such as charge cycles and longevity [6], it has not seen large increases in power density as shown in figure 1.2. This has meant that batteries has stayed the same size while the devices they powered decreased in size. To increase device lifetimes the path forwards has been to increase the power efficiency of the electrical components. This is expected as power density cannot exceed the theoretical maximum for the particular chemistry chosen for the battery. Therefore as a

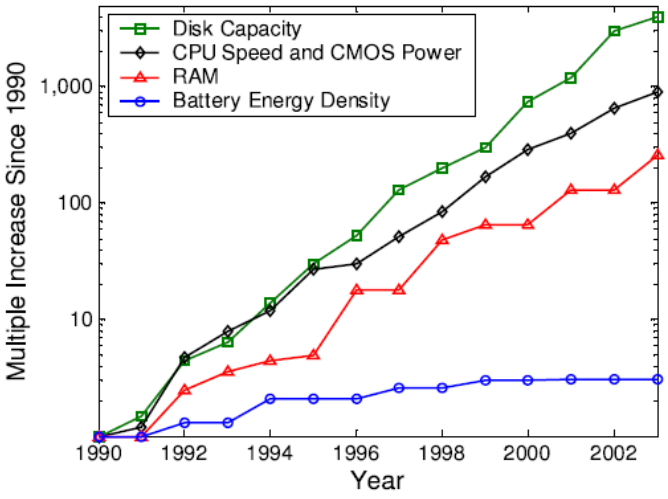

Figure 1.2: The plot shows the development of disk capacity, CPU speed and RAM sizes as well as the development in battery energy density of lithium batteries in a log-linear plot. While the electrical component lines are seen to follow a Mores law incremental development, the battery energy density saturates around the year 1999, as it gets closer to the theoretical limits. Figure from [4], data from [5].

given technology matures and efficiency is steadily increased, the return on investment with respect to energy capacity decreases. As a consequence manufacturers of mobile devices pursue longer battery lives primarily through focus on down-scaling energy requirements of the electronics rather than investing in research targeting improvements of the batteries.

Figure 1.3a provides an overview of several energy storage technologies, showing the achievable peak power densities as well as specific energy densities. The comparison shows that few alternatives to gasoline exist when considering specific energy density. It is, however, possible to achieve almost similar peak powers with lithium batteries as well as methanol fuel cells. In the region of high power output, super-capacitors and advanced flywheels are the best performers. Flywheels are rotating disks that amongst other uses are employed to store the energy generated during braking for buses and trucks. With respect to small mobile electronics devices we see that the different chemical battery technologies are mostly in similar power range, but with zinc-air having the highest specific energy density. The batteries are, however, surpassed by both methanol and hydrogen fuel cells. Table 1.1 shows a comparison of battery types along side the theoretical values for methanol. It is shown that rechargeable lithium-ion batteries have lower energy density than typically one-use alkaline batteries. Even so this technology is by far the preferred in mobile devices as they are rechargeable. When moving into the small device region the non-rechargeable zinc-air is the preferred battery due to the need for a

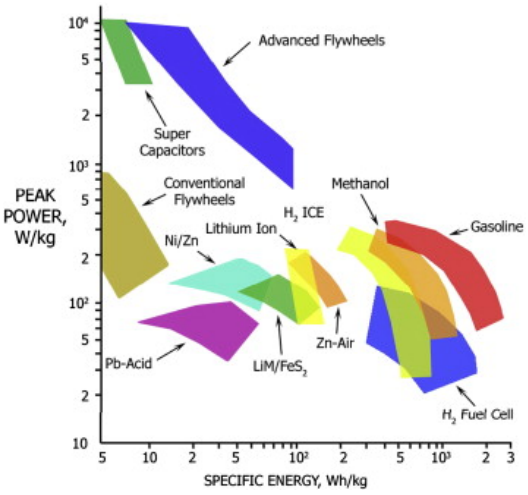

(a) The figure highlights the achievable specific energy density vs. volumetric energy density regions of different energy storage schemes.

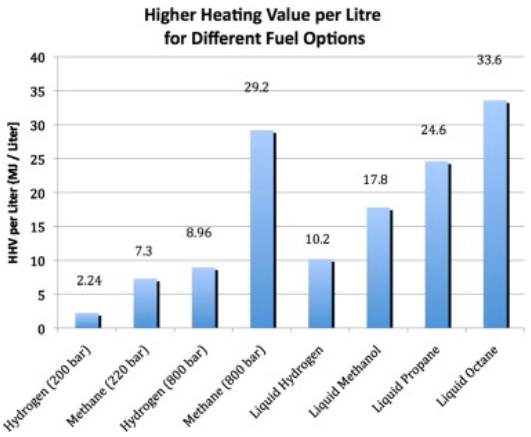

(b) Specific energy density of various fuels.

Figure 1.3: Comparison of various energy storage and delivery systems. Reference [7].

higher energy density than can be provided by lithium-ion technology. While small increases in lithium battery densities can still be achieved there are not prospects for significantly increasing energy density. Methanol is therefore an interesting alternative as it holds a much higher potential energy density compared to lithium-ion as seen in figure 1.3b, and is refueling is relatively easy.

Smaller consumer gadgets like flashlights, portable radios etc. will typically operate using alkaline batteries such as the Duracell AA battery listed in table 1.1. For mobile phones such batteries have, however, proven insufficient due to poor rechargeability and here the current market leaders are using lithium-ion batteries, but the form factor has not been the target of standardization due to high levels of competition in the market. For smaller devices such as watches, the typical total size of lithium and alkaline batteries have lead to reliance on primarily zinc-air based button cell batteries, which refer to small cylindrical standards of form factors. In hearing aids, the current state of the market is that they are operated almost exclusively on button cell zinc-air batteries, with only a small fraction operating with rechargeable systems such as miniature lithium-ion batteries or Nickel-Metal Hybrid (NiMH) batteries. Such systems, however, put severe restrictions on the hearing aids operating power consumption due to the very low energy capacities, with state of the art NiMH's having below 1/20 the capacity of zinc-air button cells.

The years 2000 to 2005 saw a large increase in the number of publications on methanol fuel cells as seen in figure 1.4. The primary focus of the general methanol fuel cell technology is for larger stack system, which are targeted towards power

	Alkaline Duracell AA	Lithium-ion	Zinc-air cell, A13	PowerOne p 13, NiMH	Methanol Theoretically
					
Rechagable	No	Yes	No	Yes	Yes*
Nomial cell potential [V]	1.5	3.6	1.45	1.2	1.2
Volumetric Energy density [wh/L]	320	190	1343	280	4400
Graviometric Energy Density [wh/kg]	130.4	170	403	100	5473
Current capacity [mAh]	700	970	310	31	–
System Volume [μL]	7774	249 885	265	265	–
Volumetric Charge capacity [mAh/μL]	0.090	0.0039	1.17	0.12	3.97

Table 1.1: Table illustrating the electrical properties of different types of energy storage systems. *Rechargeable through refueling. [8, 9, 10]

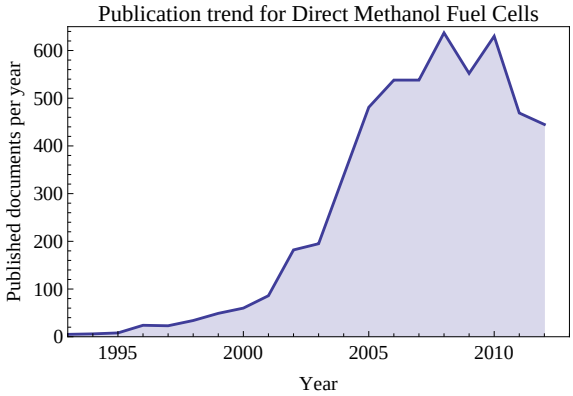

Figure 1.4: Publication trend for direct methanol fuel cell research. Numbers from SciVerse ScienceDirect [11].

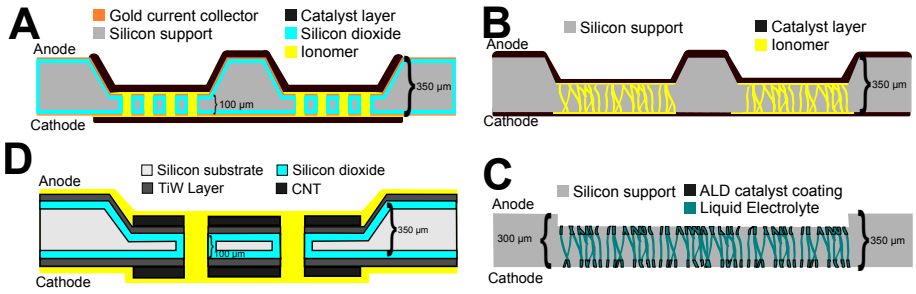

Figure 1.5: Overview of the four device types developed during the project. A and B rely on a conventional spray coated catalyst layer, while C and D utilize an integrated catalyst layer through atomic layer deposition (ALD). The devices A and D rely on a plate perforation to integrate the membrane while devices B and C are based on porous silicon.

sources for buses, trucks or ships. These larger systems are also being developed to act as local power and heating generation for houses [12]. When considering smaller scale systems, particularly systems based on Proton Exchange Membranes (PEM), are popular. These are typically based on Nafion. Nafion is a PolyTetraFluoroEthylene (PTFE) based copolymer with sulfonic acid groups. Nafions forms a solid matrix hydrophobic backbone when cured, and allows proton conductance through highly acidic hydrophobic regions permeating this matrix. The major advantage of Nafion lies in its high mechanical strength, high proton conductivity and long lifetime. For larger scale fuel cells the major disadvantage of Nafion is that operation becomes difficult above 80°C, and higher working temperatures are typically desired in order to minimize carbon-monoxide poisoning. For room temperature operation of smaller fuel cells intended for portable devices this temperature limitation is of less importance as the working temperatures will be far below 80°C.

While PEM based methanol fuel cells are a promising candidate as power sources for small devices, they do have several disadvantages. The practical energy efficiency is limited greatly by the methanol cross-over effect, where methanol diffuses through the proton conductive membrane. PEM fuel cells also rely on expensive noble metal catalysts like platinum and palladium. The challenge of methanol-cross over is typically addressed in research by engineering the chemical structure of the membrane or including additives in order to lower the permeability of methanol at the expense of the conductivity. This work will present a different approach which is based on mechanical engineering of an integrated membrane.

1.1 Project Outline

The working hypothesis of this project is that the integration of the polymer membrane into the silicon process can lead to benefits in the form of increased mechanical

support, better dimensional control, and that it opens up new potentials for micro and nanostructuring of catalyst layers using clean room technologies. The project deals with this integration process and studies two separate methods of creating the mechanical support structure through ionomer integrations into a micro perforated silicon plate structure and into a porous silicon plate. Catalyst integration has been accomplished both using conventional spray coating techniques, but also through in-situ growth of catalytic particles on the microstructures supporting plates. The four major device designs are shown for overview in figure 1.5, and will be covered in more detail in the following chapters. Specifically the full fabrication of design Type A will be covered in chapter 4. The characterization of these devices is covered in chapter 5. Device designs B and C are based on a much simpler porous silicon fabrication process and will be covered in chapter 6. Device design D is an improvement on design A, which integrates catalyst layers directly into the current collector electrodes, this design will be the focus of chapter 7.

Chapter Overview

The following will describe briefly the structure of the thesis.

Introduction to Fuel Cell For Small Scale Power Storage

This chapter discusses the working principles of fuel cells in relation to down scaling and describes the state of the art for silicon based micro fuel cells.

Theory of Direct Methanol Fuel Cells

This chapter goes through the theoretical aspects of the methanol fuel cell operating principles.

Design and Fabrication of a Semi-Monolithic Silicon Direct Methanol Fuel Cell

This chapter goes through the details of the fabrication of a perforated silicon plate based fuel-cell (Type A device).

Device Characterization

This chapter describes the characterization of the perforated silicon plate (Type A device) based fuel-cells, and the conclusions drawn from the results.

Porous Silicon Based Methanol Fuel Cell

This chapter describes an alternative approach to fabrication of the membrane support structure through a metal assisted chemical etch procedure used to create porous silicon plates. It also covers performance results of type B and C device types.

Integrated Carbon Nanotube Supported Catalyst Layers

This chapter describes the effort to create an integrated nano-structured catalyst layer through use of catalytic growth of carbon nanotubes and atomic layer deposition techniques (Type D device).

Conclusion

This chapter contains a summarisation of the important results gained throughout the work, as well as a perspective for the future application of the developed devices towards hearing aid applications.

2 Introduction to Fuel Cells For Small Scale Power Storage

This chapter will provide a general introduction into the working principles of fuel cells. The chapter will expand upon the merits of silicon technology in down scaling of fuel cells, with particular focus on the most widely used bi-polar plate design, as well as a discussion about novel alternatives such as the flow channel design.

2.1 Fuel Cell Operation

Fuel cell systems vary greatly in size depending on their intended application area. They range from large units weighing several tons used to provide heat and electricity to houses, so called Micro Combined Heating Power systems (μCHP), to smaller portable units intended for phone and laptop recharging. Figure 2.1a shows a μCHP system developed by the company IRD, and figure 2.1b shows the active fuel cell stack consisting of several layers of what is called a Membrane Electrode Assembly (MEA)s. The fundamental operational principle in fuel cells is not dependent on system size, though the auxiliary components for larger systems increase greatly in complexity. At the core the fuel cell is generating electrical energy by the physical separation of a combustion process onto two separate catalytically active electrodes. These electrodes aid the reaction through donating and accepting electrons which leads to the electrical current. At the anode a fuel is oxidized, while oxygen or an oxidizing agent is being reduced at the cathode. Depending on the system size, the transport mechanism of the fuel will vary greatly. For gas phase fuels, closed pressure control and flow systems are necessary, and these fuels are therefore limited to usage in larger scale systems. Liquid fuels have less requirements on the feeding system, and can therefore be used in smaller systems, even down to the smallest scales where pumps cannot be used and the fuel transport happens passively, typically through

(a) Graphical illustration of a $600 \times 381 \times 482$ mm, 50 kg, μCHP by IRD, with specification of 800 W electrical power and 2 kW heating power.

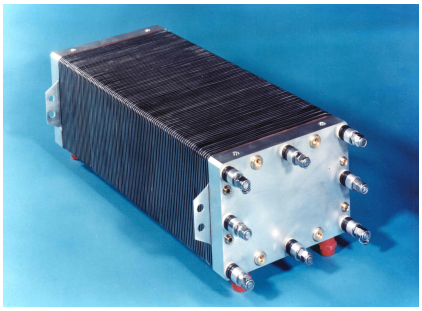

(b) The MEA stack component of a large fuel cell system, showing the many layered MEAs as well as gas inlets to the gas diffusion layers that deliver fuel and oxidant to the catalytically active regions.

Figure 2.1: The figures show the complete and central components of a μCHP system developed by IRD.

diffusion or capillary action.

2.2 Fuel Considerations

A central element of any fuel cell is naturally the origin of the energy that it supplies. The origin could be summed up to being the combustion of the fuel, but the details are of course more involved. Combustion is a redox reaction occurring between the fuel and an oxidant, which is typically oxygen, supplied either pure or in ambient air. The driving force of the reaction is the energy difference between the produced chemical species and the fuel and oxygen in their original states. The energy released in a combustion can be measured by considering a closed volume with a fuel/oxidant mixture. The mixture is heated to the point of combustion and allowed to expand in volume to keep the pressure constant. The measure attained from such a measurement is termed the value of heating. Two measures are typically given for a fuel / oxidant reaction; the lower value of heating (LHV) and the upper value of heating (HHV). These measures differ by the fact that the upper value of heating considers the case where the produced chemical species are not in their equilibrium state. Considering as an example a hydrogen/oxygen reaction, $H_2 + 1/2\,O_2 \Rightarrow H_2O$, where the resulting water is in vapor form, the energy released would be the LHV, while if the heat from the water vapor is also captured, the energy release would be the HHV. Thus the higher heating value includes the latent heat of formation required to put the reaction products into the equilibrium states.

Fuel		HHV [kJ/mol]	Molar volume [cm^3/mol]	Energy density [kJ/cm^3]
Hexamine	$(CH_2)_6 N_4$	4200	105.4	3158
Benzene	C_6H_6	3270	89.1	3731
Propanol	$CH_3CH_2CH_2OH$	2020	74.1	2514
Acetylene	C_2H_2	1300	23.7	1185
Ethanol	CH_3CH_2OH	1300	58.4	1648
Methanol	CH_3OH	726	40.4	917
Hydrazine	NH_4	622	31.4	609
Ammonia	NH_3	382	23.3	523

Table 2.1: Higher heating values per mole of a range of potential fuel cell fuels.

Fuel Types

Any chemical compound which can store energy could be classified as a fuel, the term is, however, most often used to describe different classes of hydrocarbon compounds, which generate energy through combustion to water vapor, carbon dioxide and potentially other side products. As seen in table 2.1, liquid fuels with larger energy densities than methanol are available, some are even very similar to methanol such as for instance ethanol or propanol, which simply have more carbohydrate chains. The reason these fuel types are not as popular for use in fuel cells is that the long hydrocarbon chains need to be broken down incrementally, which can lead to the formation of unwanted by products such as amorphous carbon which creates a physical blockage of the electrode surface. In electrochemical cells, it is therefore preferred to work with simpler fuels which do not posses carbon-carbon bonds. Direct ethanol fuel cells however have been pursued as a competitor to direct methanol fuel cells. Here the detrimental effects of the non-dissolved byproducts is balanced against the non-toxic nature of ethanol compared to methanol neurotic effects. The development of catalysts capable of complete combustion of ethanol to carbon dioxide is therefore an active field of study.

Hydrazine is a promising fuel which is very similar to methanol in that it is a simple chemical N_2H_4, which decomposes directly though hydrogen to water and components already in ambient air as shown by the composition of ambient air in table 2.2. Research into fuel compositions studying methanol/hydrazine mixtures have found that current contributions from formic acid and hydrazine were additive, however co-poisoning still proved to limit the currents [13]. In addition to hydrazine being strongly corrosive, it is also more expensive and toxic than methanol. Nevertheless in small scale usage it could be speculated that the problems of toxicity

Compound	N_2	O_2	Ar	CO_2	Ne	He	Kr	Xe
% by volume	78	21	0.93	0.04	0.002	0.0005	0.0001	$9\,10^{-6}$
% by weight	75	23	1.28	0.046	0.001	0.00007	0.0003	0.00004

Table 2.2: Ratios of some of the most common compounds making up ambient air. [14]

and cohesiveness might be overcome through proper encapsulation and shielded handling.

Among the disadvantages of methanol is primarily the need for expensive catalysts when operated in acidic media such as Nafion, which greatly increases the cost. In addition the effects of carbon monoxide poisoning on pure platinum electrodes, greatly limits the rate of reaction and therefore requires mixtures such as Pt/Ru, were ruthenium aids the desorption of adsorbed CO.

2.3 Electrochemical Catalysis

One of the major drawbacks of DMFCs is the need for costly catalysts. The methanol oxidation reactions does not readily occur in acidic media, and expensive catalysts such as platinum or palladium are needed. The catalytic process takes place on the surface of the particles. Assuming spherical particles with diameter, d, the surface area per weight scales as $1/d$, and therefore catalyst materials are normally prepared into particles of very small diameters in the nm-regime. Simply having a dense compact layer of such particles would, however, hinder fuel flow to the active surfaces, and such particles are therefore supported on a carrier material. Commercially such materials are primarily amorphous high surface area carbon black, formed through inexpensive scalable fabrication techniques based on incomplete combustion of petroleum products.

Methanol oxidation on platinum or paladium leads to adsorbed carbon monoxide which blocks the catalytically active sites and reduces the achievable current. To alleviate this problem, alloys are typically used which promote the desorption of CO. Table 2.3 shows the exchange current densities under methanol oxidation in phosphoric acid at 180°C [15]. It can be seen that alloys of platinum and ruthenium show a large improvement in current density compared to pure platinum, while alloys including tungsten and palladium show even better performance. The most widely used catalyst for methanol oxidation in fuel cells is PtRu alloys, typically at 1:1 [16].

For comparison the exchange current density for oxygen reduction in 100% H_3PO_4 at 190°C was found to be $0.07\,\mu A/cm^2$[15].

	Average particle size [nm]	I_{ex}^{MeOH}/A_g [mA/cm^2]	I_{ex}^{MeOH}/A_{pt} [μA/cm^2]
Pt	2.6	0.025	0.046
Pt/Ru (1:1)	4.1	0.08	0.17
Pt/Ru(1:5)	NA*	0.06	0.12
Pt/Ru/W	4.8	0.1	0.2
Pt/Ru/Pd	3.2	0.2	0.4

Table 2.3: Experimentally found values for the exchange current density of methanol oxidation at platinum alloys. A_g is the geometric electrode area and A_{pt} is the platinum surface area. *Particle size was not measured for the (1:5) Pt/Ru alloy but was assumed to be similar to the (1:1) composition for sake of comparison. Data by [15].

2.4 Proton Conductive Membranes

The ionomer Nafion, which is a trade-name of Du Pont de Nemours & Co. Inc, consists of a polytetrafluoroethylene (PTFE, also referred to as Teflon) backbone and perfluorinated pendent side-chains containing sulfonic acid groups. The systematic name is tetrafluoroethylene-perfluoro-3,6-dioxa-4-methyl-7-octenesulfonic acid co-polymer. When cast into a polymer membrane Nafion forms separate hydrophilic and hydrophobic regimes connected by an interfacial layer. This structure across the regime boundaries is shown in figure 2.2. The central region is encapsulated by a surface layer of sulfonic acid groups, leading to a polar interface which allows the permeation of water. The interfacial layer and the backbone shell layers are, however, non-polar and highly hydrophobic.

Many models have been proposed for the morphology between the two connect phases of the membrane, for instance cylindrical, lamellar or spherical. The most successful model assumes that the hydrophilic regions form clusters which connect via thin connecting channels, shown in figure 2.3. This model is most directly supported through examinations of stained Nafion sheets, in the absence of continues streaks of staining reject the cylindrical or lamellar models. This model asserts that as the membrane is hydrated, the clusters will increase in size and the connecting channels increase in diameter.

Halim et al. [19] have shown through both Small and Wide-Angle X-ray Scattering (SAXS and WAXS) that the humidity plays an important role in the conductivity of Nafion membranes. Notably it is shown that the ionic cluster size increases with increasing humidity. It is also determined that films cast at higher humidity shows higher proton conductivity. The proton conductance mechanism through Nafion is simple proton transport through the very acidic water phase that permeates the

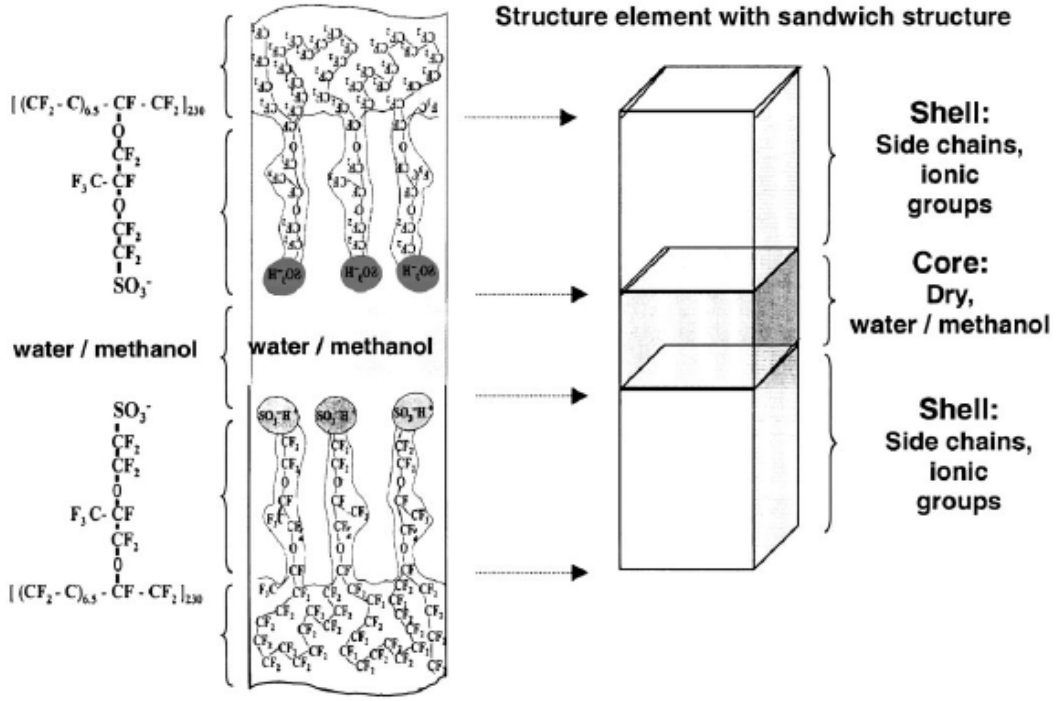

Figure 2.2: Illustration of the two phase composition of Nafion membranes. From [17].

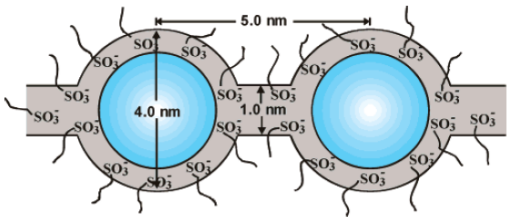

Figure 2.3: Illustration of the cluster-network model for the morphology of Nafion. From [18].

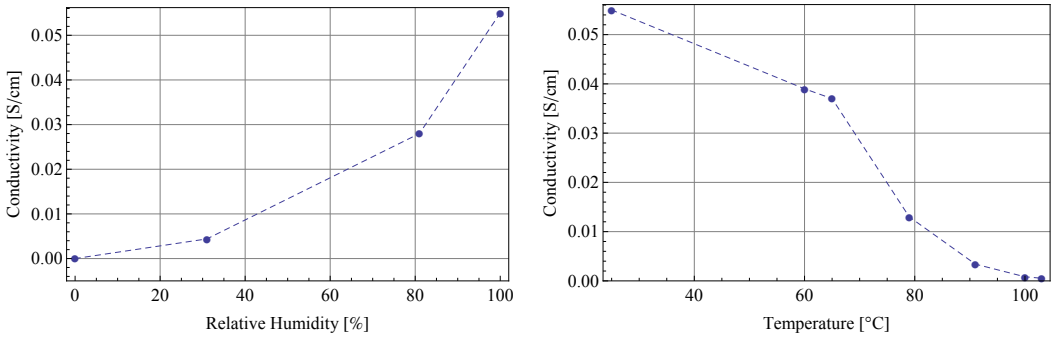

(a) Proton conductivity of Nafion at different levels of hydration at room temperature conditions.

(b) Illustration of the proton conductivity of Nafion with respect to increasing temperature at 100 % relative hydration.

Figure 2.4: Humidity and temperature dependence curves for the proton conductivity of Nafion. Numbers as reported by [22]

polymer. Nafion is typically characterized by its Equivalent Weight (EW). This indicates the weight of Nafion in molecular mass per mole of sulfonic acid group. For commercial use the most common product is Nafion 117, which has a 1100 g EW membrane with a thickness of 0.007" = 178 µm. The conductivity of Nafion will depend on the water content, as can be seen by figure 2.4a. Typically conductivity through a submerged Nafion 117 membrane at room temperature is in the range of $0.01 - 0.05\,\mathrm{S/cm}$. As can be shown in figure 2.4b, the conductivity drops off with increasing temperature with a sharp decline around 80° C. Analysis of Nafion membranes using Fourier transformed infrared spectroscopy [20], has show that for thicker layers of Nafion, full proton conductivity is achieved already at a hydration level corresponding to one water molecule per sulfonic acid group. Under immersion hydration a much larger water uptake is observed, with experiments using a post evacuation to remove excess water showing a typical hydration level of $\approx 15\,H_2O/SO_3H$ [21]. This corresponds to a 39 % increase in volume, which means the water phase takes up 27 % of the total volume.

Conceptualizing Nafion as simply a backbone matrix supporting a liquid sulfuric acid electrolyte, it is possible to reason about the parameters of this electrolyte in order to put the conductivity scale into perspective. Using an estimated density of Nafion it is possible to find the molar concentration of sulfuric acid group with respect to the total Nafion volume. Assuming a density of $1.58\,\mathrm{g/cm^3}$[23], and EW of 1100 g, the molar concentration of sulfonic acid groups is 1.44 M, which is not particularly high. The liquid phase, however, only makes up a small portion of the polymer volume. If it is assumed that only 27% of the volume is liquid phase, the effective concentration would be 5.33 M , thus the actual acidity in the Nafion pores

Cation	Mobility $[10^{-3}\,\mathrm{cm}^2/(\mathrm{Vs})]$
NH_4^+	0.763
Na^+	0.519
K^+	0.762
H^+	3.62

Table 2.4: Mobilities of simple cations solvated in water. [25]

can quite high. In conditions with very low water uptake the acidity of the Nafion membrane is high enough to be considered a super-acid [24], which describes an acid strong enough to form a hydronium ionic salt $SO_3^- - H_3O^+$.

The mobility of hydrogen ions solvated in water is much higher than other simple cations, as can be seen in table 2.4. This is due to the Grotthuss mechanism for hydrogen diffusion process. This mechanism describes the mobility hydrogen through hydronium molecules H_3O^+ passing on its excess proton to a water molecule H_2O, without a significant change of orientation or position. Such diffusion can occur through aligned water molecule chains, greatly exceeding the mobility of pure hydronium diffusion.

2.5 Silicon Based Fuel Cell Technology

The current state of silicon based micro scale fuel cells will now be the focus of discussion to highlight the strengths and weaknesses of different approaches to downscaling fuel cell technology to the region applicable for hearing aid usage. Focus is initially put on the more mature hydrogen based PEM fuel cells, which show little potential for use in hearing aids, but reliable performance and interesting processing techniques. After this the state of the art of methanol fuel cells is reviewed.

2.5.1 Indirect Proton Exchange Membrane Fuel Cell

PEM fuel cells that operate on pure hydrogen have many positive features, but cannot be directly scaled to the micro fuel cell size region due to the mechanical requirements of storing compressed hydrogen. A novel approach to circumvent this problem is to use a chemical hydrogen generation rather than storing the fuel in gaseous form. This type of cell is called an indirect fuel cell as the catalytic process does not directly on the feed fuel type.

Such fuel cells have been demonstrated by L. Zhu et al. [26] with very good performances of small devices, one such cell using an integrated solid form CaH_2 fuel source, which shows a peak power density of 16.8 $\mathrm{mW/cm^2}$ (0.41 V, 41 $\mathrm{mA/cm^2}$).

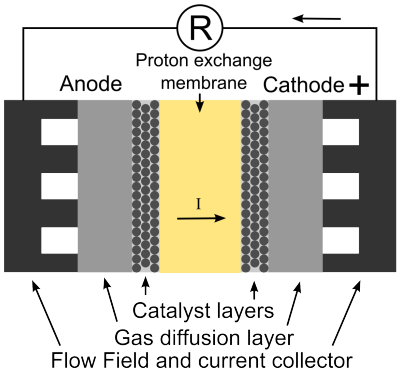

Figure 2.5: Schematic illustration of the Bipolar plate fuel cell design.

Their system size is 10.88 μL (2.5x2.5x1.74 mm). The usefulness of this particular cell for long term operation is however questioned as the hydrogen generation is a passive uncontrolled process, and the fuel volume is quite limited with a theoretical maximum energy content of 0.015 J corresponding to a stored charge of 0.004 mAh. Naturally the system size can be scaled up to increase fuel reservoir size, but this would likely complicate the passive hydrogen release mechanism, and the numbers given would not be representative. Alongside such considerations, their systems uses a solid fuel to generate the hydrogen, hence it faces large difficulties in refueling.

2.6 Silicon Based Direct Methanol Fuel Cells

The focus is now shifted to silicon direct methanol fuel cells which do not utilize any type of reforming elements but operate directly using methanol.

The most used fuel cell design is the bi-polar plate design as shown in figure 2.5. It most often consists of a proton conductive membrane at the center with catalyst layers deposited on both sides. Conductive gas diffusion layers are stacked around the PEM, making up a Membrane Electrode Assembly (MEA). This layer is then placed between stainless steel collector electrodes that include flow channels to deliver fuel to both sides of the MEA.

The gas diffusion layers are added to allow redistribution of the feed gas, such that the concentration is uniform across the plate, even as there is a pressure gradient in the flow channels driving the flow. Typically the gas diffusion layers are constructed from carbon cloth, and the catalyst support layers from different types of high surface area amorphous carbon. The use of these materials requires high compressive forces in order to lower electrical contact resistances.

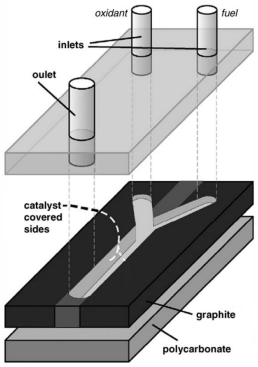

Figure 2.6: Assembly scheme of a laminar flow-based fuel cell by [27]. Fuel and oxidant are flowed through the channel forming a laminar flow between the two catalyst covered graphite electrodes forming the anode and cathode.

2.6.1 Silicon Based Planar Flow Channel Devices

An interesting alternative micro fuel cell design is the planar flow channel microfludic fuel cell design[28], which can be employed with a very wide range of fuel/oxidant combinations, and is capable of mitigating the effects of cross-over when in a system of non-selective catalyst. One such system for methanol fuels is shown by [27] who realize a membraneless microfluidic flow channel based cell as shown in figure 2.6. The fuel and oxidant are both injected into a combining flow channels under low Reynolds number (Re<2100) conditions, such that a laminar flow is formed. Of particular interest in this system is that it is capable of running the same device at either acidic or alkaline conditions, and indeed even show the performance of a mixed alkaline/acidic setup. Using a methanol concentration of 1 M a peak power density of $10\,\mathrm{mW/cm^2}$ is achieved, compared to $2\,\mathrm{mW/cm^2}$ and $6\,\mathrm{mW/cm^2}$ for acidic and alkaline medias respectively. Such systems are ideal for analysis of the influences of electrolyte concentrations and mixtures on device performances using different catalyst composition. It goes to reason however, that for actual power generation in small electronics devices, the need for pumps, and the low fuel utilization through fuel continually being washed out, are issues that make the concept infeasible.

2.6.2 Silicon Technology Based Bipolar Plate Fuel Cells

Silicon based bi-polar plate designs are not seen in larger scale systems, as the cost of silicon processing is very high compared to stainless steel electrodes, as well as the difficulty of dealing with single crystal silicon electrodes in the $5\,\mathrm{cm} \times 5\,\mathrm{cm}$ scale, since they are brittle and easily break due to slight asymmetries in the applied pressures. The area of fuel cell research where silicon is used, is in smaller scale

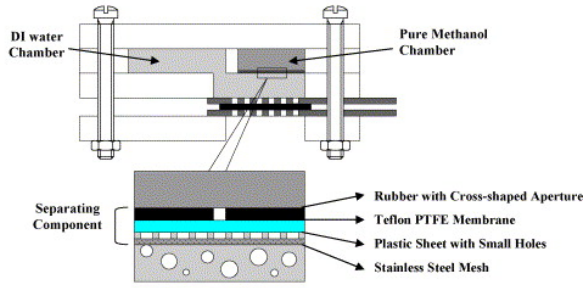

(a) Schematic of the components included in the device to provide a diluted methanol flow from a reservoir containing pure methanol.

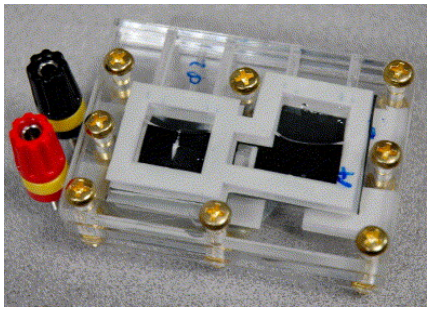

(b) Image of the finished device enclosed in poly-carbon plates that compress the stack.

Figure 2.7: A fuel cell utilizing the bipolar plate design, including a passive methanol delivery system [29].

devices. The most often seen integration of silicon is in imitations of the large scale bipolar plate designs where silicon fabricated electrodes replace the stainless steal collector electrodes. In such a setup the MEA remains virtually unchanged. The purpose of silicon in such designs is to allow for integration of novel micro-scale structures in the electrode and fluid flow channels. One such example is the usage of silicon nano-grass to increase the mechanical adhesion force between the silicon collector electrode and the gas diffusion layers. Figure 2.7 shows a novel bipolar plate silicon based design which also incorporates a pure methanol reservoir and dilution mechanism in order to reach higher energy densities while still operating the fuel cell at low methanol concentrations [29].

Table 2.5 shows a collection of bi-polar plate silicon based micro direct methanol fuel cells. It can be seen that the highest power densities are achieved by active systems and stacked passive systems, impressive power densities have however also been achieved in single stacked passive systems by [35, 36]. The systems are shown in figure 2.8. Both utilize a rigid polymer support structures to clamp the structure together with metal screws providing the clamping pressure. Despite this, Sabate et al. [36] manage to achieve a very small total system size of just $6\,\mathrm{cm}^3$ with an open fuel reservoir by fully integrating current collectors in the two silicon plates. Additionally, more complicated structures are needed in the conventional system by Shimizu et al. [35] who utilize a 4 layer stack in order to position electrodes around the central membrane/catalyst layer.

In a review of the current state of μDMFC research by Sundarrajan et al. [16] two major disadvantages of silicon fabrication techniques were highlighted: There is poor adhesion between the proton conductive polymer membrane and the silicon plates, and secondly silicon is brittle making it difficult to compress the cell to lower

Work	System size	Active area [cm^2]	P [$\frac{mW}{cm^2}$]	P_v [$\frac{mW}{cm^3}$]	OCV [mV]	T [$^\circ C$]	C_M [M]	Catalyst Loading [mg/cm^2]	Notes
Active systems									
Kelley et al.[30]	3 cm^2 x 1 cm	0.25	60	5.0	700	70	0.5	A: ~2 C: 1.5	Oxygen fed
Liu et al.[31]	1 cm^2 x 0.5 cm	1	4.7	9.4	450	RT	2	A: 2 C: 1	
Seo et al.[32]	3.5 cm^2 x 3 cm	1	0.031	0.03	650	RT	1	NA	
Passive systems									
Hashim et al.[33]	7.5 cm^2x 5cm	4	12	0.32	2500	RT	4	A: 4 C: 2	Stacked
Chan et al.[34]	~30 cm^2 x 4cm	6.25	10.3	0.54	2900	70	6	A: 4 C: 2	Stacked
Shimizu et al. [35]	49 cm^2 x 4cm	36	10	1.84	550	RT	4	A: 2.5 C: 2.6	Seperate MEA
Sabate et al. [36]	6 cm^2 x 1 cm	0.25	10	0.42	450	RT	2	A: 4 C: 4	
Gharibi et al.[37]	4.75 cm^2 x 3cm	4.75	1.2	0.40	500	RT	1	A: 1 C: 3	
This work	0.75 cm^2 x 0.7 cm	0.29	4.52	2.5	300	RT	3	A:2 C:4	

Table 2.5: Performance of different bi-polar plate designs compared to the integrated membrane of this work. The area used for the peak power density is the geometric area of the catalytic region. T is the operating temperature and RT denotes room temperature conditions. C_M denotes the methanol fuel concentration used. A and C denote the anode and cathode loadings of PtRu and Pt, respectively. P is the peak power density and P_v is the volumetric peak power density. The best performing device from this work is added for comparison and covered in chapter 5.

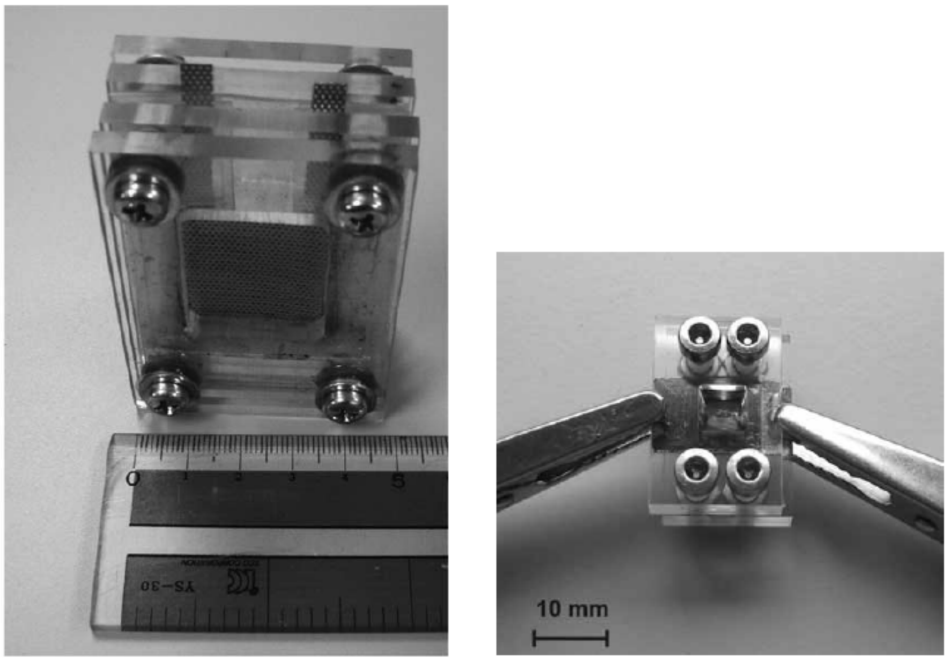

(a) Single MEA with closed fuel reservoir and 4 layer poly-carbon structure stack. By [35].

(b) Single Mea with electrodes fully integrated in silicon plates. By [36].

Figure 2.8: Silicon based bi-polar plate fuel cell systems.

the electrical resistance between the catalyst layers and the bipolar silicon plates.

The designs presented developed during this work attempts to address both these disadvantages by integrating the ionomer membrane directly into a silicon plate structure. The problem of poor adhesion is solved by mechanical locking of the membrane into the structure such that when in a dry state the polymer is held in place mechanically, and when in a wet state the expansion of the polymer will press against the sides of the locking structure and increase the adhesion. This integration is developed through development of a monolithic fuel cell. This development is the first attempts at developing monolithic bipolar plate design for methanol usage known to author, however through stack monolithic devices have been developed for hydrogen PEM cells as will be covered next.

2.6.3 Monolithic Silicon Based PEM Micro Fuel cells

The development of monolithic silicon based small scale fuel cell has largely been focused on creating proton conductive pathways through porous silicon structure. One such fuel cell is reported by [38], where Nafion is integrated into pores created in the silicon substrate though anodic etching, hence forming the proton conductive membrane of a hydrogen PEM cell. This system reports an open-circuit potential of

796 mV and a peak power density of 20 mW/cm^2 which is low for a hydrogen PEM cell, but it shows the potential in monolithic cells based on porous silicon.

A recent, very promising, development in μDMFC is the work by Moghaddam et al.[39], which deals with the functionalization of anodic porous silicon to create a proton conductive pathway through a silicon device. The proton conductance is realized by grafting of 3-mercapto-propyltrimethoxysilane to the pores of the silicon, which then have $-$SH groups oxidized to form sulfonic acid groups ($-SO_3H$). So far the working membrane has only been implemented in hydrogen systems, where it showed high performances of up to 340 mW/cm^2 at room temperature operation with hydrogen fed at 1.5 times the stoichiometric ratio and at a pressure of 1 kPa, with catalyst layers consisting of 7 mg/cm^2 platinum.

2.7 Direct Methanol Fuel Cell Power Sources for Hearing Aids

The goal of the DanATF project MicroPower.DK is to have a fuel cell capable of supplying power for a hearing aid. With this purpose in mind, the required power density is set at $P_{\max}^{\text{spec}} = 2.5\,\text{mW}$, and the cell should be capable of providing power for a period corresponding to one days usage, which is specified to be at a minimum $T_{\min}^{\text{spec}} = 16\,\text{h}$. This corresponds to a minimum battery energy of $Q_{\min} = P_{\max}^{\text{spec}} \cdot T_{\min}^{\text{spec}} = 40\,\text{mWh}$. The theoretical maximum OCV under standard conditions for a methanol cell is around 1.21 V. For most realized fuel cells the actual value of the OCV is closer to 0.6 V, and the potential at operation will be roughly half this. Assuming a load potential of $U_{\text{load}}^{\text{spec}} = 250\,\text{mV}$, the minimum energy amount corresponds to a capacity rating of 160 mAh. The conversion rate from mAh to mol methanol can be found assuming unity conversion since each methanol molecule leads to six electron transfers during oxidation. The conversion factor, κ, is thus given by; $\kappa = \frac{1}{6} 60^2 \frac{C}{e} \frac{1}{N_{\text{A}}} = 6.22 \times 10^{-6} \frac{\text{mol}}{\text{mAh}}$, where N_{A} is the Avogadro constant. From this, the minimal concentration of methanol needed to reach the current capacity requirement at a fuel reservoir volume of $V_f = 200\,\mu\text{L}$ is $C_{min} = \frac{P_{\max}^{\text{spec}} T_{\min}^{\text{spec}}}{U_{\text{load}}^{\text{spec}} V_f} \kappa = 4.98\,\text{M}$. While this assumes loss-less operation, it shows that such operation is within reason if the cell can be made to operate with low losses and higher concentrations. It however also shows that such a cell must be capable of operating at methanol concentrations significantly higher than the $1-3\,\text{M}$ ranges typically employed to benchmark devices [16]. Due to this, cross-over losses are a significant concern.

Assuming the simplest possible model for the fuel cell, the IV-characteristics is modeled as though the cell potential,U, is given by a loss-less potential difference,

U_0, which is however reduced due to the inclusion of an effective internal resistance, R_{int}. In this model the potential at a given current draw, I, is given by

$$U = U_{\mathrm{c}} - I\,R_{\mathrm{int}}. \tag{2.1}$$

The power is given by $P = U\,I$, and therefore the current and potential at maximum power can be found through solving $\partial_I P = 0$ with respect to I and inserting:

$$I_{\max} = \frac{1}{2}\frac{U_{\mathrm{c}}}{R_{\mathrm{int}}} \qquad U_{\max} = \frac{1}{2}U_{\mathrm{c}}. \tag{2.2}$$

With the maximum power then given by

$$P_{max} = \frac{1}{4}\frac{U_{\mathrm{c}}^2}{R}. \tag{2.3}$$

From this it can be gathered that the maximum internal resistance should be below the limit set by

$$R_{\mathrm{int}} < 4\,\frac{P_{\mathrm{max}}^{\mathrm{spec}}}{U_{\mathrm{c}}^2}. \tag{2.4}$$

Assuming that $U_{\mathrm{c}} = 500\,\mathrm{mV}$ this leads to a maximum internal resistance requirement of $40\,\Omega$. For comparison, the total resistance of a $0.44\,\mathrm{mm}^2$ Nafion 117 membrane assuming a conductivity of $0.01\,\mathrm{S\,cm}^{-1}$ is $40.45\,\Omega$. This indicates that this resistance is within the realm of possibilities assuming a membrane that is thinner than the conventional $178\,\mu\mathrm{m}$.

2.8 Summary

The chapter provided an introduction to the current state of the art of silicon based micro direct fuel cells. It is found that the performance regions with respect to power density and energy density are well suited for hearing aid usage. From a simplified effective internal resistance model it was found that the membrane resistance of typically employed Nafion 117 membranes is close to being to high for the application region, and it is therefore desirable to allow for thinner membranes with lower ohmic resistance. The model, however, does not consider the interplay between the cross-

over blocking effect of a thicker membrane with the conductivity enhancement of thinner membranes. This trade-off will be developed in more detail in the next chapter.

3 Theory of Direct Methanol Fuel Cells

This chapter deals with establishing the basic theory of operation for direct methanol fuel cells. The chapter will first describe the chemical system and associated considerations. It will then provide a microfluidic perspective on the ionic conductance occurring through the proton exchange membrane. The theory of the current potential relationship will then be developed, initially describing the Marcus model of electron transfer to provide a perspective on charge transfer at electrochemical interfaces. A model for a simple electron transfer system will then be developed through the Butler-Volmer equation relating current and potential across the cell. From this basic framework, an extended model encompassing mass diffusion determined transfer limitations and cross-over losses will be developed.

3.1 Methanol Fuel Cell Operation Principles

The net chemical reaction that forms the basis of operation for the fuel cell is the redox-reaction of methanol with oxygen.

$$\mathrm{CH_3OH} + \frac{3}{2}\mathrm{O_2} \quad \Leftrightarrow \quad \mathrm{CO_2} + 2\,\mathrm{H_2O} \tag{3.1}$$

The theoretical maximum energy which can be extracted is thus limited by this reaction. In order to extract useful work in the form of an electric current, the reduction and oxidation components of the reaction must occur at separate electrodes. Since at current time, no catalysts are known that can selectively oxidize methanol without reducing oxygen or vice versa, the reaction locations must also be separated physically. When separated the two relevant half reactions are, on the anode

$$CH_3OH + 7\,H_2O \;\Rightarrow\; CO_2 + 6\,H_3O^+ + 6\,e^- \tag{3.2}$$

while at the cathode side oxygen is reduced, and the electrode is oxidized,

$$6\,H_3O^+ + 6\,e^- + \frac{3}{2}O_2 \;\Rightarrow\; 9\,H_2O. \tag{3.3}$$

Conventionally reaction schemes will simply show protons, H^+, in isolation as if they moved freely through the proton conductance path, however, this is not truly the case. As the primary conductance happens through protons bound in hydronium ions, H_3O^+, it provides a clearer image of the reaction mechanics. Looking at the two sides in this form, it is clearly seen that the reaction involves a large transfer of water from the anode to the cathode, with 6 water molecules being transferred per reaction as carriers. In real applications of proton conductive ionomers, similar to Nafion, the water transfer will be further increased due to water drag [40], with a typical drag coefficient at room temperature of around 2.5 for liquid equilibrated membranes, but also with coefficients down to unity observed at vapor equilibrated membranes [41]. The reaction scheme proves useful, however, as a note that one cannot reduce water transport below this set limit except if the transport mechanism is drastically changed. One such drastic change in the conductive path has been suggested by [42]. Their treatments suggest that purely structural diffusion of hydrogen ions is possible in exotic materials such as water/ice filled carbon nanotubes. In these simulations the confined water molecules form a confined ice-like lattice through which structural diffusion happens without convection of the water molecules. Such exotic membranes will, however, undoubtedly entail lower total conductivities which might outweigh the reduction in water flux. The current state of the field is therefore that all acidic medium methanol fuel cells will need to deal with water management, which most address by incorporating micro-porous layers onto the cathode catalyst layer. These layers have a low water permeability and act to increase the hydrostatic back pressure causing a counter flow of water to the anode.

3.1.1 Methanol Oxidation Reaction at the Anode

The actual reaction that takes place on the anode where methanol is oxidized is significantly more complicated than the net effective reaction would indicate. The reaction transitions through several potential intermediate steps as shown schemat-

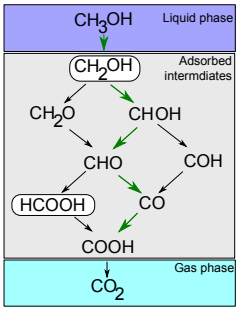

(a) Illustration of the possible stages in the oxidation of methanol.

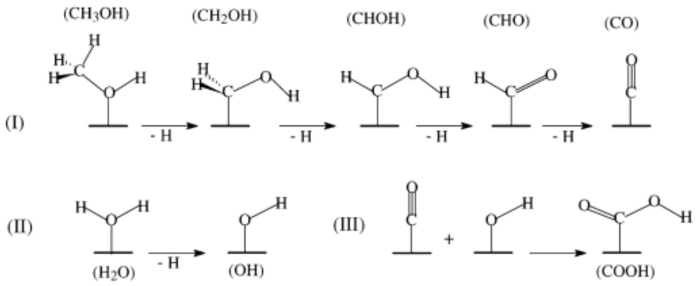

(b) Illustration of one of the possible reaction paths. (I) The structure of the adsorbed species on the platinum surfaces. (II) Water dissociating on the ruthenium surface. (III) CO desorption through reaction with the adsorbed hydroxide. Adapted from [43].

Figure 3.1: Illustrations of the relationship between partial products in the methanol oxidation reaction. The green arrows in figure 3.1a highlight the reaction path illustrated in figure 3.1b. Also in figure 3.1a, Formaldehyde and formic acid are marked in white to highlight that these intermediates are also stable in liquid form and therefore could be used as fuels directly.

ically in figure 3.1a. When considering the reaction kinetics, the effect of adsorbed intermediaries is similar to carbon monoxide poisoning in that they adsorb on the surface and reduce the catalytically active area. Due to this non-direct path, the methanol oxidation reaction is irreversible, and quickly reversing the potential after methanol has oxidized prior to diffusion of the product species would not result in recreating methanol, but rather absorbed intermediates such as formic acid [44] or simply hydrogen generation. It should be noted in passing that the stable intermediates formic acid and formaldehyde can also be used directly as fuel sources. One such system is shown by [45], who build a direct formic acid fuel cell.

The adsorbed carbon monoxide is desolated via a reaction with OH[46]. A potential pathway for the reaction would be directly through reaction with autodissociation water molecules $2\,H_2O \rightarrow H_3O^+ + OH^-$. This reaction path has a much higher activation energy than through the interaction with adsorbed OH [47]. The reaction with adsorbed hydroxide is illustrated in figure 3.1b. In addition to the difference in reaction energy, at acidic conditions the concentration of hydroxide will be extremely low, leading to a very low rate of direct reactions. Therefore the surface adsorption of OH molecules is the primary method of CO removal. Operation under alkaline conditions however will improve the dissociation rate.

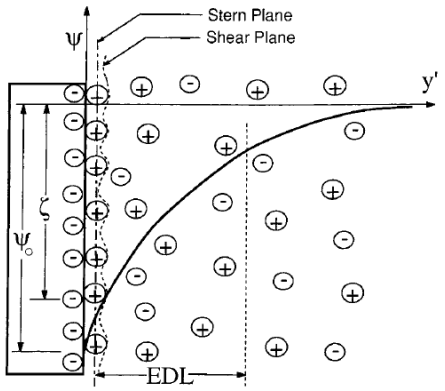

(a) Illustration of the Electric Double Layer (EDL) at the interface between an electrolyte and a charged surface. ψ is the electric potential function, ψ_0 the potential at the interface and ζ the zeta potential [48].

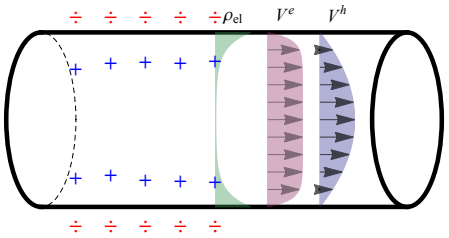

(b) Illustration of electro-osmotic and hydrostatic flow in a cylinder. The charge profile induced by the electrically charged surface is sketched alongside the flow profiles for the electro-osmotic and hydrostatic flows.

Figure 3.2: Illustrations of the charge density profile near barriers and the electro-osmotic and hydraulic flows in a simple channel flow model.

3.2 Ionic Conductance in Proton Exchange Membranes

To discuss the conductive qualities of Nafion a simplified descriptive framework is developed based on micro-fluidic considerations of a model system. It is assumed that the relevant liquid dynamics happen in single unconnected cylindrical channels of radius R, and length L. Due to the surface charges in these pores, a electric double layer will form, leading to an exponential surface potential with a characteristic length, λ_d, termed the Debye layer. The charge distribution is illustrated in figure 3.2a. The distribution of charges in the liquid occurs due to a balance of the electrostatic forces and diffusion of the mobile charge carriers in the ionic liquid. The equation for the electrical potential near the channel wall can be found through the Poisson equation by considering the charge distribution of positive, C_+, and negative, C_-, charges in the ionic liquid

$$\nabla^2\phi\left(z\right) \quad = \quad -\frac{1}{\epsilon}\rho_{el} = -\frac{1}{\epsilon}\,Z\,q\left(C_+\left(z\right) - C_-\left(z\right)\right) \tag{3.4}$$

In order to determine these concentrations we consider the chemical potential of the two species $\mu_\pm$, which will have contributions from the potential and from the deviation of the concentration from the mean:

$$\mu_{\pm}(z) = \mu_0 + \tau \log\left(\frac{C_{\pm}(z)}{C_0}\right) \pm e\,\phi(z) \tag{3.5}$$

Taking $\mu_{\pm}$ to be constant throughout the liquid, and observing that far away from the interface we must have $\mu_{\pm} = \mu_0$, the concentration can then be expressed with respect to the electrical potential as

$$C_{\pm}(z) = C_0 \exp\left(-\left(\pm\frac{Z\,q}{\tau}\phi(z)\right)\right) \tag{3.6}$$

Inserting this in equation 3.4, we attain the following

$$\nabla^2\phi(z) = -\frac{1}{\epsilon} Z\,q\,C_0\left(\exp\left(-\frac{Z\,q}{\tau}\phi(z)\right) - \exp\left(+\frac{Z\,q}{\tau}\phi(z)\right)\right) \tag{3.7}$$

In order to find a simple solution for this equation we consider the high temperature, weak coupling limit $Z\,q\,\zeta << \tau$. In this limit the exponential functions can be Taylor expanded about zero $\exp(x) \approx 1 + x$ which then leads to a simply solvable second order differential equation

$$\nabla^2\phi(z) = \frac{(Z\,q)^2}{\epsilon\,\tau} C_0\,\phi(z) \tag{3.8}$$

This equation can be recast in terms of the Debye length, λ_d , which is the characteristic length scale of the problem

$$\nabla^2\phi(z) = \frac{1}{\lambda_d^2}\phi(z) \tag{3.9}$$

$$\lambda_d = \sqrt{\frac{\epsilon\,\tau\,C_0}{(Z\,q)^2}} \tag{3.10}$$

For a infinite planar charged surface with a fixed surface potential ζ, the solution is trivially found to be $\phi_{lin}(z) = \zeta \exp(-z/\lambda_d)$. For a cylindrical flow channel the equation becomes:

$$\left(\frac{1}{\rho}\frac{\partial}{\partial\rho} + \frac{\partial^2}{\partial\rho^2}\right)\phi(\rho) = \frac{1}{\lambda_d^2}\phi(\rho) \tag{3.11}$$

which has the solution family of the Bessel functions, which with the fixed surface potential boundary condition and central symmetry condition leads to the solution expressed in the modified Bessel function of the first kind, I_0, as

$$\phi(\rho) = \zeta \frac{I_0(\rho/\lambda)}{I_0(R/\lambda)} \tag{3.12}$$

The solution converges towards the linear exponential decay, ϕ_{lin} in the region $R/\lambda >> 1$, but deviates in the lower regions where one wall would start to see the overlap of the exponential decay from the opposing wall. This means that at very small channel diameters the interactions between fluidic flow fields and charge fields might change considerably, while at larger diameters changes will be less dependent on diameter.

3.2.1 Fluidic Flows of the Channel

Two types of flows will occur in this channel as illustrated in figure 3.2b. A hydrostatic flow due to a pressure difference across the channel, and a electro-osmotic flow which occurs when a potential difference is exerted across the channel, which causes the mobile charges to flow while the immobile surface charges are unaffected, leading to a net current. These two flows will now be described in more detail. The liquid dynamics are governed by the incompressible Navier-Stokes equation including the external force term f_{ext}, which is stated as

$$\rho\left(\frac{d}{dt}V + (v\cdot\nabla)V\right) = -\nabla p - \mu\nabla^2 V - f_{ext} \tag{3.13}$$

where ρ is the density, p is the hydrostatic pressure, μ is the viscosity and V is the velocity field. The flow is assumed to be independent of angle, letting the velocity be expressed as a radial and a transverse component $V = \{V_\rho(\rho,z), V_z(\rho,z)\}$. From symmetry and constriction we then know that the radial component must be zero, i.e. $V_\rho = 0$. Assuming that the flow field is independent of distance along the channel, $V_z(\rho,z) = V_z(\rho)$ leads to

$$\nabla = \frac{\partial}{\partial\rho}\hat{\rho} \tag{3.14}$$

Since the gradient points in the radial direction and velocity only points along the channel, the convective part vanishes, $(v \cdot \nabla) V = 0$. Now assuming only electrostatic external forces, $f_{ext} = \rho_{el} E$. With the electric field given by the curvature of the potential, $E = -\Delta U / L$. From this we have the equation for the system reduced to

$$\mu \nabla^2 V_z(\rho) = \nabla p - \rho_{el} \frac{\Delta U}{L} \tag{3.15}$$

Due to the linearity of the equation it makes sense to define a hydrostatic flow field, V_z^h, and an electrostatic flow field, V_z^e, such that

$$\mu \nabla^2 V_z^h = \frac{\Delta P}{L} \tag{3.16}$$

$$\mu \nabla^2 V_z^e = -\rho_{el} \frac{\Delta U}{L} \tag{3.17}$$

where L is the channel length, ΔP is the difference in hydrostatic pressure and ΔV is the potential difference across the channel. The solution to the hydrostatic field can be found simply by assuming a second order polynomial solution and solving the parameters based on the no-slip boundary condition and the central symmetry. These derivations are skipped as focus is put on the electro-osmotic flow. The solution for the hydrostatic flow is:

$$V_z^h(\rho) = \frac{\Delta p}{L \mu} R^2 \left(\left(\frac{\rho}{R} \right)^2 - 1 \right) \tag{3.18}$$

the charge distribution at the walls is given by $\rho_{el} = -\epsilon \nabla^2 \phi$ which inserted in equation 3.17, leads to

$$\left(\frac{1}{\rho} \frac{\partial}{\partial \rho} + \frac{\partial^2}{\partial \rho^2} \right) V^e(\rho) = -\left(\frac{\Delta U}{L \mu} \epsilon \right) \left(\frac{1}{\rho} \frac{\partial}{\partial \rho} + \frac{\partial^2}{\partial \rho^2} \right) \phi(\rho) \tag{3.19}$$

From this an ansatz is made, based on the fact that the differential operator acting has a known value, and a log term due to the appearance of $1/\rho$ times the first derivative. The anzats is

$$V^e = -\left(\frac{\Delta U}{L \mu} \epsilon \right) \phi(\rho) + B \log(\rho) + C \tag{3.20}$$

Now from symmetry arguments we know that $\partial_z V^e|_{\rho=0} = 0$, and this can be used to exclude B since the potential is also bound by the same symmetry $\partial_z \phi|_{\rho=0} = 0$. Secondly from the no-slip condition at the boundary, $V^e(\pm R) = 0$, we can determine C leading to

$$V^e = -\left(\frac{\Delta U}{L\,\mu}\epsilon\right)(\phi(\rho) - \phi(0)) \tag{3.21}$$

In order to determine the electrical current, the integral of the velocity field times the charge density distribution is found

$$I = \int_0^{2\pi}\int_0^{R} V_z^e(z)\,\rho_{el}(z)\,z\,dz d\theta \tag{3.22}$$

This integral can be expressed fully with respect to the normalized potential function shape $\phi_s(\rho/\lambda) = \phi(\rho)/\zeta$, noting that $\rho_{el}(\rho) = -\epsilon\nabla^2\phi(\rho) = \epsilon\,\zeta\,\phi_s(\rho/\lambda)/\lambda_d^2$, giving

$$I = -\left(\frac{\Delta U}{L\,\mu}\epsilon^2\right)\frac{2\,\pi}{\lambda_d^2}\zeta^2\int_0^{R}(\phi_s(\rho/\lambda) - 1)\,\phi_s(\rho/\lambda)\,\rho\,d\rho \tag{3.23}$$

Normalizing the integration variable $\rho = t\,R$ and the integration limits, and expressing with respect to $a = R/\lambda_d$, this leads to

$$\begin{aligned} I &= -\Delta U\frac{1}{\mu}\left(\frac{\epsilon^2\zeta^2}{\lambda_d^2}\right)2\,\frac{\pi\,R^2}{L}\,S(R/\lambda_d) \\ S(a) &= \int_0^{1}(\phi_s(t\,a) - 1)\,\phi_s(t\,a)\,t\,dt \end{aligned}$$

Inserting the potential and solving this, leads to a relation which can be simply expressed with respect to a normalized scale factor function $S(R/\lambda_d)$ as

$$S(a) = \frac{I_1(a)}{a\,I_0(a)} + \frac{I_1(a)^2}{2\,I_0(a)^2} - \frac{1}{2} \tag{3.24}$$

From this we determine that the conductivity of the channel, adding the substitution

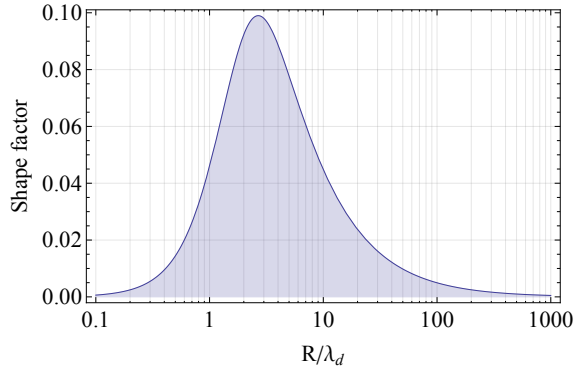

Figure 3.3: Scale factor function, which contains the terms describing the conductivity dependence on ratio between channel radius and Debye length. The maximum has a value of $S_{max} = 0.099$ and is attained at $R/\lambda_d = 2.68$.

$\rho_{surf} = \frac{\zeta}{\lambda_d}\epsilon$, is given by

$$\sigma = 2\frac{\rho_{surf}^2}{\eta} S\left(\frac{R}{\lambda_d}\right) \tag{3.25}$$

Reasoning about this, we see that the surface charge concentration appears squared, due to its role in both increasing the fluidic flow strength, but also the charge carrier density. For a Nafion system the surface charge concentration is not easily engineered, however it goes to reason that holding all else equal and increasing the EW will lead to a larger surface potential as the sulfonic acid group surface concentration increases. However it is not a given that the internal surface area of the polymer will remain constant at different EW ratings, and therefore attempts to increase the conductivity should strive to minimize internal surface area over the equivalent weight. The purely fluidic parameters show that decreasing the viscosity of the charge carrying liquid will lead to an increased conductivity, as the lowered viscous drag near the walls leads to a larger velocity field which increases the current. The normalized scale factor function, S, is shown in figure 3.3. The curve shows that for channels with radius's much larger than λ_d the conductivity will decrease, due to the current only flowing in the perimeter of the channel, while for very small channels the conductivity will be limited by the constriction effect on the velocity flow field. Thus a maximum is observed where these two tradeoffs balance, which has a value of $S_{max} = 0.099$ and is attained at $R/\lambda_d = 2.68$.

Another quite important consideration not yet taken into account in the above is the net flow of liquid. The above conductivity assumes that liquid can flow freely without building up a hydrostatic pressure, however, in a fuel cell any liquid transported to the cathode will meet a gas interface, and therefore be blocked. This

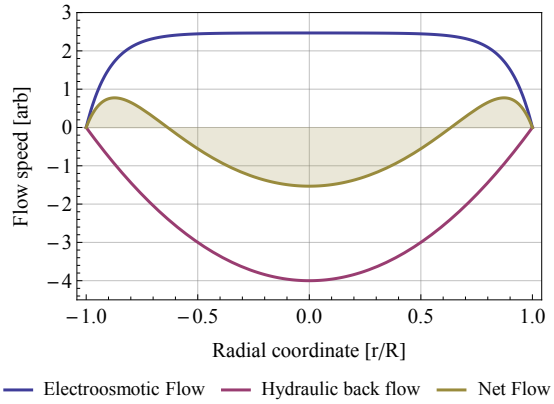

Figure 3.4: Illustration of the electro-osmotic and hydraulic flows and the resulting net flow at $\alpha = R/\lambda_d = 10$. Which is close to the region showing maximum conductivity when the effects of hydraulic back-flow are taken into account.

blockage leads to a buildup of a hydrostatic pressure which provides a hydraulic back-flow following the flow profile of equation 3.18. The total flow will then be a superposition of the electro-osmotic flow and the hydraulic flow such that the net flow rate is zero. The flow profile is shown in figure 3.4. Since the profile has a non-zero overlap with the charge distribution, the conductivity will be reduced. In order to determine the exact effect, the hydraulic flow of both electro-osmotic and hydrostatic flows are found

$$Q_h = \int V_h dA = -\frac{R^2}{2\,\mu}\frac{A}{L}\Delta p \tag{3.26}$$

$$Q_e = \int V_e dA = 2\frac{\epsilon\zeta}{\mu}\frac{A}{L}\Delta U\left(\frac{1}{2} - \frac{I_1(a)}{I_0(a)}\right) \tag{3.27}$$

The sum of the flows should be zero, which leads to the build up pressure being given by

$$Q_e + Q_h = 0 \tag{3.28}$$

$$\Delta p = 4\,\frac{\epsilon\zeta}{R^2}\left(\frac{1}{2} - \frac{I_1(a)}{I_0(a)}\right)\Delta U \tag{3.29}$$

Given this pressure, the hydrostatic back flow field can be found, and the related drop in conductivity determined.

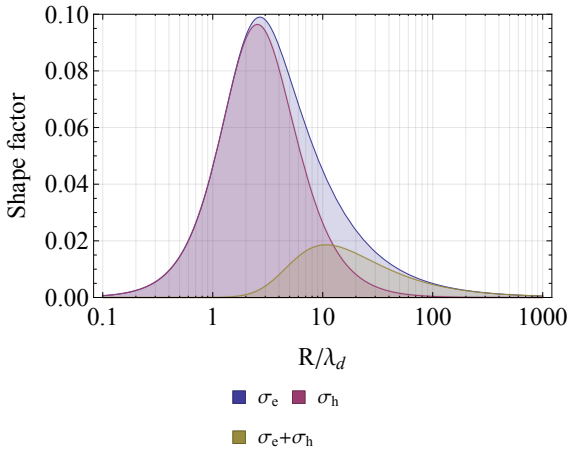

Figure 3.5: Shape factor change due to the zero net flow conditions which impose a hydrostatic back-pressure.

$$I = \int_0^{2\pi}\int_0^{R} V_{zh}^{e}(z)\,\rho_{el}(z)\,z\,dzd\theta \tag{3.30}$$

$$I = -2\,\pi\left(\frac{\Delta p}{\mu\,L}R^2\right)\frac{\epsilon\zeta}{\lambda_d^2}R^2\frac{1}{4}S_h\left(R/\lambda_d\right) \tag{3.31}$$

$$S_h(a) = 4\left(\frac{1}{2}-\frac{I_1(a)}{I_0(a)}\right)\int_0^{1}\left(t^2-1\right)\phi_s(t\,a)\,t\,dt \tag{3.32}$$

$$S_h(a) = -4\frac{2\,I_2(a)}{a^2 I_0(a)}\left(\frac{1}{2}-\frac{I_1(a)}{I_0(a)}\right) \tag{3.33}$$

The conductivity is then given by

$$I = -2\frac{A}{L}\frac{(\xi\epsilon)^2}{\lambda_d^2}\frac{1}{\mu}S_h(a)\,\Delta U \tag{3.34}$$

$$\sigma_h = -2\,\frac{\rho_{surf}^2}{\eta}S_h(a) \tag{3.35}$$

The changes to the overall conductivity from the hydrostatic back pressure can be seen in figure 3.5. It can be seen that the effect of the back flow is significant and reduces the overall conductivity at the zero net flow condition. The conductivity at the maximum shape factor is reduced by 81 %, with the maximum shape factor going from 0.099 to 0.019 and the maximum location moving from $R/\lambda_d = 2.68$ to $R/\lambda_d = 10.7$.

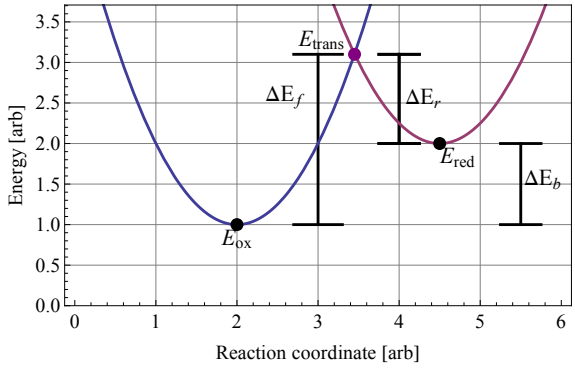

Figure 3.6: The energy landscape assumed as the basis for the Marcus model of outer sphere electron transfer.

The insight gained through this simplified model is, that while the hydrostatic flow and electro-osmotic flows are linearly superposition, this does not entail that there is no coupling between the uncharged liquid flow and the charged liquid flow. We see that a high charged flow through the channel will either lead to an increased flow, or a build up pressure. In practice the conditions will be a balance depending on the rate of evaporation at the cathode of the fuel cell, as well as the water production occurring from the net chemical reaction.

3.3 Marcus Theory of Electron Transfer Reactions

At the heart of the fuel cell and redox reaction process is the theory of electron transfer reactions. These reactions are dealt with in the field of interfacial electrochemistry. Such reactions can be extremely complicated due to the involvement of both solid state electronics of the electrodes, fluid dynamics of the electrolyte and statistical mechanics of the liquid and gas phase components as well as quantum interactions taking place in the electron transfer reaction itself. As such simple models are extremely valuable to properly distinguish features of separate regions in order to further understanding of the complex system. A model which has been incredibly successful in describing the process of electron transfer is the Marcus theory. This theory was put forth in 1956 by Rudolph A. Marcus [49, 50], who would later go on to win the Nobel price for this contribution in 1992. The theory deals with outer sphere electron transfers in which the chemical species involved exchange charge but do not undergo large structural changes, and the primary result is an expression of the formulation of the energy barrier which determines the rate of reaction.

It is assumed that the energy of the oxidized state and reduced state can both be

expressed with respect to a generalized reaction coordinate, χ, such that $\chi = 0$ corresponds to the oxidized state, and $\chi = \Delta\chi$ corresponds to the reduced state. This generalized reaction coordinates described the minimal energy path connecting the initial and final state in electron transfer. The energy for reduced and oxidized states are considered, expanded around the equilibrium positions and therefore described by parabolic curves. This energy landscape can be seen schematically illustrated in figure 3.6. In order to transition from the reduced state to the oxidized state, the system will first have to evolve into the transition state at E_{trans}. Analytically it proves simplest to express the curves with the reaction coordinate and energies taken relative to the minimum of the oxidized state. Which leads to

$$E_{ox}(\chi) = \chi^2 \tag{3.36}$$

$$E_{red}(\chi) = (\chi - \Delta\chi)^2 + \Delta E_b \tag{3.37}$$

Electron transfer will occur at the intersection where the energies of the states match, thus the energy barriers of the forward and reverse reactions can be found by equating and isolating $E_{ox}(\chi_{transr}) = E_{red}(\chi_{trans})$

$$\chi_{trans} = \frac{\Delta\chi^2 + \Delta E_b}{2\,\Delta\chi} \tag{3.38}$$

From this the energy barriers can be expressed:

$$E_{ox}(\chi) = \left(\frac{\Delta E_b + \Delta\chi^2}{2\,\Delta\chi}\right)^2 \qquad E_{red}(\chi) = \left(\frac{\Delta E_b - \Delta\chi^2}{2\,\Delta\chi}\right)^2 - \Delta E_b \tag{3.39}$$

Adding a contribution from the external potential to the energy $\Delta E_b = E_0 + U$ and linearizing, gives the coefficients of potential

$$\frac{\partial}{\partial U} \quad E_{ox}(\chi) = \frac{1}{2}\left(1 + \frac{\Delta E}{\Delta\chi^2}\right) = \alpha \tag{3.40}$$

$$-\frac{\partial}{\partial U} \quad E_{red}(\chi) = \frac{1}{2}\left(1 - \frac{\Delta E}{\Delta\chi^2}\right) = (1 - \alpha) \tag{3.41}$$

Therefore the forward and reverse reactions can be simply expressed as having a common prefactor indicating the strength of the reaction, and an asymmetry parameter, α, which indicates to which degree an applied potential will increase the

forward and reverse barriers with respect to the total increase. This means that $\alpha = 1$ indicates that an applied electrical potential only changes the oxidation reaction barrier, and $\alpha = 0$ indicates that the applied electrical potential only changes the reduction reaction barrier. From this, the rate of reaction in forwards and reverse directions can be expressed in terms of Arrhenius prefactor A_f, A_b, and with the number of electrons transferred in the reaction given by n, the electron charge denoted by e, the thermal energy given by $\tau = k_b T$, and the applied potential given by ΔU. The expression is then given by:

$$r_f = A_f \exp\left(\alpha\, n\, \frac{e\,U}{\tau}\right) \qquad r_b = A_b \exp\left(-\,(1-\alpha)\; n\, \frac{e\,U}{\tau}\right) \tag{3.42}$$

With the only difference in the forward and reverse rate being the inversion of the potential, as it will respectively lower and increase the potential barrier, as well as the asymmetry factor which simply captures any asymmetry in the potential landscape. The next section will deal with the development of a relation for the electrical current potential relationship from these rate equations.

3.4 Butler-Volmer Equation

In order to determine the current across the interface, two contributions are considered. There is a forward current density, i_f, which depends on the reactant concentration at the surface, C_r, and there is a current flowing back in the reverse direction density, i_b, which depends on the product concentrations at the surface, C_p. The net current is then given by the difference between these two contributions. Using the rate expressions developed in equation 3.42, the total current density i can then be expressed as:

$$i = i_f - i_r \tag{3.43}$$

$$i_f = C_r\, A_f \exp\left(\alpha\, n\, \frac{e\,U}{\tau}\right) \tag{3.44}$$

$$i_b = C_p\, A_b \exp\left(-\,(1-\alpha)\; n\, \frac{e\,U}{\tau}\right) \tag{3.45}$$

In order to parametrize the current expression conveniently, the expression is considered at the equilibrium potential, U_0, at which the net current is zero, $i = 0$. At this potential, forward and reverse currents must be similar in magnitude, and this magnitude is denoted the exchange current density, i_0, which is found to be:

$$C_r\, A_f\, \exp\left(\alpha\, n\, \frac{e\, U_0}{\tau}\right) = C_p\, A_b\, \exp\left(-\left(1-\alpha\right)\, n\, \frac{e\, U_0}{\tau}\right) \tag{3.46}$$

$$U_0 = \frac{\tau}{e\, n} \log\left(\frac{A_b\, C_p}{A_r\, C_r}\right) \tag{3.47}$$

$$i_0 = i_f\left(U_0\right) = i_f\left(U_0\right) = \left(A_f C_r\right)^{\alpha} \left(A_b C_p\right)^{1-\alpha} \tag{3.48}$$

By re expressing the potential as the difference from the equilibrium potential $U = U_0 + \Delta U$, and rearranging, this can be expressed as a simple form

$$i = i_0 \left(C_r \exp\left(\alpha z \frac{\Delta U}{\tau}\right) - C_p \exp\left(-\left(1-\alpha\right) z \frac{\Delta U}{\tau}\right)\right) \tag{3.49}$$

This is the Butler-Volmer equation for the current across an electrochemical interface. The dynamics is both non-linear but also has an interesting dependence on the relative surface concentration which can vary depending on time, temperature, and many other factors making application of the relation non-trivial. One simple conclusion from the equation, however, is the Nernst equation which is found by letting the current be zero and relating the potential to the surface concentration:

$$C_p \exp\left(-\left(1-\alpha\right) z \frac{U_{nl}}{\tau}\right) = C_r \exp\left(\alpha z \frac{U_{nl}}{\tau}\right) \tag{3.50}$$

$$U_{nl} = z\, \tau\, \log\left(\frac{C_p}{C_r}\right) \tag{3.51}$$

This allows the determination of the relative concentrations of reactant and product at the electrode interface assuming no other potential losses. In the general form of the Nernst equation the C_p/C_r term is in reality the reaction quotient Q. For a methanol oxidation reaction with a surface concentration of 2 M, with ambient air having 21% oxygen, and assuming a 2 atm CO_2 partial pressure, this leads to a over-potential of 48 mV. If the cathode becomes flooded by water, the oxygen concentration is considerably reduced. Taking as example the partial pressure of oxygen in air 3.167 kPa, at the same conditions, it leads to a potential loss of 120 mV. Thus a significant potential loss can be incurred due to low product concentrations at the electrode interfaces, but also a build up of high pressures of CO_2 can result in potential losses in this range. These potential losses are however far lower than the typically observed losses in PEM fuel cells, which lie in the range of 500 mV which are primarily ascribed to cross-over effects [51].

In order to include mass transfer losses into the Butler-Volmer equation, it is assumed that the surface concentration of product and reactant are linearly related to the current draw.

$$C_p = 1 + \frac{i}{i_l} \qquad C_p = 1 + \frac{i}{i_l} \tag{3.52}$$

Inserting the expression and again isolating the current, leads to:

$$\begin{aligned} \frac{i}{i_0} &= \exp\left(\alpha z \frac{U}{\tau}\right) - \exp\left(-\left(1-\alpha\right) z \frac{U}{\tau}\right) \\ &\quad -\frac{i}{i_l}\left(\exp\left(\alpha z \frac{U}{\tau}\right) + \exp\left(-\left(1-\alpha\right) z \frac{U}{\tau}\right)\right) \end{aligned} \tag{3.53}$$

$$i = i_0 \frac{\exp\left(\alpha z \frac{U}{\tau}\right) - \exp\left(-\left(1-\alpha\right) z \frac{U}{\tau}\right)}{1 + \frac{i_0}{i_l}\left(\exp\left(\alpha z \frac{U}{\tau}\right) + \exp\left(-\left(1-\alpha\right) z \frac{U}{\tau}\right)\right)} \tag{3.54}$$

Assuming $\alpha \approx \frac{1}{2}$ this expression can be greatly simplified in terms of hyperbolic trigonometric functions and becomes:

$$\frac{i}{i_0} = \frac{\sinh\left(\alpha z \frac{U}{\tau}\right)}{1/2 + \frac{i_0}{i_l}\cosh\left(\alpha z \frac{U}{\tau}\right)} \tag{3.55}$$

The curve shape of this expression at varying limiting currents can be seen in figure 3.7. The limiting behavior at the limiting current is apparent, and a large difference is seen to an assumed loss less operation even near the origin where the curvature is altered by a factor of $\partial_i \left(i/i_0\right)|_{i=0} = 1/\left(1 + 2\, i/i_0\right) \partial_i \left(i/i_0\right)|_{i=0, i_l=\infty}$ when the mass transfer loss is included. Equation 3.55, can be inverted to give an expression for the potential given from the current, which expressed in normalized currents, $i^\star = i/i_0, i_l^\star = i_l/i_0$ leads to:

$$U\left(i^\star, i_l^\star\right) = \frac{\tau}{\alpha\, z} \log\left(\frac{i\, i_l^\star + \sqrt{4\, i_l^{\star 2} - 4\, i^{\star 2} + \left(i^\star i_l^\star\right)^2}}{2\left(i_l^\star - i^\star\right)}\right) \tag{3.56}$$

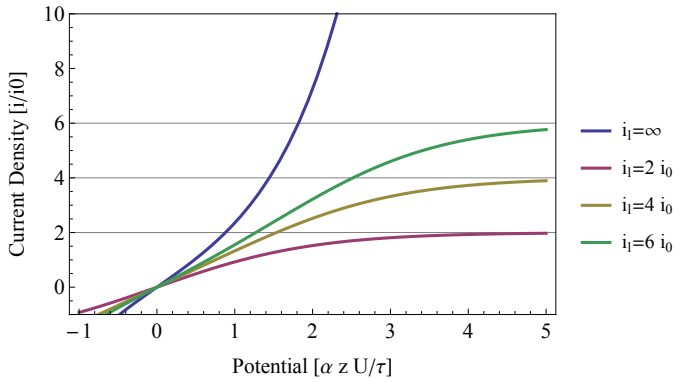

Figure 3.7: Graph showing the relationship between current and potential when the dynamics are altered to include linear mass transfer loss effects. The curve showing $i_l = \infty$ corresponds to excluding any mass transfer effects. It can be seen that the curves steady off at the appropriate limiting current levels.

3.5 Methanol Cross-Over Induced Current

To introduce a leakage current into the model, it is assumed that the concentration gradient of methanol across the membrane will drive a linear diffusion flux, and that this flux is completely oxidized at the catalyst. This adds linear contribution to the current, such that the interfacial current at the cathode, i_{c}, is actually a superposition of the cross-over current, $i_{\mathrm{xo},0}$, and the measured current, i_{m}. The initial statement is thus the expression of the measured current in terms of the interfacial current as:

$$i_{\mathrm{c}} = i - i_{\mathrm{xo}}(i) \tag{3.57}$$

$$i_{\mathrm{xo}}(i) = \sigma \Delta C_{MeOH} \tag{3.58}$$

where $\sigma = D/t$ is the length normalized diffusion constant of the membrane. Then similar to the mass transfer limitations consideration it is assumed that the concentration of methanol at the anode will decrease linearly with current draw, and the expression for the interfacial current is inserted. The resulting expression is then expressed in terms of the leakage current at zero current draw $i_{\mathrm{leak},0}$:

$$i_{\mathrm{xo}}(i_{\mathrm{m}}) = \frac{D}{L} F C^0_{\mathrm{MeOH}} \left(1 - \frac{i_{\mathrm{m}}}{i^c_{\mathrm{l}}}\right) \tag{3.59}$$

$$i_{\mathrm{leak},0} = \frac{D}{L} F C^0_{MeOH} \tag{3.60}$$

$$i_{\mathrm{xo}}(i_{\mathrm{m}}) = i_{\mathrm{xo},0} - \frac{i_{\mathrm{xo},0}}{i^c_l} i_m \tag{3.61}$$

where $i_{\mathrm{l}}^{\mathrm{c}}$ is the mass transfer limiting current for the cathode. Writing up the equation in terms of 3.56 taken for the anode, U_{a}, and cathode, U_{c}, separately, the total cell potential,U, is given by

$$U = U_0 - U_{\mathrm{a}}\left(\frac{i_{\mathrm{m}}}{i_0^{\mathrm{a}}}, \frac{i_{\mathrm{l}}^{\mathrm{a}}}{i_0^{\mathrm{a}}}\right) - U_{\mathrm{c}}\left(\frac{i_{\mathrm{m}} + i_{\mathrm{xo}}\left(i_{\mathrm{m}}\right)}{i_0^{c}}, \frac{i_{\mathrm{l}}^{\mathrm{c}}}{i_0^{\mathrm{c}}}\right) - i_{\mathrm{m}}\left(R\,A\right) \tag{3.62}$$

The objective is now to investigate the inherent tradeoff between the performance limitation of a high ohmic loss from the $i_m RA$ term, versus a high cross-over loss from the U_a when i_{leak} is large. In order to carry out this investigation it proves useful to define a equivalent ohmic limited current, i_Ω, which is define as the current at which the potential is reduced to zero assuming only ohmic losses. This is given by:

$$i_\Omega = \frac{U_0}{\left(R\,A\right)} \tag{3.63}$$

The reason for introducing this limit current is to allow a parametrization of the potential equation with respect to a parameter detailing the balance between ohmic and cross-over losses. This parameter is introduced by defining a sum of current limits parameter, i_{sum}, and a scaling parameter, κ, which describes the ratio between the two limit currents. The defining equations are:

$$i_{\mathrm{sum}} = i_{\Omega,\mathrm{min}} + i_{\mathrm{l}}^{\mathrm{c}} \tag{3.64}$$

$$\kappa = i_l^c / i_{\mathrm{sum}} \tag{3.65}$$

$$(1-\kappa) = i_{\Omega,\mathrm{min}} / i_{\mathrm{sum}} \tag{3.66}$$

In addition to this new parametrization an effective mobility parameter, μ, is introduced to describe the effect of changing the strength of both cross-over and conductance. The parameter is defined such that $\mu = 1$ corresponds to the point where $i_{\mathrm{xo},0} = i_l$, and $\mu = 0$ corresponds to the limit where there is no leakage current, $i_{\mathrm{xo}} = 0$, yet the ohmic resistance is infinite. In practice this is done by defining the parameter as $\mu = i_{\mathrm{xo},0}/i_{\mathrm{l}}^{\mathrm{c}} = i_{\Omega,min}/i_\Omega$. Inserting these factors into equation 3.62, the result is

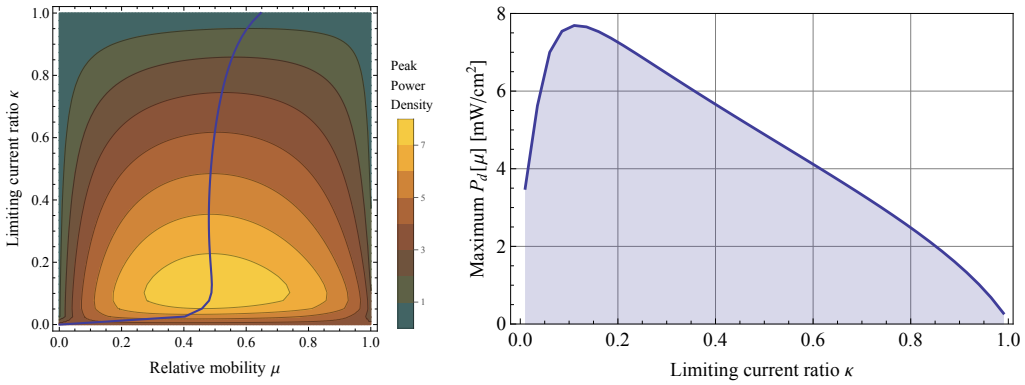

(a) (b)

Figure 3.8: Figure (a) show the peak power density as a function of limiting current scaling κ and normalized mobility μ. A solid line marks the position of the μ value which maximizes peak power density for each value of κ. Figure (b) shows the peak power density along the marked line. I can be noted that for the majority of κ values, the optimal peak power density is obtained at $\mu = 0.49$.

$$\begin{aligned} U &= U_0 - U_{\mathrm{a}}\left(\frac{i_{\mathrm{m}}}{i_0^{\mathrm{a}}}, \frac{i_l^{\mathrm{a}}}{i_0^{\mathrm{a}}}\right) - U_0 \frac{i_{\mathrm{m}}}{(1-\kappa)\, i_{\mathrm{sum}}} \\ &\quad - U_{\mathrm{c}}\left(\frac{\mu\,\kappa\, i_{\mathrm{sum}}}{i_0^c} + \frac{i_m}{i_0^c}\left(1 - \mu\,\kappa\, i_{\mathrm{sum}}/i_l^c\right), \frac{\kappa\, i_{\mathrm{sum}}}{i_0^c}\right) \end{aligned} \tag{3.67}$$

Carrying out a simulation finding the peak power density for combinations of κ and μ, the interplay between the two separate losses can be found. The result of such a simulation is shown in figure 3.8, which was carried out with the parameters $i_0^a = 5\,\mathrm{mA/cm^2}$, $i_0^c = 10\,\mathrm{mA/cm^2}$, $i_{\mathrm{sum}} = 360\,\mathrm{mA/cm^2}$, $U_0 = 550\,\mathrm{mV}$, $i_l^a = 100\,\mathrm{mA/cm^2}$.

The results of the simulation show that for the majority of limiting current scaling regions the optimal performance is obtained when the normalized mobility is $\mu = 0.49$. At this point, the repackage current is roughly half the limiting current of the cathode catalyst layer, $i_{leak,0} = 0.49\, i_l^c$, while the ohmic resistance is equal to twice the minimally obtainable value, $i_\Omega = 2.04\, i_{\Omega,\mathrm{min}}$. The results also show that the maximum peak power densities are obtainable in the region of low κ-values. With the maximum located at $\kappa = 0.12$, which means that the ratio between the limiting currents is; $i_l^c/i_\Omega = \mu\kappa/(1-\kappa) = 7\,\%$. Thus the IV-curve is primarily limited by cross-over losses in this region.

In order to better provide a framing of the IV curves general development as a function of the mobility parameter, figure 3.9 shows the open circuit potential and maximum current density, evaluated along curves of varied mobility assuming constant limiting current ratios. Starting from the low end $\mu \approx 0$, where each curve

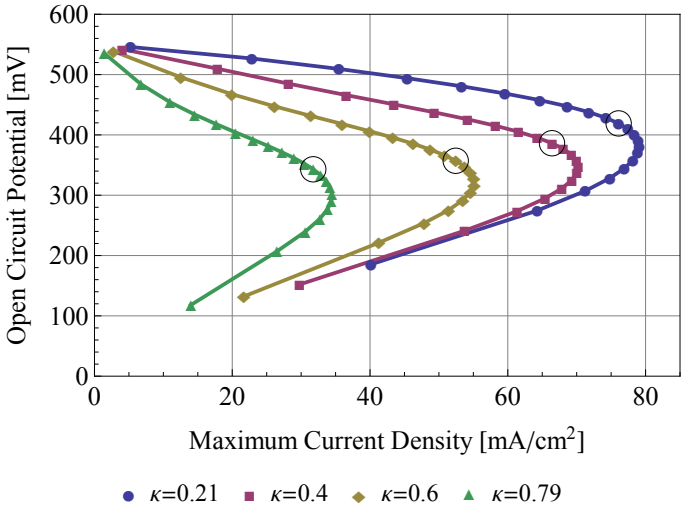

Figure 3.9: The figure shows the open circuit potential and maximum current density for which a positive power is extracted as curves where the effective mobility parameterμ is varied, while the limiting current ratio, κ, is kept constant. For each curve a black circle marks the point where maximum power is obtained, and power falls of in both directions moving away from this point.

joins at $U_{ocv} = U_0$ an increasing mobility factor has the effect of decreasing the open circuit potential, while increasing the maximum attainable current density. This leads to an increasing peak power density. At some point, the falling open circuit potential starts to reduce the gains in the lowered ohmic resistance, and the maximum attainable current density starts to fall with increasing mobility as it becomes primarily dominated by the open circuit potential. For all the curves, the maximum attainable peak power density is marked and occours just prior to this tradeoff region where a bend occurs in the curve.

The conclusion based on this theoretical simulational investigation is that the connection between cross-over induced losses and ohmic losses lead to a tradeoff between the two when attempting to optimize performance by tuning the membrane conductance. In light of the present work, this highlights the value of a membrane design where the resistance can easily be tuned across a wide range in order to locate the maximum. In this work, this ability is achieved via integrating the ionomer membrane into a perforated plate, where the effective conductance can then be tuned through variations in the plate thickness and perforation.

3.6 Activation and Mass Transfer Losses

When considering the opportunity for optimization in light of the derived equations, it would seem that the activation losses can be reduced arbitrarily simply by

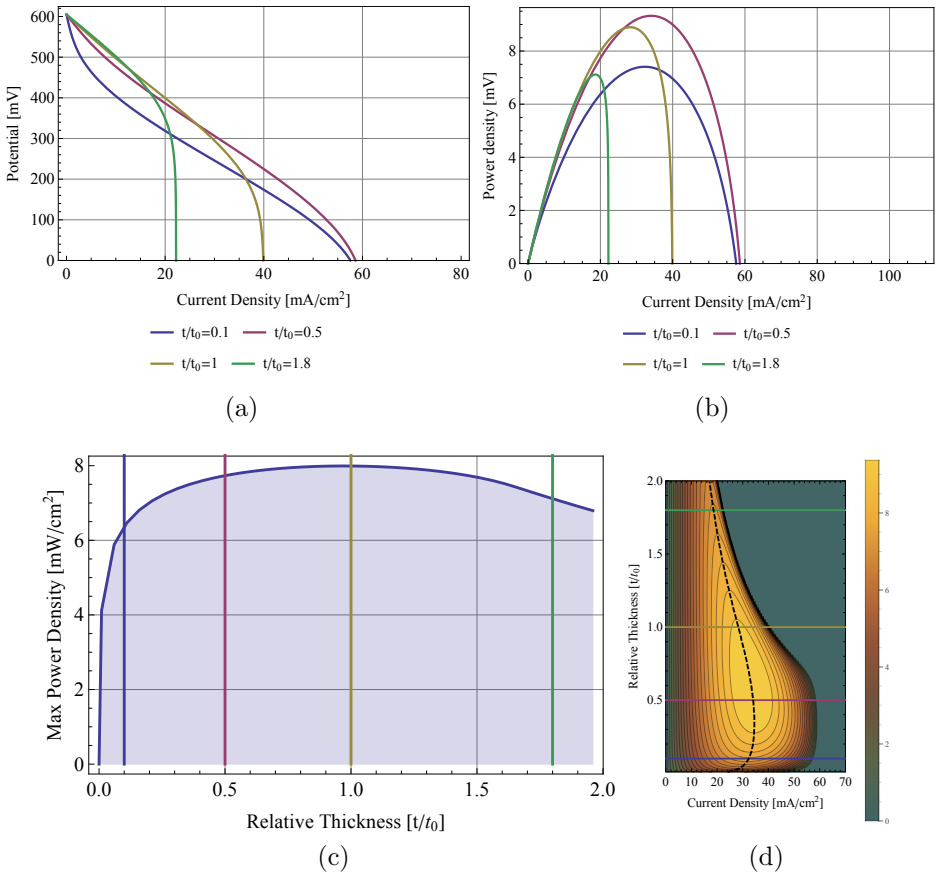

Figure 3.10: The figures illustrate the effects of increased catalyst thickness assuming an associated linear reduction in limiting current. The curves assume $U_0 = 700\,\mathrm{mV}$, $i_0^A = 5\,\mathrm{mA}$, $i_0^C = 10\,\mathrm{mA}$, $i_l^a = 40\,\mathrm{mA/cm^2}$, $i_l^C = 100\,\mathrm{mA/cm^2}$.

adding more catalyst active surface area. Such as simply increasing the catalyst layer thickness. This is, however, not the case in reality as the addition of more catalyst material will naturally lead to a reduced liquid access which will increase the mass transfer losses experienced. In order to model this tradeoff in a qualitative fashion, it is assumed that the diffusion limited current, i_l, scales inversely with catalyst layer thickness, $i_l \propto 1/t$. In order to simulate the IV curves, additional assumptions must be made for the curves, which are $U_0 = 700\,\mathrm{mV}$, a fixed ohmic loss with resistance $R\,A = 3\,\Omega\,\mathrm{cm^2}$. On the anode the exchange current density and diffusion limited currents are respective; $i_0^a = (t/t_0)\ 5\,\mathrm{mA/cm^2}$ and $i_l^a = 1/\,(t/t_0)\ 40\,\mathrm{mA/cm^2}$. For the cathode these are; $i_0^c = 10\,\mathrm{mA/cm^2}$ and $i_l^c = 100\,\mathrm{mA/cm^2}$. And finally a constant leakage current is assumed with $i_{leak} = 40\,\mathrm{mA/cm^2}$. Given all of these assumptions, the relation between peak power density and relative thickness can be investigated.

Figure 3.10a shows the IV curves for four different relative thicknesses. What can be seen is that at thicker catalyst layers the mass transfer limited characteris-

tics are not present until at much higher currents, yet the activation losses have a much sharper onset. The corresponding power curves are shown in figure 3.10b. It is observed that the maximum power is attained at a intermediate position, with the power curve taking on a more asymmetric appearance as relative catalyst thickness increases. Figure 3.10d shows the power plotted against both relative catalyst thickness and current density. The effect of the mass transfer limitation quenching the maximum attainable power is clearly seen. In addition a maximum is observed in a region where the two loss mechanisms balance out. The peak power density plotted against relative thickness is shown in figure 3.10c. It can be seen that under the simulated conditions the maximum relative thickness is $t/t_0 = 1$ where a peak power density of $8\,\mathrm{mW/cm^2}$ is attained. It can be seen that for thin accessible layers a large increase in power is achieved by small increments in the thickness while the peak power density for catalyst layers thicker than the maximum are less sensitive to changes in the thickness.

3.7 Summary

The chapter covered the theoretical considerations relevant to the performance of a methanol fuel cell. In particular a simple model for the conductivity of a single channel was developed. The model showed that conductivity had a large dependence on the pore size as well as a large dependence on the hydro-fluidic flow conditions where a free flowing condition allowed for a much higher conductivity than was achieved in blocked liquid flow conditions which is what is realized in methanol fuel cell operation.

A model for the electrical performance of a simple cell was developed and evaluated to investigate the tradeoff between cross-over vs. ohmic losses, which illustrate the need for a tradeoff between the two major looses. This investigation highlighted the big advantage of pursuing a design in which the tradeoff is easily adjusted as is the case for the plate supported fuel cell design discussed in the following chapter.

4

Design and Fabrication of a Semi-Monolithic Silicon Direct Methanol Fuel Cell

This chapter deals with design considerations for the fabrication of the semi-monolithic silicon based fuel cell system sketched in figure 4.1. This system integrates a proton conductive membrane as well as current collector electrodes in a single wafer structure. The electrodes are based on PtRu on the anode and Pt at the cathode, both layers are defined through conventional spray coating techniques. The device fabrication is also covered in the publication found in appendix G.

4.1 Structural Integration of Nafion Into Microstructures

In recent years a large focus has been paid to the usage of Nafion ionomer membranes in microtechnology based fuel cell systems [16]. While fuel cell research accounts for a large part of the interest in Nafion integrated into micro-systems, it has a wide range of applications within microtechnology. An example of alternate usage is the work by S. J. Kim et al. [52], who show the realization of a polymeric nonporous junction for high throughput nanofluidic applications. Membrane incorporation can be carried out through several different methods with their individual advantages

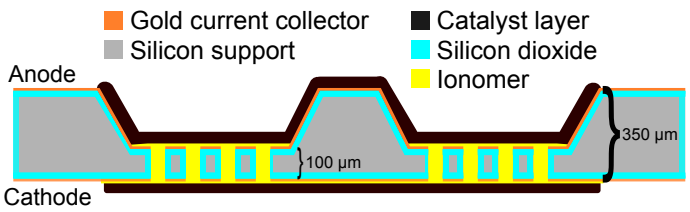

Figure 4.1: Illustration of the cross-section of a fuel cell design based on integration of a proton conductive polymer into a perforated silicon plate structure.

and disadvantages. The methods can largely be separated into three main categories:

- Dry integration
- Polymer formation through in situ polymerization
- Polymer formation through solvent evaporation

By far the most common method of incorporating such a membrane is a dry integration which imitates the layered fabrication method of larger scale systems used in the bi-polar plate design, but with the current collection elements replaced with silicon fabricated flow field electrodes [53]. The advantages of this method is the easy implementation in roll-to-roll fabrication of membrane/catalyst structure. The membrane can be cast separately through spray coating onto a moving substrate roll, which can easily have further layers deposited through additional spray depositions using the membrane as substrate. When employing dry integration in micro fuel cells the membrane typically has catalyst layers deposited and electrodes clamped around it through mechanical structures. Such an integration requires large clamping forces to apply adequate pressure on the stack to keep the silicon in contact with the membrane, and to compress catalyst layers to reduce contact resistances. This can through be problematic in silicon based devices due to the brittle nature of silicon. In addition to this, there is poor adhesion between silicon and Nafion, which also necessitate large clamping forces.

In situ polymerization allows integration by conducting the actual polymerization from monomers inside the desired micro structures. A notable problematic element of such integration is the need to avoid the formation of bubbles. An example of this method of integration is shown by Dolnik et al. [54] who infused polymer into micro-capillaries for capillary electrophoresis. In order to avoid bubble formation they used a method of polymerization at an interface traveling along the capillary.

Polymer formation through solvent evaporation works by simple evaporation of a solution containing the desired polymer. This method is used by Kim et al. [52] in the creation of nanoporous-junctions for nanofluidic applications. For Nafion solutions the solvent is typically a water/alcohol mixture, where the polymer concentrations corresponding to the final film occupying only around $< 15\%$ of the solution volume. Usage of solvents occupying lower ratios of the volume are possible, such as ethylene glycol [55], which can be used to form up to 50% volume mixtures of Nafion, however, at these higher ratios of polymer volume, low viscosity and high absorption of gasses become problematic.

In this work, Nafion integration is conducted through solvent evaporation, and the concerns with bubble formation are addressed through evacuated degassing and

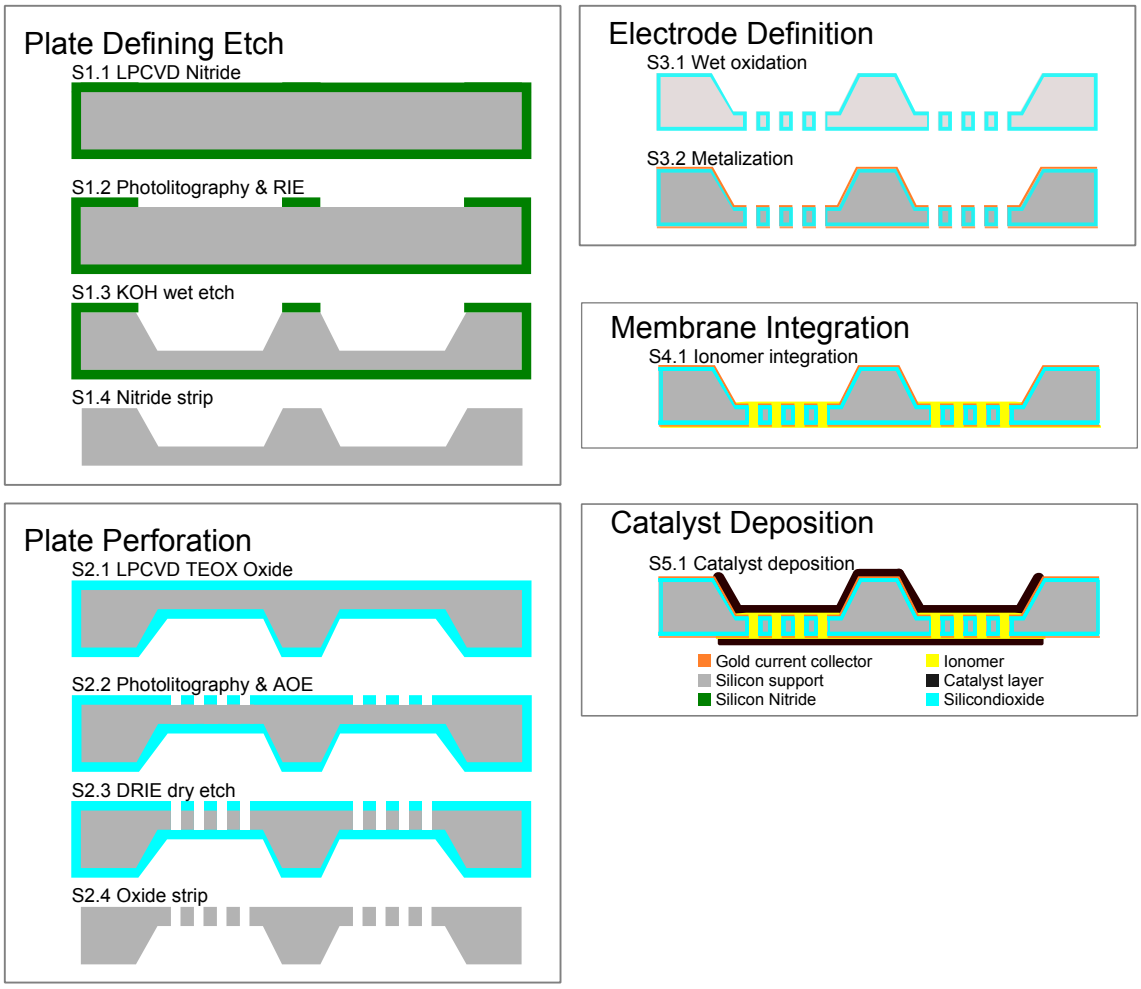

Figure 4.2: Illustration of the fabrication process flow. The process consists of two mask steps (S1.2, S2.2), passivisation and metalization steps (S3.1-2) and the ionomer integration step followed by a spray coating of catalyst layers (S5.1). Elements are not shown to scale.

slowing down the evaporation speed allowing a slow increase of polymer concentration at the drying front. The drying setup is then designed in order to guide the formation of the drying front such that the finished membrane forms inside the desired microstructures.

4.2 Fabrication of Perforated Plate Fuel Cell

A step by step schematic illustration of the fabrication process is shown in figure 4.2. The five major elements are:

1. Definition of the supporting plates

2. Perforation of the supporting plates

3. Passivisation and current collector electrode definition

4. Ionomer integration

5. Catalyst layer deposition

These elements are explained below with references to the step numbers in figure 4.2. The purpose of the frame definition is to thin down the wafer such that the finished ionomer conductance path is shorter. Thinning down the entire wafer, however, would lead to fragile devices, and therefore frames are defined to limit the etching to six smaller square plate areas. As the frames define mm scale structures on the backside of the wafer further front side processing is complicated. Vacuum clamping cannot be used on the backside, and during etching, dummy wafers are required. Due to the recesses, the bonding to the carrier wafers can be poor, and in some cases wafers spontaneously fracture. These fabrication concerns are covered in detail under the plate perforation step. The plates are perforated to allow the filling of ionomer, the size of the perforations are a tradeoff between the supporting role of the plate and maximizing conductance. A plate with a very large area perforated will have a larger conductance due to the larger amount of ionomer, but also have less supporting frame. Conversely a plate with smaller holes with larger spacings will have a larger mechanical support but lower conductivity. The fabricated devices have perforations ratios between 1% up to 40 %. For lower perforations cross-over will be limited while for higher perforations ohmic losses will be limited. The range of perforations therefore allows an investigation of the relative trade-off between these effects.

4.2.1 Silicon Plate Defining KOH Etch

In order to achieve a thin plate which still has sufficient mechanical stability to allow processing and dicing, KOH wet etching is used to define a recess in the wafer (step S1.1-4). Prior to etching, a Low Pressure Chemical Vapor Deposition (LPCVD) silicon rich low stress nitride layer of 100 nm is deposited (S1.1). The frame mask is defined through photolithography and Reactive Ion Etching (RIE) of the silicon nitride layer (S1.2). The mask geometry is shown in figure 4.3a. The wafers are submerged in a 80°C hot 28 wt% KOH solution for approximately 3.5 hours (S1.3), with a typical etch-rate is $1.2-1.3\,\mu m/min$. The thickness of the wafers is measured during the process and the timing adjusted in order to create 100 µm thick plates with the masked regions forming the 350 µm thick support frames. Alongside the frames, the anisotropic nature of the KOH etch is also used to simultaneously define

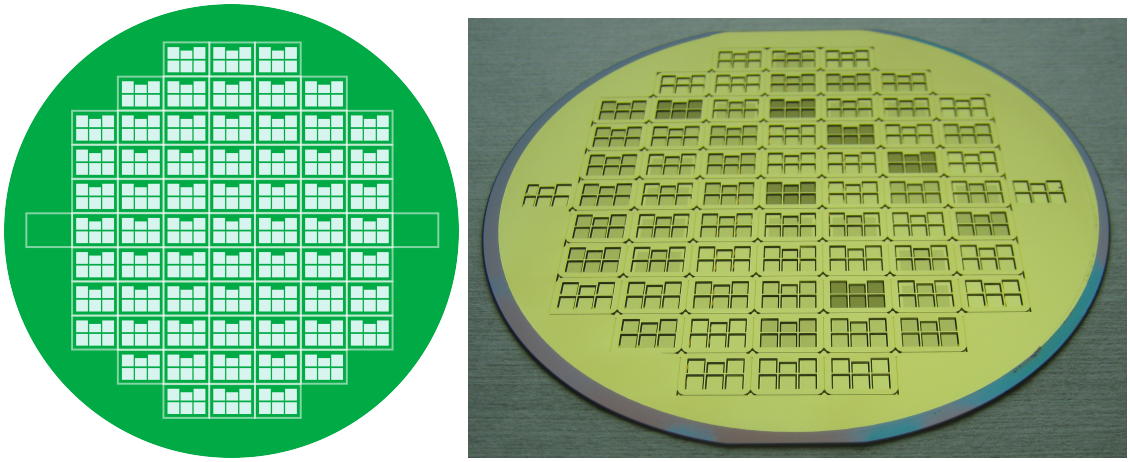

(a) Illustration of the mask layout. The dark green area is protected by a silicon nitride mask, while the white regions are open to the etchant.

(b) The image shows a wafer after the entire clean-room processing is finished, highlighting the geometry crated in the plate defining etch. The KOH etch is observed to have enlarged the regions where the device outlines meet.

Figure 4.3: Frame defining mask layout, and geometry resulting from KOH etch. Note that the wafer image has been flipped along the horizontal axis to correspond to figure 4.4.

50 µm wide V-groves along the boundaries of each device which serve as fracture lines during dicing. The etching of these groves self terminate at 50 µm depth due to the highly anisotropic etch rate of KOH in silicon. The plates and frames can be seen in figure 4.3b. The figure also shows that the KOH etch etches larger regions in the corners of the device outlines, due to the exposed edges being attacked by the etchant. After the etching the remaining silicon nitride is stripped in hot phosphoric acid (S1.4).

4.2.2 Silicon Plate Perforation

The perforation of the silicon plate is carried out using a Deep Reactive Ion Etching process (DRIE), which extends a traditional RIE process by alternating between etching using SF_6 and deposition of PTFE using C_4F_8. The etch mask is created by depositing a 2 µm LPCVD tetraethyl orthosilicate (TEOS) oxide layer (S2.1), which is patterned through positive photolithography (S2.2). The mask layout is shown in figure 4.4a. The TEOS oxide layer is much thicker than needed if only the etch selectivity is considered. This is due to the simultaneous usage of the backside as a stop layer during the etch (S2.3). As such the layer is designed to be sufficiently thick to withstand the pressure difference between the plasma chamber and the helium flow on the bottom side of the wafer which provides cooling during the etching process. It has been seen during processing that fractures can lead to the

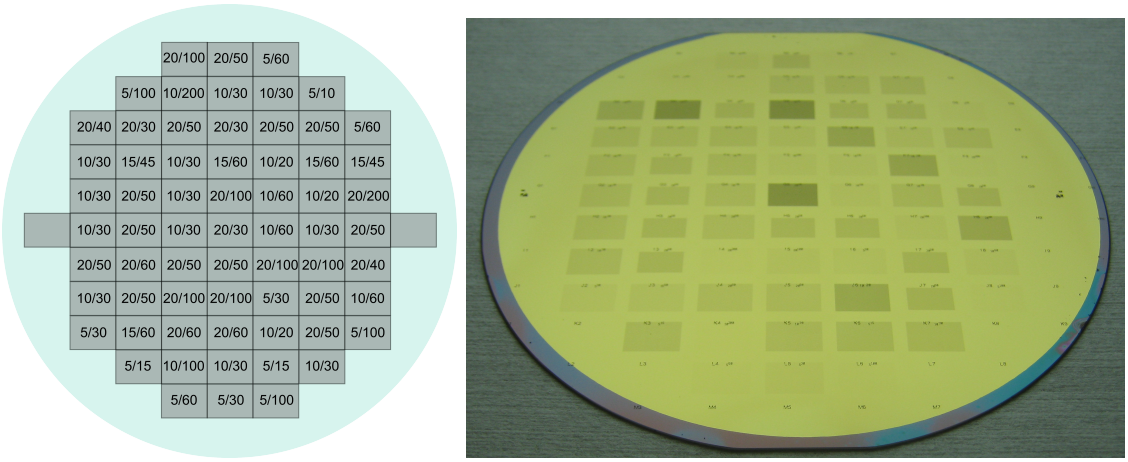

(a) The illustration shows the layout and variation of device hole diameters and plate lattice spacings in the mask used during plate perforation. The labeling follows the format hole diameter/lattice spacing and is used since the perforation lattice has too small feature size to be visible.

(b) The image shows a wafer after the entire clean-room processing is finished, highlighting the result of the perforating etch. Devices with a larger perforation ratio have a lower degree of reflection and therefore appear darker in the image.

Figure 4.4: Mask layout used for the plate perforating DRIE etch, and the resulting perforated wafer.

entire wafer declamping, which underlines the need for a thick oxide layer. Because the etch stops on the oxide layer, charging is a potential problem which can lead to notch formations. This aspect is pronounced by the variations in geometry across the wafer which leads to significant differences in etch rate. In order to ensure that the smallest features are fully etched, the larger features must be over-etched. To alleviate this problem a low frequency generator is used to remove charge during the etch process. This prevents charge build up when the oxide is reached, and therefore limits under-etching along the stopping layer. The oxide mask/stop-layer is then stripped in buffered HF (S2.4). The results of the perforation etch can be seen in figure 4.4b. The devices with a larger degree of perforation are visibly distinct due to lower levels of reflection from the surface.

Plate Etch Process Optimization

Through-out the process development three different perforation etch recipes have been employed, these are shown in table 4.1. The initial processing was carried out on the Danchip Advanced Silicon Etcher (ASE) equipment. This machine employes a DRIE process to etch silicon with high selectivity towards photoresist. Since the etch continues through the wafer, a carrier dummy wafer is required to prevent the process from etching the chuck beneath the wafer. This carrier wafer is attached

Process	ASE		Pegassus Process B		Pegassus SOI	
Step	Etch	Deposit	Etch	Deposit	Etch	Deposit
SF_6 [sccm]	260	–	350	200	400	250
O_2[sccm]	26	–	35	–	40	–
C_4F_8[sccm]	–	120	–	–	–	–
Cycle time [s]	6.5	5	7	4	3	2
Pressure [mTorr]	20	20	20(1.5s)/100	25	30	25
Coil power [W]	2800	1000	2800	2000	2800	2000
Platen power [W]	16	–	130(1.5s)40	–	75*	0
Etch/cycle [μm]	1.136	0		0	0.891	0

Table 4.1: Deep silicon etches utilized to carry out the plate perforating etch. *Uses a separate low frequency platen running at 380 MHz rather than the typical 13.56 MHz.

using crystal bond adhesive wax. The etch procedure showed cases of protruding edge defects around the plate perforating holes. An illustration of the positive protrusion defects and the process is seen in figure 4.5a. The process was carried out using either 2 µm or 4 µm resist. The defects occurred due to the tight masking margin on the etch. The ASE Deep Etch has an etch rate of $\approx$ 1.136 µm/cycle leading to a need for 88 cycles to etch through a 100 µm plate. The selectivity to photoresist is approximately 70, leading to a complete removal of the 1.5 µm resist after approximately 92 cycles. The margin for over etching is thus low, and if the plate is only slightly thicker than the targeted 100 µm the result is a uniform etching of the surface. This is not a problem on its own, as this would simply thin down the thickness of the plate slightly, however, the interaction of crystal bond with the etching chemistry creates a problem when this over-etching occurs. When the plasma reaches the crystal bond it both sputters and burns it, leaving behind geyser rings of non etched burned crystal bond around the holes. These rings act as etching masks and lead to the observed pattern in figure 4.5b. These positive protrusions were observed to interact negatively with the ionomer filling process.

In order to avoid the problem with protrusion the process was transitioned to a different equipment, Danchip DRIE Pegasus, which has a significantly higher selectivity hence allowing the resist to withstand the processing. It was, however, found that better vacuum conditions on the new equipment lead to wafers exploding due to the pressure difference between the chamber and gas-pockets between the carrier and device wafer. In order to allow processing without a dummy wafer, it was found that a thick oxide layer could be deposited and utilized as a stopping layer. The usage of an oxide stopping layer, however, leads to similar charging problems, as with the conventional deep silicon etch recipes, see figure 4.6. The

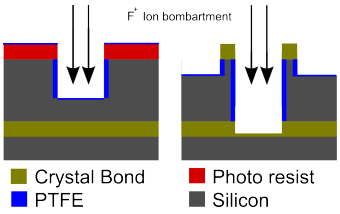

(a) Illustration of the effects of redeposited crystal bond masking the edges of the etched holes.

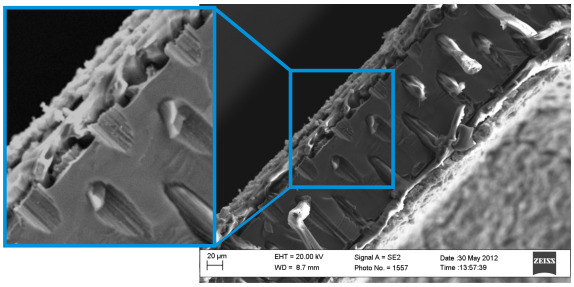

(b) Cross sectional SEM image showing a device with extrusion type defects on the surface of the anode after filling and catalyst deposition.

Figure 4.5: Illustration of protrusion defects and the result on the final devices.

problem occurs due to the ion bombardment impacting the oxide and charging it. This charge then redirects further bombardment towards the walls of the holes. The wall passivisation is consequently quickly stripped and the silicon near the stop layer etched outwards. These defects were also found to react negatively with the filling process, creating air pockets where the membrane loses contact with the catalyst layer. This problem can, however, be prevented by using a low frequency platen generator which utilizes a slowly varying electric field to allow charge removal during the processing to avoid charge buildup by allowing the ions to escape [56]. In order to include this decharging effect, the process was changed to use a recipe designed for silicon-on-insulator wafer processing. Silicon-on-insulator consist of e.g. a $\sim 10\,\mu m$ silicon layer on a $1\,\mu m$ oxide layer on a $500\,\mu m$ silicon wafer. The process is therefore not intended for deep silicon etches, but is crucially optimized to have very low etch-rates in the oxide layer and to remove charging effects. It was found that no major process parameters needed to be adjusted for this process to allow etching of very deep structures in silicon. The SOI etch has an average etch rate of 0.891 µm/cycle thus for a 100µm plate the required etch is about 112 cycles. The etch rate will, however, vary as the etch progresses depending on the individual hole sizes, and the wafer temperature which varies during the process based on cooling efficiency. A typical etch therefore requires up to 150 cycles. The selectivity towards photoresist for this etch is quite high, on average 183, resulting in only a $0.54\,\mu m$ etch in the mask if photoresist is used. In the case of a $2\,\mu m$ oxide masks where the selectivity is even higher than towards photoresist, over-etching is of no concern.

The final approach allowing full etch through of backside processed fragile wafers was thus to use an oxide mask and stop layer, SOI DRIE etch and specially developed laser-milled perforated carrier wafers. These carrier wafers have 1 mm holes laser milled away in a pattern matching the chip mask pattern, such that each individual

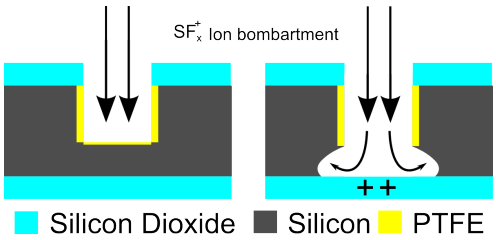

(a) Illustration of the effects of charging in the silicon dioxide stop layer during a SF6/O2 DRIE etch.

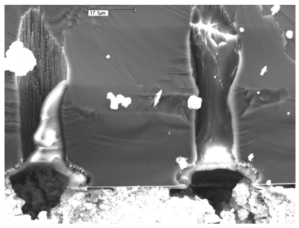

(b) Cross sectional SEM image showing the etch defect resulting from charging. Also seen is the resulting air pocket separating membrane and catalyst.

Figure 4.6: Illustration of the charging defects and the effects on the final devices.

void created by the frame recesses on the devices has an outlet. This prevents the build up of over-pressures and allows the use of the carrier wafer to improve stability during the etch to prevent mechanical failures.

4.2.3 Current Collector Electrodes Definition

In order to prevent the creation of electrical short circuit between the two current collector electrodes on each side of the silicon plate, the wafers are passivated in a wet oxidation, of a 1 µm silicon dioxide layer (S3.1). Metalization can be accomplished by either sputter deposition or e-beam deposition, however, trials using sputter deposited gold has shown short circuits with larger hole geometries 40 µm – 100 µm [57], as well as occasional shorts with 20 µm. Short circuits were not observed with e-beam evaporation due to the highly directional deposition. E-beam is consequently the preferred method of electrode definition. The current collector electrodes are defined by first an E-beam deposition of a 10 nm thick Ti anti-diffusion barrier and adhesion layer followed by an e-beam evaporation of 100 nm Au (S3.2).

4.2.4 Proton Conductive Membrane

The method of integration is described briefly here in the perspective of the fabrication but will be covered in more detail in section 4.3. The proton conducting ionomer membrane is integrated into the silicon plate using drying by evaporation from a solution under low pressure $\approx$ 300 mBar (S4.1). The setup used during the drying process is shown in figure 4.7. The drying is carried out with the finished silicon plates mounted in Polydimethylsiloxane (PDMS) molds. The dimensions of these molds critically affects the dynamics of the ionomer deposition on the plate

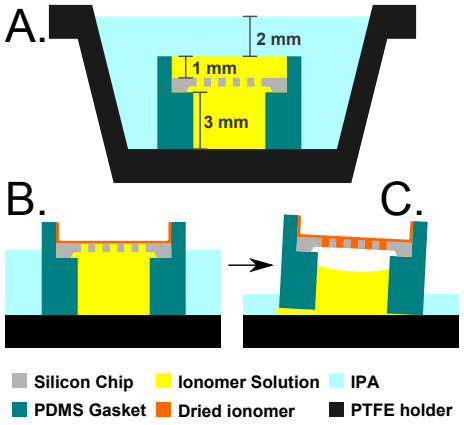

Figure 4.7: Schematic showing the setup for the evacuated evaporation drying used to integrate the ionomer in S4.1 of the fabrication process as shown in figure 4.2.

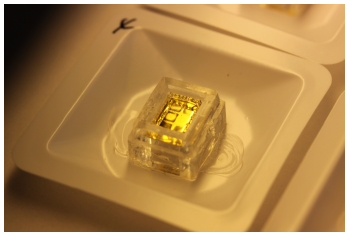

(a) A dried device. The excess Nafion can be seen to have leaked through the bottom and into the PTFE boat.

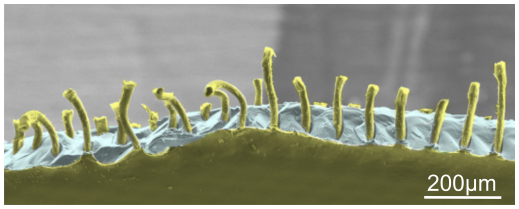

(b) False color scanning electron microscopy image showing the ionomer integrated into the silicon plate after membrane integration and annealing. The ionomer is colored green against the silicon which is colored blue. The strands of ionomer were elongated during the fracture of the device, and therefore appear longer than the thickness of the plate.

Figure 4.8: Results of the Nafion ionomer integration process.

surface.

The solution used is Nafion® DE 2020 by Sigma Aldrich consisting of 20 wt% Nafion ion-exchange resin in lower alcohols with 34 wt% water. Initially the solution is submerged entirely in pure isopropanol (step A, fig 4.7). This delays the drying of the Nafion solution for approximately 2 hours, during which it can thoroughly degas. After this initial delay the Nafion solution will start to dry. As the solution dries, the Nafion concentration at the drying front steadily increases until it forms a solid membrane which deposits on the edges of the PDMS holder and on the device surface (step B, fig 4.7). As the drying continues through the device, the dried Nafion detaches from the solution, and gas develops on the backside of the device (step C, fig 4.7). This pushes up the holder and causes the remaining ionomer solution to leak through the bottom as shown in figure 4.8a. After the drying, the devices are annealed at 140°C for 30 min in ambient air. The annealing process

Liquid solution	Anode	Cathode	Dry weights	Anode	Cathode
Catalyst composition	PtRu 75%	Pt 70%	Carbon [mg]	50	64.3
Catalyst solution [mg]	200.0	214.3	Catalyst particles [mg]	150	150
Nafion solution 20 wt% [mg]	266.7	285.7	Nafion [mg]	53.3	57.1
PVP solution 10 wt% [mg]	51.7	55.4	PVP [mg]	5.2	5.5

Table 4.2: Catalyst spray coating composition. The final catalyst mass loadings are 58% and 54% for anode and cathode, respectively.

removes solvent remains and has been shown to reduce ionic resistance and increase mechanical stability [58]. The finished integrated membrane can be seen in figure 4.8b.

4.2.5 Catalyst Layer Deposition

The catalyst layer is added with spray deposition (S5.1). The final layer is made up of of carbon black supported catalyst particles bound by ionomer. The spray deposition solutions consisted of a dry catalyst powder dissolved in a water alcohol mixture which evaporates during the coating process. The solution composition without the evaporating solvents is shown in table 4.2. The dry powder consists of 70 wt% Pt and 75 wt% PtRu particles on the cathode side and anode side, respectively, supported on amorphous carbon of the type Ketjenblack. The mixture also includes Nafion and a dispersion agent, polyvinylpyrrolidone, leading to the deposited catalyst layers having relative loadings of 58 wt% and 54 wt% of the catalyst particles. During the coating process, the devices are mounted on a back-plate which is heated to 80°C to aid solvent evaporation during spray deposition. The spray nozzle is hand operated and each chip is coated through several short $\approx$ 1 sec pulse bursts, with pauses $\approx$ 40 sec between to aid evaporation. Through micro-scale measurements prior and after deposition the mass gain can be used to estimate the platinum loading on each device. The target value is 2 mg/cm^2 of Pt on each side, which requires a 4 mg/cm^2 loading of PtRu on the anode side. The results of the depositions can be seen in a smooth kernel histogram in figure 4.9. The loadings are slightly below the targeted value, and for the cathode layer the variance is much larger due to the thinner layer needed. Two outliers are present in the cathode loading data. It is believed that these have a reduced loading as a result of the repeated pulses following in too rapid succession. This could lead to the still wet solution being forced off the

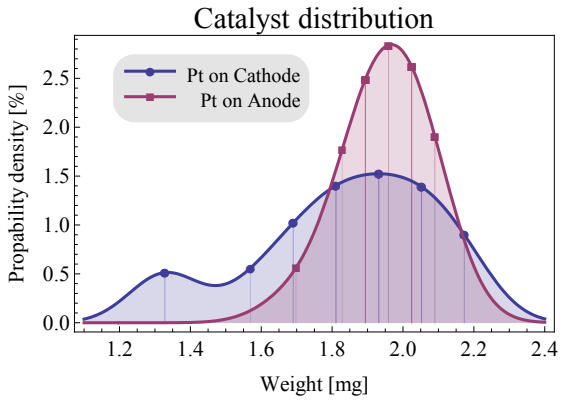

Figure 4.9: A smooth kernel histogram of the platinum loading on anode and cathode. On the anode, the platinum is a component of a (1:1) PtRu alloy and as such the total weight of the catalyst particles is twice that of the Pt loading. with The bandwidth is 0.1 mg. The points indicate locations of measurements.

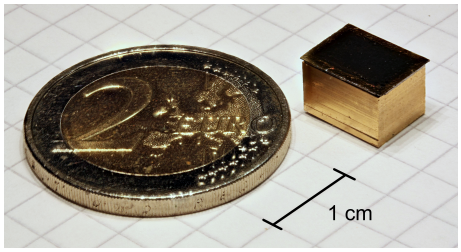

Figure 4.10: A device shown on top of a 220 µL capacity fuel reservoir shown next to a two euro coin for scale. Fuel is injected through holes in the bottom of the reservoir which are not visible.

surface. Excluding these outliers the average loading on the anode and cathode are 1.91 mg ± 0.18 mg, and 1.95 ± 0.10 mg, respectively. The edges of the device are masked during the deposition, however, the central frame is not. The actual loading on the active area will therefore be slightly less than these estimates on the anode side of the device.

4.2.6 Fuel Cell Assembly

Finally the finished silicon device is attached to a CNC-milled brass reservoir using a conductive adhesive. The reservoir consist of a 1 mm wall with dimensions 10 × 7.5 × 6 mm which gives an outer volume of 375 µL and a fuel volume of 220 µL. A device mounted on a fuel reservoir can be seen in figure 4.10. In this configuration the reservoir acts as the anode connection, while the edge of the device on the top acts as the cathode connection. Depending on mounting usage, an additional top casing can be fixed to the top to protect the membrane from mechanical damage.

4.3 Polymer Integration

The integration of Nafion into the perforated plates is a vital process step in the fabrication process.

Many techniques exist for casting Nafion sheets for use in conventional fuel cells such as roll-to-roll gel casting, spray casting or dispersion casting [59]. Common for all these techniques is that they create thin uniform sheets of polymer on flexible substrates. These techniques are not easily transferable to silicon integration processes. For gel processes the high viscosity of the gel would limit the ability to get it into the micro-pores. Spray casting would similarly show difficulties in getting the polymer to properly fill the pores as any over-layer would block access. Dispersion casting techniques can, however, almost be applied. The method here is to distribute a thin solution of the polymer over a sheet and allow the solvent to evaporate. Two major issues occur when transferring this technique to micro pore integration; getting the dispersion into the pores as a start, and secondly getting the solvent out of the pores. The major challenge in the first issue is that air bubbles might get trapped and leave behind voids in the micro-structure. The second issue is that as the solvent evaporates, dissolved gas bubbles can form which also lead to voids in the finished structure.

Evaporation is a statistical process were the driving force is a difference in vapor pressure between the solvent and gas phase. The interface will experience both evaporation and condensation, and based on the liquid and gas partial pressures this will either lower the concentration of the solvent in the water or gas phase. The equation describing the governing evaporation rate is the Langmuir evaporation equation, which defines the rate of mass flux through a surface $F = \frac{\partial M}{\partial t}$, given from the molecular mass, m, the thermal energy, $\tau = k_b T$, and the partial pressures of compound in liquid and gas phases, p_l, p_g:

$$F = (p_l - p_g)\sqrt{\frac{m}{2\,\pi\,\tau}}$$

Here it should be noted that both liquid and gas phase are assumed to be at the same temperature. This is why the flux decreases with increasing temperature, which would otherwise seem counter intuitive compared to liquids that are at elevated temperatures compared to the gas phases they are evaporating into. Also it should be strongly emphasized that this equation deals only with the rate at the interface. During an evaporation process the partial pressures may quickly reach equilibrium at the interface and the actual flux be limited by mass transfer pro-

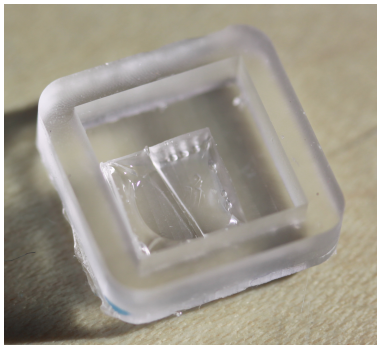

(a) A 2 mm deep PDMS cast recess. The dried polymer membrane is seen to have shrunk significantly during drying, and has bubbles attached in the lower corners of the resulting membrane. The cut was created to measure center thickness.

(b) A 1 mm deep PMMA recess. The polymer membrane is seen to have fractured during drying as it contracted. The center thickness is measured on the center sheet.

Figure 4.11: Experimental setup used to investigate the sheet thickness of Nafion films formed through solvent evaporation.

cesses such as convection or diffusion in the gas phase. From the equation it can be seen that the evaporation rate flux can be decreased either by elevating temperature, or by changing the vapor pressure of the solvent in the gas phase.

In order to pin down the amount of Nafion over-layer needed, a drying test was carried out in a PMMA and PDMS test structures. Recesses of varying sizes were filled with the polymer solution and left to dry, examples are shown in figure 4.11. The solution consists of 20 wt% Nafion, 34 wt% water and 46 wt% alcohols which is almost entirely of 1-propanol, but also contains about 1 wt% ethanol. The densities of water and 1-pronaol are 1 g/mL and 0.8 g/mL, respectively, and the density of a dried Nafion membrane varies between 1 g/mL and 2 g/mL, depending on curing. Assuming a membrane of density 1.4 g/mL the final film occupies 12.7 % of the total solution volume.

The test structure used for the experiment consisted of four recesses each 1 cm × 1 cm, which were filled to the top with the Nafion solution and left to dry out in ambient conditions. For each deposition the resulting membrane was significantly fractured along the edges, but flat depositions could be found in the center. The thicknesses are shown in figure 4.12 along side a 15% volume estimate of the thickness. The figure shows that there is a tendency for the thickness to be close to the 15 vol% estimate, however, at 4 mm the thickness breaks the trend. This is due to the geometrical effects of the drying, where the three first recesses were seen to deposit a small membrane at the bottom which detached from the edges when it

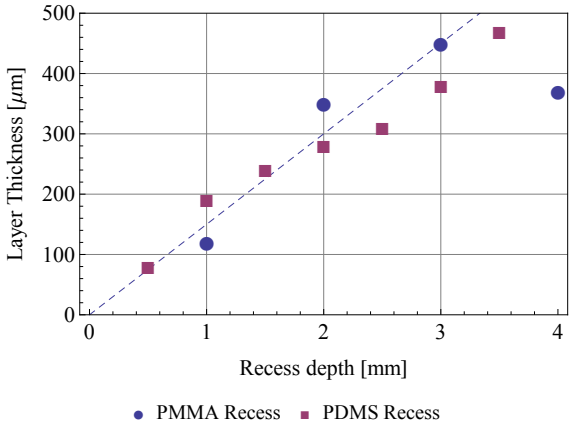

Figure 4.12: The relation between recess depth and deposited layer thickness in PMMA drying experiments. The solid line indicates a 15 % volume estimate.

fractured the 4 mm recess fractured earlier and thus deposited the membrane very unevenly. The conclusion can be gathered that a 1-2 mm over-layer of Nafion should be sufficient to deposit the 100 µm membrane, and that thicker layers might cause trouble as they detach during the drying.

Given a membrane with thickness $t = 100\,\mu\text{m}$ and an active area of $A_{act} = 28.52\,\text{mm}^2$ with perforation ratio $\alpha = 40\,\%$, the total internal volume is 2.85 µL. Thus assuming a density of the cast Nafion film of $\rho \approx 1.4\,\text{mg}/\mu\text{L}$ [60], the weight needed to fill the pores is $\Delta m = 3.99\,\text{mg}$. Assuming a surface excess layer of t_s divided across both sides an additional weight gain of $\Delta m_s/t = A_{total}/\rho = 0.05\,\text{mg}/\mu\text{m}$ must be added. Results from fillings can be seen in figure 4.13. It can be seen that the excess surface area is independent of the effective area but does increase for smaller holes. The absolute magnitude is somewhat uncertain due to the front side surface effects. A SEM inspection of a finished device is shown in figure 4.14. The excess thickness i here observed to be 16 µm on the anode side only, while the weight estimated from mass gain predicts an excess layer of 16.3 µm on both sides, leading to an absolute magnitude which is off by a factor 2.

The polymer solvent is a propanol-water mixture, and this leads to the natural question of how the evaporation process evolves through time. The relation between equilibrium vapor composition and solvent composition is shown in figure 4.15. At atmospheric conditions isopropanol/water has an azeotrope point at a concentration of 70 mol% IPA, which means that a mixture above this point will evaporate primarily water, while a mixture below this point will evaporate primarily IPA, thus leading solutions to move towards the azeotrope point during evaporation. The actual evaporation is carried out at lower pressures, and it therefore proves valuable to study the specific dynamics under the experimental conditions. In order to carry

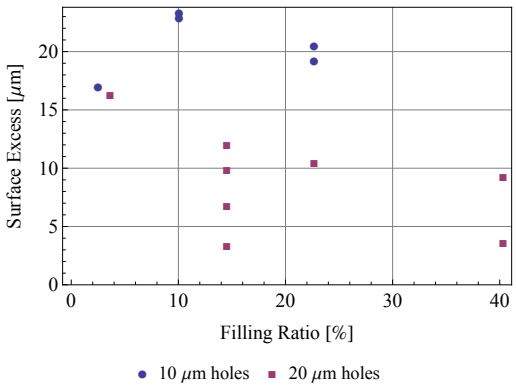

(a) Excess surface thickness shown in relation to the device filling ratio.

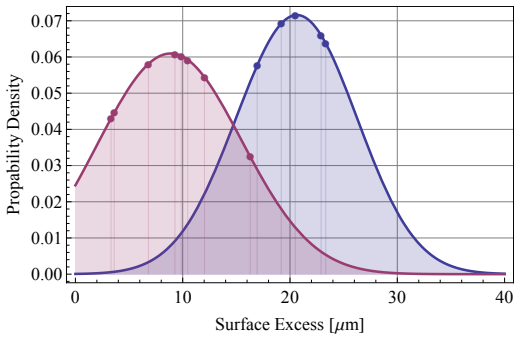

(b) A smooth histogram distribution showing the probability density function for expected surface thickness with geometries with holes of 20 μm (Red) and 10 μm (Blue). The measured points are marked.

Figure 4.13: Excess surface thickness estimations from mass gain during drying. The figures show that for geometries of constant hole size the excess thickness show no clear dependence on lattice spacing, while decreasing hole dimensions does lead to an increase in surface excess.

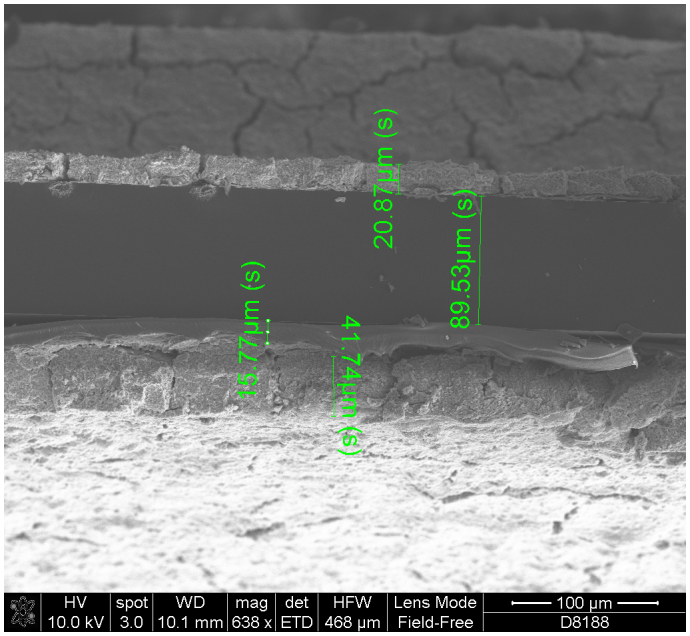

Figure 4.14: Cross-sectional SEM image of a device after catalyst deposition showing the appearance of a 16 µm thick excess Nafion layer on the anode side of the device.

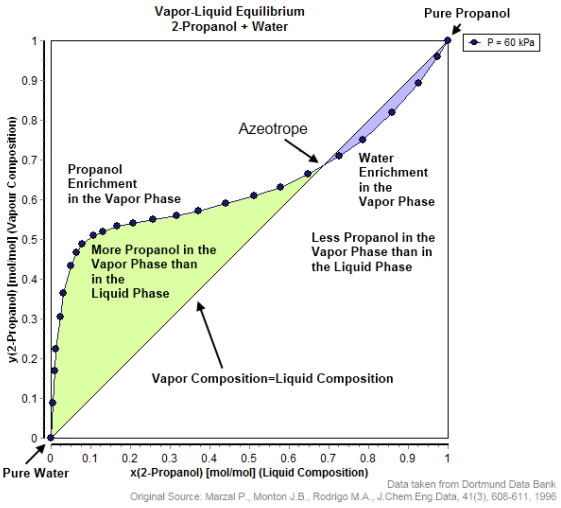

Figure 4.15: The relation between equilibrium vapor phase and liquid phase in a mixture of IPA and water.

out such a study, several mixtures of IPA/water were filled into 5 mL beakers to a height of 20 mm and put into a Memmert Vacuum furnace, with pressure controlled to 100 mBar and temperature at 40°C, and left to evaporate while monitored by a camera. The resulting image sequence was then used to extract the color intensity along lines perpendicular to the beaker surface, which allows tracing of the moving liquid front. The results of the measurement is shown in figure 4.16. The resulting evaporation curves show a transition between a fast and a slow linear evaporation rate. This behavior is consistent with the assumption that the two species are evaporating independently, which means that propanol evaporation is dominating the short time frame while the water evaporation dominates after the IPA has fully evaporated. Modeling the liquid front position as an abrupt transition in evaporation rate would yield a sharply transitioning linear curve, which would not resemble the observed results. The results can be described by assuming that the instantaneous total evaporation rate, $r_t\,(t)$, follows a smooth transition from the evaporation rate of propanol, r_1, to the evaporation rate of water, r_2,. This model seems to reasonably reproduce the observed curve. For this purpose an exponentially based sigmoid function is used to guide the transition, with a transition point t_0 and a transition region span of κ.

$$r_t \;=\; r_1 \frac{1}{1+\exp\left(\left(t-t_0\right)/\kappa\right)} + r_2 \frac{1}{1+\exp\left(-\left(t-t_0\right)/\kappa\right)}$$

The results of fitting this model are shown in figure 4.17. The results show that

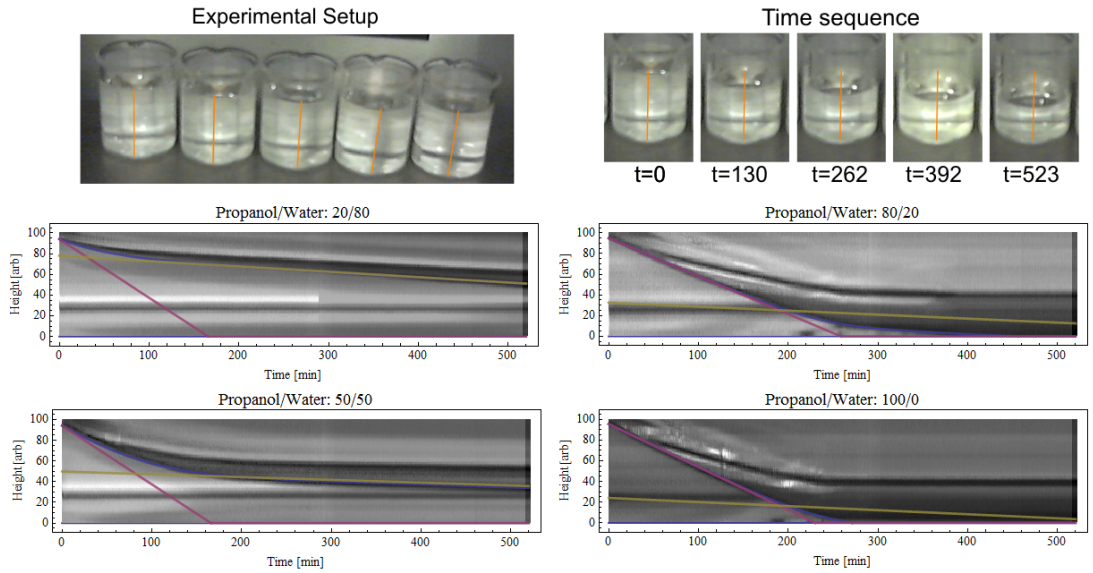

Figure 4.16: The figures show the method used to determine the evaporation rate of the propanol water mixtures. The Orange lines mark the region which is extracted as a function of time. The blue lines illustrate a fit to a evaporation model with a smooth evaporation rate transition between the propanol evaporation rate and water evaporation rate. The red and yellow curves show respectively the evaporation component of the propanol and water content in the mixture.

the transition point, t_0, is in good agreement with the assertion that the rate of evaporation decreases at the point when the propanol content is fully evaporated,$t_{e,IPA} = V_{IPA}/r_1$. It can also be seen that a large variance is observed in the estimate of the time of full evaporation, t_k, which is due to the low rate of evaporation of water. This rate however apears close to an estimate given by the sum of evaporation rates $t_{e,T} = V_{\mathrm{IPA}}/r_1 + V_{\mathrm{H_2O}}/r_2$. From the data the evaporation rates under the experimental conditions are found to be 5.2 mm/hour for IPA and 0.63 mm/hour for water.

4.4 Summary

In summation of the fabrication, a reliable fabrication method for a perforated plate structure with an integrated Nafion membrane was developed. A perforation process was developed which facilitated the through etch perforation, despite the process including very large aspect ratio back side structures and fragile wafers.

In order to cast the membrane into the structure a fabrication method was developed consisting of immersed vacuum drying, which allowed for a bubble free casting result. Mass gain estimates of the filling suggest the presences of larger excess surface layers of Nafion in the range of $10-20\,\mu$m, however, SEM microscopy

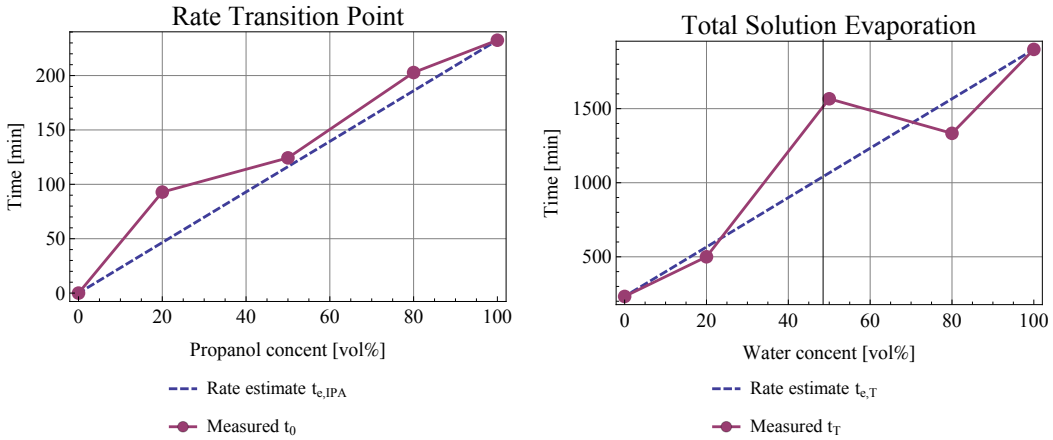

(a) The evaporation model transition time, which marks the change from a fast evaporation rate to a slower evaporation rate. The estimate assumes that this time is point at which the equivalent propanol content would have fully evaporated.

(b) The figure shows the time at which the mixture has fully evaporated. The estimate is based on the sum of the evaporation times for the water and propanol contents separately. The horizontal line marks a volumetric The horizontal line marks a concentration of 48.5 vol%, which is the solution concentration used in this work in Nafion integrations.

Figure 4.17: Evaporation time results from tests with different propanol to water ratios.

of the finished devices indicate that the excess layers lower than these estimates.

5 Device Characterization

This chapter will describe the characterization methods and results for the silicon plate based fuel cell devices described in chapter 4. The characterization has been carried out through separate setups which are used to characterize the electrical performance of the cell, and the ionic conductive properties of the integrated membrane cells. In addition the cell performance is tested using different fuel compositions to highlight limiting factors in performance. The device characterization is also covered in the publication found in appendix G.

5.1 Characterization Methods

To characterize a fuel cells performance the most often used characterization method is a simple IV-characterization where the potential is measured while the current draw is swept. This method presents the potential of the cell for the working range of currents, and can be used to find the peak power performance, which sets the limit for the power the cell can deliver to a device.

Another method is Electrochemical Impedance Spectroscopy (EIS), which is used to characterize the ionic properties of the membrane. The method works by exerting a time varying potential across the cell and measuring the amplitude and phase of the resulting electrical current. Such a method allows a frequency resolved measurement of the complex impedance. The method can be used to resolve different contributions to the cell resistance through differences in their typical response time.

5.2 IV-Characterization

The characterization setup used to determine the IV characteristics of the devices is a simple two electrode source-meter setup shown in figure 5.1. The electrodes are

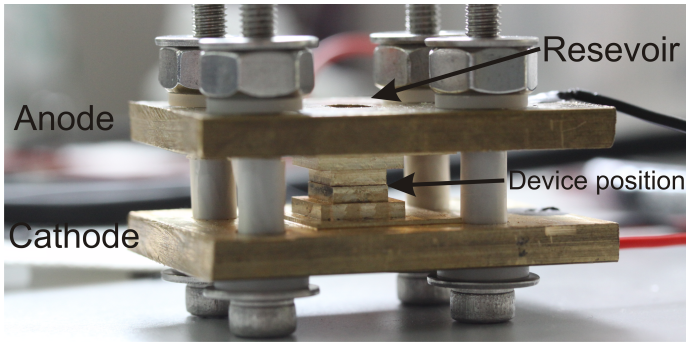

Figure 5.1: IV-characterization clamping setup. The two electrodes are milled out of brass, and allow inspection of the device edge to ensure that leaks do not form.

constructed such that side of the device being tested is easily visible for inspection. This allows visual assurance that fuel is not creeping around the outside of the device from anode to cathode. A conductive rubber gasket is employed to prevent gas contact from the anode catalyst layer through the side of the chip to the atmosphere, this gasket has a rather high ohmic resistance of $5\,\Omega$, but is necessary to prevent direct gas contact between catalyst layer and air. Such a contact aids in the removal of CO_2, but also allows oxygen transport to the catalyst, which has been observed to cause degradation of the catalyst layer.

A typical measurement is carried out by mounting the chip and filling the top electrode reservoir with 3 M methanol. Figure 5.2 shows the initial rise of potential for three separate initiations of the same device. The curves are captured in sequence after 0 hours, 1 hour and 2 hours of water submerged hydration. The initial curve sequence which shows a rise, and then an effect which slows or even reverses the charge accumulation. This effect is well described by assuming that the initial charging current drives the cross-over flow of methanol which initiates a potential drop at the cathode as the methanol is oxidized. As the membrane is further hydrated a noticeable increase in conductivity is observed, leading to faster charging times. Due to the effect of hydration, devices were stored submerged in water to ensure a high degree of hydration during measurements.

IV characterizations of two separate devices are shown in figure 5.3. In order to determine the effective internal resistance, the curves are fitted to a straight line in the current region above the peak power point. This removes the influence of the activation losses which tend to subside at currents of about $10\,\mathrm{mA/cm^2}$.

The relationship between achieved peak power density and perforation ratio is seen in figure 5.4. All devices have peak powers in the $\mathrm{mW/cm^2}$ range, however, a variation is observed for devices with similar geometries, and a trend of increasing power density is observed as perforation is increased. This indicates that the tradeoff

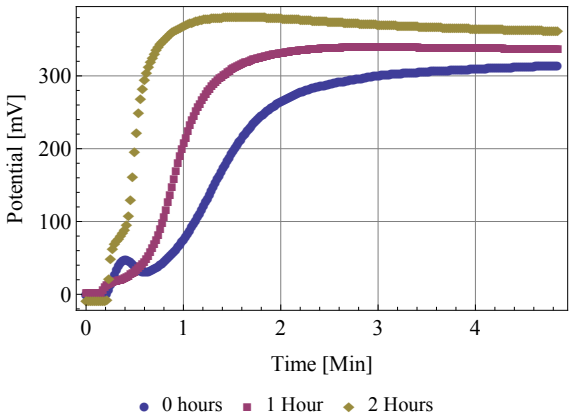

Figure 5.2: The initial potential rise after introducing methanol to the anode. The three curves are shown for different periods of hydration.

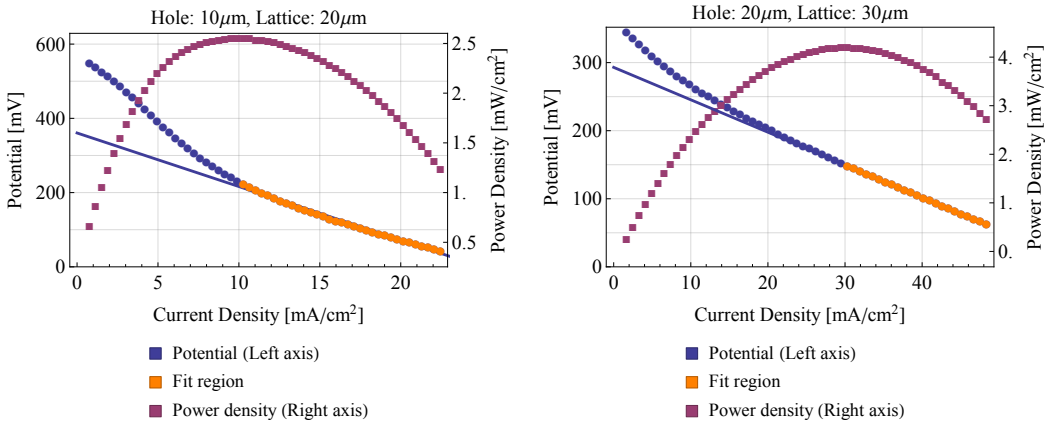

(a) A device with a perforation ratio of 22.7 %, showing a peak power density of 2.30 mW/cm^2. The effective internal resistance is found to be 49.8 Ω.

(b) A device with a perforation ratio of 40.3 %, showing a peak power density of 4.52 mW/cm^2. The effective internal resistance is found to be 16.4 Ω.

Figure 5.3: IV-characterizations of two devices, each with an active area of $A = 0.29\,\mathrm{mm}^2$. The characterization was carried out using 3 M methanol, at room temperature conditions. The solid line shows a linear fit in the region above the peak power, used to determine the effective internal resistance.

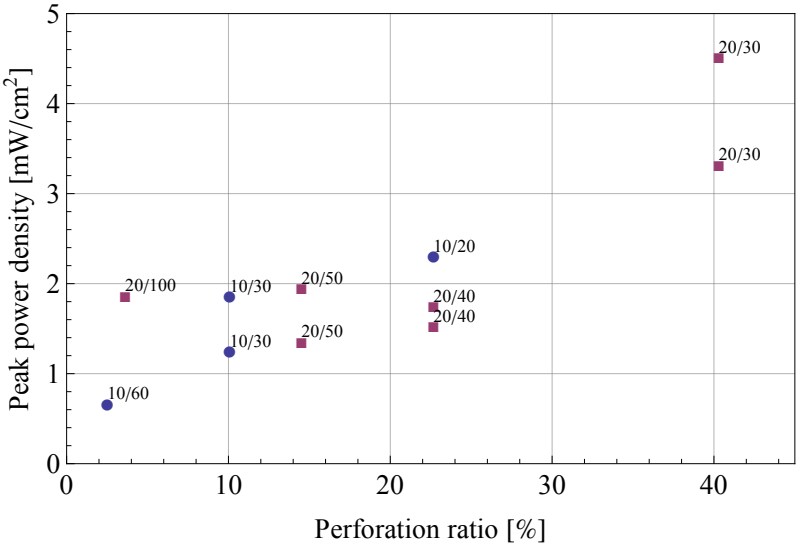

Figure 5.4: Peak power density ratio shown against effective perforation ratio. Points are labeled as Hole diameter/Lattice spacing. A tendency of increased performance with higher ratios of perforation is observed. A large variation is observed between devices of similar designs and similar perforation.

between increasing the permeation and conductance of the membrane is such that the lowered ohmic losses outweigh the increased cross-over losses.

The relationship between the maximum attained current density at positive powers and open circuit potential is shown in figure 3.5. The results can be seen in comparison to the theory developed in section. While there is little direct agreement between experimental data end theory, the tendency for a correlation of peak power density and lowered open circuit potential with higher attainable current densities for are clearly evident. The data shows promise that an increase in perforation ratio or thinning of plate membranes might lead to a parameter region where the characteristic bend in performance characteristics is visible.

In order to compare the performance level with other devices in the literature, performance numbers from other similar devices are shown along side the best obtained devices of this work in table 5.1. These numbers are repeated from table 2.5. Comparing the best obtained device performance with literature, the conclusion could be drawn that the integrated plate devices do not outperform similar devices in terms of peak power per active, and yet even then and taking into account that the perforated plate only accounts for 37 % of the total device area, it still manages to out perform other devices in literature in terms of power per volume where it reaches 2.5 mW/ cm^3. The devices accomplish this by forgoing the need for compression structures, thereby allowing a simple attachment of a reservoir with little volume wasted. The low power density per active area at the same time suggests

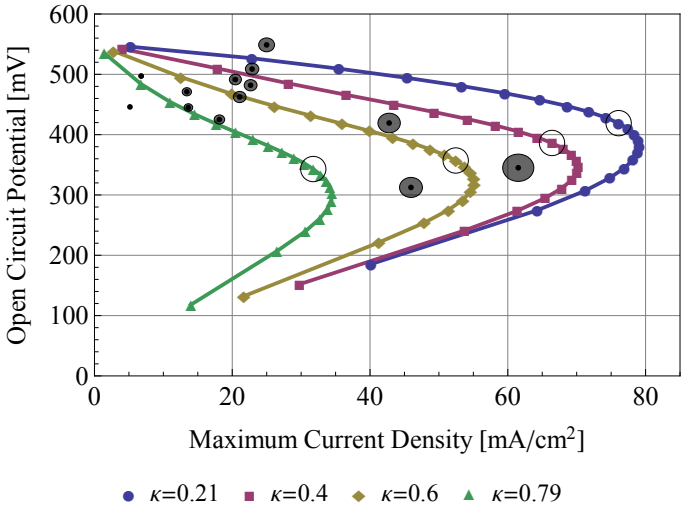

Figure 5.5: The figure shows the open circuit potential and maximum current density for which a positive power is extracted as curves where the generalized mobility parameterμ is varied, while the limiting current ratio, κ, is kept constant. For each curve a black circle marks the point where maximum power is obtained, and power falls of in both directions moving away from this point. The solid black markers indicate experimental data for fabricated devices, where the radius of the disk is proportional to peak power density.

Work	System size	Active area [cm^2]	P [$\frac{\text{mW}}{\text{cm}^2}$]	P_v [$\frac{\text{mW}}{\text{cm}^3}$]	OCV [mV]	C_M [M]	Catalyst Loading [mg/cm^2]
Passive systems							
Shimizu et al. [35]	49 cm^2 x 4cm	36	10	1.84	550	4	A: 2.5 C: 2.6
Sabate et al. [36]	6 cm^2 x 1 cm	0.25	10	0.42	450	2	A: 4 C: 4
Gharibi et al.[37]	4.75 cm^2 x 3cm	4.75	1.2	0.40	500	1	A: 1 C: 3
This work	0.75 cm^2 x 0.7 cm	0.29	4.52	2.5	300	3	A:2 C:4

Table 5.1: Performance comparison between the perforated plate supported devices of this work and similar micro direct methanol fuel cells. Numbers repeated from table 2.5.

that the power density could be significantly improved.

5.2.1 Fuel Type Performance Evaluation

The devices will work with a range of liquid and gas phase fuels. Figure 5.6 shows the performance of a device tested with hydrogen, hydrazine and methanol. The OCV for the hydrogen potential curve in figure 5.6a is 732 mV, which is much lower than the theoretical OCV at standard conditions of 1.21 V. This suggests that the cell contains large overpotentials. Part of these can be attributed to the deviation in concentrations from standard conditions as noted in section 3.4, of which the majority is most likely associated with a low cathode performance. Due to the phase barrier between hydrogen and the liquid proton conducting phase, cross-over effects are inhibited. Methanol in comparison shows a large potential loss close to zero current density, which is due to the large cross-over losses. Interestingly hydrazine does not show significant cross-over losses, and in fact shows performance close to pure hydrogen, however, it does show the onset of mass-transfer limitations around 25 mA/cm^2. The related power density curves are shown in figure 5.6b. A high power density of 12 mW/cm^2 is seen for hydrogen, located at a large current density of 38 mA/cm^2, which leads to the conclusion that the achieved power density is primarily limited by ohmic losses. For the Hydrazine fuel, the peak power density is located at a much lower current density, 12 mA/cm^2, and reaches a lower power density of 5 mW/cm^2, while this power might be improved to some degree by reducing the ohmic resistance the power would likely not increase dramatically due to the appearance of mass transfer limitations. For the methanol fuel, the power is significantly lower than both at 1.8 mW/cm^2, reaching the maximum power at a current density of 6 mA/cm^2. The IV curve suggest the primary limitation was ohmic in nature, however, drawing comparisons between the methanol and hydrazine curves, the results suggest that the cross-over inhibiting effect of increasing the current draw discussed in section 3.5, leads to this misinterpretation, while the curve is in fact limited by mass-transfer.

5.3 Electrochemical Impedance Spectroscopy

In order to determine the membrane conductance, an Electrochemical Impedance Spectroscopy (EIS) setup is used. For such a measurement the typical approach is to use electrodes in direct contact with the membrane [61]. This method is not possible for these devices, as the membrane is integrated into the silicon support frame, making it difficult to achieve adequate physical contact without breaking the

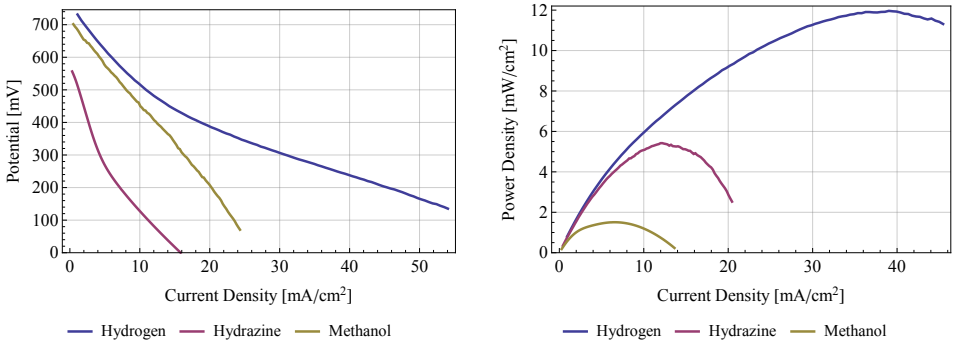

(a) (b)

Figure 5.6: a) IV-curves and b) power curves for a device with 20 µm holes and lattice spacing 50 µm. The tests were conducted with 3M methanol, 1M Hydrazine and hydrogen at a constant flow of 50% hydrogen in nitrogen at 20 mL/min .

device. In addition to this, the resistance for the devices must be measured through the device, and not along the plane. Due to these considerations, a special setup was created that instead relies on liquid lead contacts to determine the membrane resistance through the entire device stack. The setup can be seen in figure 5.7a, with figure 5.7b illustrating a schematic side view. The setup consists of a specially constructed polycarbonate fixture with two liquid reservoirs in which platinum grid electrodes are mounted in a 4-point-probe configuration. The setup is build to put the electrodes as close to the chips surface as was possible to prevent an excessively long conductance path between the sensing electrodes and the device.

To determine the membrane resistance from the impedance spectra, a simple equivalent circuit model is used. This model is based on a Randles circuit [62], which consists of a parallel connection of a capacitor and a resistor. The model is shown in figure 5.8. The device separates the two electrolyte baths, and acts as a capacitor, which is shorted through the ionic membrane. Current is drawn across the outer platinum grid electrodes and the potential is measured using the inner electrodes. This eliminates the potential losses associated with current flow through the measuring electrodes as well as the ohmic losses of the liquid labeled $R_{el1} \wedge R_{el4}$. The measurement do contain the ohmic resistance between the electrodes and devices $R_{el2} \wedge R_{el3}$, which add a series resistance of which has been measured to be $R_0 = R_{d2} + R_{d3} = 6.9\,\Omega$. The impedance of the Randles circuit is thus

$$Z_R = R_0 + \frac{1}{\frac{1}{R_{td}+Z_w} + \frac{1}{Z_C}} \tag{5.1}$$

where the impedance of the Warburg element and the capacitor is given by

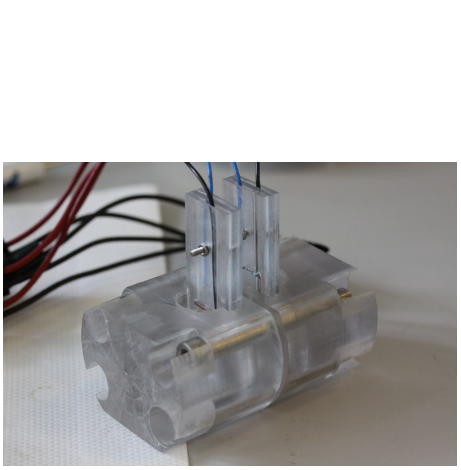

(a) Device setup used to determine the membrane resistances.

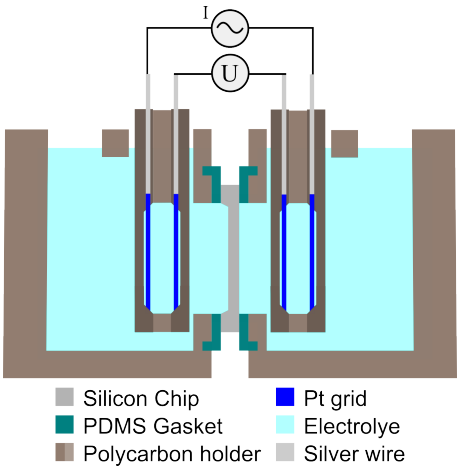

(b) Illustration of the measurement setup used to collect impedance spectra for the devices.

Figure 5.7: Experimental setup used to collect electrochemical impedance spectra, and schematic illustration of the internal structure.

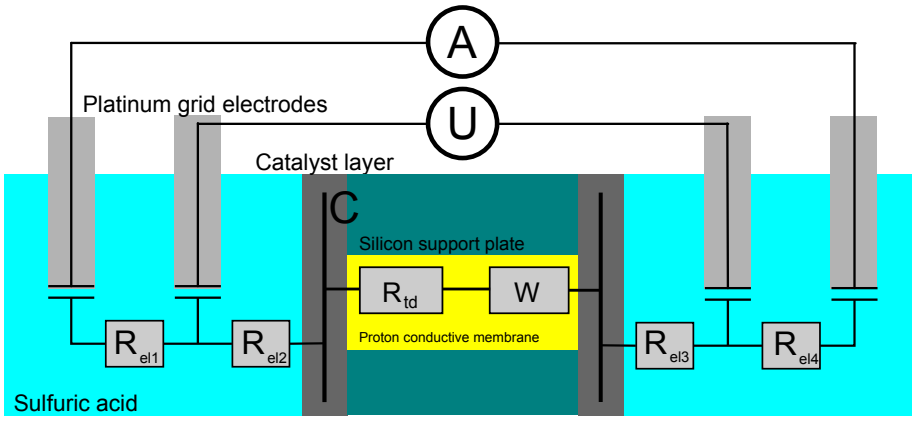

Figure 5.8: Schematic illustration of the equivalent circuit model superimposed on the electrolyte cell interfaces.

$$Z_w = \sqrt{2}\frac{A_w}{\sqrt{i\,\omega}} \qquad Z_C = \frac{1}{i\,\omega\,C}. \tag{5.2}$$

The straight forward application of the Randles circuit is, however, not sufficient to model the measured spectra, and is therefore modified. The Randles circuit is based on the assumption of a perfect capacitor as well as semi-infinite linear diffusion at the sensing electrodes. These assumptions are not applicable for the devices investigated, and the circuit is therefore modified to take non-ideal effects into account. Two changes are made. The first change is the substitution of the Warburg element for a constant phase element [63], Z_{Qw}, with amplitude A_w and phase angle parameter, n_w, close to the value of $1/2$ that would correspond to an ideal Warburg element. The impedance of the constant phase element is then given by

$$Z_{Qw} = \sqrt{2}\frac{A_w}{(i\,\omega)^{n_w}} \tag{5.3}$$

The second change is the substitution of the capacitor also for a constant phase element. The Randles circuit assumes an ideal capacitor which is likely not the case in here since the ideal capacitor assumes a uniform medium and planar electrodes while the device has porous electrodes and a non uniform medium [64]. Therefore the capacitive element is replaced with a constant phase element, Z_{Qc}, with prefactor $1/Q_c$, and a phase angle parameter, n, close to the value of 1, which would correspond to an ideal capacitor. The impedance of this element is given by

$$Z_{Qc} = \frac{1}{Q_c}\frac{1}{(i\,\omega)^{n}} \tag{5.4}$$

Finally the impedance of the modified Randles circuit, Z_M, becomes

$$Z_M = R_0 + \frac{1}{\frac{1}{R_{td}+Z_{Qw}} + \frac{1}{Z_{Qc}}} \tag{5.5}$$

During the fitting of impedance data to the modified Randles circuit the fitted phase angles for these two constant phase elements gave results close to the ideal values. For the Warburg and capacitive elements the typical values are $n_w \approx 0.32$ and $n \approx 0.9$, respectively. Since the data is collected in a logarithmic frequency space,

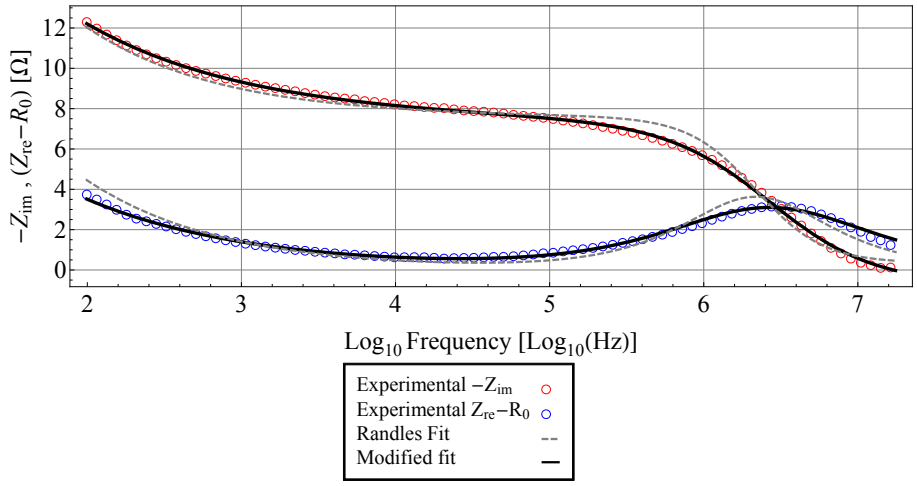

(a) Bode plot of the real and imaginary component of the impedance as a function of logarithmic frequency.

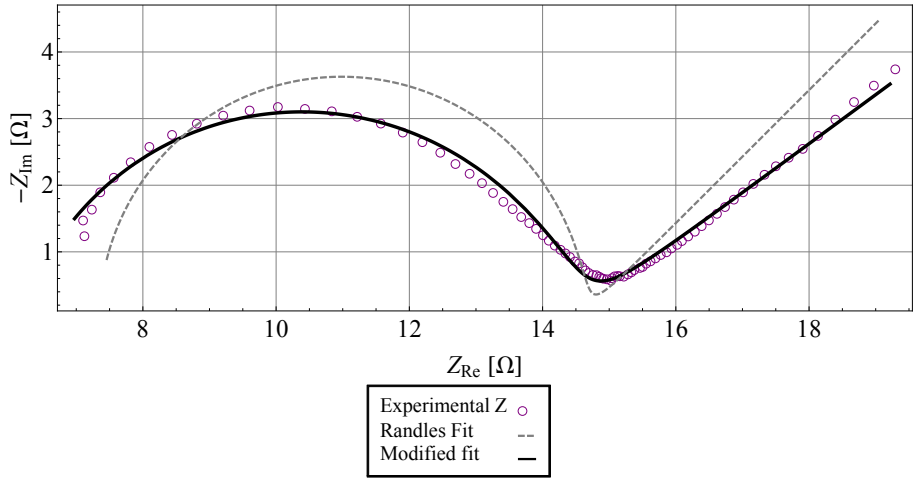

(b) Nyquist plot showing the real and imaginary components plotted against each other.

Figure 5.9: Electrochemical impedance spectra from a device with 20 µm holes and a lattice spacing of 50 µm.

$F = \log_{10}(\omega/2\pi)$, during actual fitting the models are re-expressed as

$$\begin{aligned} F_0 &= \log_{10}\left(2\pi Q_c \sqrt[n]{R_{td}}\right) \\ Z_M(\Omega) &= R_0 + R_{td}\frac{1}{\left(1 + a\left(i\,10^F\right)^{-n_w}\right)^{-1} + i\,10^{n(F-F_0)}} \end{aligned} \tag{5.6}$$

The resulting impedance spectrum of a device can be seen in figure 5.9. Subfigure 5.9a shows the real and imaginary components each plotted as a function of frequency, where it can be seen that both have a rising trend towards lower frequen-

cies and at a point in the high frequency regime, the real part undergoes a step like transition while the imaginary component peaks. Sub-figure 5.9b shows the real and imaginary components plotted against each other. This obscures the frequency component of the measurement but very clearly separates the two distinct regions observed in the data. At the high frequency transition/peak point a suppressed semi-circle is observed, and the low frequency trends in both real and imaginary components results in a constant angle tail in the curve. Due to the large frequency separation the two regions are very sharply separated in the Nyquist plot. The high frequency region corresponds to a perturbation occurring rapidly enough that influence of the Warburg element is small, which means that the field is oscillating so rapidly that diffusion effects in the membrane do not considerably contribute to the impedance In this region, the interplay between the charge storage capacity of the capacitor between the electrodes and the ohmic resistance to current flow creates an RC oscillator. In the low frequency region, the perturbing field is acting slowly enough that the ohmic losses assosiated with the current are constant, which leads to the main impedance contributing effect being the diffusion effects of the membrane modeled by the Warburg element.

The modified Randles model fits the data well as seen in figure 5.9, with the average standard error on the estimated membrane resistance R_{td} being $\sim 0.02\Omega$. The unmodified Randles circuit fit is also shown and clearly shows problems in describing the low frequency curve angle and circle suppression. In the modified Randles circuit, a systematic deviation is apparent in the low frequency side, or equivalently higher resistance side of the depressed semicircle. Here the model is defined to be symmetric about the central frequency, however, a linear constant angle slope is observed in the Nyquist plot in figure 5.9b. An equivalent capacitance can be found for the constant phase element through $C_{eq} = \left(R_{td}\, 2\,\pi\, 10^{F_0}\right)^{-1}$ [64]. For this device the capacitance is found to be $C_{eq} = 43.8\,\mathrm{nF}$, which is close to the expected range of the geometric capacitance for two $0.44\,\mathrm{cm}^2$ electrodes separated by $100\,\mu\mathrm{m}$ silicon assuming a relative permittivity of $\epsilon_r = 11.6$ which is $C_g \approx 45\,\mathrm{nF}$. The difference could be ascribed to the lowered relative permittivity of the plate due to the Nafion filled pores. The resistance found through this measurement is not strictly equal to the resistance through the membrane, as conductance through the porous ionomer containing catalyst layers also contribute. It is, however, assumed that the primary contribution arises from the membrane, due to the porous volume of the catalyst layers filling with electrolyte and due to the membrane being $100\,\mu\mathrm{m}$ thick vs. the $\sim 10\,\mu\mathrm{m}$ thick catalyst layers.

The relationship between open circuit potential and through device resistance

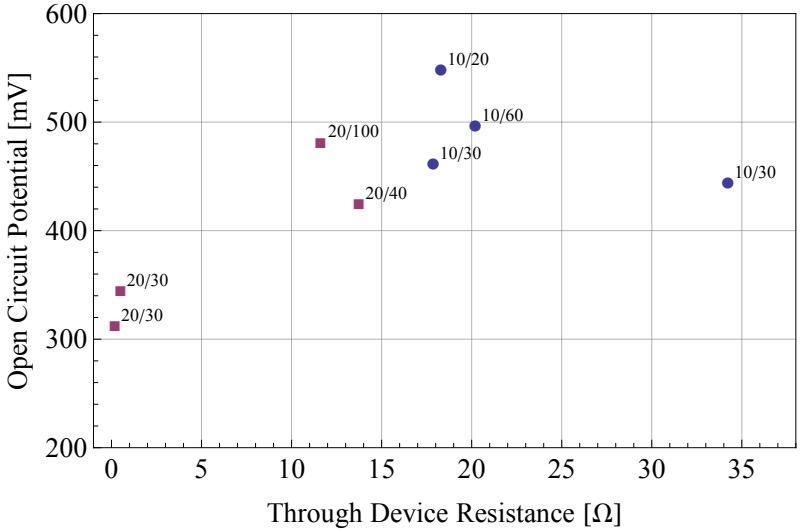

Figure 5.10: Open circuit potential shown against the through device resistance (R_{td}). All devices are shown to have OCV in the range of 300-550 mV. A tendency of higher OCV correlating to higher resistance through the device is observed.

R_{td} for different types of devices is shown in Figure 5.10. A tendency is seen towards higher open circuit potentials for devices with larger through device resistance, indicating that the lowered mobility through the membrane is indeed impeding the cross-over flow of methanol and raising the cathode potential.

The relation between effective internal resistance and through device resistance of a collection of devices with varying geometries is shown in Figure 5.11. A roughly linear relation is observed but with very large variations. For all devices a effective internal resistance larger than the through device resistance is observed $R_{int} > R_{td}$. Excluding the 10/60 outlier device, the mean linear ratio between the two is found to be $R_{\mathrm{td}}/R_{\mathrm{int}} = 41.34\%$. The linear relation, however, is highly indicative of a relation between the two, suggesting that the experimental conditions under which the ionic resistance is measured lead to an underestimate of the resistance. This behavior, however, can be explained through the hydraulic back-pressure reduction in conductivity covered in section 3.2. The conductivity loss was stated in equation 3.35, the conclusion was that under hydraulic back-flow conditions the maximum attainable conductivity was only 19 % of the maximum conductivity without back-flow. The two maxima were, however, also seen at different channel dimensions, which means that this ratio is not immediately applicable. Assuming that the channel dimensionality is constant independent of the hydraulic flow conditions, the conductivity change at $R/\lambda_d = 10.7$ is $(\sigma - \sigma_h)/\sigma = 44\,\%$. The ratio, however, varies depending on the relative channel size as illustrated in figure 5.12. The line assuming $R_{\mathrm{td}} = 44\,\% R_{\mathrm{int}}$ is shown in figure 5.11, and seems to describe the

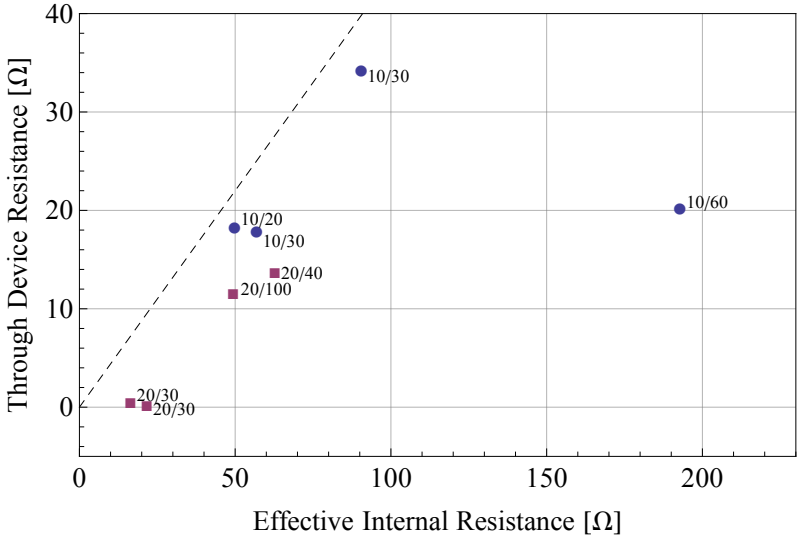

Figure 5.11: Correlation between effective internal resistances (R_{int}) of the devices and the measured through device resistance (R_{td}). Apart from the 10/60 device outlier, a linear trend is observed. The dashed line indicates the point were $R_{td} = 0.44\,R_{int}$, which is related to the expected resistance change due to hydraulic conditions derived in secion 3.2.

tendency of a subset of the measurements, however, with a constant offset in the internal resistance of about 20 Ω. The uncertainty in the exact membrane deposition geometry, however, makes it difficult to distinguish between the internal resistance contribution from the membrane and from other effects. For the outlier with very high internal resistance it is suspected that the membrane has deposited such that it forms a thick layer between the catalyst layer and collector electrode thus greatly increasing the electrical contact resistance.

Concluding on the investigation through electrochemical impedance spectroscopy, it was shown that the ionic conductance can be found through 4 point probe measurements using an interesting liquid lead probe setup. It is, however, found that ionic conductance which is found, varies from that found in the devices under operation due to the changed flow conditions, which makes it infeasible to extract the exact contribution to the cells internal resistance originating in from the ionic membrane. The method is still capable of working as a benchmark for the membranes in relation to each other.

5.4 Summary

The conclusion based on the performance investigation of these devices is that the achievable peak power density is limited and was at maximum 4.5 mW/cm^2 which

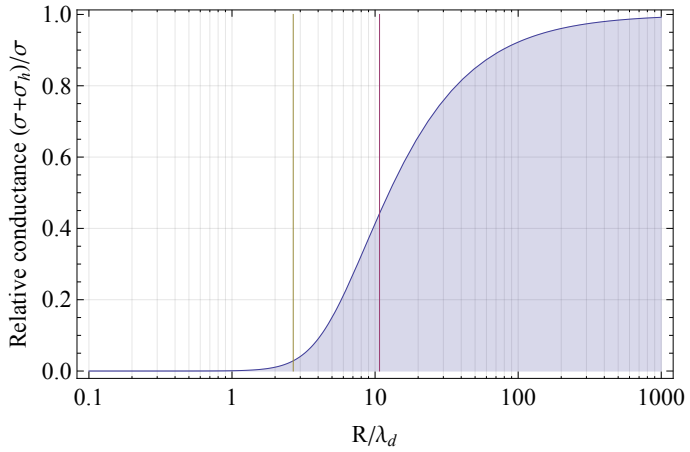

Figure 5.12: Calculated relative conductivity vs dimensionality in the cylindrical flow channel model. The ratio of conductance is taken between a situation with no hydraulic flow σ, and when including a hydraulic back flow $\sigma + \sigma_h$. A yellow line marks the dimensionality of maximum conductivity when no back-flow is present, and a red line marks the optimum when the back-flow is included.

would require an active area of 55 mm^2 in order to reach the minimum peak power specification set for for the usage in hearing aids. The current devices have active areas of just 29 mm^2 which is primarily limited by the plate support frames and the 1 mm outer rim of the device. The devices are, however, fairly large when judged in context of hearing aid usage, and improving power density through optimization of the cell components would be more desirable than needing to increase cell size. That being said, future designs could explore in more detail how large the active area can be made without compromising mechanical stability and likely increase the ratio of effective area to device size considerably.

It was found that low perforation ratios were effective at increasing the OCV by reducing the cross-over effect, the effect of this increase in OCV, however, had little impact on the peak power density. This fits well within the framework of the model developed in section 3.5. The peak power density was found to be very correlated to the effective resistance of the cell, and less so to the open circuit potential. Furthermore, the internal resistance compared to the ionic conductance found through EIS measurements showed a linear relationship confirming that ionic conductance is a large component of the effective internal resistance.

Moving forward from these conclusions, it is found that the peak power density can be improved by increasing the perforation ratio, as well as addressing the mass transfer limitation by improving diffusion access of the fuel to the catalyst. One method of achieving much higher effective perforation rates is to consider porous silicon devices, which can have a large degree of open volume and this approach will

be detailed in the next chapter. Another method of increasing the ionic conductivity is to reduce the plate thickness, which will also address in the chapter 7, which also addressed the limited mass transport though a novel integrated catalyst structure which allows much easier access between fuel and catalyst.

6

Porous Silicon Based Methanol Fuel Cell

This chapter describes the usage of electrochemical etching to form porous silicon based fuel cells. Two device types will be discussed and are shown schematically in figure 6.1. Porous silicon has previously been used as the basis for micro fuel cell systems, notably by Pichonat et al. [38] and Moghaddam et al. [39]. Both these projects are based on porous silicon formed through anodic etching, which is a serial process which requires specialized setups to perform due to the driving electrical field. In contrast this work deals with the process of Metal Assisted Chemical Etching (MACE), which is a simpler auto-catalytic process which can be scaled to bath based batch processing. The following will describe briefly the process followed by results from methanol operated cells working with integrated Nafion and hydrogen operated cells utilizing a liquid electrolyte.

6.1 Metal Assisted Chemical Etching

In order to develop highly porous silicon membrane plates, a technique known as Metal Assisted Chemical Etching (MACE) was employed. It consists of using a metal layer to act as a catalyst for a etching process, such that a seed layer of metal particles will drill pores into the solid silicon substrate, making it porous.

The MACE technique was first published by Li and Bohn in 2000 [65]. The process is a simple and inexpensive method which can be scaled to batch processing

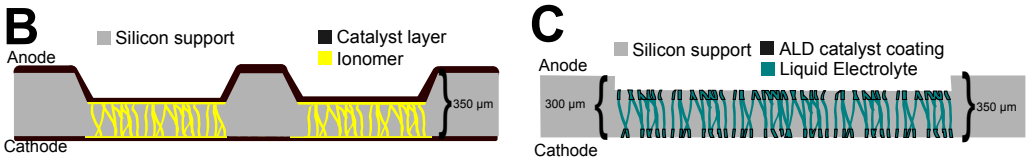

Figure 6.1: Cross-sectional illustration of the two porous silicon based designs discussed during this chapter.

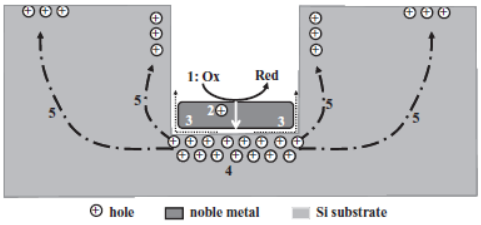

(a) Scheme of processes involved in metal assisted chemical etching. The electron holes injected into the silicon migrate to the sides and surface of the substrate which leads to a small degree of etching at these locations.

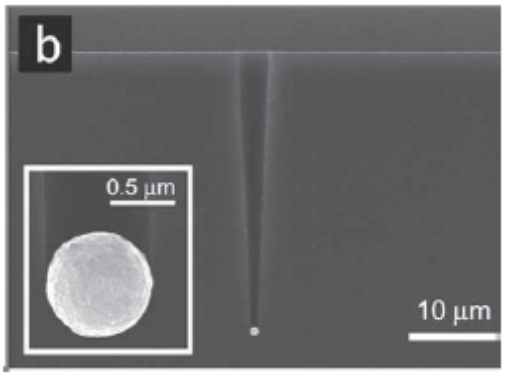

(b) Cross sectional SEM image of a single gold catalyst particle after MACE etching. The particle can be seen to etch highly directional, with hole diffusion leading to a widening of the path as the particle progresses.

Figure 6.2: Schematic illustration and SEM image of the metal assisted chemical etch process.

as it is carried out in a liquid baths. The principle relies on using catalytic particles to inject holes into the silicon substrate. These holes react with an oxidizing agent in the liquid bath creating silicon dioxide which is then etched away by HF. While ratios vary the most common etchant composition is a mixture of $HF : H_2O_2 : CH_3CH_2OH$. The exact chemical reactions taking place are debated and difficult to define exactly, a proposed simple overall reaction diagram is:

$$\mathrm{Si}^{(sol)} + \frac{3}{2}\mathrm{H_2O_2}^{(liq)} + 6\mathrm{HF}^{(liq)} \quad \Rightarrow \quad 3\,\mathrm{H_2O}^{(liq)} + \mathrm{H_2SiF_6}^{(gas)} + \frac{1}{2}\mathrm{H_2}^{(gas)}$$

The processes occurs through several steps that involve charge transfer between liquid, catalyst particle and silicon substrate. The reduction of the oxidant is preferentially occurring at the surface of the catalytic particle which inject holes that diffuse and electromigrate through the silicon as shown in figure 6.2a. This leads to etching occurring both at the interface of the catalytic particle but also continuing at surfaces far away. For a single particle this leads to a widening of the path as the particle continues, as shown in 6.2b, while for full surface etches with a large particle density, the resulting pattern becomes highly disordered.

The etch result is very dependent on catalyst particle type and on the thickness. Figure 6.3 show work by Bjarke Dalslet [66]. It can be seen that platinum is highly reactive, and in terms difficult to use for reproducible results. Both silver and gold show reasonable predictable behavior with gold leading to slightly larger pore sizes and faster etches.

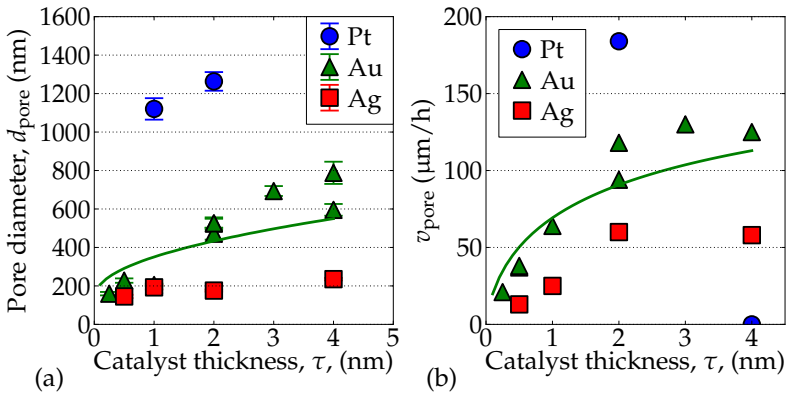

Figure 6.3: a) Mean pore diameter and b) pore etch velocity as a function of catalyst thickness and material. All samples were etched for 1 hour except for the 1 nm pt sample which was etched for just 5 min.

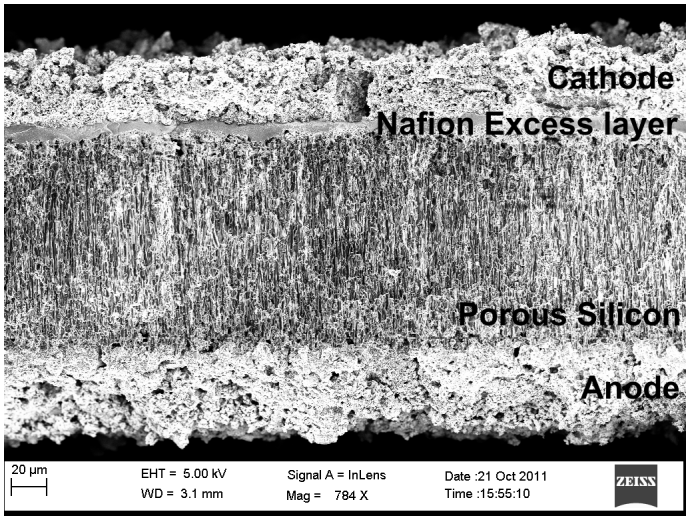

Figure 6.4: SEM cross-section of a finished device. A thin 10 µm Nafion layer can be seen at underneath the cathode catalyst layer at the top of the device, while no Nafion layer is observed on the anode side at the bottom of the device.

6.2 Devices Based on Integration of Nafion into Porous Silicon

Devices have been fabricated by following the fabrication process described in section 4.2.5, but replacing the perforation step with a MACE etch. A cross sectional SEM image of one such devices is shown in figure 6.4. As can be seen, the Nafion integration does not lead to a desirable filled internal volume, but instead it is deposited primarily at the surfaces of the porous silicon device. This can be explained through the very small internal volumes which leads to both act as nucleation sites for dissolved gas and lowers the gas permeability through the structure. Working fuel cell devices have, however, been fabricated through a drop-by-drop integration

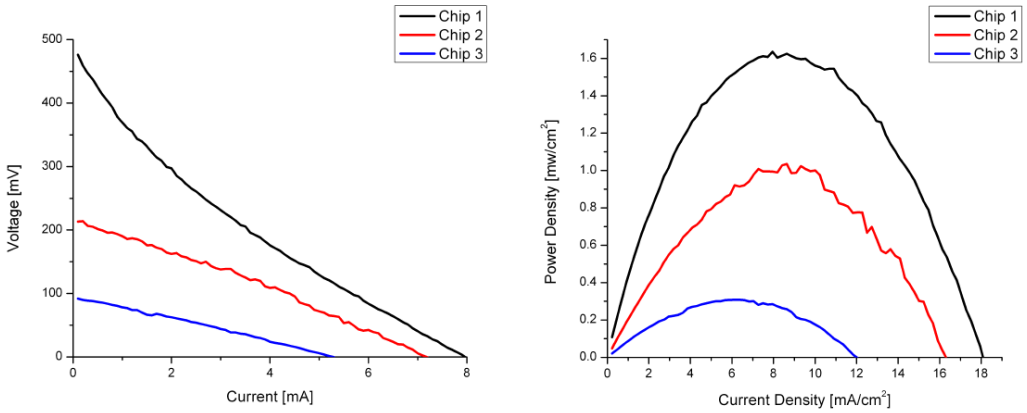

(a) IV-Curves for the porous silicon based fuel cells. Two devices are seen to have very low OCV, presumably due to direct liquid transport through an unfilled volume of the device.

(b) Power performance of the porous silicon based fuel cell.

Figure 6.5: Performance characterization of three porous silicon devices, where the membrane has been integrated through drop-by-drop integration. The effective internal resistance of the devices are respectively 48 Ω, 30 Ω, 18 Ω. From [67]

of the Nafion solution. As a single droplet is placed on the surface of the porous silicon, the porous volume will suck in the liquid, however gas at the droplet surface will still be capable of diffusing out through the surface until many droplets have been deposited. Using this method of integration Louise Borregaard [67], managed to fabricate working cells, for which the resulting performances are shown in figure 6.5. The large variation is attributed to the unreliability in the ionomer filling process as described. For the best working cell the open circuit potential is approximately 500 mV, which suggests cross-over losses are less significant, for this device an effective internal resistance of 18 Ω is observed, and a peak power density of 1.6 mW/cm^2 which is considerably less than what has been achieved with the perforated plate designs covered in chapter 5.

6.3 Liquid Electrolyte Fully Monolithic Porous Silicon Based Device

Porous silicon structures have a very large capillary force due to the very small pores, and rapidly absorb any liquid it is exposed to. A liquid electrolyte can therefore easily be integrated, but for liquid fuel applications this would likely lead to rapid electrolyte degradation as it diffuses into the fuel. Liquid electrolyte porous silicon based devices have therefore been tested as hydrogen fuel cells.

Depth [µm]	O [%]	Si[%]	Pt[%]
0	45	42.2	12.8
10	35.8	63.7	0.5
30	35.8	81.6	0

Table 6.1: Atomic percentages of platinum as a function of depth from the surface after ALD deposition of 150 cycles of platinum on a 100 µm porous silicon membrane. Data collected through EDX by Anne-Charlotte Johansson.

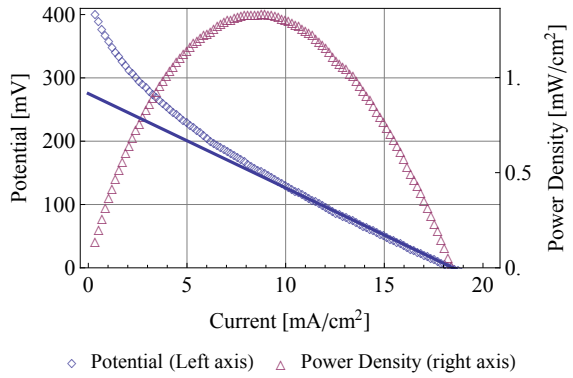

Figure 6.6: IV-characterization of a liquid electrolyte fully monolithic porous silicon based fuel cell. The measurement was conducted with a constant flow of 10 sccm N_2 and 10 sccm H_2. The low limiting current indicates a large ohmic loss. The solid line shows a fit to the IV curve from peak power and forward and corresponds to a 62 Ωohmic loss.

The catalyst layer for these devices was created through Atomic Layer Deposition (ALD) of Pt on the cathode and PtRu on the anode. The process is described in more detail in chapter 7.4. The deposition results in a catalyst layer that is confined to the upper micro meters of the surface. Table 6.1 shows atomic ratios after deposition of 150 cycles, illustrating that the majority of the catalyst is deposited below 10 µm, with no deposition occurring below 30 µm. This ensures that the ALD coated layer does not create a electrical shortage through the device for the 100 µm thick plates.

The characterized devices show a large degree of variation of open circuit potential and peak power density as a function of time as shown in figure6.7. Both open circuit potential and peak power densities increase over a period of approximately half an hour. This continual improvement in performance is ascribed to the excess electrolyte at the interface slowly evaporating exposing a larger degree of catalyst. The IV performance is illustrated in figure 6.6, which shows a peak power density of 1.34 mW/cm^2. This is lower than the achieved peak power density achieved with the spray coated porous silicon device, but cannot be directly compared. The membrane thickness for the liquid electrolyte type C device is 330 µm versus the 100 µm of device type B. Also the catalyst loading is much lower for the ALD based liquid

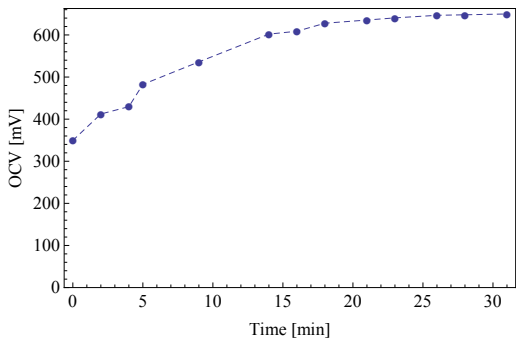

(a) The figure shows the open circuit potential as a function of time.

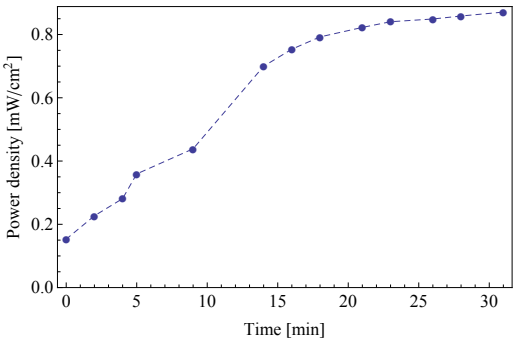

(b) The figure shows the peak power density as a function of time.

Figure 6.7: The figures illustrate the time dependence of a electrolyte loaded 350 µm thick porous silicon based hydrogen fuel cell. The electrolyte used for these measurements is 3 M sulfuric acid. A clear trend of increasing performance in time is observed, which is attributed to the excess electrolyte layer evaporating and exposing a larger surface area to both hydrogen and oxygen.

eletrolyte device. Both these elements should greatly reduce the performance of the type C device, however the use of high concentration hydrogen fuel vs. low concentration methanol should greatly improve performance. The take away from the performance should simply be the conclusion that this device verifies the possibility of an ALD based integrated catalyst, with a moderate performance compared to spray coated catalysts.

While these devices are infeasible for usage in hearing aid fuel cells, they provide a proof of concept for ALD based catalyst cells, and highlight the potential for alternative approaches to fully monolithic, clean-room technology based micro fuel cell.

6.3.1 Discussion

This cell type system is interesting but not very applicable to neither small scale or large scale fuel cell systems as is. The need for a liquid electrolyte makes operation with methanol infeasible, unless the system is extended to allow operation as a vapor-feed cell. For larger scale systems which operate at higher flow rates, the stability of the liquid electrolyte is questionable. It is likely that higher pressures across the membrane would simply flush out the electrolyte degrading operational performance rapidly over short periods of time. None the less the system is novel in nature and might have other uses.

The highly integrated and simple nature of the device could make it interesting as a potential electrochemical sensor. Water purity is often characterized through

the conductivity, which this sensor could easily measure using very small volumes, which are trivially loaded as capillary forces draw in the small volume of liquid needed. For such a device, the total device volume is of little concern as long as currents are within range of what is measurable with the method employed to collect readings, and therefore even smaller system volumes could work. For gas based sensing, a very small array of porous silicon cells could be loaded with a range of different electrolyte solutions and be individually contacted to provide a small scale gas sensor, with signal differentiation based on chemical interactions with the individual solutions. In any of these cases the fabrication is very fast and inexpensive as it can be comprised of patterning through masked metal deposition and wet-bench etching processes.

6.4 Summary

The conclusions based on the work towards porous silicon based fuel cells is that reproducibility of the membrane integration is very difficult owing the the small pore dimensionality. While the capillary force aids in rapid integration of the ionomer liquid initially, during the drying the small size of the capillaries trap gas and lead to a low level of volume filling. Therefore while porous silicon presents a method of increasing perforation ratios compared to the perforated plate design, the performances in terms of peak power density have not been comparable, with the best performing device showing a $1.3\,\mathrm{mW/cm^2}$ at 50 % perforation while the perforated showed performance of $4.5\,\mathrm{mW/cm^2}$ at 40 % perforation operating with 3 molar methanol fuel.

The porous silicon based fabrication process illustrates the potential for a monolithic fuel cell operating with a liquid electrolyte utilizing atomic layer deposition as a method of integrating catalyst layers directly into the porous structure. This liquid electrolyte cell showed modest performance as a hydrogen fuel cell, but also showed long term instabilities in both peak power and open circuit potential due to the liquid interface dynamics. This type of liquid electrolye porous silicon based electrolytic cell might prove promising for small sized integrated chemical sensors where power is of less importance than detection sensitivity and ease of integration.

7 Integrated Carbon Nanotube Supported Catalyst Layers

This chapter describes an improvement on the monolithic fuel cell design detailed in chapter 4. The design, shown in figure 7.1, is improved by utilizing an integrated carbon nanotubes (CNT) catalyst support in place of the spray coated catalysts with the intent of improving the 3 phase boundary, increasing the connectivity of the catalyst and reducing the electrical resistance between catalyst and collector electrode. A schematic of the design is shown in figure 7.1.

7.1 Introduction to Carbon Nanotubes

CNTs are a nanoscale structure composed of layers of carbon atoms arranged in a hexagonal graphene lattice rolled up into tubes. They have received large amounts of attention in recent years as they exhibit many exotic phenomena, particularly single walled CNTs which display relativistic electron transport, large mechanical strengths and electrical properties that range between semiconducting to conducting depending on the structure and orientation of the carbon layers making up the tube. An illustration of zig-zag type and armchair type single wall CNTs are shown in figure 7.2, both of these types of CNTs show metallic properties. The figure

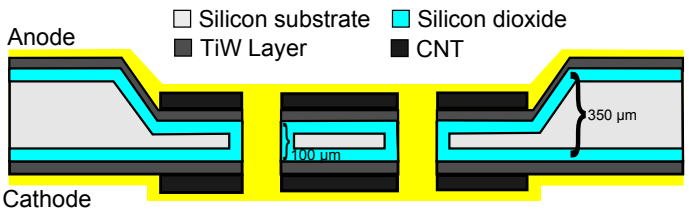

Figure 7.1: Cross-sectional illustration of a fuel cell with integrated CNT supported catalyst layers.

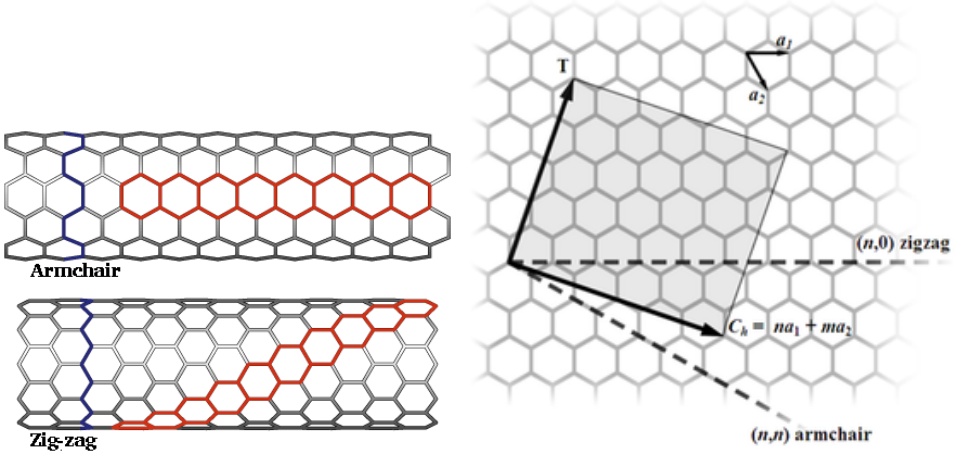

Figure 7.2: Illustrations of the atomic structure of single walled carbon nanotubes. Armchair and zig-zag type carbon nanotubes illustrating the different folding directions. The tubes shown to the left are 5.42 Å in diameter and the illustrated segments are 24.6 Å long.

also shows an illustration of the concept of a CNT being simply a folded sheet of graphene, for which the lattice vector defining the folding direction then determines the electronic properties, which can vary greatly between different folding vectors. When used in integrated devices, single wall CNTs are both difficult to manufacture, and selection of only specific folding vectors is not currently possible. In cases such as electrodes where high conductivity is sought, Multi-Walled CNTs (MWCNT) are preferred, as the multiple layers ensure conductivity while this also greatly simplifies the fabrication process.

For fuel cell usage, CNTs are of interest primarily as catalyst support structures, which can be manufactured and structured on the micro and nanoscale. Conventionally catalyst supports are formed in liquid solutions and integrated into the MEA structure through spray coating and hot pressing. This type of integration does not allow for direct structuring of the micro and nanoscale structure of the layer, which can only be manipulated indirectly though changes in pressing pressure and solution components. Integration of CNT catalyst supports into devices allows such direct structuring. Such catalyst support materials have, in work by Li. et al. [68], shown to increase performance in methanol fuel cells. In this work, CTNs are used as replacements for conventional carbon support materials in liquid solution which is spray coated to form a catalyst layer. In their work platinum on CNTs showed six times the mass activity than of platinum on XC-72 type amorphous carbon. Surprisingly the same work also showed that CNTs were capable of acting as a methanol cathode even without any catalyst coatings, however, at much lower performances. The same bare CNT did not show any activity towards the oxygen reduction reaction. CNTs have also been used as the electrode materials of super-capacitors which

seek to store charge in the capacitive layer that forms in the electrode-electrolyte interface. Here an important element of the electrode is that the structure is open enough to allow the electrolyte to penetrate into the structure, which reduces the mass-transport losses in the cell [69]. This desire is somewhat aligned with the wish of creating a large 3 phase boundary in a fuel cell application. Previous work with CNTs for this purpose, [70], suggest that Plasma Enhanced Chemical Vapor Deposition (PECVD) grown CNTs, are highly aligned and therefore an appropriate electrode material to overcome the perceived disadvantages of high viscosity of ionic liquids used in super-capacitors, and thus suggest that they might also be useful in fuel cells as well.

When utilizing CNTs as support structures for other compounds, a functionalization is needed. Pristine CNTs are chemically inert [71] and techniques are therefore needed to ready the surface structure prior to deposition. Most work dealing with ALD depositions on CNTs utilize either a plasma functionalization or an acid treatment [72, 73, 74]. Both these treatments introduce structural damages into the carbon lattice, in order to allow nucleation during the growth process.

For this work focus was instead put on usage of nitrogen doped carbon nanotubes (NCNT), as the nitrogen doping introduces growth-sites to the structure of the tubes.

7.2 Monolithic Silicon Plate Micro Fuel Cell Device Fabrication

The described device follows the fabrication process of the semi-monolithic silicon based fuel cell described in chapter 4. The process is, however, changed from the metalization step and onwards to accommodate the CNT growth, and naturally without the spray coating of catalyst layer.

In this case, the process followed after step (S3.1) of figure 4.2, is a joined metalization / growth step, which is followed by ALD deposition, and finally the membrane integration is carried out similar as described in section 4.2.4.

7.2.1 Metalization on Carbon Nanotube Based Devices

The metalization of these devices serve both the purpose of defining the collector electrodes, but also include a definition of a Ni catalyst layer used in the growth of CNTs. The current collector is define in TiW rather than Au, due to the need for a diffusion barrier for the catalyst. For the semi conventional designs, the buried

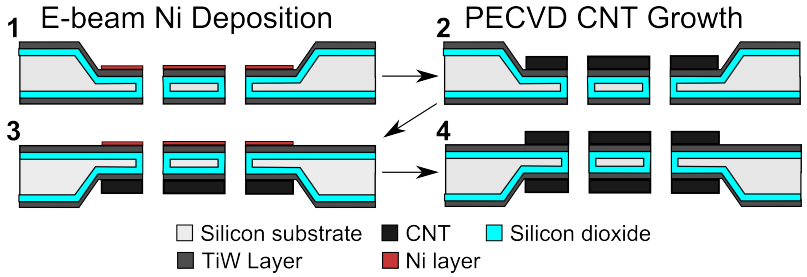

Figure 7.3: The procedure followed during CNT growth, in order to protect the results of the initial growth.

electrodes are defined through 20 nm Ti adhesion layer, along with a 200 nm Au electrode, this ensures less than 1 Ω resistance across the wafer. For the CNT wafers an anti-diffusion layer is needed as a support for the catalytic nickle layer, in order to ensure some conductance of this layer a 200 nm layer of TiW is used, which leads to approximately 80 Ω resistance across the wafer. As shown in table 7.1 TiW has roughly 27 times higher resistivity than Au and 35 times that of Cu. This is quite high and could be improved by utilizing a burred Au layer and making a collector stack consisting of Ti/Au/TiW/N in thicknesses 20/200/100/7 nm. In order to utilize such a structure, it would be needed to ensure that Au does not enter into the growth chamber during the CNT growth. This examination of the potential for contamination has not been investigated.

The catalyst is to be deposited on both sides of the wafer. Depositing on both sides before growth, however, would lead to one layer degrading during the growth-processes targeting the other side. In order to allow growth on both sides of the wafer two growth-process are carried out. The procedure is illustrated in figure 7.3. Initially the catalyst Ni layer is deposited (step 1). The deposited layer is 7 nm thick, and is deposited via a shadow mask such that it is only deposited over the membrane region. The CNTs are then grown through PECVD (step2). The wafer is then turned over, and catalyst is deposited on the other side (step 3), after which a final PECVD growth process is carried out. In order to not damage the result of the first growth, during the second growth, the initial growth is carried out on the recessed side of the wafer. In this way the CNTs will be protected from mechanical damage during the second growth. In addition the second Ni-catalyst layer is deposited only after the initial growth has been carried out. This is to ensure it does not melt and redistribute during the first growth, which would result in suboptimal growth results due to larger seed particles and uneven distribution.

Material	Conductivity [S/m]	Resistance [Ωm]
Titanium	$1.80 \cdot 10^6$	$5.56 \cdot 10^{-7}$
Titanium Tungsten	$1.66 \cdot 10^6$	$6 \cdot 10^{-7}$
Copper	$58 \cdot 10^6$	$0.17 \cdot 10^{-7}$
Gold	$44 \cdot 10^6$	$0.22 \cdot 10^{-7}$

Table 7.1: Table of conductivities for relevant current collector materials.

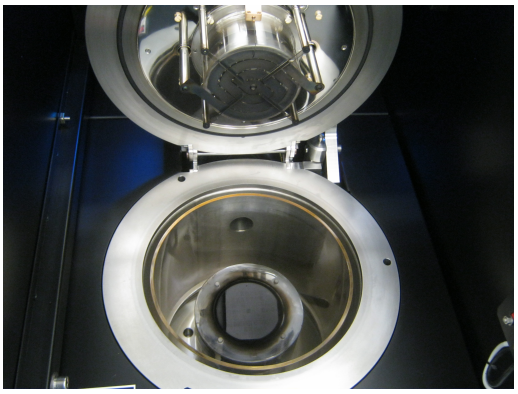

(a) The Aixtron Black Magic PECVD CNT growth system with the top open to allow wafer loading. The top heater spiral is visible in the top, and a wafer is loaded on top of the bottom electrode at the bottom.

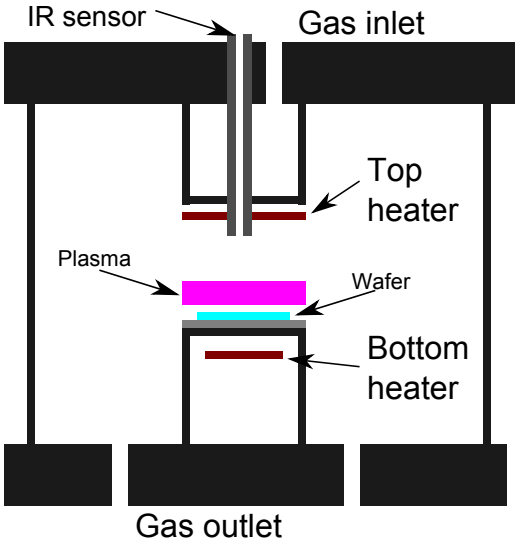

(b) Schematic illustration of the PECVD during growth. Gas is let in from the top, flows down pas the top heater, after which it is ionized and forms a plasma over the wafer.

Figure 7.4: PECVD system used for growth of carbon nanotubes.

7.3 Method of Carbon Nanotubes Growth

The equipment employed to grow carbon nanotubes is a Aixtron Black Magic Plasma Enhanced Chemical Vapor Deposition (PECVD) system shown in figure 7.4a. Chemical vapor deposition growth of CNTs is a process where a carbon containing gas is cracked at high temperatures in order to form atomic carbon from the gas. The used method employs Acetylene, C_2H_2.

The first step of the process is to purge ambient air from the chamber by going to a low pressure. After this the temperature is slowly ramped up to the anneal temperature of 600°C with a constant flow of 160 sccm NH_3. At this point a 80W plasma is initiated and the temperature is held constant. During the annealing step the thin 7 nm nickel sheet will condense into smaller particles which act as growth catalysts for the CNTs. The ammonia plasma acts to reduce the surface, preventing oxidation of the nickel particles. After annealing the temperature is ramped to

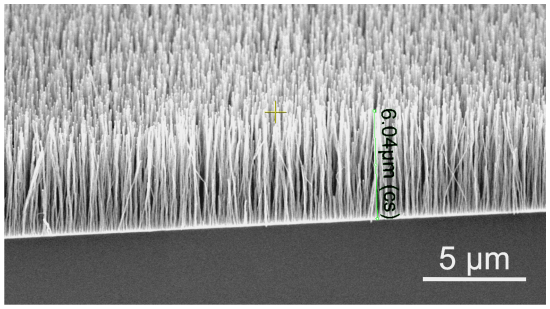

Figure 7.5: Results of a NCNT growth process with a 2 min anneal at 600°C, and 15 min growth at 850°C. The resulting tubes are 6 µm long.

Element	C	N	O	W	Ni	Ti	F
Atomic %	81.6	7.0	5.0	4.1	0.9	0.8	0.5

Table 7.2: Element composition of nitrogen doped multi wall carbon nanotubes found through XPS. The CNTs were grown on a TiW diffusion barrier using Ni catalysts.

$850°C$, and a flow of Acetylene is initiated, while the plasma power is increased to 100 W. The growth plasma is then maintained for a period depending on the desired length of the resulting tubes. The result of a growth run for 15 min can be seen in figure 7.5. The CNTs are seen to be uniformly distributed with a low variation in the achieved height, and very nicely aligned in the vertical direction.

The nitrogen doping of the CNTs is introduced via ammonia, NH_3. The finished CNTs have been examined using X-ray Photoelectron Spectroscopy (XPS), and the atomic composition ratios are shown in table 7.2. Results show that the sample contain trace amounts of both the TiW diffusion barrier and the remains of the Ni catalyst particle. It is believed that the oxygen is due to oxidized metals. The presence of fluorine indicates that there might be small amounts of PTFE, which would mean that not all the carbon detected is bound in the CNTs, the amount is, however, very small. Assuming that the carbon ratio is only due carbon bound in CNTs, the atomic doping ratio of nitrogen is 8.6 %. This is a large doping ratio, however, alternate methods of NCNT formation have shown larger doping ratios, with work on aerosol methods reporting atomic doping ratios of up to 20 % [75].

An important aspect of the growth for use as catalyst support is the amount of exposed surface area. Ideally the surface structure would be such that as much surface area is created while keeping the density low enough to ensure ionic and liquid contact throughout. The nanotube diameter, d, and areal density, n, will be bound by the amount of catalyst deposited in in the initial seed layer. The seed layer has a thickness t, and assuming volume conservation during the annealing phase, the following relation must hold;

$$\frac{4}{3}\pi\left(\frac{d}{2}\right)^3 n \;=\; t. \tag{7.1}$$

This relation fits well with observed results which show that a 7 nm seed layer leads to a $d \approx 100\,\text{nm}$, $n \approx 12\,\mu\text{m}^{-2}$, for which the relation leads to an estimated seed layer thickness of 6.28 nm. From the relation the ratio between the tube surface area, A_{surf}, and the geometric area, A_{geom}, after growth of CNTs with height h, can be found to be given by

$$\frac{A_{\text{surf}}}{A_{\text{geom}}} \;=\; \pi\, d\, h\, n = 6\, h\, \frac{t}{d^2}. \tag{7.2}$$

It is seen that the achieved surface area depends critically on the relation between the achieved diameter and seed layer thickness. This relation will depend on the annealing conditions, as longer anneal times will lead to smaller particles joining together, increasing diameter, while simultaneously decreasing density. The effect of long anneal times is thus to decrease the ratio of area increase. The full relation between these parameters and annealing conditions has not been studied as the stability of the growth system was only achieved recently. Under the achieved stable and reproducible conditions it was observed that a 3 nm seed layer led to $d \approx 40\,\text{nm}$ while a seed layer of 7 nm led to $d \approx 100\,\text{nm}$. These data support an assumption that the catalyst particle diameter under similar annealing conditions depend linearly on the seed layer thickness, $d = c\,t$, with proportionality factor $c = 13.8$. Taking this assumption into equation 7.2, the result is

$$r_A = \frac{A_{\text{surf}}}{A_{\text{geom}}} \;=\; 6\, h\, \frac{1}{t}\frac{1}{c^2} \tag{7.3}$$

$$n \;=\; \frac{6}{\pi}\frac{1}{c^2}\frac{1}{t} \tag{7.4}$$

Leading to the conclusion that decreasing the seed layer thickness increases the surface area which allows incorporation of larger amounts of catalyst particles, however, it also increases the density which increases the resistance towards liquid flow and ionomer integration. The parameters used for devices was 7 nm, with typical growth height of 6 µm, leading to an area increase ratio of $r_{\text{A}} = 27$. This shows the potential of the method as the optimal tradeoff between the two elements could be found via simple variation in seed layer thickness. This study has, however, not

been conducted as noted, due to the need to increase stability of the growth system, which will be detailed in the following section.

7.3.1 Growth Process Temperature Control

Temperature control in the system is very important and has shown to greatly influence the results of processing. The temperature is controlled via a resistive plate heater underneath the substrate as well as a top heater as shown in figure 7.4b. During processing gas is feed through the shower-head at the top and heated, it then enters into the plasma region after which it flows out through the bottom of the chamber. This causes a temperature gradient to exist between the top and bottom of the gas chamber.

Both heaters are controlled via individual PID control systems. The bottom heater is controlled against a temperature measured via an IR reader located in the top of the champers aimed at the wafer surface. The top heater is controlled against a thermocouple attached to the heater plate. The PID controllers sets the power of the heaters,$P(t)$, based on three components related to the proportional, integral and differential of the measured error term, ΔT, which is the difference between the measured T_{meas} temperature and the set-point T_{set}. The components are scaled with the PID parameter settings K_P, K_I, K_D.

$$\Delta T(t) = T_{\text{set}}(t) - T_{\text{meas}}(t) \tag{7.5}$$

$$P(t) = K_P \Delta T(t) + K_I \int_{t_{\text{start}}}^{t} \Delta T(t)\, dt + K_D \frac{\partial}{\partial t} \Delta T(t) \tag{7.6}$$

The effect of adding a PID controller to a system is to change its transfer function in such a way that the output is consistent with the control effort exerted by the PID with the output looped back to the controller. The Laplace transform of the PID controller is given is given by:

$$PID(s) = K_P \frac{Td}{s} \left(s^2 + \frac{1}{T_d} s + \frac{1}{T_i T_d} \right) \tag{7.7}$$

Lacking a full description of the system, its input response,$T(s)$, is modeled as a fast response with response rate r_f, and a following slower decay with rate r_s, which can be used to find the transfer function,$H(s)$, as:

$$T(s) = c\left(\exp\left(-t\, r_f\right) - \exp\left(-t\, r_s\right)\right) \tag{7.8}$$

$$H(s) = \frac{c}{s^2 + s\left(r_s + r_f\right) + r_s r_f} \tag{7.9}$$

Considering the product of these transfer functions $T \times H$, The PID parameters can be chosen such that the latter part cancels out the system response leading to

$$T_d = \frac{1}{r_f + r_s} \approx 1/r_f \tag{7.10}$$

$$T_i = \left(\frac{1}{r_f} + \frac{1}{r_s}\right) \approx 1/r_s \tag{7.11}$$

$$T\,H = c\,\frac{Td}{s} K_P \tag{7.12}$$

With this result, the closed loop control function is given by

$$N = \frac{T\,H}{1 + T\,H} \tag{7.13}$$

$$N = \frac{1}{1 + c\,s/Td} \tag{7.14}$$

The inverse Laplace transform of this is $N(t) = \exp\left(-t\, c/Td\right) K_P Td/c$, which means that at these settings the fastest possible response is achieved, which is bound by the systems own fast response time. The problem now is how to judge the actual PID parameters from the actual system dynamics. An often used method of empirical tuning of these PID parameters is the Ziegler-Nichols (ZN) method, which determines the three parameters based on control settings and two experimentally determined parameters, namely the ultimate gain, K_u, and the ultimate period, T_u. Depending on the mode of operation desired the parameters calculated using the scaling factors are given in table 7.3, which relate to the PID parameters through

$$K_P = a_P K_u \qquad T_I = a_I/T_u \qquad T_D = a_D T_u \tag{7.15}$$

The reason for the multiple control type variants is that the classical PID ZN parameters are optimized for aggressive disturbance rejection which can in instances cause problems with the individual control problem.

For the CNT growth process, the primary concerns are stable temperature during

Control Type	a_P	a_I	a_D
P	$1/2$	0	0
PI	$1/2.2$	$1/1.2$	0
Classic PID	0.6	$1/2$	$1/8$
Some Overshoot	0.33	$1/2$	$1/3$
No overshoot	0.2	$1/2$	$1/3$

Table 7.3: Table of Ziegler-Nichols PID Tuning parameter scaling factors

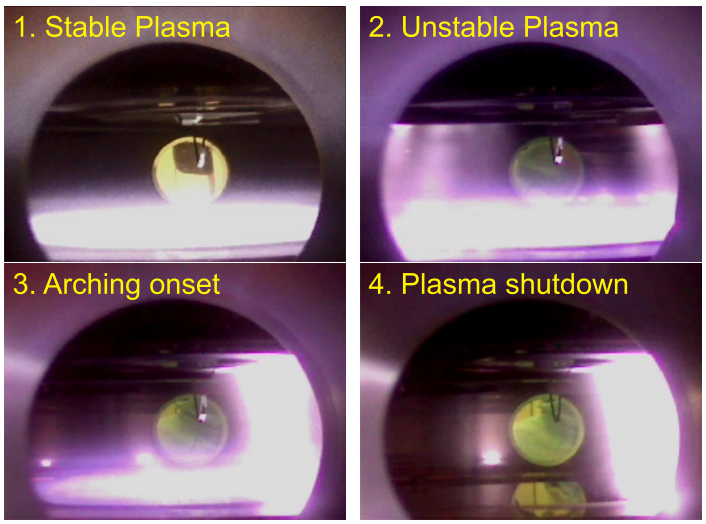

Figure 7.6: Images from the growth chamber during the growth phase of the process. 1) Shows the growth plasma under long term stable conditions. 2-4 show the progression of the plasma from an initially unstable turbulent plasma to initial arch formation and resulting plasma shutdown.

holding periods, and a stable plasma throughout the process, as plasma instabilities can cause arching which damages the device surface. Images of plasma arching cause by turbulent plasma conditions is shown in figure 7.6.

Direct usage of the ZN parameter sets does not work due to the interaction between plasma stability and heater power changes. Rapid changes in the heater power has been seen to cause shape fluctuations in the plasma, which can lead to arching and in cases completely plasma shutdown. Thus the PID control is tuned based on the tradeoff between disturbance rejection and minimization of control power fluctuations.

The heat transfer from the heater to the system may have an averaging effect such that a rapidly varying heater can hold a stable temperature across this boundary. There would, however, be no benefit to such a mode of operation as the control would still not be able to operate faster than the characteristic frequency of this averaging, therefore a slower mode of operation with the heater keeping a stable power level is much preferred.

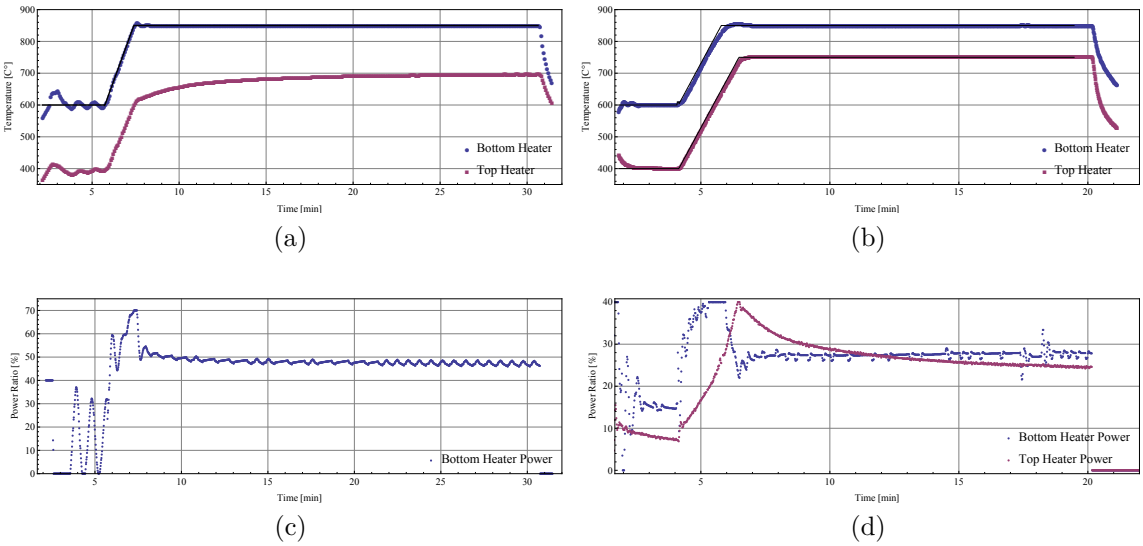

Figure 7.7: Temperature profiles for the PECVD carbon nanotube growth process before and after optimization of the process. Figure a) shows the temperatures using machine auto PID settings, with c) showing the corresponding heater power. Figure b) shows the temperatures using adjusted PID parameters using the ZN-method for a base estimate, with d) showing the corrosponding heater powers for the top and bottom heaters.

The final control parameter determination method was settled upon the relative parameters: $\alpha_{pP} = 0.2$, $\alpha_I = 0.25$, $\alpha_D = 0.1$, with the ultimate gain and time during these experiments estimated to be $K_u = 340, T_u = 0.65$. Keeping the parameters constant and estimating the change in the ultimate gain that might result from heater wear might allow for a much improved performances moving forwards. The result of using these optimized PID settings can be seen in figure 7.7. For both sets of settings shown the variation in temperature during the growth varies less than a degree, however, for the machine auto settings, the power oscillates continually throughout the growth, indicating poor rejection performance, and potentially leading to unstable plasma.

7.4 Atomic Layer Deposition of Catalysts on Carbon Nanotubes

In order to make the NCNT catalytically active, catalyst particles are defined through atomic layer deposition.

Atomic Layer Deposition (ALD) is a chemical vapor deposition technique that uses precursor gasses that are self terminating to deposit single atomic layers of a material. The terminating surface can then be removed through another precursor

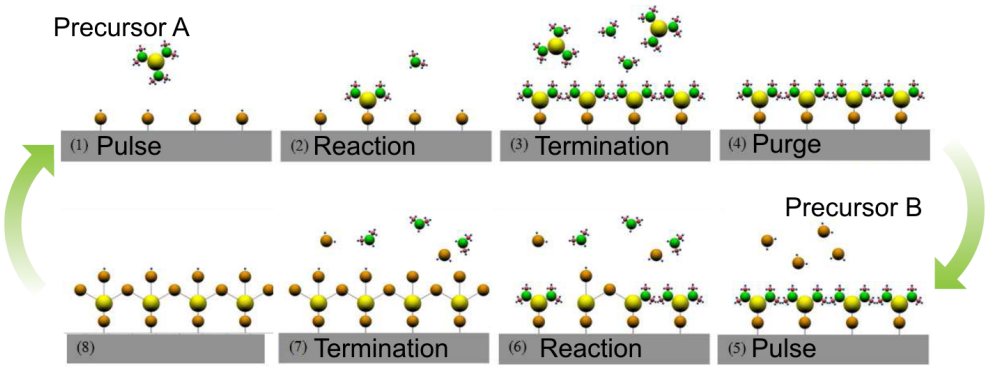

Figure 7.8: The ALD process cycle. 1) The pulse of the precursor A is injected. 2) The precursor reacts with the surface. 3) The process self terminates as the surface sites all become covered. 4) Excess precuros is purged. 5-8) The same process follows for precursor B, which creates a new surface of reaction sites for precursor A, and the cycle continues until the desired number of layers have been deposited. Adapted from [76].

reaction that recreates a surface structure that allows the continued growth. This cycle is illustrated in figure 7.8. First a prepared surface is subjected to a precursor which adsorbs on the surface in such a way that it terminates any potential adsorption sites. On flat uniform substrates this process leads to the deposition of a mono-atomic layer. The surface is then subjected to a second precursor which alters the initial surface to allow for repeated depositions. These cycles are then repeated until the desired thickness is achieved. For the catalyst defining processes considered in this project, the depositing precursors used were $MeCpPtMe_3$ to deposit Pt, and $Ru\,(EtCp)_2$ to deposit Ru, and oxygen was used as the second precursor during both these deposition routines. The ALD deposition process used in this project was developed by Anne-Charlotte Johansson and is the covered in [77], as well as the coauthored article [78]. The deposition processes have been carried out by Anne-Charlotte Johansson and Kenneth Haugshøj. In order to study the particles, after CNT growth and ALD deposition, the CNTS where cleaved from the wafer and turned into a conventional catalyst coating which was spayed on glassy carbon electrodes and investigated in a three electrode setup. This process was carried out by Anne-Charlotte Johansson at The Danish Technological Institute.

Two separate particle types have been studied for incorporation into the fuel cells, co-grown Pt/Ru, and Ru shelled Pt. The co-grown particles were created by first growing, N_{Pt}, cycles of Pt and then growing, N_{Ru}, cycles of Ru, this is repeated until a total cycle number of approximately 150 is reached. As the particles grow the hypothesis is that these layers will partly form a PtRu alloy rather than simply forming discrete layers. For the Ru shell Pt particles, first 150 cycles of Pt is grown, after which an over-layer of N_{Ru} is grown. Here the working hypothesis is that

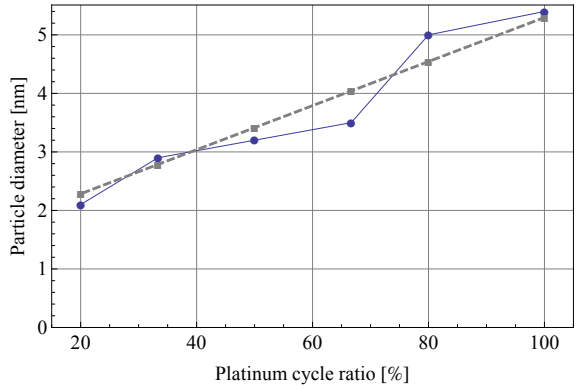

Figure 7.9: Particle diameters found through XRD for growths of different Pt/Ru co-grown catalyst particles ratios of platinum sub-cycle length vs. ruthenium sub-cycle length. The dashed line indicates a best fit of the diameter linear model estimating the diameter growth to 5.3 nm at 150 cycles Pt, and 1.53 nm at 150 cycles Ru. XRD data for pure ruthenium particles was not available. Data from [78].

the final layer will form such that the platinum surface is still accessible, with a high surface concentration of Ru available. In the Ru shelled particles the average particle diameter after growth is 5.4 nm, while in the co-grown particles the average particle size depends on the relative ratio of platinum to ruthenium cycles. Figure 7.9 shows the average particle diameters found through XRD for 6 growths with sub-cycles of Pt/Ru of: 4/16, 4/8, 4/4, 8/4, 16/4,150/0. Assuming that each layer deposits perfectly uniformly with a constant thickness per cycle for each material, then the diameter should be given by $T = a\,N_{Pt} + b\,N_{Ru}$. The result of fitting this linear model is also shown in the figure and the result is an estimated thickness of 5.3 nm at 150 cycles Pt and 1.53 nm at 150 cycles Ru. The curve is seen to be a poor estimation of the exact points, and it is speculated that the number of similar cycles in repetition also plays a part in the final composition leading to a nonlinear relation of the particle diameters. For the three growths with PtRu 8/4, 4/4, 4/8 (33 %, 50 %, 66 %), a perfectly linear relation is seen in the particle diameter showing ratios of 4.1 nm at 150 cycles Pt and 2.3 nm at 150 cycles Ru. It could on the basis of this be speculated that between 8 and 16 cycles of the same material the metal layer will start to form a film, while for fewer cycle repeats the result is a more uniform alloying of the metals. But this speculation rests is based only on linear relation between three points, and is therefore highly speculative. The results of the deposition can be seen in figure 7.10.

The deposition mass is found through measurements on a micro-scale of the total wafer mass prior to and after ALD deposition. Averaging the depositions on 3 separate wafers, the mass gain of 150 cycles Pt on both sides was found to be 9.73mg $\pm$ 0.28 mg. Assuming this loading was uniformly deposited across the

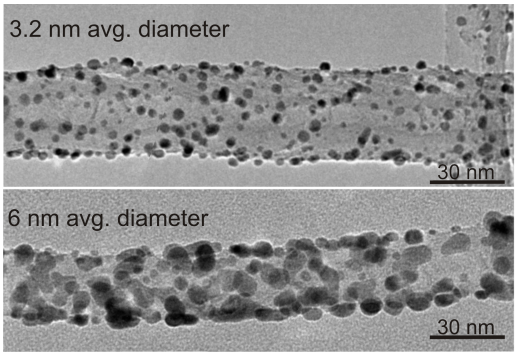

Figure 7.10: TEM image showing two n-doped carbon nanotubes with respectively 100 and 150 cycles of Pt deposited leading to an average particle diameters of 3.2 nm and 6 nm.

geometric area of both sides of the wafer, this would correspond to the very low loading of 62 $\mu g/cm^2$.

The resulting particles deposited on NCNTs have been investigated using chronoamperometry. The curves are shown in figure 7.11 on a logarithmic time-scale which highlights the transition between a early and late decay in the dynamics. The data is well described, however, with the bi-exponential decay model with the second exponential modified to develop in the square of time. This exponential solves the diffusion limited decay function, $\partial_t f(t) = \frac{1}{l_d} f(t)$, where the species is transported across a diffusion barrier of length $l_d \propto \sqrt{t}$. This contribution is therefore expected to be related to the surface concentration of methanol, while the faster linear exponential is assumed to be associated with the rapid surface adsorption which happens initially as the carbon monoxide surface adsorption coverage develops an equilibrium. In addition a constant offset, I_d, is added to account for transient effects in the concentration diffusion layer. Denoting the linear and diffusion limited decay time t_l and the diffusion limited decay time t_d, and expressing the total current, I, as contributions from the linear I_l decay and the diffusion limited decay I_d the expression is

$$I = I_l \exp(-t/t_l) + I_d \exp\left(-\sqrt{t/t_D}\right) + I_d \tag{7.16}$$

The results of fitting this equation to the measured decays can be seen in figure 7.11. In general the model is well fitting with lowest coefficient of determination being $R^2 = 0.998$. The residuals, however, show signs of period variations indicating that the behavior is not fully described by this model and that more detail might be needed to fully explain the system. Fits of the model are shown in figure 7.11. Figure 7.12 shows the decay current prefactors for the linear and diffusion limited

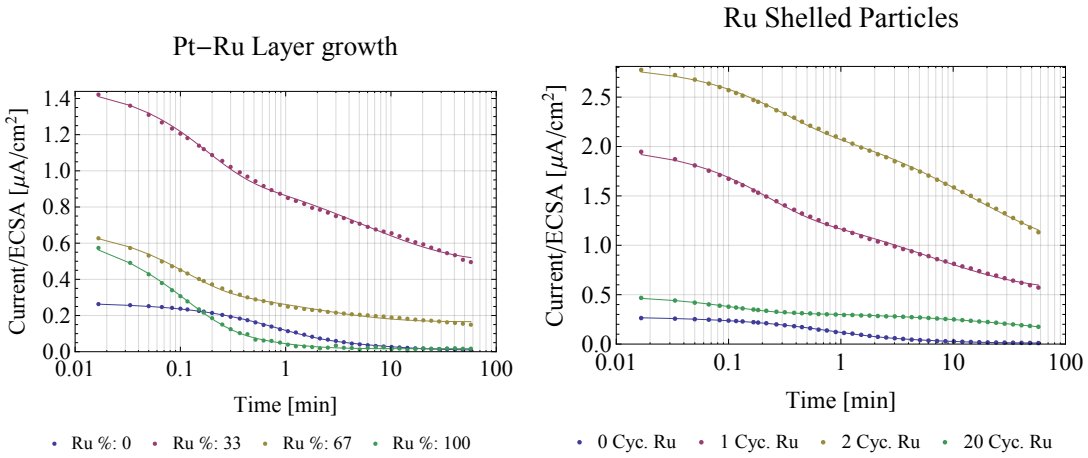

(a) Pt/Ru layer co-growth particles. The current is much larger for the 33% Ru ratio, while higher ratios lead to reduced current. For pure Ru and pure Pt a seemingly single exponential decay is observed, with the pure Pt curve having a much lower curvature than the Ru curve.

(b) Ru shelled Pt catalyst particles grown on NCNT. The current is shown to be much larger for thin layers, while thicker layers reduces the current down to the levels of unshelled Pt particles. The biexponential behavior of the decay is apparent in the kink around 1 min for every curve except the pure platinum particles.

Figure 7.11: Chronometric measurements carried out on two types of catalytic particles grown on NCNTs. Currents are normalized with the electrochemically active surface area (ECSA). Solid lines indicate a fit using equation 7.16.

decays, I_l and I_d respectively. These are extracted through fitting this model to the measurements obtained on catalyst particles using the two evaluated growth methods. The results clearly show the trade-offs in the alloying of Pt/Ru and has a optimum near low Ru content for both methods. The superior method is the Ru shelled growth, which reaches its optimum after only two cycles of ALD growth.

7.5 Nafion Integration in CNT Based Devices

Figure 7.13 shows a cross sectional SEM images of a 20 µm plate device prior to membrane integration. Very uniform NCNT growth is observed, with no degradation in the lower CNT layer observed during the growth of the upper layer.

Prior to annealing the filling process creates a nice uniform surface coverage of Nafion which conforms to the underlying geometry of the CNT covered collector electrodes as shown in figure 7.14. From the cross-section it can be seen that the NCNT likely trap gasses under the depositing layer, these trapped gasses are, however, released during annealing phase as can be seen in figure 7.15. The final result looks promising as a method of increasing the three phase boundary.

Sadly the final cells experienced short circuits. The exact cause of the short

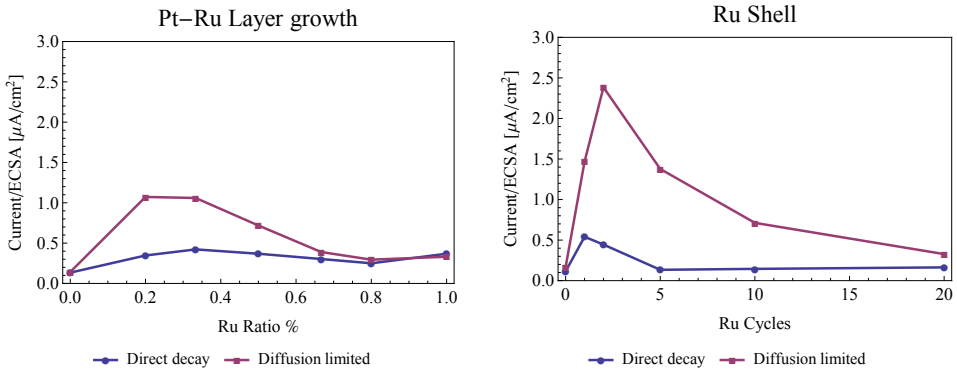

(a) Current contributions for catalyst particles defined via layered ALD co-growth of platinum and ruthenium.

(b) Current contributions for platinum particles with a thin ruthenium shell.

Figure 7.12: Contributions to the decay curves from early and late decay modes

circuits is unknown, though likely candidates are the laser dicing, which has produced non-shorted devices previously, however, the exact process parameters might have changed, as the machine is still under the process of being introduced to general usage in Danchip. Changes in focus parameters as well as intensity could have lead to a larger and more violent redeposition which could cause shorts around the passivisation at the edges. For the thinner cells another likely cause is parasitic carbon growth during the CNT growth procedure, however, the shorts have also been observed in gold plated non-CNT devices.

7.6 Performance Characterization

The performance of the a single successfully fabricated fuel cell with ALD-CNT based catalyst layer has been tested, and is shown in figure 7.16. This device performs poorly, notably having an extremely high effective resistance of 2.6 kΩ. Several factors can contribute to this, it is, however, believed that the primary limitation was the very poor quality of CNTs of the studied device, as it was fabricated prior to the optimization of the growth system outline in section 7.3.1. The result does however serve as a proof of concept for the device design and underlines potential for better performing devices through integrated catalyst layers.

7.7 Summary

The chapter described the development of a micro fuel cell design which incorporates a micro and nano-structured catalyst layer through growth of carbon nanotubes

Figure 7.13: Cross-sectional SEM image of a NCNT-ALD catalytic cell plate prior to membrane integration shown in comparison to a conventional commercial MEA structure. The relative compactness and much higher ordering of the NCTN device is self evident.

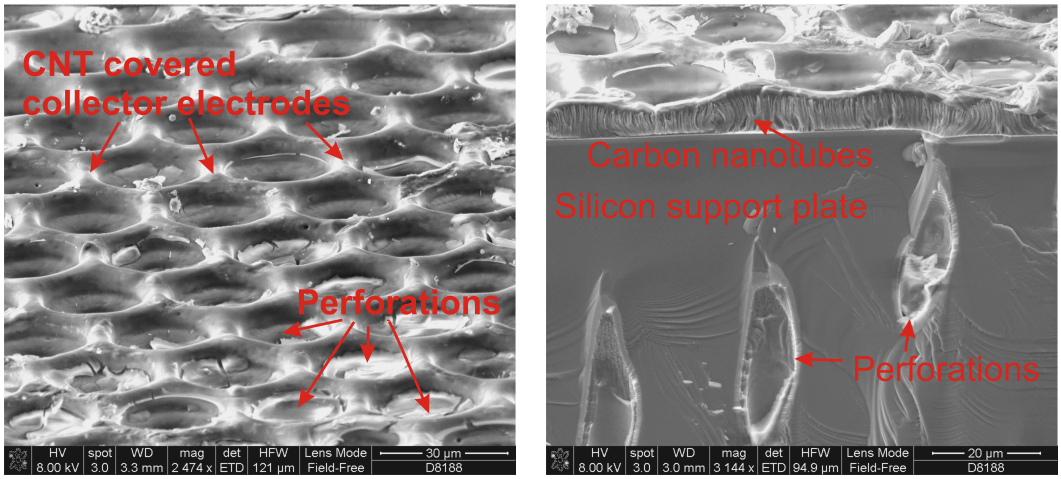

Figure 7.14: Nafion covered ALD-coated NCNTs. The film is seen to have deposited almost uniformly over the CNTs and into the perforations. The cross-section shows that the CNTS have trapped gas under the Nafion film prior to annealing.

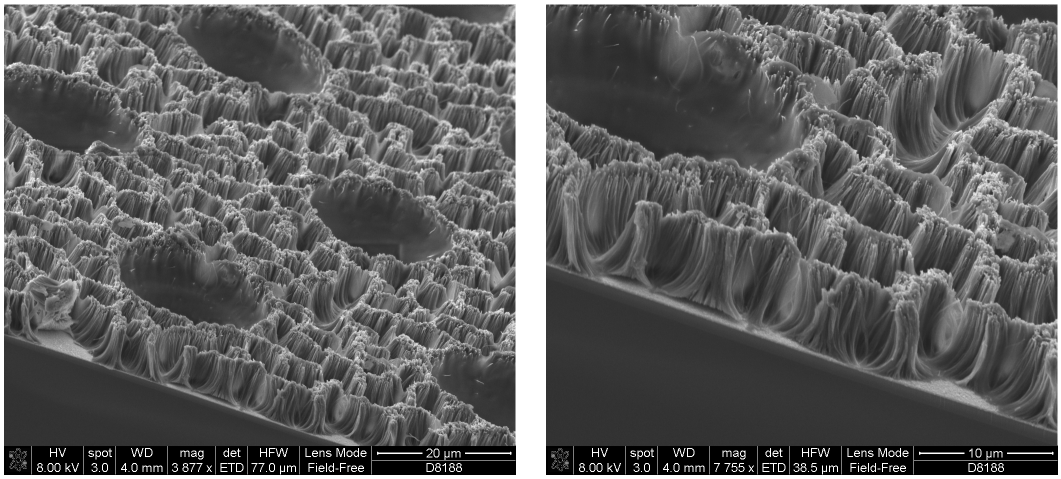

Figure 7.15: Nafion covered ALD-coated NCNTs after annealing. The tubes are seen to cluster together, forming a very open large surface area structure. The large indentations correspond to the perforations through the plate. The shown surface is the flat side of the device which was oriented upwards during the ionomer integration.

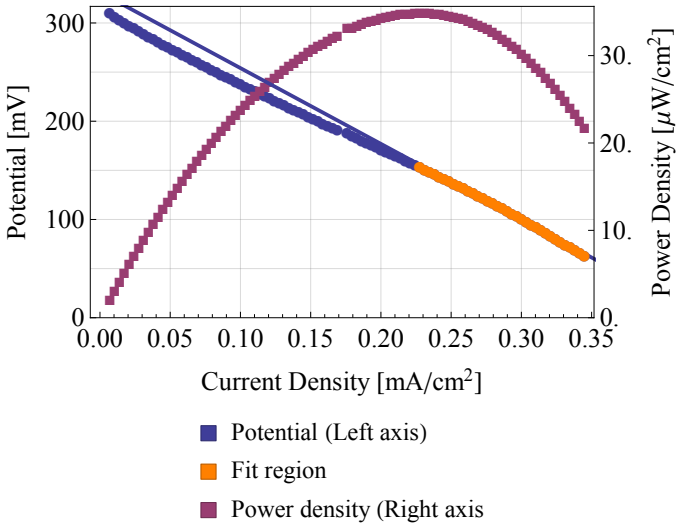

Figure 7.16: IV and power curves for a ALD-CNT device. The device has a hole diameter of 20 µmand lattice spacing 50 m, leading to a perforation ratio of 15 %.The current densities are very low, leading to a peak power density of just 35 µW/cm^2. The effective internal resistance is found to be 2.6 kΩ.

directly on the collector electrode. Through optimization of the growth equipment a reliable growth procedure was developed, which allowed for highly directional and uniform growth of high quality n-doped carbon nanotubes.

The in situ growth of catalytic particles by use of atomic layer deposition was studied, with focus on two separate catalyst particle structures, and it was found that platinum particles with just two monolayers of ruthenium deposited showed the optimal performance with respect to the methanol oxidation reaction.

Owing to fabrication short comings, the fabricated devices were not operational due to electrical short circuits. A single working device was, however, characterized and provides a proof of concept of the device design, the resulting performance was, however, quite low. It is expected that the design will allow much greater performance with the short circuit problem solved and the much higher quality of the CNT catalyst layer possible with the optimized growth procedure.

8 Conclusion

The objective of this project was to create miniature fuel cell systems by utilization of micro fabrication techniques. In this regard, several systems were developed and evaluated towards the goals of powering hearing aids, which sets much tighter restrictions on the dimensionality than has been shown by other silicon based micro fuel cell systems reported in literature.

Several different approaches to monolithic silicon based fuel cell systems were fabricated. The achieved best performances for the studied designs can be seen summarized in table 8.1. The best performing device proved to be a micro perforated plate with an integrated Nafion membrane with a perforation of 40 % showing a peak power density of 4.5 $\mathrm{mW/cm^2}$. This device design was realized via KOH etching and DRIE perforation. Initial results showed a large variation in the ionomer integration results, and a process that allowed higher reproducibility was developed. Medium peak power densities per active area were found for devices, which show a tendency of increasing performance for higher perforation.

In order to study the potential for structures with a perforation ratio, porous silicon was studied, which allow higher ionomer filling ration while still allowing surface engineering. In order to cheaply fabricate porous silicon the method of metal assisted chemical etching was implemented. From this technique porous silicon based fuel cells were developed that showed a peak power density of up to 1.6 $\mathrm{mW/cm^2}$ for use as methanol fuel cells. The process of filling these devices, however, remained highly irreproducible.

Porous silicon cells were also evaluated as a novel hydrogen cell operating with a liquid electrolyte membrane. These devices showed a peak power density of 1.34 $\mathrm{mW/cm^2}$. The operation was, however, highly dependent on the exact hydration conditions and showed large time dependencies in time scales in the order of 30 min. Thus while interesting the design should be studied further before conclusions on the viability of the design can be made.

#	Design	OCV [mW]	U_{max} [mW]	I_{max} [mA/cm^2]	P_{max} [mW/cm^2]	Parameters
A	Perforated plate, Spray deposited Catalyst	300	150	30	4.52	Perforation 40%
B	Porous silicon, Spray deposited Catalyst	480	180	8.5	1.6	Internal Volume rate $\approx 50\,\%$
C	Liquid electrolyte, Integrated Catalyst	400	154	8.5	1.34	Hydrogen Fueled
D*	Perforated plate, Integrated Catalyst	310	150	0.25	0.035	Perforation 15 %

Table 8.1: Studied designs and best achieved performances. *The studied device had particularly low quality CNTs.

Finally based on the desire to improve electrical contact and allow nano- scale design was created which was based on CNTs grown directly on the current collecting electrode. The CNTs were then used as support structures for atomic layer deposition based Pt and PtRu catalyst particles. Two types of catalyst particle structures were evaluated, and the superior was found to be platinum particles with very thin shell layers of ruthenium. The optimal performance was found at just two ALD cycles of deposition. The fully integrated cells have not been fully characterized due to fabrication shortcomings, however, a single cell was characterized and showed a low performance of $35\,\mu W/cm^2$which serves as a proof of concept for the fabrication but is far below the expected performance. The performance for this particular device is expected to be limited both by a poor quality CNT layer and potentially electrical short circuits between the electrodes, and as such is not an estimator for the full performance potential in this design. Which will hopefully be investigated in the future.

8.1 Outlook

The work has highlighted the feasibility of using integrated ionomer membranes in a bipolar plate design to avoid the need for multiple layers and large compressive forces. This new type of design shows promise as a method of decreasing system sizes for silicon based micro direct methanol fuel cells. One of the values of a filly

monolithic fuel cell design is the potential for additional integrated components. Future work on the design could for instance work in integrating thermistors directly under the current collector electrode to carry out in-situ temperature measurements during operation. In addition, assuming power management electronics could be scaled to fit in the outlying frame of the device, such integrated electronics could also be integrated into the device.

Through the work with porous silicon as a candidate for the ionomer support material, a novel monolithic liquid electrolyte cell was developed, which operated on gas fuel. This type of cell might be useful as a electrochemical sensor as the porous silicon structure and ALD catalyst components allow for very simple fabrication. For such devices to be feasible a detailed in investigation of the liquid gas interface stability should be pursued to ensure that the liquid electrolyte interface can be made stable over much longer times. Another interesting potential for these cells is usage as a device for electrochemical analysis of liquid samples, which would not require very long term stability of the liquid gas interface, but would still require a well controlled interface.

Through the combination of CNT growth and ALD deposition, the work lead to the realization of a catalyst support layer that is fully integrated into the current collector electrodes. This type of integration opens the potential for the integration of reference micro electrodes directly onto the surface of the devices, which will be able to carry out in-situ electrochemical spectroscopy both as performance evaluation testing, but also capable of providing live feedback during operation. This type of integration will provide a much richer insight into the influences of operating conditions. For instance by integrating both a reference electrode in plate region and further away on the frame region, the amount of cross-over could be determined continually. In addition this would allow a much greater distinction between separate contributions to the effective internal resistance and therefore allow an accelerated design optimization in future cells.

Bibliography

[1] Lawrence W. Jones. Toward a liquid hydrogen fuel economy. 1970. http://deepblue.lib.umich.edu/bitstream/2027.42/5800/5/bac5758.0001.001.pdf.

[2] Brian Seger, Thomas Pedersen, Anders Bo Laursen, Peter Christian Kjærgaard Vesborg, Ole Hansen, Ib Chorkendorff, Brian Seger, Thomas Pedersen, Anders Bo Laursen, Peter Christian Kjærgaard Vesborg, Ole Hansen, and Ib Chorkendorff. Using TiO2 as a conductive protective layer for photocathodic h2 evolution. *American Chemical Society. Journal*, 135(3):1057–1064, 2013.

[3] MyFC hybrid fuel cell & battery charger.

[4] Yabin Liao and Henry A. Sodano. Model of a single mode energy harvester and properties for optimal power generation. *Smart Materials and Structures*, 17(6):065026, December 2008.

[5] J.A. Paradiso and T. Starner. Energy scavenging for mobile and wireless electronics. *IEEE Pervasive Computing*, 4(1):18–27, 2005.

[6] Jingliang Zhang and Jay Lee. A review on prognostics and health monitoring of li-ion battery. *Journal of Power Sources*, 196(15):6007–6014, August 2011.

[7] Ahmed F. Ghoniem. Needs, resources and climate change: Clean and efficient conversion technologies. *Progress in Energy and Combustion Science*, 37(1):15–51, February 2011.

[8] Nokia ultra extended 850 mAh lithium ion battery for nokia 3390 series phone.

[9] Powerone accu plus NiMH.

[10] Powerone zinc air battery.

[11] SciVerse ScienceDirect: http://www.sciencedirect.com/.

[12] A.D. Hawkes and M.A. Leach. Cost-effective operating strategy for residential micro-combined heat and power. *Energy*, 32(5):711–723, May 2007.

[13] Leigh Aldous and Richard G. Compton. Towards mixed fuels: The electrochemistry of hydrazine in the presence of methanol and formic acid. *ChemPhysChem*, 12(7):1280–1287, May 2011.

[14] NOAA US Department of Commerce. Trends in carbon dioxide. The NOAA Earth System Research Laboratory was formed to observe and understand the Earth system and to develop products, through a commitment to research that will advance the National Oceanic and Atmopsheric Administration's environmental information and services on global to local scales.

[15] Chunzhi He, H. R. Kunz, and J. M. Fenton. Evaluation of Platinum-Based catalysts for methanol electro-oxidation in phosphoric acid electrolyte. *Journal of The Electrochemical Society*, 144(3):970–979, March 1997.

[16] Subramanian Sundarrajan, Suleyman I. Allakhverdiev, and Seeram Ramakrishna. Progress and perspectives in micro direct methanol fuel cell. *International Journal of Hydrogen Energy*, 37(10):8765–8786, May 2012.

[17] H.-G. Haubold, Th. Vad, H. Jungbluth, and P. Hiller. Nano structure of NAFION: a SAXS study. *Electrochimica Acta*, 46(10–11):1559–1563, March 2001.

[18] William Y. Hsu and Timothy D. Gierke. Ion transport and clustering in nafion perfluorinated membranes. *Journal of Membrane Science*, 13(3):307–326, February 1983.

[19] John Halim, Günther G Scherer, and Manfred Stamm. Characterization of recast nafion films by small- and wide-angle x-ray scattering. *Macromolecular Chemistry and Physics*, 195(12):3783–3788, December 1994.

[20] M Ludvigsson, J Lindgren, and J Tegenfeldt. FTIR study of water in cast nafion films. *Electrochimica Acta*, 45(14):2267–2271, March 2000.

[21] Thomas A. Zawodzinski, Charles Derouin, Susan Radzinski, Ruth J. Sherman, Van T. Smith, Thomas E. Springer, and Shimshon Gottesfeld. Water uptake by and transport through nafion® 117 membranes. *Journal of The Electrochemical Society*, 140(4):1041–1047, April 1993.

[22] J. J. Sumner, S. E. Creager, J. J. Ma, and D. D. DesMarteau. Proton conductivity in nafion® 117 and in a novel bis[(perfluoroalkyl)sulfonyl]imide ionomer membrane. *Journal of The Electrochemical Society*, 145(1):107–110, January 1998.

[23] Kristi J. Oberbroeckling, Drew C. Dunwoody, Shelley D. Minteer, and Johna Leddy. Density of nafion exchanged with transition metal complexes and tetramethyl ammonium, ferrous, and hydrogen ions: Commercial and recast films. *Analytical Chemistry*, 74(18):4794–4799, September 2002.

[24] Takehiko Yamato, Chieko Hideshima, G. K. Surya Prakash, and George A. Olah. Solid superacid catalyzed organic synthesis. 6. perfluorinated resinsufonic acid (nafion-h) catalyzed ring closure reaction of 2,2'-dihydroxybiphenyls. a preparative route to dibenzofurans. *The Journal of Organic Chemistry*, 56(9):3192–3194, April 1991.

[25] Song Hi Lee and Jayendran C. Rasaiah. Molecular dynamics simulation of ion mobility. 2. alkali metal and halide ions using the SPC/E model for water at 25 °C†. *The Journal of Physical Chemistry*, 100(4):1420–1425, January 1996.

[26] L. Zhu, V. Swaminathan, B. Gurau, R.I. Masel, and M.A. Shannon. An onboard hydrogen generation method based on hydrides and water recovery for microfuel cells. *Journal of Power Sources*, 192(2):556–561, July 2009.

[27] E.R. Choban, J.S. Spendelow, L. Gancs, A. Wieckowski, and P.J.A. Kenis. Membraneless laminar flow-based micro fuel cells operating in alkaline, acidic, and acidic/alkaline media. *Electrochimica Acta*, 50(27):5390–5398, September 2005.

[28] Erik Kjeang, Ned Djilali, and David Sinton. Microfluidic fuel cells: A review. *Journal of Power Sources*, 186(2):353–369, January 2009.

[29] Yuming Yang and Yung C. Liang. A direct methanol fuel cell system with passive fuel delivery based on liquid surface tension. *Journal of Power Sources*, 165(1):185–195, February 2007.

[30] S. C. Kelley, G. A. Deluga, and W. H. Smyrl. Miniature fuel cells fabricated on silicon substrates. *AIChE Journal*, 48(5):1071–1082, 2002.

[31] Xiaowei Liu, Chunguang Suo, Yufeng Zhang, Xilian Wang, Chi Sun, Ling Li, and Lifang Zhang. Novel modification of nafion 117 for a MEMS-based micro

direct methanol fuel cell (uDMFC). *Journal of Micromechanics and Microengineering*, 16(9):S226–S232, September 2006.

[32] Young Ho Seo and Young-Ho Cho. Micro direct methanol fuel cells and their stacks using a polymer electrolyte sandwiched by multi-window microcolumn electrodes. *Sensors and Actuators A: Physical*, 150(1):87–96, March 2009.

[33] N. Hashim, S.K. Kamarudin, and W.R.W. Daud. Design, fabrication and testing of a PMMA-based passive single-cell and a multi-cell stack micro-DMFC. *International Journal of Hydrogen Energy*, 34(19):8263–8269, October 2009.

[34] Y.H. Chan, T.S. Zhao, R. Chen, and C. Xu. A small mono-polar direct methanol fuel cell stack with passive operation. *Journal of Power Sources*, 178(1):118–124, March 2008.

[35] Takahiro Shimizu, Toshiyuki Momma, Mohamed Mohamedi, Tetsuya Osaka, and Srinivasan Sarangapani. Design and fabrication of pumpless small direct methanol fuel cells for portable applications. *Journal of Power Sources*, 137(2):277–283, October 2004.

[36] N. Sabate, J. P. Esquivel, J. Santander, N. Torres, I. Gracia, P. Ivanov, L. Fonseca, E. Figueras, and C. Cane. Fabrication and characterization of a passive silicon-based direct methanol fuel cell. In *2008 2nd European Conference Exhibition on Integration Issues of Miniaturized Systems - MOMS, MOEMS, ICS and Electronic Components (SSI)*, pages 1–4, 2008.

[37] Hussein Gharibi, Farhad Golmohammadi, and Mehdi Kheirmand. Fabrication of MEA based on optimum amount of co in {pdxco/c} alloy nanoparticles as a new cathode for oxygen reduction reaction in passive direct methanol fuel cells. *Electrochimica Acta*, 89:212–221, February 2013.

[38] Tristan Pichonat, Bernard Gauthier-Manuel, and Daniel Hauden. New proton-conducting porous silicon membrane for small fuel cells. *Fuel Cells Bulletin*, 2004(8):11–14, August 2004.

[39] Saeed Moghaddam, Eakkachai Pengwang, Ying-Bing Jiang, Armando R. Garcia, Daniel J. Burnett, C. Jeffrey Brinker, Richard I. Masel, and Mark A. Shannon. An inorganic–organic proton exchange membrane for fuel cells with a controlled nanoscale pore structure. *Nature Nanotechnology*, 5(3):230–236, March 2010.

[40] Xiaoming Ren, Wesley Henderson, and Shimshon Gottesfeld. Electro-osmotic drag of water in ionomeric membranes new measurements employing a direct methanol fuel cell. *Journal of The Electrochemical Society*, 144(9):L267–L270, September 1997.

[41] Thomas A. Zawodzinski, John Davey, Judith Valerio, and Shimshon Gottesfeld. The water content dependence of electro-osmotic drag in proton-conducting polymer electrolytes. *Electrochimica Acta*, 40(3):297–302, February 1995.

[42] David J. Mann and Mathew D. Halls. Water alignment and proton conduction inside carbon nanotubes. *Physical Review Letters*, 90(19):195503, May 2003.

[43] Yasuyuki Ishikawa, Meng-Sheng Liao, and Carlos R. Cabrera. Oxidation of methanol on platinum, ruthenium and mixed Pt–M metals (M=Ru, sn): a theoretical study. *Surface Science*, 463(1):66–80, August 2000.

[44] A.A. El-Shafei. Electrocatalytic oxidation of methanol at a nickel hydroxide/-glassy carbon modified electrode in alkaline medium. *Journal of Electroanalytical Chemistry*, 471(2):89–95, August 1999.

[45] C. Rice, S. Ha, R.I. Masel, P. Waszczuk, A. Wieckowski, and Tom Barnard. Direct formic acid fuel cells. *Journal of Power Sources*, 111(1):83–89, September 2002.

[46] Alfred B. Anderson and Nikolay M. Neshev. Mechanism for the electro-oxidation of carbon monoxide on platinum, including electrode potential dependence theoretical determination. *Journal of The Electrochemical Society*, 149(10):E383–E388, October 2002.

[47] Jayakumar Narayanasamy and Alfred B. Anderson. Mechanism for the electrooxidation of carbon monoxide on platinum by H2O. density functional theory calculation. *Journal of Electroanalytical Chemistry*, 554–555:35–40, September 2003.

[48] Prashanta Dutta and Ali Beskok. Analytical solution of combined Electroosmotic/Pressure driven flows in two-dimensional straight channels: Finite debye layer effects. *Analytical Chemistry*, 73(9):1979–1986, May 2001.

[49] R. A. Marcus. Electrostatic free energy and other properties of states having nonequilibrium polarization. i. *The Journal of Chemical Physics*, 24(5):979–989, May 1956.

[50] R. A. Marcus. On the theory of Oxidation-Reduction reactions involving electron transfer. i. *The Journal of Chemical Physics*, 24(5):966–978, May 1956.

[51] Won Choon Choi, Ju Dam Kim, and Seong Ihl Woo. Modification of proton conducting membrane for reducing methanol crossover in a direct-methanol fuel cell. *Journal of Power Sources*, 96(2):411–414, June 2001.

[52] Sung Jae Kim and Jongyoon Han. Self-sealed vertical polymeric nanoporous-junctions for high-throughput nanofluidic applications. *Anal. Chem.*, 80(9):3507–3511, 2008.

[53] Xianguo Li and Imran Sabir. Review of bipolar plates in PEM fuel cells: Flow-field designs. *International Journal of Hydrogen Energy*, 30(4):359–371, March 2005.

[54] Vladislav Dolnik, Kelly A Cobb, and Milos Novotny. Preparation of polyacrylamide gel-filled capillaries for capillary electrophoresis. *Journal of Microcolumn Separations*, 3(2):155–159, March 1991.

[55] Siavouche Nemat-Nasser and Shahram Zamani. Experimental study of nafion- and flemion-based ionic polymer metal composites (IPMCs) with ethylene glycol as solvent. volume 5051, pages 233–244, 2003.

[56] Scott Munro. SOI wafer notch reduction using the low frequency pulsing option on the STS ICP-RIE. July 2009.

[57] Joachim Thomsen and Sara Engberg. *Micro Fabricated Direct Methanol Fuel Cells: Design, Fabrication, and Characterisation*. PhD thesis, June 2011.

[58] Xiaoyu Ding, Sima Didari, Thomas F. Fuller, and Tequila A. L. Harris. Effects of annealing conditions on the performance of solution cast nafion membranes in fuel cells. *Journal of The Electrochemical Society*, 160(8):F793–F797, January 2013.

[59] Tequila A.L. Harris and Daniel F. Walczyk. Development of a casting technique for membrane material used in high-temperature PEM fuel cells. *Journal of Manufacturing Processes*, 8(1):8–20, 2006.

[60] Lois Anne Zook and Johna Leddy. Density and solubility of nafion: Recast, annealed, and commercial films. *Anal. Chem.*, 68(21):3793–3796, 1996.

[61] Tatyana Soboleva, Zhong Xie, Zhiqing Shi, Emily Tsang, Titichai Navessin, and Steven Holdcroft. Investigation of the through-plane impedance technique

for evaluation of anisotropy of proton conducting polymer membranes. *Journal of Electroanalytical Chemistry*, 622(2):145–152, October 2008.

[62] J. E. B. Randles. Kinetics of rapid electrode reactions. *Discussions of the Faraday Society*, 1(0):11–19, January 1947.

[63] C. Criado, P. Galán-Montenegro, P. Velásquez, and J.R. Ramos-Barrado. Diffusion with general boundary conditions in electrochemical systems. *Journal of Electroanalytical Chemistry*, 488(1):59–63, June 2000.

[64] G.J. Brug, A.L.G. van den Eeden, M. Sluyters-Rehbach, and J.H. Sluyters. The analysis of electrode impedances complicated by the presence of a constant phase element. *Journal of Electroanalytical Chemistry and Interfacial Electrochemistry*, 176(1-2):275–295, September 1984.

[65] X. Li and P.W. Bohn. Metal-assisted chemical etching in HF/H2O2 produces porous silicon. *Applied Physics Letters*, 77(16):2572–2574, 2000.

[66] Bjarke Thomas Dalslet, Louise Møller Borregaard, Kaspar Haume, Gustav Kvaal, Thomas Pedersen, Ole Hansen, and Erik Villain Thomsen. Metal assisted chemical etching of silicon for porous membranes.

[67] Louise Boregaard. *Design, Fabrication and Characterization of Porous Silicon based Miniaturized Direct Methanol Fuel Cells*. PhD thesis, November 2011.

[68] Wenzhen Li, Changhai Liang, Jieshan Qiu, Weijiang Zhou, Hongmei Han, Zhaobin Wei, Gongquan Sun, and Qin Xin. Carbon nanotubes as support for cathode catalyst of a direct methanol fuel cell. *Carbon*, 40(5):791–794, April 2002.

[69] Wenzhen Li, Xin Wang, Zhongwei Chen, Mahesh Waje, and Yan. Carbon nanotube film by filtration as cathode catalyst support for proton-exchange membrane fuel cell. *Langmuir*, 21(21):9386–9389, October 2005.

[70] Wen Lu and Liming Dai. Carbon nanotube supercapacitors. In Jose Mauricio, editor, *Carbon Nanotubes*. InTech, March 2010.

[71] Surbhi Sharma and Bruno G. Pollet. Support materials for PEMFC and DMFC electrocatalysts—A review. *Journal of Power Sources*, 208:96–119, June 2012.

[72] Zhaolin Liu, Xuanhao Lin, Jim Yang Lee, Weide Zhang, Ming Han, and Leong Ming Gan. Preparation and characterization of platinum-based elec-

trocatalysts on multiwalled carbon nanotubes for proton exchange membrane fuel cells. *Langmuir*, 18(10):4054–4060, May 2002.

[73] Yang-Chih Hsueh, Chih-Chieh Wang, Chi-Chung Kei, Yu-Hung Lin, Chueh Liu, and Tsong-Pyng Perng. Fabrication of catalyst by atomic layer deposition for high specific power density proton exchange membrane fuel cells. *Journal of Catalysis*, 294:63–68, October 2012.

[74] Ting Shu, Shi-Jun Liao, Chien-Te Hsieh, Anup Kumar Roy, Yung-Ying Liu, Dong-Ying Tzou, and Wei-Yu Chen. Fabrication of platinum electrocatalysts on carbon nanotubes using atomic layer deposition for proton exchange membrane fuel cells. *Electrochimica Acta*, 75:101–107, July 2012.

[75] M. Glerup, M. Castignolles, M. Holzinger, G. Hug, A. Loiseau, and P. Bernier. Synthesis of highly nitrogen-doped multi-walled carbon nanotubes. *Chemical Communications*, (20):2542–2543, October 2003.

[76] Ren Bin Yang. *Gas-phase synthesis of bismuth and antimony chalcogenide nanos- tructures.* PhD dissertation, 2010.

[77] Anne-Charlotte Johansson, Bjarke T. Dalslet, Ren Bin Yang, Kenneth B. Haugshøj, Mathias J. G. Mølgaard, Kim Christiansen, Leif H. Christensen, and Erik V. Thomsen. Electrocatalytic activity of pt grown by ALD on carbon nanotubes for si-based DMFC applications. *ECS Transactions*, 50(13):117–125, March 2013.

[78] Anne-Charlotte Johansson, Jackie Vincent Larsen, Marcel A Verheijen, Kenneth B Haugshøj, Henrik Fanø, Wilhelmus M. M. Kessels, Erik Villain Thomsen, and (Fornavn) . Electrocatalytic activity of atomic layer deposited pt-ru catalysts onto n-doped carbon nanotubes.

A

List of Publications

1. Jackie V. Larsen, B. T. Dalslset, C. Kallesøe,S Engberg, J. Thomsen, E. V. Thomsen. Micro Direct Methanol Fuel Cell Utilizing Silicon Supported Ionomer Membrane. Accepted for the proceedings of: the 11'th International Conference on Micro- and Nano-Technology for Power Generation and Energy Conversion Applications: PowerMEMS 2011.

2. J.V. Larsen, B.T. Dalslet, C.Kallesøe and E.V.Thomsen. Characterization of Micro Direct Methanol Fuel Cells with Silicon Plate Supported Integrated Ionomer Membranes. Accepted for the proceedings of the 17th international conference on solid-state sensors, actuators and Microsystems Transducers 2013.

3. J. V. Larsen, B. T. Dalslet, A.-C. Johansson, C. Kallesøe, E. V. Thomsen. Micro Direct Methanol Fuel Cell with Perforated Silicon-Plate Integrated Ionomer Membrane. Submitted for review at the Journal of Power Sources IEEE.

4. A.-C. Johansson, R.B. Yang, K.B. Haugshøj, J.V. Larsen, L. H. Christensen, E.V. Thomsen. Ru-decorated Pt nanoparticles on N-doped multi-walled carbon nanotubes by atomic layer deposition for direct methanol fuel cells. Submitted for review at the International Journal of Hydrogen Energy IEEE.

B

Fabrication Recipe

KOH-etched Frame

Jackie Vincent Larsen, DTU Nanotech/prototyping

September 30, 2013

1 Frame-etch

1. Collect ten double polished ||100|| n-type wafers, $t_W = 350\,\mu m$.
2. Deposit LPCVD nitride (Furnace LPCVD nitride)
   (a) Recipe LOWSTR
   (b) Target is 70 nm
   (c) Deposition rate 4.6-4.8 nm/min =¿ 15 min.
3. Frame Photolitography
   (a) HMDS treatment. (HMDS oven) standard recipe 4.
   (b) Spin on 1.5 μm photoresist on the wafer. Using SSE spinner.
4. Lithographic patterning of the resist with Pillar front side mask.
   - First exposure with the mask $t = 3\,s$. (6"-aligner)
   - Developer 70s
5. Frame Etch Mask opening. Etch Nitride (RIE1)
   (a) Recipe BGE-NITR
   (b) Etch rate 30 nm/min
   (c) Etch 3.5 min.
   (d) *Use aluminum carrier and edge protection ring*
6. Strip resist (rough/fine strip bench)
7. KOH etch wafers in KOH3 bench.
   - 0.4 μm/min (60C$^\circ$) 0.7 μm/min (70C$^\circ$) 1.3 μm/min (80C$^\circ$)

   Wafers should be taken out at regular intervals to obtain different wafer thicknesses. Use wafer thickness measuring station for rough test, use DEKTAK for fine test. Precise thickness control is not necessary as long as the thickness is known.
8. Strip remaining Nitride in hot phosphoric acid
   (a) Etch rate is $\approx 50\,Å/min$, with very low over-etching, so 30 min is appropriate.
   (b) 7-up clean wafers.
9. Plate Etch Mask/Stop Layer Definition
   (a) RCA clean the wafers
   (b) Deposit the maximum single run thickness of TEOS, 3 hours, $\approx 2\,\mu m$.
10. Front side: Lithographic patterning of the resist with (Etch-through) mask, positive process. 1.5 μm resist.
    (a) HMDS treatement (HMDS oven)
    (b) Spin on 1.5 µm photoresist on the wafer. Use manual spinner with wafer free chuck.
    (c) Exposure with the mask $t = 4\,s$ (6"-aligner Back side alignment).
    (d) Developer 70 s
11. Oxide Mask Opening Etch (AOE)
    (a) Using m-res-new (Make sure it's the one under Danchip subfolder, there are multiple recipes with this name in other subfolders which are no identical!)

C

Black Magic Carbon Nanotube Growth Recipe

```
1  COMM N2,N2,C2H2,NH3
2  VALV 1 OPEN
3  TUNE PCON Fully open
4  PCON ON 1 1
5  WAIT PRES < 0.10
6  FLOW 4 ON 160
7  FLOW 1 ON 100
8  SENS IR 500
9  TUNE HTIR warmup 510C
10 HEAT ON 800.0 300.0
11 WAIT TEMP > 510.0
12 TUNE HTIR 600C- 750C INT
13 TUNE TOPH top heat 750 INT
14 HEAT ON 600.0 300.0
15 TOPH ON 400.0 0.0
16 WAIT TEMP > 595.0
17 TUNE PLAS 80W dc drive
18 PLAS ON 800
19 WAIT TIME > 10
20 TUNE PCON pecvd at 6mbar
21 PCON ON 6.0 1.0
22 VALV 1 CLOSE
23 WAIT TIME > 120
24 FLOW 3 ON 40
25 HEAT ON 610.0 0.0
26 WAIT TIME > 3
27 HEAT ON 850.0 150.0
28 TOPH ON 750.0 150.0
29 WAIT TIME > 60 TUNE
30 PLAS 100W dc
31 WAIT TIME > 900
32 FLOW 3 OFF
33 FLOW 4 OFF
34 PLAS OFF
35 HEAT OFF
36 TOPH OFF
37 VALV 1 OPEN
38 PCON OFF SENS TC 650
```

```
39 FLOW 1 OFF
40 WAIT PRES < 0.20
41 FLOW 1 ON 1000
42 FLOW 2 ON 2000
43 WAIT TEMP < 600.0
44 FLOW 2 ON 8000
45 WAIT TEMP < 400.0
46 FLOW 2 OFF
47 FLOW 1 OFF
48 WAIT PRES < 0.50
```

The PID parameters of the Tune settings are

- HTIR warmup 510C: P:10 I:30 D:10 limit: 40%

This tuning has not been the target of any optimization as it only controls the initial machine warmup.

- HTIR 600C- 750C INT: P:69 I:26 D:4 limit: 40%

This corrosponds to an ultimate gain of $K_u = 340$ and an ultimate period of $T_u = 0.65$, with pid tuning coefficients $\alpha_P = 1/5$, $\alpha_I = 1/4\,\alpha_D = 1/10$.

- TOPH top heat 750 INT: P:156 I:15 D:2 limit 40%

These settings are not chosen to be optimal with respect to ultimate gain and period, but are less important as the bottom heater also warms up the top region, leading to very little active control of the top heater. This is a favorable situation as it prevents loops from forming between top and bottom heater.

Supervised Student Projects

Fabrication of micro fuel cell (3 Week course)

Joachim Thomsen (s082616), Sara Engberg (s082650), Søren Gregersen (s082619)

Micro Fabricated Direct Methanol Fuel Cells: Design, Fabrication, and Characterization (Bachelor Project)

Joachim Thomsen (s082616), Sara Engberg (s082650)

Design, Fabrication and Characterization of Porous Silicon Based Miniaturized Direct Methanol Fuel Cells (Master Project)

Louise Møller Borregaard

Carbon Nanotubes for Fuel Cells (Bachelor Project)

Kaspar Haume

Nano Porous silicon for micro fuel cell membranes (3 Week special course)

Henrik Teglborg (s082629), Adnan Silajdzic (s082626)

Fabrikation og test af multi wafer mikro-brændselsceller design (Bachelor Project)

Mikkel Maag Pedersen (s070465), Alexander Bagger (s103126), Kristoffer Skaftved Mathiesen (s103107)

Fabrikation af silicon nanogras baserede micro direct methanol fuel cells (Bachelor Project)

Kasper Ingerslev (s103112), Nicolai Frost-Jensen Johansen (s103094), Birgitte Bakke (s103120)

Hybrid Silicon-Nafion Membranes utilizing CNTs grown on porous silicon for Direct Methanol Fuel Cells (Bachelor Project)

Mathias J. G. Mølgaard (s093010), Kim Christiansen (s093005)

Silicon Encapsulated Micro Direct Methanol Fuel Cell (Bachelor Project)

Milan Laustsen (s081837)

E

PowerMEMS 2011 Manuscript

This manuscript covers an early design of the devices covered in chapter 4.

Micro Direct Methanol Fuel Cell Utilizing Silicon Supported Ionomer Membrane

Jackie V. Larsen[1*], B. T. Dalslset[1], C. Kallesøe[2],S Engberg[1], J. Thomsen[1], E. V. Thomsen[1]
[1]DTU Nanotech, Technical University of Denmark, Kgs. Lyngby, Denmark
[2]Danish Technological Institute (DTI), Denmark
*Presenting Author: jvila@nanotech.dtu.dk

Abstract: This paper reports the design, fabrication, and IV-characteristics of pump-free micro direct methanol fuel cells, based on silicon technology. The fuel cell design features a rigid silicon support with micropores containing the proton conducting ionomer Nafion®. This design intends to limit the effects of methanol cross-over by constraining the hydrophilic conducting channels of the ionomer. The IV characteristics of the cells are evaluated and the device is shown to be able to deliver 4 mW/cm^2 using ambient air and 3M methanol at room temperature. The performance limiting characteristics are investigated and indicate that large cavity defects in the ionomer membranes are formed during fabrication.

Keywords: Fuel Cell, DMFC, Methanol, Crossover

INTRODUCTION

In many small scale low power devices rechargeable battery technology cannot meet the power requirements without breaking the size constraints of the system. This is, for example, the case in most modern hearing aids. Today, such devices are often powered by non-rechargeable zinc-air batteries. A potential alternative to these batteries are micro fuel cells, which can be refuelled in seconds. For such systems pump-free (i.e. passive) operation is desirable due to size constraints which do not allow for active components such as pumps and heaters, without lowering the achievable total device power density significantly.

Our candidate for such a micro fuel cell is the direct methanol fuel cell (DMFC)[1]. The performance of DMFC's however, are limited by the direct permeation (crossover) of fuel through the proton exchange membranes (PEM) [2], which greatly limits the efficiency, and maximum power output. DMFC's lifetimes can also be limited by the mechanical stability of the cell membrane. The PEM expands when hydrated which can delaminate the catalyst layers. Therefore improving mechanical stability should enhance the total device lifetime.

Methanol crossover

Fuel crossover in DMFCs is the main limiting factor in performance. One effect of this crossover is a loss of useful fuel, which reduces the overall efficiency. The other performance limiting effect is oxidation of methanol on the cathode which greatly increases the polarization loss of the cell. For typical cells this loss can lead to more than a 50% reduction in open circuit potential (OCV), where the crossover is mainly due to diffusion. At positive currents, the concentration of methanol at the anode electrode, and thus the diffusion flux, will decrease. However, for increasing currents convection through the membrane will increase and becomes a relevant factor in the crossover.

Nafion® is a solid ionomer, consisting of fluorinated hydrocarbon backbone, with sulfonic acid groups. This structure leads to formation of hydrophilic and hydrophobic regions in the solid polymer. Due to the high acidity of the acid groups the hydrophilic regions become highly proton conductive. Methanol is miscible in water and can therefore diffuse through the liquid phase of the hydrophilic regions. Reducing water content will therefore reduce proton conductivity[4].

FABRICATION AND CHARACTERISATION

Our fuel cell design is intended to investigate the effects of crossover. It constrains both the proton and liquid flow channels by employing a porous silicon membrane as support for the proton conducting ionomer membrane. This allows for a detailed study of the influence of the hole-sizes and spacing on proton conductivity.

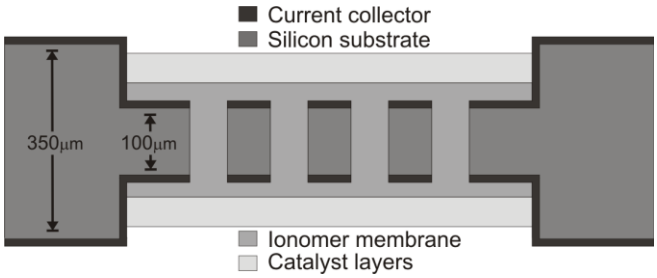

Fig. 1: Schematic illustration of the fuel cell. Aspect ratios are not to scale.

The porous silicon membrane is fabricated using conventional cleanroom silicon fabrication techniques. There are three defining etch steps, two openings and one hole etch. All three etch steps are carried out using deep reactive ion etching. Initially the holes are etched through the entire 350 μm thick wafer. After the holes

have been defined a large opening is etched in both sides of the wafer, defining a 100 μm thick membrane with a 350 μm thick border as illustrated in Figure 1. The membrane contains a triangular lattice of holes with diameters ranging from 2 μm to 100 μm. The use of this technique also allows structures to be defined on the membrane, such as pillars which could improve the electrical contact of the catalyst layer. A scanning electron microscope (SEM) image of such a structure can be seen in Figure 2.

After definition of the membrane structure, a thermal oxide is grown to insulate the two sides of the membrane from each other. Then a 200 nm layer of gold is deposited on both sides to act as current collectors. Sputter deposition is used to ensure coverage of the frame sidewalls which connect the collector with the surface of the frames. The device is briefly etched with aqua regia to remove any gold contacts between the current collectors. A SEM image of the resulting membrane can be seen in Figure 3. The final device measures 10 mm x 7.5 mm with a 1 mm frame, such that the total active area is 8 mm x 5.5 mm (0.44 cm^2).

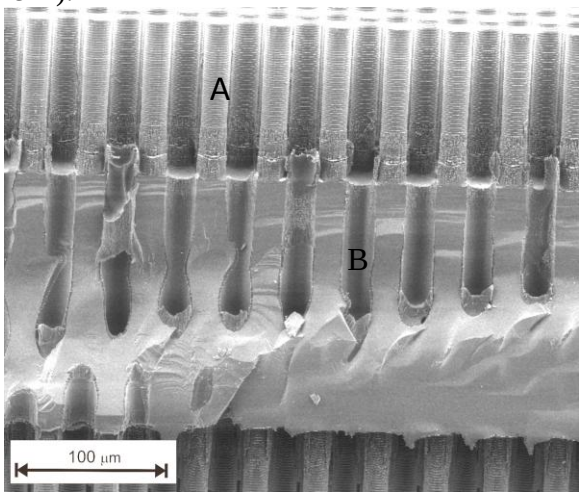

Fig. 2: SEM image of a cross-sectional fracture of a membrane with pillars (A) defined around the pores (B). The characteristic scallops of the Bosch process are visible on the pillars.

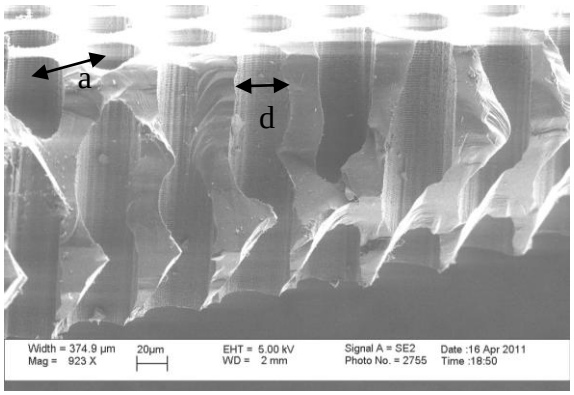

Fig. 3. SEM image showing a cross-section of the membrane prior to Nafion® treatment. The holes are approximately 20 μm in diameter (d) with 30 μm spacing(a)

Nafion® is soluted in a water and isopropylalcohol (IPA), mixture, and inserted into the membrane pores using capillary forces. The water and IPA is then slowly evaporated casting solid Nafion® in the pores.

After the membrane has been fabricated, the two catalysts layers are applied. Figure 4 shows a cross-sectional SEM image of the anode catalyst layer. The layer is a spray coated porous layer of Nafion® and PtRu on carbon black (80 wt.% catalyst loading on Vulcan-XC72) on the anode side, and Nafion® and Pt on carbon black on the cathode side. The loadings are approximately 4 mg/cm^2 on the anode and 2 mg/cm^2 on the cathode side.

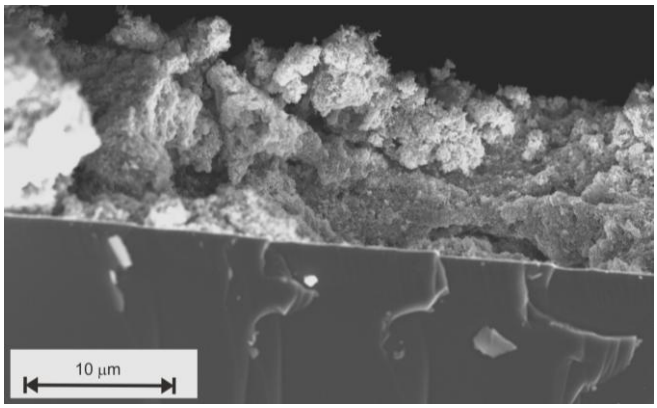

Fig. 4: SEM image of a membrane cross-section after catalyst layer deposition. The catalytic layer is a spray coated 10 μm thick porous PtRu/cabon black/ionomer mixture.

Device performance

The IV-characteristics three fuel cells (A, B and C) are shown in figure 5. The testing was conducted with 3M methanol on the anode side, ambient air on the cathode and room temperature and pressure conditions, and with a current scan rate of 0.3 mA/s. All three fuel cells have 20 μm diameter hole sizes, but different lattice spacings. The results are tabulated in table 1. For fuel cells A and B the peak power density (Pmax) is in the 4 mW/cm^2 range, with OCVs of 500-600 mV. Fuel cell C has much lower OCV of only 160mV and a peak power of 0.42 mW/cm^2. For fuel cell A and B the OCV is still well under the theoretical standard potential of 1.2V which indicates that as with typical DMFCs crossover loss is very large. For fuel cell A and B, the difference in lattice spacing leads to a difference in the pore area of 6.84 mm^2 for A and 4.36 mm^2 for B. Though A has the highest power output, B has the highest power output per active area. The IV-characteristics for these two devices are very similar, with almost identical ohmic regions, which suggests that the main difference in performance is caused by slight differences in the membrane quality, and not by the difference in pore area.

Table 1: Device performance parameters. All devices have 20 μm holes

	Lattice spacing	OCV [mV]	Pmax [mW/cm^2]	Hole Area [mm^2]
A	40	636.68	4.63	6.84
B	50	500.25	3.69	4.36
C	50	159.61	0.42	4.36

We belive that the OCV and a low maximum power density of fuel cell C, is caused by increased fuel crossover, and lack of proton conducting pathways through the membrane, as the pores in its membrane contained cavities not filled with Nafion®, similar to the case shown in Figure 6. These cavities are currently believed to be the essential limiting factor in the device performance. When hydrated such cavities are filled with water and add significantly to the diffusion flow of methanol, but insignificantly to the proton conductivity. Through proper control the process it is possible to create membranes without these defects, such as the one shown in Figure 7. At the time of writing we are making a detailed study of the membrane formation but have none available for electric testing.

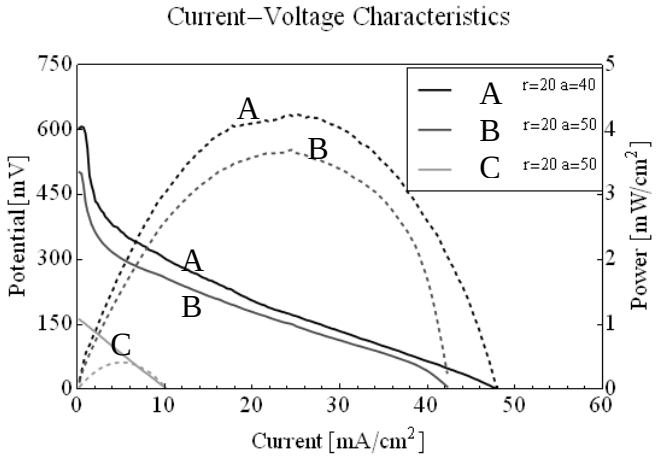

Fig. 5: Current-Voltage characteristics of three different devices, with two different membrane design specifications. Dashed curves are power curves (right axis). Full lines are potential curves (left axis). Data points are to closely spaced to be distinguishable.

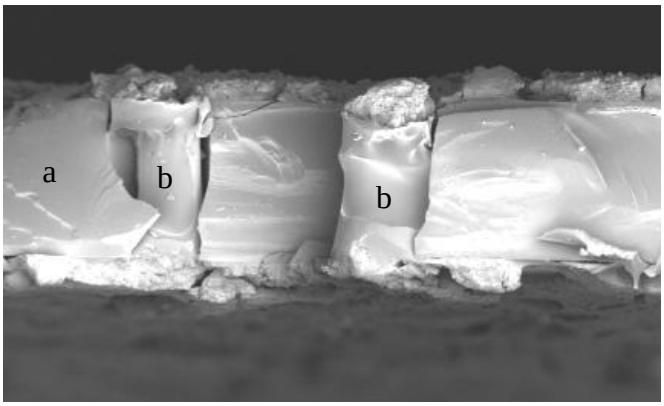

Fig. 6: SEM image of a cross-sectional fracture of a silicon membrane (a) after ionomer treatment. Cavities are visible in the center of the membrane filed pores (b).

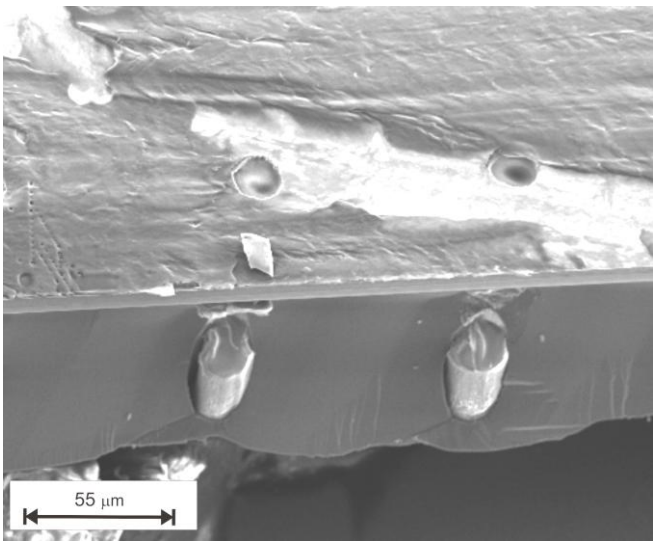

Fig. 7: SEM image of a cross-sectional fracture of a membrane after ionomer treatment. The fracture line is not perpendicular to the surface, and therefore exposes two ionomer filled columns.

DISCUSSION

Ionomer membrane creation has proven to be a critical point of the fabrication, and improved control of the structure of the finished membrane is currently being investigated. Methods of futher improving the membrane post insertion have yet to be considered, though for classical membranes both heat treatments as well as potential ramping methods have been reported to improve the proton conductivity.

Using silicon to reduce the active membrane area should, (1), reduce the ionic conductivity and, (2), fuel crossover of themembrane by the same fraction and, (3), slightly reduce electrode performance due to increased distances between reaction sites and the membrane.

IV-characteristics have shown that even though the active membrane area is 8-10 times lower than the total membrane area, the performance of the devices are comparable to all-Nafion® membranes. This suggests that it is not the ionic conductivity of the membrean, but rather the electrode performance and the fuel crossover that limits the fuel cell performance. Further testing will show if variations of the geometry can optimize the tradeoff between proton conductivity and crossover to the specific device needs. Reliability testing is still needed to determine if the membrane is capable of providing mechanical stability to reduce delamination problems in the catalyst layers.

CONCLUSION

This work has resulted in small working direct methanol fuel cells, capable of operation within the power range of very low-power small scale portable systems. The full consequences of the design choices have yet to be characterized, especially regarding methanol crossover. The qualitative effects of membrane quality on performance have indicated that membrane formation is a critical point in the device fabrication and requires further optimization. Two fuel cells were capable of operation with peak powers of 4 mW/cm^2, which is in the lower range of power requirements for small size portable electronics such as hearing aids or other medical devices. This shows promise that future improvements will increase the power into the range where batteries in such devices can be replaced with micro fuel cells.

REFERENCES

[1] A. Heinzel, V.M. Barragán, Journal of Pwer Sources 84 (1999), pp. 70-74

[2] Y.H. Seo, Y. Cho, *Sensors and Actuators. 150 (2010)*, pp. 87-96.

[3] Z. Lie, T. Haolin, P. Mu, *Journal of Membrane Science. 312* (2008), pp. 41-47.

[4] P. Choi, N.H. Jalani, R. Datta, *Journal of The Electrochemical Society 152* (2005), E123-E130

F

Transducers & Eurosensors 2013 Manuscript

This manuscript covers early characterization of the final design used by the devices covered in chapter 4.

CHARACTERISATION OF MICRO DIRECT METHANOL FUEL CELLS WITH SILICON PLATE SUPPORTED INTEGRATED IONOMER MEMBRANES

J.V. Larsen[1], B.T. Dalslet[1], C.Kallesøe[2] and E.V.Thomsen.[1]*
[1]Technical University of Denmark (DTU), DTU Nanotech, Lyngby, DENMARK
[2]Danish Technical Institute (DTI), Materials Science, Taastrup, DENMARK

ABSTRACT

This work deals with the investigation and fabrication of Micro Direct Methanol Fuel Cells (μDMFC). They are investigated as a possible alternative for zinc-air batteries in small size consumer devices such as hearing aids. In such devices the conventional rechargeable batteries such as lithium-ion batteries have insufficiently low energy density in the range 240 Wh/L to 300 Wh/L. Methanol is a promising fuel for such devices due to the high energy density, with pure methanol having an energy density of 4400 Wh/L. Using a liquid fuel also allows refueling, which can be achieved much faster than battery recharging. These features make μDMFC a suitable replacement energy source for small scale devices. Presented are two devices that delivered a peak performance of 1.77 mW/cm^2 and 2.5 mW/cm^2 while having drastically different perforated areas; 0.9% and 40% respectively.

KEYWORDS

Electro Chemical Power Generation, Micro Direct Methanol Fuel Cells, Integrated Ionomer Membrane

INTRODUCTION

Presented is a μDMFC based on Micro Electro-Mechanical Systems (MEMS) silicon technology. In contrast to typical stack based silicon devices [1], this development focuses on an integrated ionomer membrane in a bipolar plate configuration. Where traditional bipolar plate silicon designs include the ionomer membrane by clamping silicon electrodes around a precast membrane, this design casts the membrane directly into the silicon support structure.

Previously others [2] have shown integrated membranes used with in-plane flow devices. These devices rely on a pumping system and are therefore not inherently scalable to the desired scales, but they are very interesting devices for studying the dynamics of fuel cell systems on small scale devices.

The ionomer used in this work is Nafion^R, a proton conducting sulfonated tetraflouroethylene based fluoropolymer-copolymer. This polymer is cast from a resin solution into a defined silicon structure, which is intended to improve mechanical stability, and lead to a reduction in permeation through geometrically restricting the membrane area. This lower permeability comes at the cost of lower conductivity, and therefore the potential inherent in the tradeoff is studied through variation in the geometry of the perforation.

The chips include mechanical support frames to increase mechanical stability of the finished support frames. These frames are visible on the anode side of the chip as shown in figure 1. As the Nafion^R swells significantly during water uptake [3], it is expected that the mechanical fixation will help reduce the swelling while increasing the stress in the membrane.

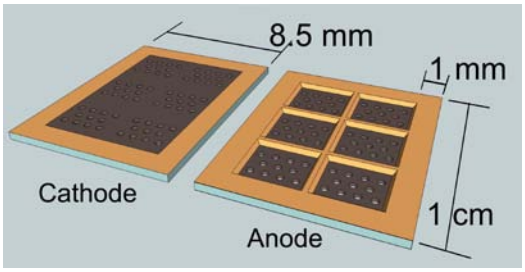

Figure 1: 3D schematic illustration of chip prior to ionomer integration and catalyst deposition. Holes are shown in larger scale to be visible.

FABRICATION

The support frame and plates are defined through KOH etching, after which the perforation is carried out by dry-etching a triangular lattice of holes using Deep Reactive Ion Etching (DRIE). A schematic of the device cross-section is shown in figure 2. The lattice structure of two chip geometries can be seen in figure 3. The silicon structure is then wet oxidized to define a 1 μm thick oxide to provide electrical insulation. The collector-electrodes are then defined by e-beam evaporation deposition of 10 nm Ti adhesion layer and 200 nm Au.

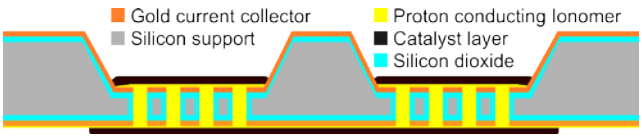

Figure 2: Schematic view of device cross section, showing two perforated plates and the supporting frame structure. Elements are not shown to scale.

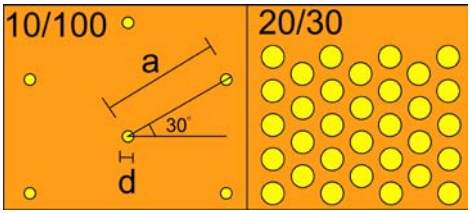

Figure 3: Illustration of a top-down view of the lattice showing the large difference in perforated area between two geometries. To the left is shown 10 μm holes with 100 μm lattice spacing (0.9% perforation) and right is 20 μm holes with 30 μm spacing (40%). d indicates hole diameter and a indicates lattice constant.

The ionomer membrane is then cast into the finished support structures. During the fabrication different methods of casting the ionomer into the silicon structure were evaluated. The solvent occupies up to 80% of the volume of the original ionomer liquid solution, and the challenge is to allow evaporation without formation of voids in the structure. The most successful method was found to be an immersion drying method with a post baking step. The support structures are immersed in ionomer solution along with a 2 mm topping layer of isopropyl alcohol, in a polydimethylsiloxane (PDMS) gasket seen in figure 4. The topping layer slows the initial evaporation and facilitates the removal of dissolved gas and surface bubbles from the solvent through evacuation. The liquid is then removed through drying under evacuated conditions at a pressure of ~300 mbar. After drying the devices are baked at 150°C for 20 min.

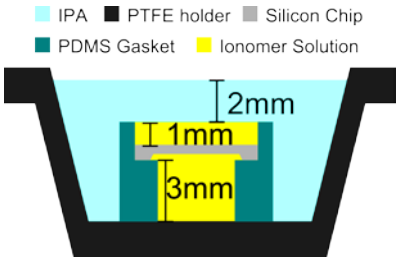

Figure 4: Illustration of the geometry employed during casting of the membrane.

The results of this integration method can be seen in the cross-section SEM image shown in figure 5, which shows SEM image of a chip cross-section after ionomer casting but prior to catalyst deposition. It can be seen that the polymer fills the plate perforation. The strands can also be seen to be longer than the holes. This is due to the stretching incurred during the chip fracture. The surface is covered in an approximately 1 μm thick layer of Nafion^R, which potentially limits the contact between the catalyst layer and buried collector electrode.

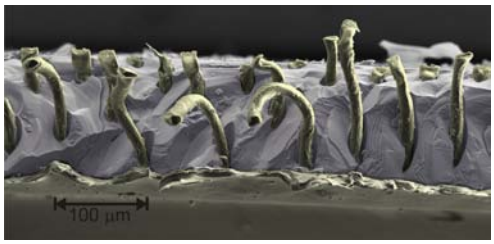

Figure 5: SEM image of a chip cross section, showing the ionomer filled perforated silicon plate. The lattice spacing is 100 µm and the holes are 20 µm. The image is shown in false color, where the grayscale SEM image has had silicon regions tinted blue and ionomer regions tinted yellow

The catalyst layers are spray coated mixtures of Pt for the cathode and PtRu for the anode, both on carbon black in a Nafion^R containing alcohol solution. The catalyst loadings are 2 mg/cm^2 for the anode and 4 mg/cm^2 for the cathode. The silicon support is heated to 80°C during the spray deposition to aid solvent evaporation. Figure 6 shows both sides of the chip after catalyst deposition.

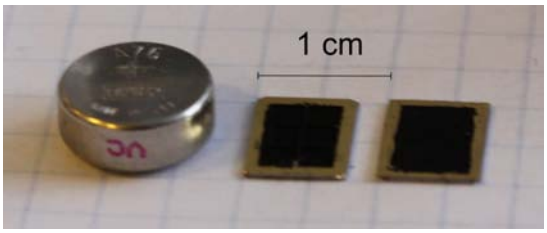

Figure 6: Image of the device after catalyst deposition, without reservoir next to an A76 Battery for scale comparison.

CHARACTERISATION

The devices are operated under pump-free passive conditions. The finished membrane electrode assembly is 7.5 mm x 10 mm x 350 µm with the membrane supporting plate having a thickness of 100 µm. If considered including a 200 µL fuel reservoir the total device volume would be approximately 0.5 cm^3. When specifying current density the area used for normalization is the chip surface minus the 1 mm edges leading to a 0.44 mm^2 surface area.

The performance of the devices were tested through IV characterization, by sweeping the current and measuring potential, using 3 molar methanol in water as fuel at the cathode, and using air at ambient conditions as oxidizer. Scan rates were chosen to provide stable curves with low hysteresis in forward reverse scans.

The devices have shown peak power performances in the range 1-2.5 mW/cm^2, with open circuit potentials (OCV) between 300-480 mV. The highest performance was seen with a high ratio of perforation; 2.5 mW/cm^2 for a device with 20 µm diameter holes and a lattice constant of 30 µm, corresponding to 40% perforation, see figure 7.

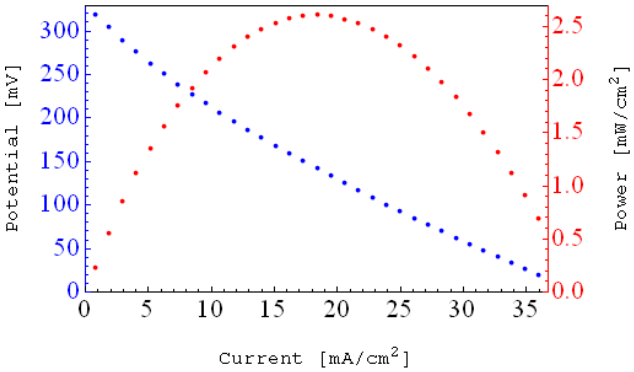

Figure 7: IV curve showing the performance of a device with 20 µm diameter holes and 30 µm lattice spacing, corresponding to 40% perforation. Scan rate was 0.2 mA/s. The red curve indicates power and corresponds to the right axis. The blue curve indicates potential and corresponds to the left axis.

Devices with a lower ratio of perforation have also

been tested and showed reasonable performance, specifically a 10 µm diameter, 100 µm lattices spacing corresponding to 0.9% perforation showed a peak power of 1.77 mW/cm^2. The IV-curve is shown in figure 8. While the two devices show similar performances, the current density through the Nafion^R polymer in these two cases varies greatly between 45 mA/cm, and 1577 mA/cm, due to the large difference in perforation.

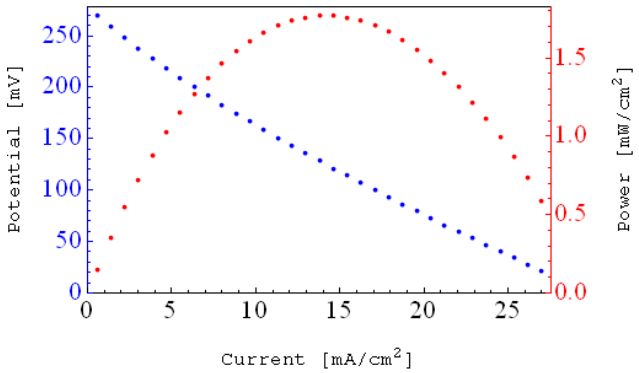

Figure 8: IV curve showing the performance of a device with 10 µm diameter holes and 100 µm lattices spacing, corresponding to 0.9% perforation. Scan rate was 0.2 mA/s.

CONCLUSION

The fabrication and characterization of a silicon plate integrated ionomer membrane fuel cell was shown to lead to working fuel cell.

It is shown that acceptable performance is possible within a large variation of plate geometry, varying between a low and high relative membrane coverage of 0.9% perforation, and 40% perforation, with power densities achieved respectively 1.77 mW/cm^2 and 2.5 mW/cm^2.

The current densities at peak power conditions were found to be 45 mA/cm^2 and 1577 mA/cm^2 for high and low perforation respectively, showing the very large difference in the membrane conditions during operation, even as the power densities are in similar scales.

ACKNOWLEDGEMENTS

This work was supported by the Micropower project. A collaboration between The Danish National Advanced Technology Foundation, Widex, Danish Technological Institute and the DTU Nanotech department of The Technical University of Denmark.

REFERENCES

[1] S. Sundarrajan, "Progress and perspectives in micro direct methanol fuel cell", in *International J. Hydrogen Energy. Vol 37, issue 10, pp Pages 8765–8786*. 2012.

[2] M.Shen, S.Walter, M.A.M. Gijs, "Monolithic micro-direct methanol fuel cell in polydimethylsiloxane with microfluidic channel-integrated Nafion strip", *J. Power Sources.*, vol. 193 issue 2, pp. 761–765, 2009.

[3] P Dimitrova, K.A Friedrich, B Vogt, U Stimming, "Transport properties of ionomer composite membranes for direct methanol fuel cells" J. Electroanalytical Chemistry, vol. 532 issue 1-2 pp. 75-83, 2002

CONTACT

*J.V.Larsen, tel: +0045-45256313; jvila@nanotech.dtu.dk

G

Article Submitted to Journal of Power Sources

This article covers the IV and EIS characterization of devices covered in chapter 4 and chapter 5.

Micro Direct Methanol Fuel Cell with Perforated Silicon-Plate Integrated Ionomer Membrane

J. V. Larsen[a,*], B. T. Dalslet[a], A.-C. Johansson[a,b], C. Kallesøe[b], E. V. Thomsen[a]

[a] *Department of Micro- and Nanotechnology, Technical University of Denmark, DTU Nanotech, Building 345B, DK-2800 Kongens Lyngby, Denmark*
[b] *Danish Technological Institute, Nano- and Microtechnology - Materials Characterization and High-Tech Production, DK-2630 Taastrup, Denmark*

Abstract

This article describes the fabrication and characterization of a silicon based micro direct methanol fuel cell using a Nafion ionomer membrane integrated into a perforated silicon plate. The focus of this work is to provide a platform for micro- and nanostructuring of a combined current collector and catalytic electrode. AC impedance spectroscopy is utilized alongside IV characterization to determine the influence of the plate perforation geometries on the cell performance. It is found that higher ratios of perforation increases peak power density, with the highest achieved being 2.5mW/cm^2 at a perforation ratio of 40.3%. The presented fuel cells also show a high volumetric peak power density of 2 mW/cm^3 in light of the small system volume of 480 μL, while being fully self contained.

1. Introduction

In recent times as consumer electronic devices have continued to scale down in size and increase in complexity, so has the requirements on their power-sources increased. On the typical device scale, the power requirements of mobile phones and laptops can be fulfilled to some extend with lithium ion batteries allowing modest battery lifetimes as well as easy recharging. However on the smaller device scale such as personal medical devices and hearing aids, the size requirements have made typical rechargeable batteries infeasible. These devices, which must operate at room temperature, are primarily powered by single use zinc-air batteries. This work deals with silicon based micro Direct Methanol Fuel Cells (μDMFC) as a possible replacement power source for such small medical devices. These can potentially deliver higher energy density, as well as very fast recharging through fuel exchange, which can be carried out in seconds. Methanol fuel cells work by oxidizing methanol at a catalyst layer at the anode which is typically constructed from platinum/ruthenium alloys to mitigate carbon monoxide poisoning, while oxygen is reduced at the catalyst layer at the cathode typically constructed from platinum. Silicon technology when used in μDMFC is typically employed to create micro-structured current collector electrodes, which are then stacked around a conventional catalyst coated proton conductive polymer layer, conventionally 100 μm thick Nafion 117 sheets. Such a design is termed a bipolar plate design [1]. This design is often used in active systems utilizing pumps and operating at elevated temperatures [2, 3, 4] but has also been implemented in room temperature operating passive air-breathing cells [5, 6, 7].

In this article the focus is on a novel silicon based bipolar plate design with an integrated membrane as opposed to the conventional stacked electrode design [5], for which the silicon electrodes are mechanically attached around a conventional membrane structure. The presented design allows the full cell to be defined in a single silicon wafer without need for bonding or mechanical assembly, and with the fuel reservoir attached simply through conductive adhesives or soldering.

In a review of the current state of μDMFC research by Sundarrajan et al. [8] two major disadvantages of silicon fabrication techniques were highlighted: There is poor adhesion between the proton conductive polymer membrane and the silicon plates, and silicon is brittle making it difficult to compress the cell to lower the electrical resistance between the catalyst layers and the bipolar silicon plates.

The design presented in this work, shown in figure 1, addresses both of these disadvantages by integrating the ionomer membrane directly into a silicon plate structure. The problem of poor adhesion is solved by mechanical locking of the membrane into the structure such that when in a dry state the polymer is held in place mechanically, and when in a wet state the expansion of the polymer will press against the sides of the locking structure and increase the adhesion.

The problem of contact resistance is addressed by integrating the current collector electrodes into the silicon support, burying them beneath the catalyst layer. This can potentially re-

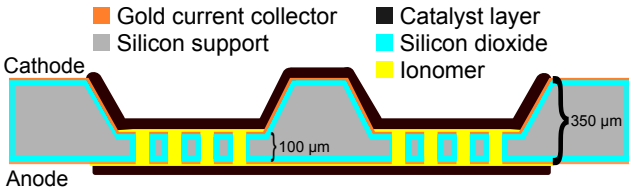

Figure 1: Schematic illustration of the fuel cell design. The cell geometry is a bipolar plate configuration with the ionomer membrane integrated into a silicon plate structure. Elements are not to scale.

*J. V. Larsen, jvila@nanotech.dtu.dk

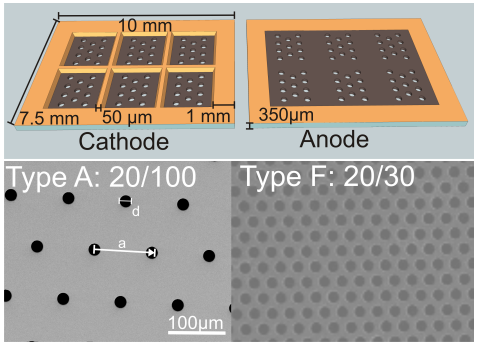

Figure 2: Top) A 3D view of the anode and cathode sides of the device. The frames are shown to scale, the hole lattice is enlarged greatly to make it visible. Bottom) Top view SEM image of the hole lattice for Type A and Type F devices.

duce the needs for high force clamping, and allows for non-conducting materials to be used as Gas Diffusion Layers (GDL). Typically these layers must fill the role of both GDL as well as contact layer between catalyst and current collector plates, and are therefore limited to conductive materials.

2. Experimental

2.1. Micro Direct Methanol Fuel Cell Design

The devices covered in this article were designed with the purpose of studying the influences of geometrical variations in a silicon plate integrated ionomer membrane, a side view is shown schematically in figure 1. Current collector electrodes were integrated into the silicon plate surface by deposition of 100 nm thick gold layers. The plate structure is etched into a 350 μm thick silicon wafer, the 100 μm thick plates are then perforated by etching a lattice structure of holes as shown in figure 2. The lattice spacing, a, and hole diameters, d, were then varied to study the effects of different aspect ratios with devices constructed to have 6 different geometries denoted type A-F as listed in table 1.

The perforation ratio, α, is given by the ratio of the area of three holes ($A_h = 3\,\frac{\pi}{4}\,d^2$) to a lattice unit cell area ($A_{lu} = 3\,\sqrt{3}/2\,a^2$). Both resistance and methanol permeation will scale inversely with this active area ratio ($\alpha = \frac{\pi}{2\sqrt{3}}(\frac{d}{a})^2$). Under the assumption that the pores defined by the holes are completely filled, the higher perforation should lead to an increased proton conductance between the anode and cathode but also an increased diffusive flow of methanol through the membrane.

2.2. Fabrication of Silicon Plate Supported Fuel Cell

A step by step schematic illustration of the fabrication process is shown in figure 3. The major elements are; definition of the supporting plates, perforation of the plates, electrode definition, ionomer integration and catalyst layer deposition. These elements are explained below with references to the step numbers in figure 3.

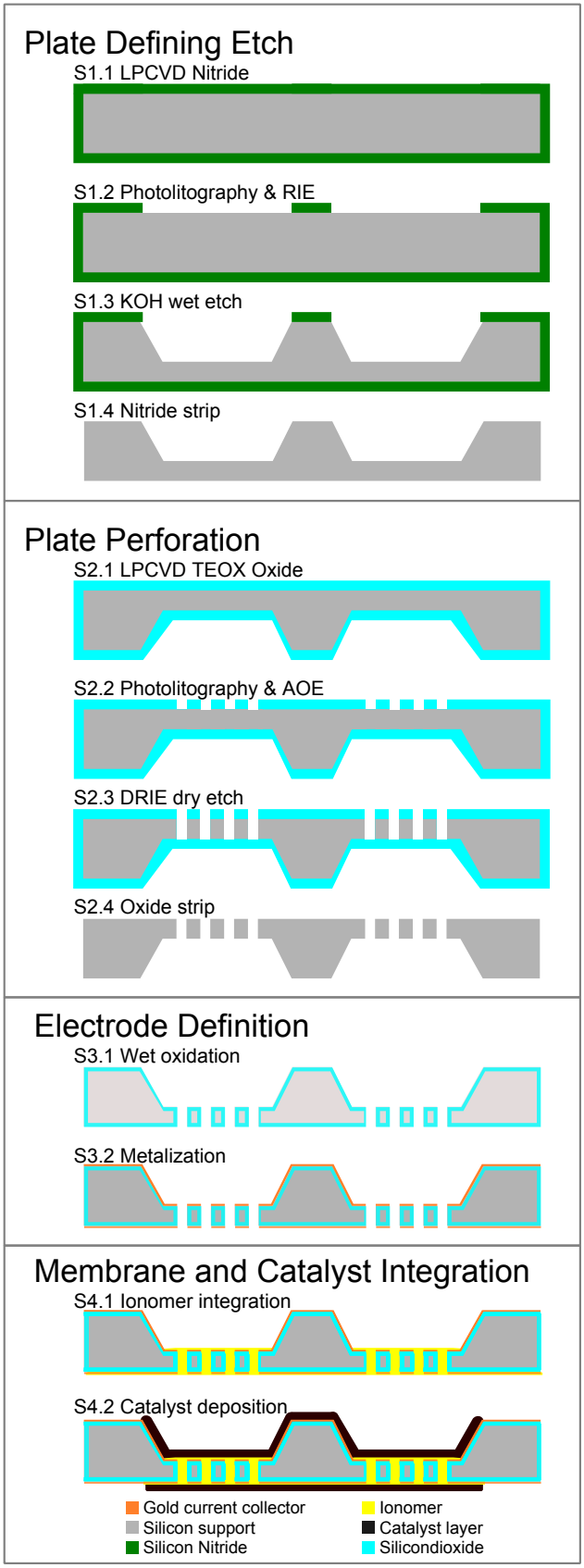

Figure 3: Illustration of the fabrication process flow. The process consists of two mask steps (S1.2, S2.2), passivisation and metalization steps (S3.1-2) and the ionomer integration step followed by a spray coating of catalyst layers (S4.1-2). Elements are not to scale.

Device Type	Hole Diameter [μm]	Lattice Spacing [μm]	Perforation ratio [%]
A	20	100	3.6
B	10	60	2.5
C	10	30	10.1
D	15	45	10.1
E	10	20	22.7
F	20	30	40.3

Table 1: Table of perforation lattices investigated during this work. The perforation ratio is the fraction of the proton conductive area to the catalytically active area.

2.2.1. *Silicon Plate Defining KOH Etch*

In order to achieve a thin plate which still has sufficiently high mechanical strength to allow processing and dicing, KOH wet etching is used to define a recess in the wafer (step S1.1-4). Prior to etching a Low Pressure Chemical Vapor Deposition (LPCVD) silicon rich low stress nitride layer of 100 nm is deposited (S1.1). The frame mask is defined through photolithography and Reactive Ion Etching (RIE) of the silicon nitride layer (S1.2). The wafers are submerged in a 80°C hot 28% mass fraction KOH solution for approximately 3.5 hours (S1.3). The process is timed in order to create 100 μm thick plates with the masked regions forming 350 μm thick support frames as shown in the top part of figure 2. Alongside the frames, the anisotropic nature of the KOH etch is also used to simultaneously define 50 μm wide V-groves along the boundaries of each device which serve as fracture lines during dicing. The etching of these groves self terminate at 50 μm depth due to the highly anisotropic etch rate of KOH in silicon. These fracture lines are used as an alternative dicing method, because conventional sawing is damaging to fragile surface structures. After the etching the remaining silicon nitride is stripped in hot phosphoric acid (S1.4).

2.2.2. *Silicon Plate Perforation*

The perforation of the silicon plate is carried out using Deep Reactive Ion Etching (DRIE). The etch mask is created by first depositing a 2 μm LPCVD tetraethyl orthosilicate (TEOS) oxide layer (S2.1), which is patterned through positive photolithography (S2.2). The layer is much thicker than needed considering only etch selectivity. This is due to the simultaneous usage of the backside as a stop layer during the etch (S2.3). As such the layer is designed to be thick enough to withstand the pressure difference between the plasma chamber and the helium flow on the bottom side of the wafer which provides cooling during the etching process. It has been seen during processing that fractures can lead to the entire wafer declamping, which underlines the need for a thick oxide layer. Because the etch stops on the oxide layer charging is a potential problem which can lead to notch formations. This aspect is pronounced by the variations in geometry across the wafer which leads to large differences in etch rate. In order to ensure that the smallest features are fully etched, the larger features must be over-etched.

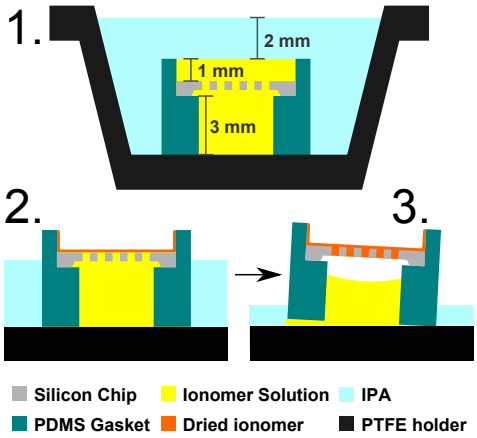

Figure 4: Schematic showing the setup for the evacuated evaporation drying used to integrate the ionomer in S4.1 of the fabrication process as shown in figure 3.

To alleviate this problem a low frequency generator is used to remove charge during the etch process, which stops the process when the bottom oxide is reached without under-etching along this stopping layer. The oxide mask/stop-layer is then stripped in buffered HF (S2.4).

2.2.3. *Electrode Definition*

In order to prevent shorts forming between the two current collector electrodes on either side of the silicon plate, the wafers are passivated in a dry oxidation, defining a 200 nm silicon dioxide layer (S3.1). The current collector electrodes are defined by first a sputter deposition of a 10 nm thick TiW anti-diffusion barrier followed by an e-beam evaporation of 100 nm gold (S3.2). The high directionality of e-beam evaporation prevents shorts through the plate perforation holes, however in trials with larger 100 μm holes short circuits have been observed.

2.2.4. *Membrane and Catalyst Integration*

The proton conducting ionomer membrane is integrated into the silicon plate using drying by evaporation from a solution under low pressure $\approx$ 300 mBar (S4.1). The geometry during the drying process is shown in figure 4. The drying is carried out with the finished silicon plates mounted in Polydimethylsiloxane (PDMS) molds. The dimensions of these molds critically affect the dynamics of the ionomer deposition on the plate surface.

The solution used is Nafion® DE 2020 by Sigma Aldrich consisting of 20 wt. % Nafion ion-exchange resin in lower alcohols with 34 wt. % water. Initially this solution is submerged entirely in pure isopropanol (Step 1). This delays the drying of the Nafion solution for approximately 2 hours, during which the solution can thoroughly degas. After this initial delay the Nafion solution will start to dry. As the solution dries, the Nafion concentration at the drying front steadily increases until it forms a solid membrane which deposits on the edges of the PDMS holder and on the device surface (Step 2). As the drying continues through the device, the dried Nafion detaches from the solution, and gas develops on the backside of the device

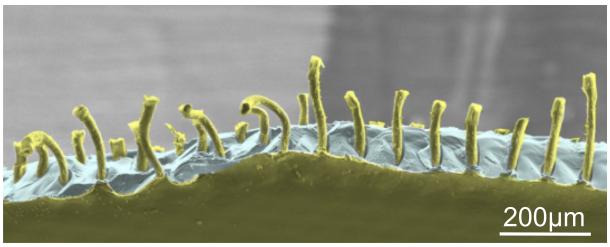

Figure 5: Scanning electron microscopy image showing the ionomer integrated into the silicon plate after annealing. The ionomer is colored green against the silicon which is colored blue. The strands of ionomer were elongated during the fracture of the device, and therefore appear longer than the thickness of the plate.

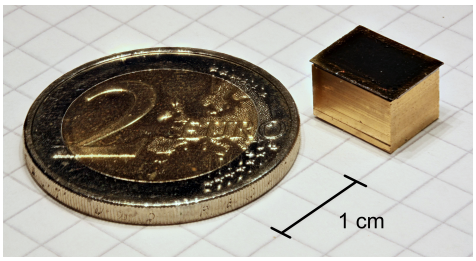

Figure 6: A finished device shown on top of a 220 μL capacity fuel reservoir shown next to a one euro coin for scale. Fuel is injected through holes in the bottom of the reservoir which are not visible.

(step 3). This pushes up the holder and causes the remaining ionomer solution to leak through the bottom. After the drying, the devices are annealed at 140°C for 30 min in ambient air. The annealing process removes any solvent remains and has been shown to reduce ionic resistance and increase mechanical stability [9].

The catalyst layer is added with spray deposition (S4.2). The final layer consists of carbon black supported catalyst particles bound by ionomer. The spray deposition solutions consisted of a dry catalyst powder dissolved in a water alcohol mixture which evaporates during the coating process. The dry powder consists of mass fractions of 70% Pt and 75% PtRu particles on the cathode side and anode side, respectively, supported on carbon black. The mixture also includes Nafion and a dispersion agent, polyvinylpyrrolidone, leading to the deposited catalyst layers having relative mass fraction loadings of 57% and 53% and catalyst loadings of 4 mg/cm^2 and 2 mg/cm^{2}on the cathode and anode, respectively To aid alcohol evaporation during spray deposition the devices are heated to 80°C during the coating process.

2.2.5. *Fuel Cell Assembly*

Finally the finished silicon device is attached to a CNC-milled brass reservoir, using a conductive adhesive. The reservoir consist of a 1 mm wall, with dimensions $10 \times 7.5 \times 6$ mm which gives an outer volume of 375 μL and a fuel volume of 220 μL. A finished device mounted on a fuel reservoir can be seen in figure 6. In this configuration the reservoir acts as the cathode connection, while the edge of the device on the top acts as the cathode connection. Depending on mounting usage, an additional top casing can be fixed to the top to protect the membrane from mechanical damage.

2.3. *Characterization Setups*

The finalized fuel cells have been characterized using current potential sweeps to determine their external performance characteristics in form of the power density and internal resistance. Also an AC impedance spectroscopy setup was used to characterize the through device resistance, to determine the integrated membrane conductivity. In both characterization setups the measurements are carried out using reusable electrodes and the devices were tested without fuel reservoirs mounted.

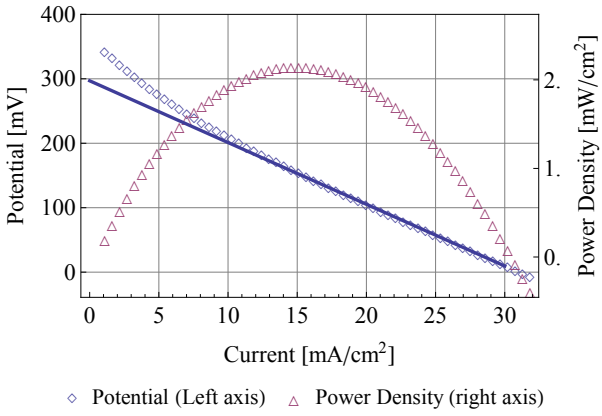

Figure 7: IV curve for a Type F device with 20 μm diameter holes with lattice spacing of 30 μm. The peak power is found to be 2.3 mW/cm^2. The solid line shows a linear fit used to determine an effective internal resistance which was found to be 21.77Ωcorresponding to 9.58 Ω/cm^2.

2.3.1. *Current Potential Characterization*

The characterization of the cells was carried out by varying the drawn current and measuring the potential using a Keithley 2100 source-meter. The silicon devices are placed between two copper electrodes, and a 200 μL reservoir filled with 3 M methanol. After the Open Circuit Potential (OCV) stabilizes, the current is swept from zero until the potential has decreased to zero at a scan rate of 0.2 mA/s. The peak power density is found by taking the maximum point in the power curve, and a measure of the total internal resistance (R_{int}) is found through a least squares fit to a linear ohmic potential loss. The fit is made in the region from the peak power density and upwards in current.

2.3.2. *AC Impedance Spectroscopy*

In order to relate the performance of the devices to a measure of the ionomer membrane conductivity, a measurement setup, based on AC impedance spectroscopy [10], was created and used to measure the ionic resistance through the devices. The setup consists of two liquid reservoirs filled with 1M sulfuric acid in water as can be seen in figure 8. The reservoirs are connected to the device such that it constitutes the sole conducting pathway between them. To generate and measure the electrical signals a four-point probe setup is used. Two platinum grid electrodes are situated in each reservoir clamped be-

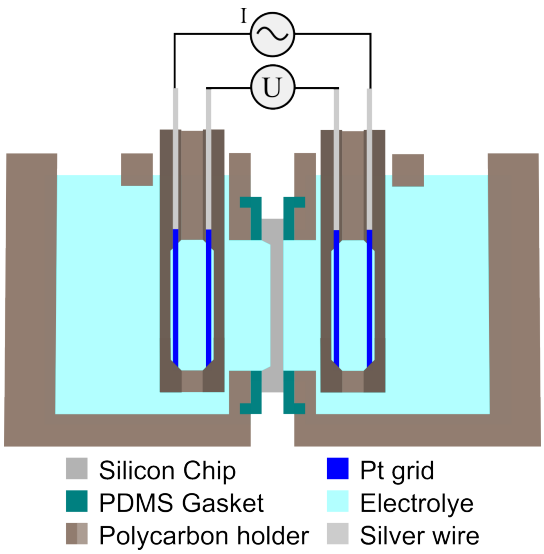

Figure 8: Illustration of the measurement setup used to determine the through device resistance, R_{td}. The four platinum grid electrodes are configured in a four-point probe geometry to eliminate resistances associated with the current through the source and current collector electrodes. The electrodes are fitted into two sets of three polycarbon plates, here shown in different shades to distinguish the individual plates.

tween polycarbonate plates. The impedance is measured using a Agilent 4294A precision impedance analyzer, with a potential signal amplitude of 100 mV rms.

3. Results and Discussion

3.1. Ionomer integration filling

A Scanning Electron Microscopy (SEM) image showing the cross section of a dried membrane can be seen in figure 5. The ionomer can be seen to fill the internal volume of the membrane. A thin approximately 5μm layer of Nafion is deposited on the bottom of the device. This side is the top side of the device illustrated in figure 4. The ionomer strands are longer than the membrane thickness due to being stretched during the cross-sectional fracture.

3.2. Power Density and Internal Resistance

A measured IV curve for a device of type F is shown in figure 7. The nonlinear shape of the potential curve is due to the non-linear losses associated with the chemical overpotentials. The exact curve-shape can be fitted using more detailed models [11], however instead an effective internal resistance is found to simplify comparisons. The power densities of the studied geometries, Types A-F, are all located in the range of to $0.5 - 2.5\,\mathrm{mW/cm^2}$, while the open circuit potentials are in the range of $300 - 470$ mV. The large deviation from the ideal standard potential of 1.18 V associated with the methanol oxidation reaction vs. an oxygen reduction reaction [12] is attributed to the formation of a mixed potential [13], as methanol diffuses through the membrane to the cathode side.

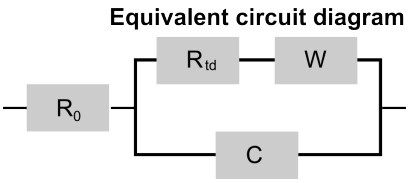

Figure 9: A Randles circuit is used to model the measured impedance spectrum. W is a Warburg diffusion element and$C$ is a capacitive element. R_{td} is the through device resistance, and R_0 is the serial resistance of the connecting elements.

3.3. Through Device Resistance

Two equivalent circuit models were used to model the measured impedance data and as fitting functions. The first model is a classical Randles circuit [14] shown in figure 9.

The resistance of the electrolyte is described by R_0. The resistance connected in parallel, R_{td}, is the resistance through the entire device, and therefore contains both contributions from the membrane and the porous catalyst layers. The capacitive element, C, models the geometric capacitance between the two sides of the device, and the Warburg element, W, models diffusion at the sensing electrodes. The impedance of the Warburg element, Z_w, and the capacitor, Z_C, are

$$Z_w = \sqrt{2}\frac{A_w}{\sqrt{i\,\omega}} \qquad Z_C = \frac{1}{C\,i\,\omega}$$

where A_w is the Warburg constant, ω the angular frequency and i the imaginary unit. The impedance of the Randles circuit is given by

$$Z_R = R_0 + \frac{1}{\frac{1}{R_{td}+Z_w} + \frac{1}{Z_C}} \tag{1}$$

The results of fitting this model to data can be seen in figure 10, where it is clearly shown that the model does not provide a satisfactory fit for the measured data.

The other model used is a modified Randles circuit. The Randles circuit is based on the assumption of a perfect capacitor as well as semi-infinite linear diffusion at the sensing electrodes. These assumptions are not applicable for the devices investigated, and the circuit is therefore modified to take non-ideal effects into account. Two changes are made. The Warburg element is substituted out for a constant phase element [15], Z_{Qw}, with amplitude W_a and phase angle parameter, n_w, close to the value of 1/2 that would correspond to an ideal Warburg element. The impedance is given by

$$Z_{Qw} = \frac{W_a}{(i\,\omega)^{n_w}}$$

Similarly the Randles circuit assumes an ideal capacitor, this assumption does not hold for these devices, since the ideal capacitor assumes a uniform medium and planar electrodes while the device has porous electrodes and a non uniform medium

[16]. Therefore the capacitive element is replaced with a constant phase element, Z_{Qc}, with prefactor $1/Q_c$, and a phase angle parameter, n, close to the value of 1, which would correspond to an ideal capacitor. The impedance of this element is given by

$$Z_{Qc} = \frac{1}{Q_c}\frac{1}{(i\,\omega)^n}$$

Finally the impedance of the modified Randles circuit, Z_M, becomes

$$Z_M = R_0 + \frac{1}{\frac{1}{R_{td}+Z_{Qw}} + \frac{1}{Z_{Qc}}}$$

During the fitting of impedance data to the modified Randles circuit the fitted phase angles for these two constant phase elements gave results close to the ideal values. For the Warburg and capacitive elements the average fitted values are $n_w \approx 0.32$ and $n \approx 0.9$, respectively.

Since the data is collected in a logarithmic frequency space, $F = \log_{10}(\omega/2\pi)$, during actual fitting the models are re-expressed as

$$\begin{aligned} F_0 &= \log_{10}\left(2\pi Q_c \sqrt[n]{R_{td}}\right) \\ Z_M(\Omega) &= R_0 + R_{td}\frac{1}{\left(1 + a\,(i\,10^F)^{-n_w}\right)^{-1} + i\,10^{n(F-F_0)}} \end{aligned} \quad (2)$$

where $a = W_a/R_{td}$ is the normalized Warburg element amplitude, and the phase angles are fixed to $n_w = \frac{1}{2} \wedge n = 1$ when fitting the unmodified Randles circuit.

The modified Randles model fits the data well, with the average standard error on the estimated membrane resistance R_{td} being $\sim 0.02\Omega$. A Nyquist plot of fit and data for a type D device is presented in the top of figure 10, a Bode plot is shown in the bottom part of the figure. The results show good agreement between data and the modified Randles circuit fit. The unmodified Randles circuit fit is also shown, and it clearly shows problems in describing the low frequency curve angle and circle suppression. In the modified Randles circuit, a systematic deviation is apparent in the low frequency side, or equivalently higher resistance side of the depressed semicircle. Here the model is defined to be symmetric about the central frequency, however a linear constant angle slope is observed in the Nyquist plot in the top of figure 10. An equivalent capacitance can be found for the constant phase element through $C_{eq} = \left(R_{td}\,2\,\pi\,10^{F_0}\right)^{-1}$ [16]. For the shown device the capacitance is found to be $C_{eq} = 43.8\,\text{nF}$, which is close to the expected range of the geometric capacitance for two $0.44\,\text{cm}^2$ electrodes separated by $100\,\mu$m silicon assuming a relative permittivity of $\epsilon_r = 11.6$ which is $C_g \approx 45\,\text{nF}$. The difference could be ascribed to the lowered relative permittivity of the plate due to the Nafion filled pores. The resistance found through this measurement is not strictly equal to the resistance through the membrane, as conductance through the porous ionomer containing catalyst layers also contribute. It is, however, assumed that the primary contribution arises from the membrane, due to the porous volume of the catalyst layers filling with electrolyte and due to the membrane being $100\,\mu$m thick vs. the $\sim 10\,\mu$m thick catalyst layers.

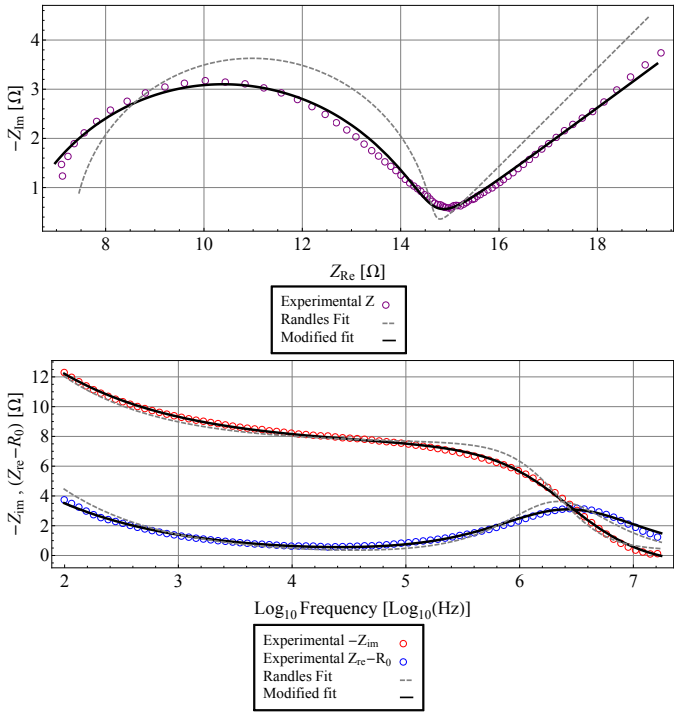

Figure 10: Measured impedance across a type D device with $15\,\mu$m holes in a $45\,\mu$m lattice, corresponding to 10% porosity. The top part of the figure shows a Nyquist plot and the bottom part shows a Bode plot. The results of the modified Randles circuit fit is a resistance of $8.3\,\Omega$, with an equivalent capacitance of 43.8 nF.

3.4. Influence of Plate Geometry on Performance

A batch of 9 devices were examined, for each device the internal resistance and peak power density were found through IV characterization and the through device resistance/conductance was determined by use of AC impedance spectroscopy.

A plot of the OCV as a function of the through device resistance is shown in figure 11. It can be seen that the OCVs of the devices were all located in the range of 300-550 mV. Devices with higher through device resistance are seen to also have higher OCV, indicating that reduction in membrane conductivity also reduces methanol permeation. The correlation between effective internal resistances of the devices and the measured through device resistance is plotted in figure 12. The figure shows a linear tendency which indicates that the differences in internal resistances are largely determined by the conductivity of the ionomer and contact resistances between catalyst layers and ionomer.

Figure 13 shows the relation between power density and the through device conductance, $\sigma_{td} = 1/R_{td}$. As expected a tendency of higher power density with higher conductance is observed. It is, however, apparent that devices with the same

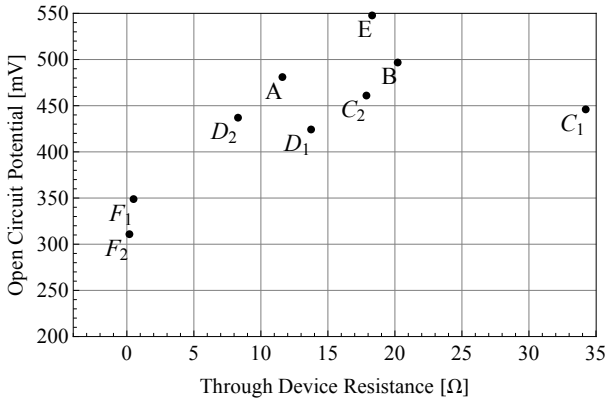

Figure 11: Open circuit potential shown against the through device resistance (R_{td}). All devices are shown to have OCV in the range of 300-550 mV. A tendency of higher OCV correlating to higher resistance through the device is observed.

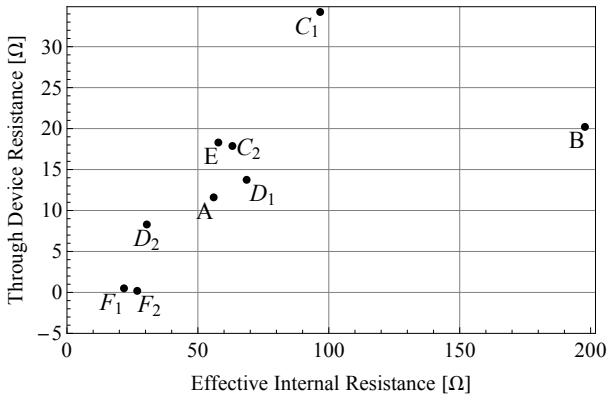

Figure 12: Correlation between effective internal resistances (R_{int}) of the devices and the measured through device resistance (R_{td}). Apart from the type B device outlier, a linear trend is observed.

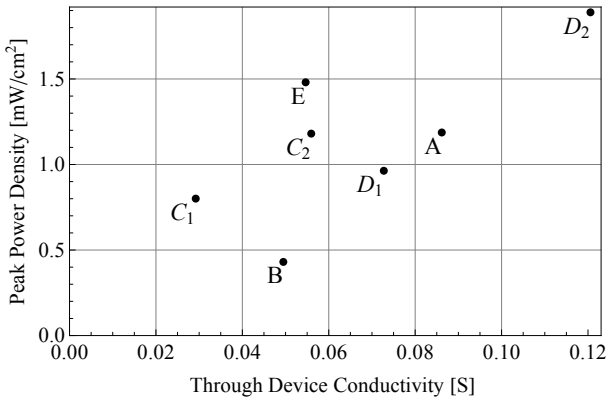

Figure 13: Power density shown against the through device conductivity. Devices of Type F are excluded as they are an order of magnitude higher.

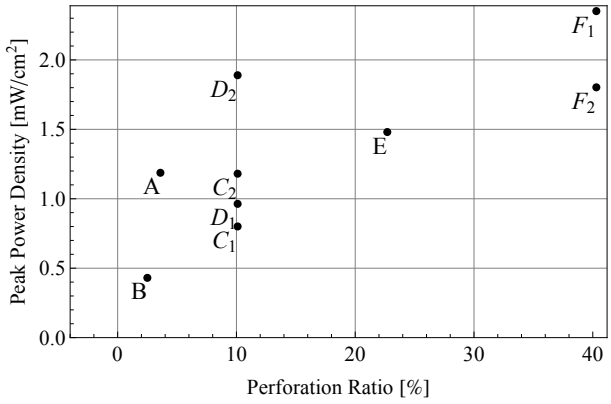

Figure 14: Power ratio plotted against effective perforation ratio. A tendency of increased performance with higher ratios of perforation is observed. A large variation is observed between devices of similar designs and similar perforation.

design, i.e. C_1 and C_2, have large variations in conductivity indicating that the membrane quality variation for each deposition overshadows the influences of the differences in plate geometry. The relation between peak power density and perforation ratio, shown in figure 14, illustrate that there is only a slight trend between perforation ratio and achieved peak power density. It is observed that a larger perforation ratio leads to a higher peak power, with the best device design being type F with a perforation ratio of 40.3%. When considered in light of the open circuit potential drop associated with lower resistances, seen in figure 11, this leads to the conclusion that the performance gains associated with an increase in conductivity is greater than the loss associated with increased methanol cross over in the devices studied.

3.5. Discussion

The performance of the fabricated devices are compared to other silicon based direct methanol fuel cell systems in Table 2. The systems are separated into passive and active categories based on the mode of operation. The table shows the peak power density per catalytic active geometric area, which shows the ability of the catalyst/membrane to deliver power. Also shown is the volumetric power density with respect to the outer system volume. The system volume is estimated from the referenced original works, and includes the mechanical structures needed to support the active cell.

The active systems utilize pumps to transport methanol to the anode, therefore their peak power densities are typically significantly higher than passive systems [2]. Especially systems utilizing an actively pumped oxygen flow are capable of achieving very high peak power density [1]. Another method often employed to increase power output is stacking multiple cells to achieve larger potentials [19, 18]. Active or stacked systems have a large volume and have been insufficient for use as power source in miniature electronic devices. Therefore it is interesting to compare the results against miniature passive fuel cell systems.

In comparison to a similar passive system by Gharibi et al. [7], the devices presented here show a higher performance with

Work	System size	Active area [cm^2]	Peak power density [mW/cm^2]	Volumetric peak power density [mW/cm^3]	OCV [mV]	T [$^\circ C$]	C_M [M]	Catalyst Loading [mg/cm^2]	Notes
Active systems									
Kelley et al.[1]	3 cm^2 x 1 cm	0.25	60	5.0	700	70	0.5	A: ~2 C: 1.5	Oxygen fed
Liu et al.[4]	1 cm^2 x 0.5 cm	1	4.7	9.4	450	RT	2	A: 2 C: 1	
Seo et al.[3]	3.5 cm^2 x 1 cm	1	0.031	0.000078	650	RT	1	NA	
Passive systems									
Hashim et al.[17]	7.5 cm^2x 5cm	4	12	0.32	2500	RT	4	A: 4 C: 2	Stacked
Chan et al.[18]	~30 cm^2 x 4cm	6.25	10.3	0.54	2900	70	6	A: 4 C: 2	Stacked
Shimizu et al. [6]	49 cm^2 x 4cm	36	10	1.84	550	RT	4	A: 2.5 C: 2.6	
Sabate et al. [5]	6 cm^2 x 1 cm	0.25	10	0.42	450	RT	2	A: 4 C: 4	
Gharibi et al.[7]	4.75 cm^2 x 3cm	4.75	1.2	0.40	500	RT	1	A: 1 C: 3	
This work	0.75 cm^2 x 0.7 cm	0.44	2.5	2.01	500	RT	3	A: 4 C: 2	

Table 2: Performance of different bi-polar plate designs compared to the integrated membrane of this work. The area used for the peak power density is the geometric area of the catalytic region. T is the operating temperature and RT denotes room temperature conditions. C_M denotes the methanol fuel concentration used. A and C denote the anode and cathode loadings of PtRu and Pt, respectively.

a smaller system size, and operating with open circuit potentials in a similar range, however using a higher methanol concentration. More mature systems like those presented by [6] show much larger power densities, up to $10\,mW/cm^2$, though operating at significantly larger total system sizes. It should be noted that their initial reported values were in the range of $1-4\,mW/cm^2$ and only through continual optimization was the higher value obtained. In that respect the designs presented here prove interesting as the catalyst layers have yet to be optimized for the membrane configuration, while elements such as micro-porous layers also have not yet been implemented. Designs such as [5] require that the electrodes and the conventional MEA are pressed together. Therefore a large amount of the total system volume is wasted on this mechanical assembly. When comparing system sizes, it can be seen that the presented design has a much lower total system size as there is no need for mechanical assembly. Comparing the volumetric power density numbers in table 2 it can be seen that the integrated design presented here is comparable to the stacked passive systems, while it's still somewhat below the active systems. These are however over estimates as the volume does not include the pumps needed during operation.

4. Conclusion

This work shows a silicon-plate integrated ionomer membrane for a passive direct methanol fuel cell. The designs were shown to lead to working fuel cells with IV characterization showing power densities of up to $2.5\,mW/cm^2$ under passive operation at room temperature. This performance compares favorable to other reported single stack silicon based passive air-breathing DMFCs [7], but is lower than state of the art in silicon based cell [5]. The presented devices however do not require high amounts of pressure to reduce contact resistance between silicon and catalyst layers. This allows them to operate with a much smaller total system volume, and the present work reports a volumetric power density of up to $2.5\,mW/cm^3$, which is superior to similar passive systems [17, 20, 6, 5, 7] and compares favorable to active systems even when not accounting for the volume taken up by their pumping systems [1, 4].

The devices were analyzed using AC impedance spectroscopy, which revealed a large geometry independent variation in the through device conductivity, indicating that the membrane integration is a critical fabrication step, which still needs improvement to ensure the deposited membrane conforms reproducibly to the underlying perforation geometry.

A tendency of increasing OCV associated with an increase in the membrane resistance was observed. The corresponding lower conductivity and associated ohmic losses however showed that the constriction did not provide a net performance gain. The highest performances were thus seen at the devices with the highest ratio of perforation.

Acknowledgment

The present work was supported by the Danish National Advanced Technology Foundation, under the project; "MicroPowerDK".

5. References

[1] S. C. Kelley, G. A. Deluga, and W. H. Smyrl. Miniature fuel cells fabricated on silicon substrates. *AIChE Journal*, 48(5):1071–1082, 2002.

[2] Chan Kim, Yong Jung Kim, Yoong Am Kim, Takashi Yanagisawa, Ki Chul Park, Morinobu Endo, and Mildred S. Dresselhaus. High performance of cup-stacked-type carbon nanotubes as a Pt-Ru catalyst support for fuel cell applications. *Journal of Applied Physics*, 96(10):5903–5905, November 2004.

[3] Young Ho Seo and Young-Ho Cho. Micro direct methanol fuel cells and their stacks using a polymer electrolyte sandwiched by multi-window microcolumn electrodes. *Sensors and Actuators A: Physical*, 150(1):87–96, March 2009.

[4] Xiaowei Liu, Chunguang Suo, Yufeng Zhang, Xilian Wang, Chi Sun, Ling Li, and Lifang Zhang. Novel modification of nafion 117 for a MEMS-based micro direct methanol fuel cell (uDMFC). *Journal of Micromechanics and Microengineering*, 16(9):S226–S232, September 2006.

[5] N. Sabate, J. P. Esquivel, J. Santander, N. Torres, I. Gracia, P. Ivanov, L. Fonseca, E. Figueras, and C. Cane. Fabrication and characterization of a passive silicon-based direct methanol fuel cell. In *2008 2nd European Conference Exhibition on Integration Issues of Miniaturized Systems - MOMS, MOEMS, ICS and Electronic Components (SSI)*, pages 1–4, 2008.

[6] Takahiro Shimizu, Toshiyuki Momma, Mohamed Mohamedi, Tetsuya Osaka, and Srinivasan Sarangapani. Design and fabrication of pumpless small direct methanol fuel cells for portable applications. *Journal of Power Sources*, 137(2):277–283, October 2004.

[7] Hussein Gharibi, Farhad Golmohammadi, and Mehdi Kheirmand. Fabrication of MEA based on optimum amount of co in PdxCo/C alloy nanoparticles as a new cathode for oxygen reduction reaction in passive direct methanol fuel cells. *Electrochimica Acta*, 89:212–221, February 2013.

[8] Subramanian Sundarrajan, Suleyman I. Allakhverdiev, and Seeram Ramakrishna. Progress and perspectives in micro direct methanol fuel cell. *International Journal of Hydrogen Energy*, 37(10):8765–8786, May 2012.

[9] Xiaoyu Ding, Sima Didari, Thomas F. Fuller, and Tequila A. L. Harris. Effects of annealing conditions on the performance of solution cast nafion membranes in fuel cells. *Journal of The Electrochemical Society*, 160(8):F793–F797, January 2013.

[10] N. Wagner, W. Schnurnberger, B. Müller, and M. Lang. Electrochemical impedance spectra of solid-oxide fuel cells and polymer membrane fuel cells. *Electrochimica Acta*, 43(24):3785–3793, August 1998.

[11] Brenda L. Garcia, Vijayanand Sethuraman, John W. Weidner, Roger Dougal, and Ralph E. White. Mathematical model of a direct methanol fuel cell. Technical report, May 2004.

[12] Jiujun Zhang and Hansan Liu, editors. *Electrocatalysis of Direct Methanol Fuel Cells*. Wiley-VCH, 1 edition, October 2009.

[13] Fuqiang Liu and Chao-Yang Wang. Mixed potential in a direct methanol fuel cell modeling and experiments. *Journal of The Electrochemical Society*, 154(6):B514–B522, June 2007.

[14] J. E. B. Randles. Kinetics of rapid electrode reactions. *Discussions of the Faraday Society*, 1(0):11–19, January 1947.

[15] C. Criado, P. Galán-Montenegro, P. Velásquez, and J.R. Ramos-Barrado. Diffusion with general boundary conditions in electrochemical systems. *Journal of Electroanalytical Chemistry*, 488(1):59–63, June 2000.

[16] G.J. Brug, A.L.G. van den Eeden, M. Sluyters-Rehbach, and J.H. Sluyters. The analysis of electrode impedances complicated by the presence of a constant phase element. *Journal of Electroanalytical Chemistry and Interfacial Electrochemistry*, 176(1-2):275–295, September 1984.

[17] N. Hashim, S.K. Kamarudin, and W.R.W. Daud. Design, fabrication and testing of a PMMA-based passive single-cell and a multi-cell stack micro-DMFC. *International Journal of Hydrogen Energy*, 34(19):8263–8269, October 2009.

[18] Y.H. Chan, T.S. Zhao, R. Chen, and C. Xu. A small mono-polar direct methanol fuel cell stack with passive operation. *Journal of Power Sources*, 178(1):118–124, March 2008.

[19] M.M. Ahmad, S.K. Kamarudin, W.R.W. Daud, and Z. Yaakub. High power passive uDMFC with low catalyst loading for small power generation. *Energy Conversion and Management*, 51(4):821–825, April 2010.

[20] B. D. Cahan and J. S. Wainright. AC impedance investigations of proton conduction in nafion. *Journal of The Electrochemical Society*, 140(12):L185–L186, December 1993.

Article Submitted to International Journal of Hydrogen Energy

This article was authored by Anne-Charlotte Johansson, and authored by Jackie V. Larsen, who contributed primarily to the fabrication of the carbon-nanotube support materials, as well as data analysis.

INTERNATIONAL JOURNAL OF HYDROGEN ENERGY 38 (2013) 11406–11414

Available online at www.sciencedirect.com

SciVerse ScienceDirect

journal homepage: www.elsevier.com/locate/he

Ru-decorated Pt nanoparticles on N-doped multi-walled carbon nanotubes by atomic layer deposition for direct methanol fuel cells

A.-C. Johansson [a,b,*], R.B. Yang [a], K.B. Haugshøj [a], J.V. Larsen [b], L. H. Christensen [a], E.V. Thomsen [b]

[a] Danish Technological Institute, Nano- and Microtechnology – Materials Characterization and High-Tech Production, DK-2630 Taastrup, Denmark

[b] Department of Micro- and Nanotechnology, Technical University of Denmark, DTU Nanotech, Building 345B, DK-2800 Kongens Lyngby, Denmark

ARTICLE INFO

Article history:
Received 24 February 2013
Received in revised form
10 June 2013
Accepted 19 June 2013
Available online 20 July 2013

Keywords:
Atomic layer deposition
Ru-decorated Pt catalyst
N-doped carbon nanotube
DMFC

ABSTRACT

We present atomic layer deposition (ALD) as a new method for the preparation of highly dispersed Ru-decorated Pt nanoparticles for use as catalyst in direct methanol fuel cells (DMFCs). The nanoparticles were deposited onto N-doped multi-walled carbon nanotubes (MWCNTs) at 250 °C using trimethyl(methylcyclopentadienyl)platinum $MeCpPtMe_3$, bis(ethylcyclopentadienyl)ruthenium $Ru(EtCp)_2$ and O_2 as the precursors. Catalysts with 5, 10 and 20 ALD Ru cycles grown onto the CNT-supported ALD Pt nanoparticles (150 cycles) were prepared and tested towards the electro-oxidation of CO and methanol, using cyclic voltammetry and chronoamperometry in a three-electrode electrochemical set-up. The catalyst decorated with 5 ALD Ru cycles was of highest activity in both reactions, followed by the ones with 10 and 20 ALD Ru cycles. It is demonstrated that ALD is a promising technique in the field of catalysis as highly dispersed nanoparticles of controlled size and composition can be deposited, with up-scaling prospects.

1. Introduction

There is a growing interest to power portable electronic devices using direct methanol fuel cells (DMFCs) due to the high energy density of methanol and the advantage of instant fuel replenishment (versus recharging) compared to conventional batteries [1]. In addition, the possibility of room temperature operation makes the DMFC ideal. For small scale, low power (~1 mW) portable devices, e.g., miniature medical devices such as hearing aids [2], those considerations are indeed important. The miniaturization is realized by having a passive supply of reactants, enabling a simple fuel cell system without auxiliary liquid pumps and gas blowers/compressors [3]. Silicon (Si) technology has been proposed as a route for the fabrication of such miniature DMFCs [4–8]. It is a mature field where versatile structuring of Si is available at the micro and nano regime.

The catalysts in a conventional DMFC are typically carbon black-supported noble metal nanoparticles, synthesized by wet chemistry methods [9]. For Si-based DMFCs it is desirable

* *Corresponding author*. Danish Technological Institute, Nano- and Microtechnology – Materials Characterization and High-Tech Production, DK-2630 Taastrup, Denmark.
E-mail addresses: anjoh@nanotech.dtu.dk, annecharlotte.johansson@gmail.com (A.-C. Johansson).
0360-3199/$ – see front matter
http://dx.doi.org/10.1016/j.ijhydene.2013.06.089

to apply a catalyst deposition method compatible to Si microfabrication. We have previously suggested atomic layer deposition (ALD) for the fabrication of a monolithic Si-based DMFC [10]. It is a vapour phase, thin film growth technique, based on self-limiting chemical reactions of alternating precursors on the sample surface [11]. ALD enables an excellent conformal and uniform growth with atomic layer precision control of layer thickness and composition. However, in certain circumstances ALD results in the growth of discrete nanoparticles [12–14]. For catalytic applications particles are generally preferred over a thin film because they have a larger surface-area-to-volume ratio and thus more catalytic active sites where the electrochemical reactions can take place. Lately, ALD is receiving attention in the field of catalysis [15–25] and it has turned out to be a promising catalyst deposition technique with up-scaling prospects [26,27].

Pt–Ru systems have been examined since the 1960s based on their high catalytic activity towards the methanol oxidation reaction (MOR) in acidic media [28,29]. The MOR mechanism for such systems is explained by two widely accepted models, the bifunctional and the ligand models [30].

Pt sites adsorb methanol and get poisoned by intermediates, mainly CO as it is the most stable one. For the oxidation of CO molecules surface-bonded oxygen groups are needed. According to the bifunctional mechanism, they are provided by Ru sites at lower potentials than Pt by water dissociation:

$$Ru + H_2O \rightarrow Ru - OH + H^+ + e^- \quad (1)$$

CO can then react with OH:

$$Pt - CO + Ru - OH \rightarrow Pt + Ru + CO_2 + H^+ + e^- \quad (2)$$

Consequently, the removal of CO is much faster on a Pt–Ru surface than on pure Pt.

The ligand effect is based on the alteration of the electronic structure of Pt, resulting in a decrease in the Pt–CO bond strength, so that less energy is required to oxidize the surface-bonded CO molecules.

Highly organized carbon support structures are needed in order to increase the utilization of the expensive noble metals and the mass transport within the catalyst layer [8]. Vertically standing CNTs have been demonstrated as a possible direction [31–33]. CNTs are also compatible with Si technology as they can be grown directly on Si substrates. Additionally, properties like high electrical conductivity and corrosion resistance make the CNTs potential substitutes to carbon black [34,35].

Pristine CNTs are chemically inert [36] and must therefore be functionalized prior ALD [37]. ALD Pt onto CNTs has been reported in the literature [16,22,24,25,38] and in all cases the CNTs were pre-treated by acid or plasma. However, due to the introduction of defects, the chemical and electrical properties of the CNTs are deteriorated [39].

Doping with nitrogen is a benign approach of making the CNTs chemically active [39–41]. Besides, there are advantages of using N-doped CNTs as support material over undoped ones. The electrical conductivity is improved [39]. In addition, it has been demonstrated that better catalyst dispersion, stability and activity are obtained [34,42–44].

Ru-decorated Pt electrocatalysts have been studied since the 1970s [29]. Ru has been added to the Pt surface using several methods, e.g., spontaneous deposition, electrodeposition and chemical vapour deposition [45]. The choice of method influences the resulting surface structure, with consequences for electrocatalysis.

Here we explore ALD as a new method for the preparation of Ru-decorated Pt catalysts for use in e.g., Si-based DMFCs. ALD catalysts of various Ru loading were prepared by controlling the number of ALD Ru cycles and evaluated using CO oxidation and MOR. The carbon support in this study was N-doped multi-walled CNTs (MWCNTs). Due to the chemical activity of the CNTs, we will show that no pre-treatment is required for the deposition of highly dispersed Pt particles.

The paper is organized as follows. The ALD Pt and Ru processes are first studied, then a brief study of the N-doped MWCNT growth and deposition of ALD Pt particles onto the CNTs is given. Finally the results from the electrochemical measurements of the Ru-decorated Pt nanoparticles are presented and compared with undecorated Pt nanocatalysts.

2. Material and methods

2.1. CNT growth

Vertically aligned, N-doped MWCNTs were grown in an AIXTRON Black Magic plasma-enhanced chemical vapour deposition (PECVD) system. The growth substrates were flat Si(100) 4″ wafers, coated with 100 nm of sputtered TiW (Wordentec QCL 800) and 3 nm of E-beam evaporated Ni (Wordentec QCL 800), serving as the diffusion barrier and CNT growth catalysts, respectively. The CNTs were grown at 850 °C at a pressure of 6 mbar with 100 W of plasma power. The flows of nitrogen, acetylene and ammonia during growth were 100, 40 and 160 sccm, respectively.

The elemental composition of the CNTs was acquired using X-ray photoelectron spectroscopy (XPS), K-Alpha from Thermo Scientific, equipped with a monochromated AlK_α X-ray source with energy of 1486.6 eV and X-ray sport size of 400 μm.

2.2. Study of the ALD Pt and Ru processes

Pt and Ru were deposited using a hot-wall, top-flow ALD reactor from Picosun (Sunale R-150). The precursors were trimethyl(methylcyclopentadienyl)platinum $MeCpPtMe_3$, bis(ethylcyclopentadienyl)ruthenium $Ru(EtCp)_2$ (Sigma Aldrich) and O_2 as the reactant in both ALD processes. The temperatures of the Pt and Ru precursors were set to 55 °C and 80 °C, respectively, and both were heated by a Picosolid Booster source system. The substrates used for the ALD study were flat Si(100) with native SiO_2, wet-thermally oxidized Si(100) or Si(100) substrates coated with ALD Al_2O_3 (on top of the native SiO_2). Our study concerns the definition of the so-called ALD window, i.e., the temperature range where the growth rate is independent of the deposition temperature, and optimization of the pulse time of the noble metal precursors. The purge time after both $MeCpPtMe_3$ and $Ru(EtCp)_2$ pulses was 6 s and the pulse/purge times of O_2 were 5 s/8 s throughout the ALD study.

The thickness of the ALD films was determined from X-ray reflectivity (XRR), measured with a PANalytical X'Pert Pro X-ray

diffractometer. The crystalline phases were identified by grazing incidence X-ray diffraction (GIXRD) using the same diffractometer with an angle of incidence of 1°. The resistivity of the Pt films was evaluated by a four-point probe electrical set-up. XPS was employed to determine the purity of the films using the same parameters as for the CNT sample. XPS depth profiles of Pt and Ru films were obtained by sputtering with Ar^+ ions of 500 eV.

2.3. ALD of Pt onto N-doped CNTs

Pt nanoparticles were deposited onto the N-doped CNTs and examined using transmission electron microscopy (TEM), FEI Technai T20 G2 or Philips CM100. The size distribution of the Pt particles deposited with various ALD cycles (50, 100 and 150 cycles) was calculated.

2.4. Preparation of the working electrode

Different catalysts were prepared by depositing various ALD Ru cycles (5, 10 and 20 cycles) on top of the CNT-supported ALD Pt nanoparticles (150 cycles), labelled Ru5Pt150-CNTs, Ru10Pt150-CNTs and Ru20Pt150-CNTs, respectively. Undecorated Pt catalyst, labelled Pt150-CNTs, was also prepared. The deposition temperature during the ALD Pt and Ru runs was 250 °C. The pulse/purge times of $MeCpPtMe_3$ and $Ru(EtCp)_2$ were 1 s/6 s and 3 s/6 s, respectively. The O_2 pulse/purge times during both the Pt and Ru cycles were 5 s/8 s.

An ink was prepared for each type of catalyst as follows. Si wafer pieces (in total half a 4″ wafer) with the CNT-supported ALD catalysts were dispersed in ethanol using an ultrasonic bath. The ethanol was then evaporated in a vacuum desiccator and the remaining catalyst powder was dispersed in 0.4 g of Millipore H_2O (18 MΩ·cm), 0.1 g of ethanol and 0.01 g of 5 wt% Nafion solution (DE 520, DuPont) for 10 min using a horn sonicator to obtain a well dispersed ink.

10 μl of the catalyst ink was pipetted onto a glassy carbon disk electrode (PINE), followed by drying in an air oven at 80 °C for 15 min. The catalyst-coated glassy carbon disk functioned as the working electrode in a three-electrode electrochemical set-up.

2.5. Electrochemical characterization

The catalysts were characterized at room temperature in a three-electrode electrochemical set-up. A Pt disk was used as the counter electrode and a Hg/Hg_2SO_4 saturated with K_2SO_4 (Radiometer analytical) served as the reference electrode. All potentials here are quoted in reference to the normal hydrogen electrode (NHE). We used 0.5 M H_2SO_4 and 1.0 M CH_3OH + 0.5 M H_2SO_4 as electrolytes, prepared from H_2SO_4 (Suprapur, Merck), CH_3OH (TraceSELECT, Fluka) and Millipore water (18 MΩ·cm). All solutions were degassed with N_2 (99.999%) before and during the measurements.

Cyclic voltammetry (CV) was carried out with a potentiostat from Gamry Instruments (Reference 600). The CVs were run first in 0.5 M H_2SO_4 solution at 50 mV/s for 60 cycles between 0 and 1.0 V for the Pt catalyst and up to 0.8 V for the Ru-decorated catalysts. This was followed by 10 cycles at 20 mV/s, using the same potential window.

CO-stripping was performed in 0.5 M H_2SO_4 electrolyte. Adsorption of CO on the electrode catalyst was conducted by bubbling the electrolyte with CO gas (5% CO in Ar, 99%) for 45 min, followed by purging with N_2 for 30 min to remove any residual CO from the solution. During CO and N_2 purging the working electrode potential was set to 50 mV and the electrolyte was magnetically stirred. The CO-stripping and blank CV curves were obtained from two consecutive scan cycles at 20 mV/s in the potential window of 50 mV and 1.0 V for the Pt catalyst and up to 0.8 V for the Ru-containing catalysts.

The ECSA for each catalyst was calculated using the CO oxidation peak area with the second cycle as the baseline, in order to correct for double-layer charging and oxide formation. For calculation of the ECSA, we used the value 420 μC/cm^2, which represents the charge density required to oxidize a monolayer of CO from a polycrystalline surface of Pt, assuming linear CO adsorption configuration [46].

The methanol electro-oxidation study on the CNT-supported catalysts was performed by CV measurements in 1.0 M CH_3OH + 0.5 M H_2SO_4 solution at room temperature. The CV curves were recorded from 0.2 to 0.8 V at a sweep rate of 10 mV/s.

Chronoamperometry was performed in 1.0 M CH_3OH + 0.5 M H_2SO_4 by holding the potential at 0.4 V for 1 h.

3. Results and discussion

3.1. Evaluation of the ALD Pt and Ru processes

3.1.1. The ALD Pt process

The dependence of growth rate and resistivity of Pt films (600 cycles) on deposition temperature is plotted in Fig. 1. The Pt films were deposited onto SiO_2/Si and the pulse time for $MeCpPtMe_3$ was 1 s. No Pt is deposited below 225 °C. The self-limiting behaviour is observed from 225 to 300 °C. The growth rate at 300 °C is 0.5 Å/cycle, which is equivalent to previous work [18,47]. However, at 325 °C the growth rate is

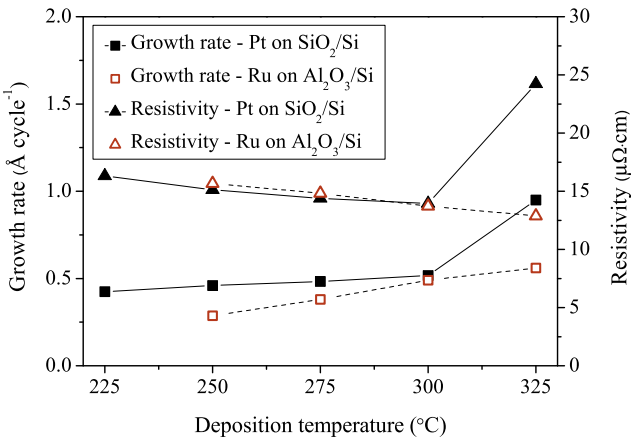

Fig. 1 – Growth rate and resistivity as a function of deposition temperature for Pt films (600 cycles) deposited on SiO_2/Si and Ru films (1000 cycles) deposited on Al_2O_3/Si. The $MeCpPtMe_3$ and $Ru(EtCp)_2$ pulse times were 1 s and 3 s, respectively.

significantly higher due to thermal decomposition of $MeCpPtMe_3$ [47]. The resistivity is reduced slightly with increasing temperature in the ALD window, from 16 to 14 μΩ·cm [47,48]. Moreover, the resistivity is considerably higher for the film deposited at 325 °C, probably caused by incorporation of Pt precursor ligands in the film.

Pt films deposited at 250 °C were further characterized using XPS depth profiling and GIXRD. The XPS depth profile in Fig. 2 shows the atomic percentages of platinum (Pt 4f), carbon (C 1s), oxygen (O 1s) and silicon (Si 2s) versus etch time for a Pt film (300 cycles) deposited on Si. The carbon and oxygen contaminations on the Pt surface were removed after one Ar^+ sputter cycle of 30 s and not detected in the bulk Pt film. The small oxygen peak at the interface of the Pt film and the Si substrate originates from the native SiO_2. The XPS depth profile shows that the Pt film is pure without incorporation of carbon from ligands or oxygen from partial oxidation of the Pt film.

The GIXRD pattern shown in Fig. 3a reveals that the Pt film (600 cycles) deposited on SiO_2/Si is polycrystalline. Pt (111), (200), (220), (311) and (222) diffraction peaks were observed [49].

Fig. 4 shows growth rate and resistivity as a function of $MeCpPtMe_3$ pulse times for the Pt films (600 cycles) deposited on SiO_2/Si at 250 °C. Saturated growth is obtained after 0.5 s. Furthermore, the resistivity is ~15 μΩ·cm for the films deposited with a Pt precursor pulse time of 0.5, 1 and 3 s and only slightly higher for the films grown with a $MeCpPtMe_3$ pulse time of 0.1 and 0.2 s.

3.1.2. *The ALD Ru process*

Growth rate and resistivity of Ru films (1000 cycles) deposited on Al_2O_3/Si as a function of temperature are plotted in Fig. 1. The $Ru(EtCp)_2$ pulse time was 3 s. Below 250 °C there was no deposition of Ru. Furthermore, the ALD temperature window is not as well defined as for the ALD Pt process. However, similar to Pt, the resistivity is low, 15 μΩ·cm for the film deposited at 250 °C, and is decreased somewhat with increasing deposition temperature, to 13 μΩ·cm at 325 °C.

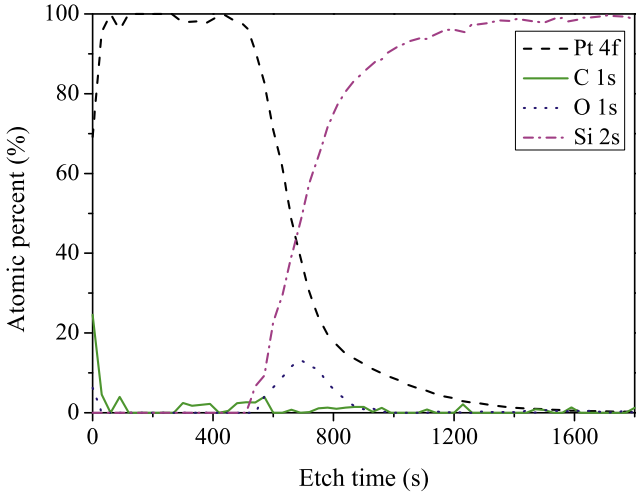

Fig. 2 – XPS depth profile of Pt film deposited on Si (300 cycles) at 250 °C. The $MeCpPtMe_3$ pulse time during deposition was 1 s.

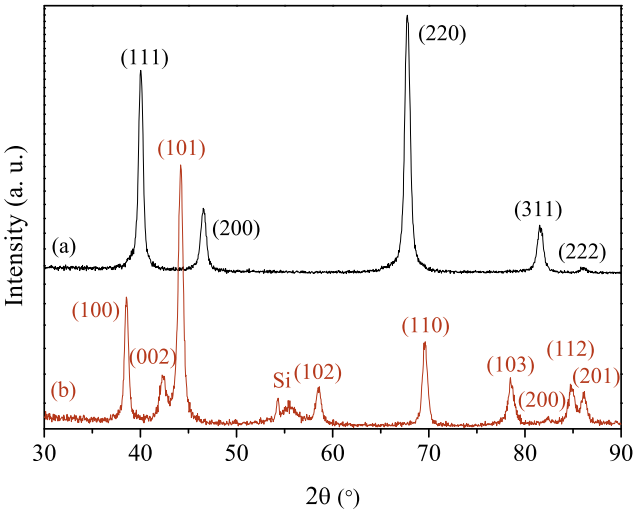

Fig. 3 – GIXRD of (a) a Pt film deposited on SiO_2/Si and (b) a Ru film deposited on Si, both at 250 °C, revealing polycrystalline films. The Pt and Ru precursor pulse times during deposition were 1 s and 3 s, respectively.

The Ru film deposited at 250 °C was further characterized using GIXRD, Fig. 3b. The Ru (100), (002), (101), (102), (110), (103), (200), (112) and (201) diffraction peaks [50] indicate that the Ru film is polycrystalline. The two peaks at 2θ angle of 54–55° are from the Si substrate.

Fig. 4 displays the dependence of growth rate and resistivity on the $Ru(EtCp)_2$ pulse times for Ru films (1000 cycles) deposited on Al_2O_3/Si at 250 °C. No saturation behaviour was observed. Moreover, the resistivity of the films deposited with a $Ru(EtCp)_2$ pulse time of 0.5 s and 1 s was around six times higher compared to that of the Ru films deposited with a Ru precursor pulse time of 3 s and 6 s. XPS depth profiling was performed in order to understand the difference in resistivity. The XPS depth profile in Fig. 5 depicts the atomic percentages of ruthenium (Ru 3d), oxygen (O 1s), aluminium (Al 2s) and

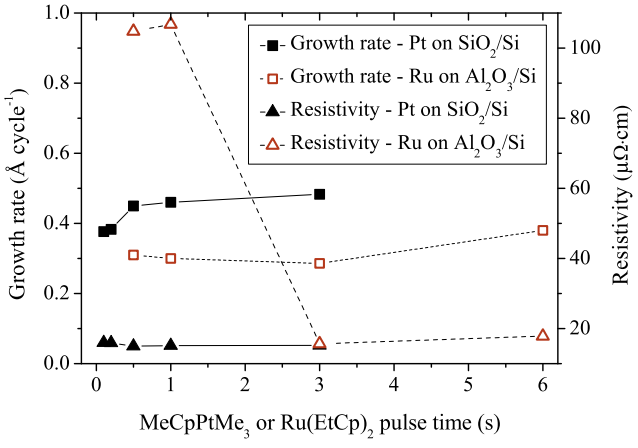

Fig. 4 – The dependence of growth rate and resistivity on the $MeCpPtMe_3$ or $Ru(EtCp)_2$ pulse time for Pt films (600 cycles) deposited on SiO_2/Si and Ru films (1000 cycles) deposited on Al_2O_3/Si at 250 °C.

silicon (Si 2p) versus etch time for the film deposited with a $Ru(EtCp)_2$ pulse time of 6 s. The XPS depth profile reveals that the surface is oxidized, but no oxygen was incorporated in the bulk of the film. Carbon impurities, on the other hand, cannot be determined directly since carbon (as C 1s) has the same binding energy as the Ru $3d_{3/2}$ orbital. The area ratio of Ru $3d_{5/2}$ to Ru $3d_{3/2}$ was 1.3–1.4 before Ar^+ sputtering. After sputtering for 30 s, the ratio is close to 3:2, corresponding to the theoretical value due to spin-orbit interactions of d electrons [51]. This ratio remains virtually constant throughout the film and indicates that the carbon concentration in the bulk of the film is minimal.

The XPS depth profile for the film grown with a Ru precursor pulse time of 0.5 s, Fig. 6, shows a Ru:O atomic ratio close to 1:1 throughout the deposited film. Thus, the higher resistivity is explained by the incorporation of oxygen.

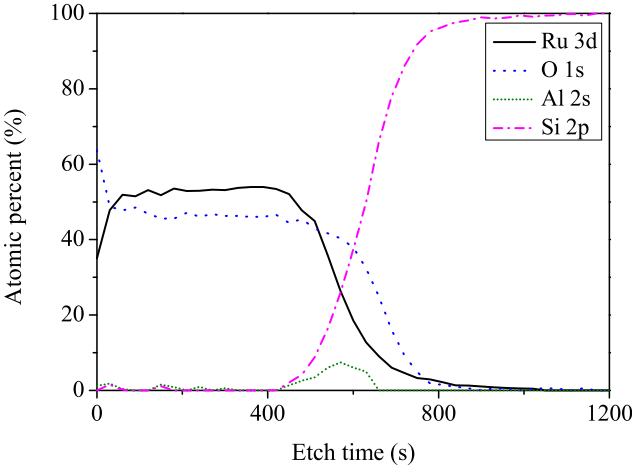

Fig. 6 – XPS depth profile of a Ru film (1000 cycles) deposited on Al_2O_3/Si at 250 °C with a pulse time of 0.5 s.

3.2. *Characterization of N-doped MWCNTs*

The CNTs were grown in an ammonia atmosphere and therefore expected to have nitrogen incorporated in the tube walls. The N-doping was confirmed by XPS, by acquiring the elemental composition of the CNTs grown on the Ni/TiW/Si substrate. The atomic percentages of each identified element are summarized in Table 1. In total 5.3 at% of N was detected. High resolution XPS spectra of O 1s showed that most of the oxygen originates from metal oxides. Besides that, smaller amounts of oxygen were incorporated in the CNTs as C–O and C=O. Ni is from the CNT growth catalysts, and Ti and W originate from the TiW diffusion barrier film. The tiny amount of F is due to contamination.

3.3. *ALD of Pt followed by Ru onto N-doped CNTs*

Pt was deposited onto the N-doped MWCNTs without pretreatment. The TEM images of CNTs coated with 50, 100 and 150 cycles of Pt in Fig. 7a–c, respectively, indicate that the Pt particles are well dispersed onto the carbon support. The arrows point at the Ni catalysts. The TEM images were used to examine the relationship between the particle size distribution and the number of ALD Pt cycles, see Fig. 8. There is an uncertainty in the particle size measurements due to difficulties in observing particles smaller than 1 nm. Nevertheless, as expected, the particle size is increased with ALD Pt cycle number. The average particle size is between 1.5 and 6 nm for ALD cycles between 50 and 150. Furthermore, we observed a nucleation delay at the first few tens of cycles, which is common for noble metal processes [11].

Due to the small amount of Ru deposited (5, 10 and 20 ALD Ru cycles), the particle size distribution for those catalysts has not been determined. Fig. 7d shows a TEM image of a 2 μm long CNT with well dispersed ALD catalysts (150 cycles of Pt and 10 cycles of Ru). Ru has higher surface energy than Pt, ~3.1 versus ~2.5 J/m^2 [52]. Therefore, Ru is expected to nucleate as islands on Pt.

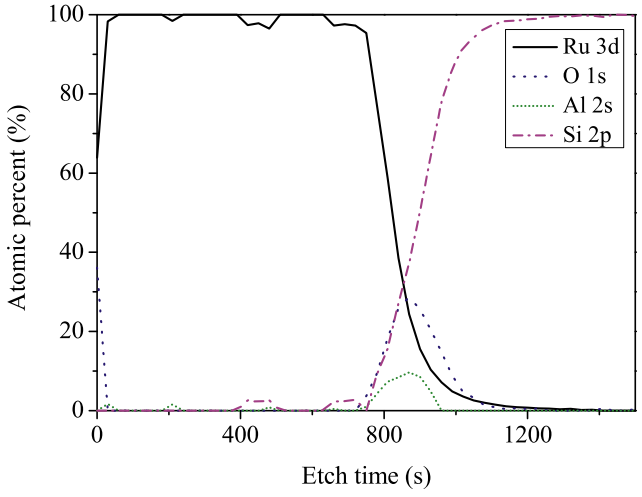

Fig. 5 – XPS depth profile of a Ru film (1000 cycles) deposited on Al_2O_3/Si at 250 °C with a Ru precursors pulse time of 6 s.

3.4. *Catalytic activity of the CNT-supported ALD nanoparticles*

The current densities in the following subsection are given per electrochemically active surface area (ECSA), calculated from the CO-stripping measurements.

The CVs for the Pt150-CNT, Ru5Pt150-CNT, Ru10Pt150-CNT and Ru20Pt150-CNT catalysts in Fig. 9 are obtained in 0.5 M

Table 1 – Elemental composition of the N-doped MWCNTs grown on Ni/TiW/Si.

Element	Atomic%
C	83.2
N	5.3
O	6.7
Ni	2.3
Ti	1.4
W	0.8
F	0.4

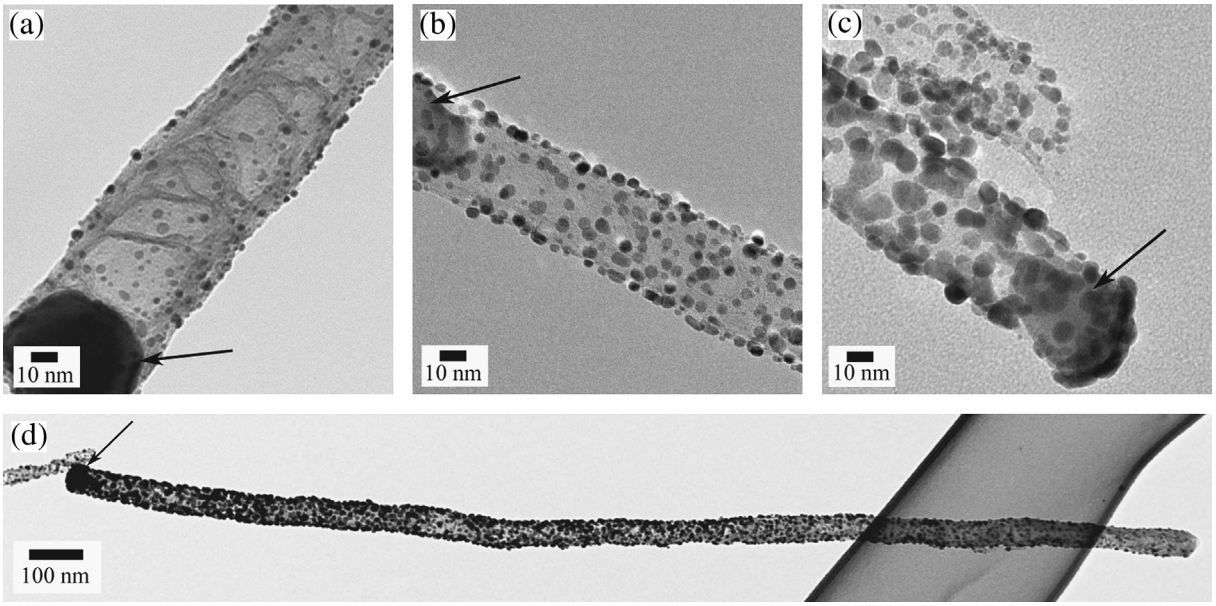

Fig. 7 – (a), (b) and (c) are TEM images of N-doped MWCNTs coated with 50, 100 and 150 ALD Pt cycles, respectively. (d) TEM image of a 2 μm long CNT with ALD catalysts (150 cycles of Pt + 10 cycles of Ru). The arrows point at the Ni catalyst particles.

H_2SO_4 at 20 mV/s and the 10th cycle is plotted. The three characteristic potential regions for the Pt150-CNT catalyst are well defined (Fig. 9a): The hydrogen adsorption–desorption (H_{upd}) region between 0 and ~0.35 V, the double layer charging-discharging region up to about 0.7 V, followed by the third region with adsorption–desorption of oxygenated species on the surface of Pt. The peaks in the H_{upd} region are due to the presence of different Pt crystalline facets, showing that the Pt nanoparticles are polycrystalline [46], as also seen in Fig. 3a. The origin of the hump at around 0.48 V is not completely clear. It has been observed by others [53,54] and is probably associated with oxygenated species on the carbon support.

For comparison, the CVs for the catalysts with added Ru (Ru5Pt150-CNT, Ru10Pt150-CNT and Ru20Pt150-CNT) are plotted in Fig. 9b. The features of the CV graphs show the effect of Ru. The peaks in the H_{upd} region are not visible as Ru, which is significantly less active than Pt for H adsorption–desorption [55], is blocking Pt sites. Furthermore, there is an overlap of the hydrogen and oxygen adsorption regions since Ru oxide formation commences at around 0.2 V. As a consequence, the double layer region is less pronounced with larger current density than for pure Pt. In addition, the current density increases with the number of ALD Ru cycles.

The tolerance towards CO poisoning of the Pt and Ru-decorated Pt catalysts was evaluated from CO-stripping experiments in 0.5 M H_2SO_4. Fig. 10 depicts the CVs recorded for the different catalysts. The solid and the dashed lines are the first and the second cycles, respectively, measured after CO

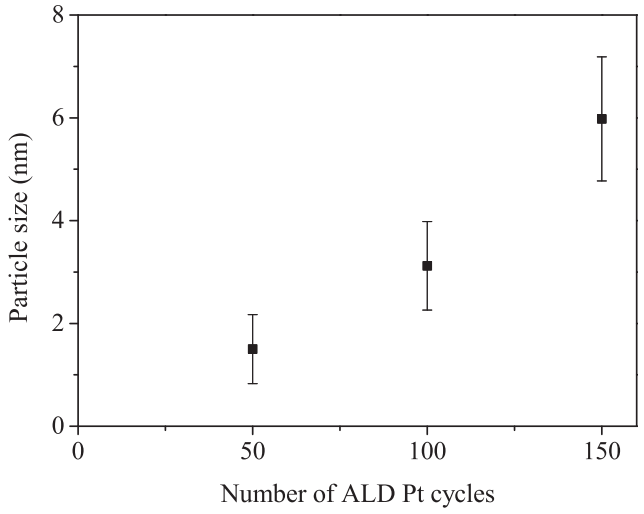

Fig. 8 – Dependence of Pt particle size on the number of ALD cycles.

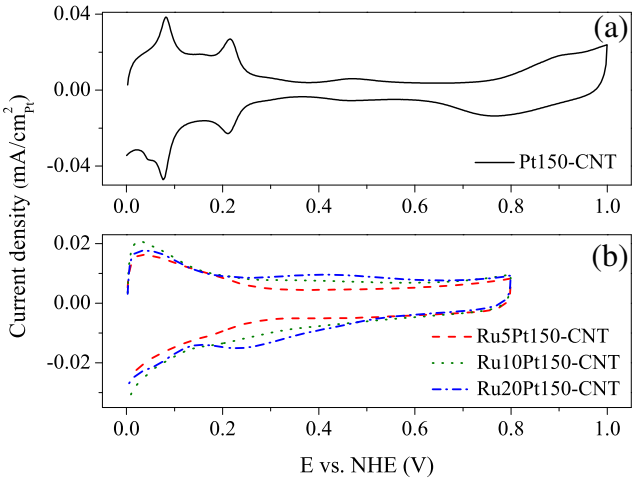

Fig. 9 – CVs of (a) the Pt-CNT catalyst and (b) the Ru5Pt150-CNT, Ru10Pt150-CNT and Ru20Pt150-CNT catalysts in 0.5 M H_2SO_4 at 20 mV/s.

adsorption at 50 mV. The suppression of the features in the H_{upd} region and the pseudo-capacitive current during the first forward sweep indicates that the electrode surface was saturated with CO molecules [56]. The anodic peak corresponds to the oxidative stripping of the adsorbed, irreversible CO monolayer. Furthermore, the second cycle reveals that all CO molecules were removed from the electrolyte.

The CO-stripping peak for the Pt150-CNT catalyst in Fig. 10a has a shoulder before the main oxidation peak, again attributed to different crystalline facets on the Pt surface. Compared to the Pt catalyst, the addition of 5 ALD Ru cycles onto the Pt nanoparticles, Fig. 10b, resulted in a CO oxidation peak potential shift of around −0.2 V. The vertical solid lines 1 and 2 mark the location of the CO oxidation peaks for the Ru5Pt150-CNT and Pt150-CNT catalysts, respectively. As observed in Fig. 9, Ru adsorbs oxygen-containing species at more negative potentials than Pt, thereby enabling CO oxidation at lower potentials. The CO oxidation peak potentials for the Ru10Pt150-CNT and Ru20Pt150-CNT catalysts, Fig. 10c and d, are located at potentials approximately 20 mV higher compared to the Ru5Pt150-CNT catalyst, showing that 5 ALD Ru cycles are sufficient for the preparation of a CO oxidation tolerant catalyst.

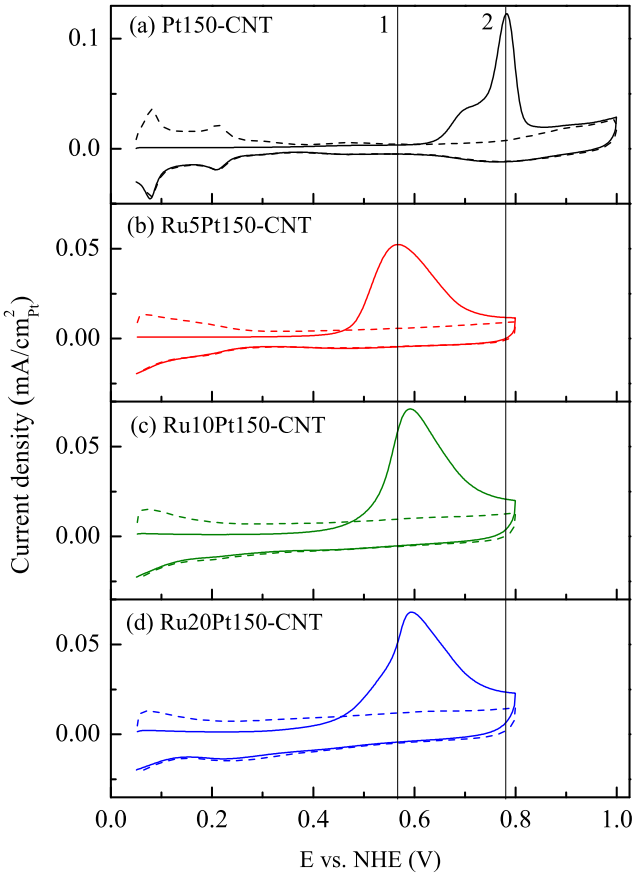

Fig. 10 – CO-stripping voltammograms of the (a) Pt150-CNT, (b) Ru5Pt150-CNT, (c) Ru10Pt150-CNT and (d) Ru20Pt150-CNT catalysts in 0.5 M H_2SO_4 solution at 20 mV/s. The solid and dashed lines are the first and second CVs after CO adsorption at 50 mV, respectively. The vertical solid lines 1 and 2 mark the location of the CO-stripping peaks for the Ru5Pt150-CNT and Pt150-CNT catalysts, respectively.

Catalytic activity of the Pt-CNT, Ru5Pt150-CNT, Ru10Pt150-CNT and Ru20Pt150-CNT for methanol electro-oxidation was measured using cyclic voltammetry and chronoamperometry. Fig. 11 presents the anodic scans of the 10th CV cycle at 10 mV/s, obtained in 1.0 M CH_3OH + 0.5 M H_2SO_4. The insert displays a magnification at low potentials. The background in 0.5 M H_2SO_4 at 10 mV/s was subtracted from the CVs. Since this is the 10th cycle we assume that methanol dehydrogenation fragments, mainly CO, are adsorbed onto the catalyst surfaces at low potentials, blocking further adsorption of methanol. At 0.4 V the Pt catalyst with 5 ALD Ru cycles added (Ru5Pt150-CNT) has the highest catalytic activity, followed by the Ru10Pt150-CNT, Ru20Pt150-CNT and Pt-CNT catalysts. The anodic scans show that the promotional effect of Ru is most pronounced at low overpotentials, which is also the potentials of technological interest in a direct methanol fuel cell [30]. Furthermore, it is clear that the oxidation current of the Pt150-CNT catalyst is superior from around 0.7 V, at which potential the Pt alone can dissociate water with a reasonable rate to form OH-groups and oxidize poisoning carbon species.

Chronoamperometry was performed on the catalysts at 0.4 V for 1 h in the methanol containing solution to investigate the steady-state behaviour, see Fig. 12. The current density for the Pt150-CNT is quickly lowered due to poisoning of mainly CO that block Pt surface sites, diminishing its ability to further electro-oxidize methanol. All three Ru-decorated Pt catalysts deliver a higher current density and get poisoned at a lower rate, indicating that all of them are better catalysts towards the MOR. The current densities after 1000 s for the Pt150-CNTs, Ru5Pt150-CNTs, Ru10Pt150-CNTs and Ru20Pt150-CNTs were 0.3, 5.1, 3.4 and 1.5 μA/cm^2, respectively.

According to the bifunctional mechanism, both Pt and Ru sites are needed at the surface of the catalyst in order to oxidize methanol at low potentials. Furthermore, three neighbouring Pt sites are required in order to dehydrogenate

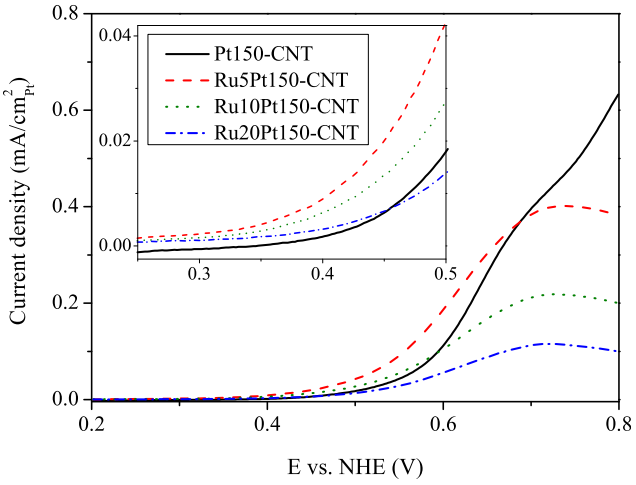

Fig. 11 – Anodic scans of the 10th CV cycle at 10 mV/s, obtained in 1.0 M CH_3OH + 0.5 M H_2SO_4 for the Pt150-CNT and the Ru-decorated Pt catalysts. The inset is a magnification at low potentials where the electro-oxidation of methanol commences.

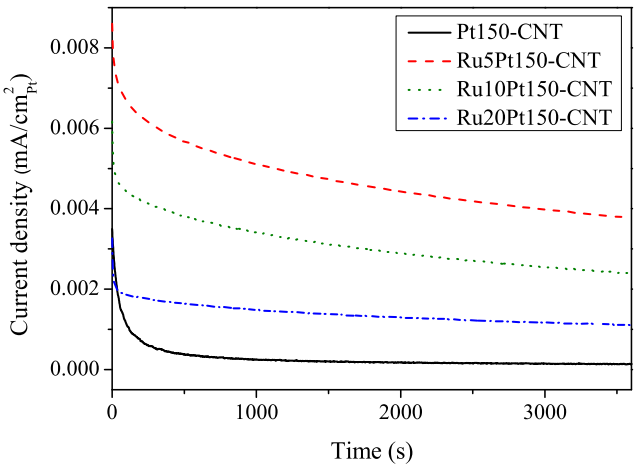

Fig. 12 – Chronoamperograms of the Pt and Ru-decorated Pt catalysts in 1.0 M CH_3OH + 0.5 M H_2SO_4 at 0.4 V.

methanol [57]. The best catalytic activity was measured for the catalyst with only 5 ALD Ru cycles. By depositing more Ru we see a dilution effect of the Pt, meaning there are fewer places fulfilling the requirement of Pt ensembles. However, since Ru is inert towards methanol adsorption [28] and that the Ru20Pt150-CNT catalyst is active towards MOR, we expect that the Pt surface of the Ru20Pt150-CNT catalyst is not completely coated with Ru. Furthermore, we probably also have a ligand effect, but it is typically less effective [58].

4. Conclusion

Highly dispersed ALD Pt nanoparticles were deposited onto N-doped MWCNTs without pre-treatment. Pt particles with average size between 1.5 and 6 nm could easily be obtained by varying the ALD cycle number. The Pt nanoparticles were decorated with Ru of various loading, i.e., various ALD Ru cycles (5, 10 and 20) and evaluated towards CO oxidation and MOR using cyclic voltammetry and chronoamperometry. The Pt nanoparticles decorated with 5 ALD Ru cycles exhibited highest catalytic activity in both reactions, followed by the catalysts with 10 and 20 ALD Ru cycles. The undecorated Pt catalyst had lowest activity, showing that small amount of Ru results in a significant enhancement in performance. The results were explained by the bifunctional and ligand models. We demonstrate that ALD is an excellent technique for depositing well dispersed catalyst particles of controlled size and composition. The compatibility of ALD in Si technology makes it a suitable catalyst deposition technique e.g., in the fabrication of micro DMFCs.

Acknowledgement

The research leading to these results has received funding from the European Community's Seventh Framework Programme (FP7/2007-2013) under grant agreement number ENHANCE-238409.

REFERENCES

[1] Aricò AS, Srinivasan S, Antonucci V. DMFCs: from fundamental aspects to technology development. Fuel Cell 2001;1(2):133–61.
[2] Hales J, Kallesøe C, Lund-Olesen T, Johansson AC, Fanøe H, Yu Y, et al. Micro fuel cells power the hearing aids of the future. Fuel Cell Bull 2012;2012(12):12–6.
[3] Zhao TS, Chen R, Yang WW, Xu C. Small direct methanol fuel cells with passive supply of reactants. J Power Sources 2009;191(2):185–202.
[4] Lu G, Wang C, Yen T, Zhang X. Development and characterization of a silicon-based micro direct methanol fuel cell. Electrochim Acta 2004;49(5):821–8.
[5] Motokawa S, Mohamedi M, Momma T, Shoji S, Osaka T. MEMS-based design and fabrication of a new concept micro direct methanol fuel cell (μ-DMFC). Electrochem Commun 2004;6(6):562–5.
[6] Pichonat T, Gauthier-Manuel B. Recent developments in MEMS-based miniature fuel cells. Microsyst Technol 2007;13(11–12):1671–8.
[7] Kamarudin SK, Achmad F, Daud WRW. Overview on the application of direct methanol fuel cell (DMFC) for portable electronic devices. Int J Hydrogen Energy 2009;34(16):6902–16.
[8] Sundarrajan S, Allakhverdiev SI, Ramakrishna S. Progress and perspectives in micro direct methanol fuel cell. Int J Hydrogen Energy 2012;37(10):8765–86.
[9] Liu H, Song C, Zhang L, Zhang J, Wang H, Wilkinson DP. A review of anode catalysis in the direct methanol fuel cell. J Power Sources 2006;155(2):95–110.
[10] Johansson AC, Dalslet BT, Yang RB, Haugshøj KB, Molgaard MJG, Christiansen K, et al. Electrocatalytic activity of Pt grown by ALD on carbon nanotubes for Si-based DMFC applications. ECS Trans 2012;50(13):117–25.
[11] Miikkulainen V, Leskelä M, Ritala M, Puurunen RL, Miikkulainen V. Crystallinity of inorganic films grown by atomic layer deposition: overview and general trends. J Appl Phys 2013;113(2):021301.
[12] Meng X, Zhong Y, Sun Y, Banis MN, Li R, Sun X. Nitrogen-doped carbon nanotubes coated by atomic layer deposited SnO_2 with controlled morphology and phase. Carbon 2011;49(4):1133–44.
[13] Lee HBR, Bent SF. Microstructure-dependent nucleation in atomic layer deposition of Pt on TiO_2. Chem Mater 2012;24(2):279–86.
[14] Weber MJ, Mackus AJ, Verheijen MA, van der Marel C, Kessels WMM. Supported core/shell bimetallic nanoparticles synthesis by atomic layer deposition. Chem Mater 2012;24:2973–7.
[15] King JS, Wittstock A, Biener J, Kucheyev SO, Wang YM, Baumann TF, et al. Ultralow loading Pt nanocatalysts prepared by atomic layer deposition on carbon aerogels. Nano Lett 2008;8(8):2405–9.
[16] Liu C, Wang CC, Kei CC, Hsueh YC, Perng TP. Atomic layer deposition of platinum nanoparticles on carbon nanotubes for application in proton-exchange membrane fuel cells. Small 2009;5(13):1535–8.
[17] Christensen ST, Feng H, Libera JL, Guo N, Miller JT, Stair PC, et al. Supported Ru-Pt bimetallic nanoparticle catalysts prepared by atomic layer deposition. Nano Lett 2010;10(8):3047–51.
[18] Jiang X, Gür TM, Prinz FB, Bent SF. Atomic layer deposition (ALD) co-deposited Pt-Ru binary and Pt skin catalysts for concentrated methanol oxidation. Chem Mater 2010;22(10):3024–32.
[19] Enterkin JA, Setthapun W, Elam JW, Christensen ST, Rabuffetti FA, Marks LD, et al. Propane oxidation over Pt/$SrTiO_3$ nanocuboids. ACS Catal 2011;1(6):629–35.

[20] Hsu IJ, Hansgen DA, McCandless BE, Willis BG, Chen JG. Atomic layer deposition of Pt on tungsten monocarbide (WC) for the oxygen reduction reaction. J Phys Chem C 2011;115(9):3709–15.
[21] Rikkinen E, Santasalo-Aarnio A, Airaksinen S, Borghei M, Viitanen V, Sainio J, et al. Atomic layer deposition preparation of Pd nanoparticles on a porous carbon support for alcohol oxidation. J Phys Chem C 2011;115(46):23067–73.
[22] Dameron AA, Pylypenko S, Bult JB, Neyerlin K, Engtrakul C, Bochert C, et al. Aligned carbon nanotube array functionalization for enhanced atomic layer deposition of platinum electrocatalysts. Appl Surf Sci 2012;258(13):5212–21.
[23] Hsieh CT, Chen WY, Tzou DY, Roy AK, Hsiao HT. Atomic layer deposition of Pt nanocatalysts on graphene oxide nanosheets for electro-oxidation of formic acid. Int J Hydrogen Energy 2012;37(23):17837–43.
[24] Hsueh YC, Wang CC, Kei CC, Lin YH, Liu C, Perng TP. Fabrication of catalyst by atomic layer deposition for high specific power density proton exchange membrane fuel cells. J Catal 2012;294:63–8.
[25] Shu T, Liao SJ, Hsieh CT, Roy AK, Liu YY, Tzou DY, et al. Fabrication of platinum electrocatalysts on carbon nanotubes using atomic layer deposition for proton exchange membrane fuel cells. Electrochim Acta 2012;75:101–7.
[26] Cavanagh AS, Wilson CA, Weimer AW, George SM. Atomic layer deposition on gram quantities of multi-walled carbon nanotubes. Nanotechnology 2009;20(25):255602.
[27] Li J, Liang X, King DM, Jiang YB, Weimer AW. Highly dispersed Pt nanoparticle catalyst prepared by atomic layer deposition. Appl Catal B Environ 2010;97(1–2):220–6.
[28] Gasteiger HA, Marković N, Ross PN, Cairns EJ. Methanol electrooxidation on well-characterized Pt-Ru alloys. J Phys Chem 1993;97(46):12020–9.
[29] Petrii OA. Pt-Ru electrocatalysts for fuel cells: a representative review. J Solid State Electrochem 2008;12(5):609–42.
[30] Rojas S, Martinez-Huerta MV, Pena MA. Supported metals for application in fuel cells. Catal Sci Ser 2012;11:407–92.
[31] Li W, Wang X, Chen Z, Waje M, Yan Y. Carbon nanotube film by filtration as cathode catalyst support for proton-exchange membrane fuel cell. Langmuir 2005;21(21):9386–9.
[32] Wang J, Yin G, Chen Y, Li R, Sun X. Pd nanoparticles deposited on vertically aligned carbon nanotubes grown on carbon paper for formic acid oxidation. Int J Hydrogen Energy 2009;34(19):8270–5.
[33] Tian ZQ, Lim SH, Poh CK, Lin J, Tang Z, Chua D, et al. A highly order-structured membrane electrode assembly with vertically aligned carbon nanotubes for ultra-low Pt loading PEM fuel cells. Adv Energy Mater 2011;1(6):1205–14.
[34] Shao Y, Yin G, Gao Y. Understanding and approaches for the durability issues of Pt-based catalysts for PEM fuel cell. J Power Sources 2007;171(2):558–66.
[35] Antolini E. Carbon supports for low-temperature fuel cell catalysts. Appl Catal B Environ 2009;88(1–2):1–24.
[36] Sharma S, Pollet BG. Support materials for PEMFC and DMFC electrocatalysts – a review. J Power Sources 2012;208:96–119.
[37] Marichy C, Pucci A, Willinger MG, Pinna N. Coating of carbon nanotubes. In: Pinna N, Knez M, editors. Atomic layer deposition of nanostructured materials. Weinheim: Wiley-VCH; 2012. p. 327–43.
[38] Hsueh YC, Wang CC, Liu C, Kei CC, Perng TP. Deposition of platinum on oxygen plasma treated carbon nanotubes by atomic layer deposition. Nanotech 2012;23(40):405603.
[39] Mabena LF, Sinha Ray S, Mhlanga SD, Coville NJ. Nitrogen-doped carbon nanotubes as a metal catalyst support. Appl Nanosci 2011;1(2):67–77.
[40] Terrones M, Jorio A, Endo M, Rao A, Kim Y, Hayashi T, et al. New direction in nanotube science. Mater Today 2004;7(10):30–45.
[41] Chen Y, Wang J, Meng X, Zhong Y, Li R, Sun X, et al. Atomic layer deposition assisted Pt-SnO_2 hybrid catalysts on nitrogen-doped CNTs with enhanced electrocatalytic activities for low temperature fuel cells. Int J Hydrogen Energy 2011;36(17):11085–92.
[42] Saha MS, Li R, Sun X, Ye S. 3-D composite electrodes for high performance PEM fuel cells composed of Pt supported on nitrogen-doped carbon nanotubes grown on carbon paper. Electrochem Commun 2009;11(2):438–41.
[43] Chen Y, Wang J, Liu H, Li R, Sun X, Ye S, et al. Enhanced stability of Pt electrocatalysts by nitrogen doping in CNTs for PEM fuel cells. Electrochem Commun 2009;11(10):2071–6.
[44] Chen Y, Wang J, Liu H, Banis MN, Li R, Sun X, et al. Nitrogen doping effects on carbon nanotubes and the origin of the enhanced electrocatalytic activity of supported Pt for proton-exchange membrane fuel cells. J Phys Chem C 2011;115(9):3769–76.
[45] Spendelow JS, Babu PK, Wieckowski A. Electrocatalytic oxidation of carbon monoxide and methanol on platinum surfaces decorated with ruthenium. Curr Opin Solid State Mater Sci 2005;9(1–2):37–48.
[46] Liu H, Zhang J, editors. Electrocatalysis of direct methanol fuel cells – from fundamentals to applications. 3rd ed. Weinheim: Wiley-VCH; 2009.
[47] Aaltonen T, Ritala M, Sajavaara T, Keinonen J, Leskelä M. Atomic layer deposition of platinum thin films. Chem Mater 2003;15(9):1924–8.
[48] Jiang X, Bent SF. Atomic layer deposition of platinum for solid oxide fuel cells. ECS Trans 2007;3(15):249–59.
[49] PDF 00-001-11994, The International Centre for Diffraction Data (ICDD); 2003.
[50] PDF 03-065-7645, The International Centre for diffraction Data (ICDD); 2003.
[51] Kim WH, Park SJ, Kim DY, Kim H. Atomic layer deposition of ruthenium and ruthenium-oxide thin films by using a $Ru(EtCp)_2$ precursor and oxygen gas. J Korean Phys Soc 2009;55(1):32–7.
[52] Vitos L, Ruban A, Skriver HL, Kollar J. The surface energy of metals. Surf Sci 1998;411:186–202.
[53] Zhou ZH, Li WS, Fu Z, Xiang XD. Carbon nanotube-supported Pt-H_xMoO_3 as electrocatalyst for methanol oxidation. Int J Hydrogen Energy 2010;35(3):936–41.
[54] Hernández-Fernández P, Montiel M, Ocón P, Gómez de la Fuente JL, García-Rodríguez S, Rojas S, et al. Functionalization of multi-walled carbon nanotubes and application as supports for electrocatalysts in proton-exchange membrane fuel cell. Appl Catal B Environ 2010;99(1–2):343–52.
[55] Gasteiger HA, Marković NM, Ross Jr PN. H_2 and CO electrooxidation on well-characterized Pt, Ru, and Pt-Ru. 1. Rotating disk electrode studies of the pure gases including temperature effects. J Phys Chem 1995;99(20):8290–301.
[56] Gasteiger HA, Marković NM, Ross Jr PN, Cairns EJ. CO electrooxidation on well-characterized Pt-Ru alloys. J Phys Chem 1994;98(2):617–25.
[57] Gasteiger HA, Marković N, Ross Jr PN, Cairns EJ. Electro-oxidation of small organic molecules on well-characterized Pt-Ru alloys. Electrochim Acta 1994;39(11–12):1825–32.
[58] Lu C, Rice C, Masel RI, Babu PK, Waszczuk P, Kim HS, et al. UHV, electrochemical NMR, and electrochemical studies of platinum/ruthenium fuel cell catalysts. J Phys Chem B 2002;106(37):9581–9.